The development of room temperature transparent conductive adhesive-laminate technology and its use in flexible opto-electronic devices.

Bryant, Daniel T. J

The Development of Room Temperature Transparent Conductive Adhesive-Laminate technology and its Use in Flexible Opto-Electronic Devices

Daniel T J Bryant

Thesis Submitted for the Degree of Engineering Doctorate

University of Wales Swansea
Department of Materials Engineering

ProQuest LLC.
789 East Eisenhower Parkway
P.O. Box 1346
Ann Arbor, MI 48106 – 1346

DECLARATION

This work has not previously been accepted in substance for any degree and is not being concurrently submitted in candidature for any degree.

Signed . ..... (Candidate)

Date 25/3/15

STATEMENT 1

This thesis is the result of my own investigations, except where otherwise stated. Other sources are acknowledged by footnotes giving explicit references. A bibliography is appended.]

Signed ..... (Candidate)

Date 25/3/15

STATEMENT 2

I hereby give consent for my thesis, if accepted, to be available for photocopying and for inter-library loans after expiry of a bar on access approved by Swansea University.

Signed . ..... (Candidate)

Date 25/3/15

So you run and you run to catch up with the sun but it's sinking,
Racing around to come up behind you again.
- Pink Floyd, Time

Summary

The field of printable next generation low cost opto-electronic devices has been a rapidly growing and developing scientific field. Specifically much interest has been gaining about new so called third generation printable photovoltaics and the impact they could have on an industrial scale. However the key to the realisation of this field as a technology and not merely lab curiosities is solving certain manufacturing processes required to scale these lab devices into large area modules. Typically charge collection at the counter electrode in such devices is achieved via evaporation of an opaque metallic contact onto the active material. This is an effective contact however it limits the potential for commercial manufacture and versatility given the expense of the metals employed (often gold and silver) and the non-transparent nature. Here we present the development and use of a novel semi-transparent electrode design combining a polymer embedded nickel grid with a transparent conducting contact adhesive that can be applied to solid state opto-electric devices providing conductivity, charge extraction, mechanical adhesion and protection. A further development is also presented whereby a method to enable the application of a highly conductive PEDOT:PSS layer onto devices, such as solid state dye solar cell (s-DSC), without damaging them due to heat or solvents. This has increased the effectiveness of the electrode by allowing an effective mechanical and electrical contact to be made between the semi-transparent electrode and device. This has allowed indium-tin oxide (ITO), Au and Ag free entirely non-vacuum processed s-DSC devices to be fabricated with only ~0.5% solar-to-electrical power conversion efficiency (PCE) loss compared with cells made with metal evaporated contacts. This major breakthrough also enabled devices to be deposited on metal foils which can be easily manufactured on a roll to roll process and again with only a ~0.5% PCE loss, a significant benefit to the potential scale up and production for flexible and light weight PV applications.

To demonstrate the versatility of the semi-transparent electrode it was also successfully applied to ZnS based electroluminescent devices which then subsequently allowed them also to be manufactured low cost metallic foils such as aluminium. Unlike s-DSC these devices emit light when an alternating voltage is applied across them showing that the contact can be used in this alternative set up and not simply as a current collector.

In a further aim to develop the field of low cost optoelectronic devices work was also conducted using ZnO as an alternative semiconductor and near infrared radiation to cure the organic layers for lower temperature and faster processing, both important factors when the scale up of these devices is considered.

This work has unlocked the potential for opto-electronic devices to be applied at low cost onto flexible metal substrates which opens up their application to building roofs and facades. It will also be of interest to the scientific population since as it will allow groups to experiment devices without the need for metal contact evaporation. This represents an interesting and unique method of improving the performance of opto-electronic devices as a whole with a method that is entirely compatible with current scale-up and commercialisation processes.

Acknowledgements

I would like to acknowledge the financial support from Tata Steel, Swansea University and the ESF throughout this research program. Huge thanks go to my academic supervisors Dr Trystan Watson and Professor Dave Worsley for their patience and continued support, encouragement and guidance. I would like to thank Joel Troughton and Peter Greenwood for their support, input and all the laughs that went into this project and made it actually possible.

I am very grateful to all the people at Tata Steel Colours in Shotton who have been involved in this project. I would particularly like to thank Dr Maarten Wijdekop for his direction, technical knowledge and for his invaluable input into the IP associated with this project that has helped highlight its industrial significance immeasurably. Thanks go to Ingmar Bruder and all the team in BASF Ludwigshafen for their invaluable contribution to the project with their developments on solid state dye cells and continued research and support.

My appreciations also go to Chris Coleman for his exceptional input and support with regards to the mathematical aspects of this work, the word genius is reserved for people like you!

Thanks to Matt, Mat, Cecile, James, Chesney, Katherine, Wraggy, and all the rest of the PV team that have helped, taught and guided over these past few years, without you this project would be nowhere near as good and certainly nowhere near as fun.

A special mention and big thank you to Daniel Isaac for his continued input and support into my work and professional career.

Thanks to Beverly Williams, Rhian Nurse and Hayley McAuliffe for looking after, organising and your superhuman patience with all of us on the Eng D.

I would like to especially thank my parents David and Jenny I wish there was a better way to show how truly grateful I am and how much your love both and support means to me as I don't think words can do it enough justice. To my brother Simon and sister Amy, thank you for your unquestioning support and encouragement regardless of the situation or need.

I would like to thank my friends for the laughter and good times that have made the last four years so enjoyable

Finally I would like to thank my beautiful girlfriend Emma for all her help, support, love and always being there whenever I need, you mean the world to me.

Contents

List of Symbols

S	**Ground sate of sensitizing dye**
h	**Planks constant**
v	**Wave Speed**
S*	**Excited Sensitising dye**
e^-	**Electron**
S^+	**Oxidised Sensitizing dye**
V_{oc}	**Open circuit Voltage**
I_{sc}	**Short circuit current**
J_{sc}	**Short circuit current density**
L	**Diffusion length of an electron**
V	**Voltage**
FF	**Fill factor**
η	**Power conversion efficiency**
P	**Power incident light**
q	**is the electron charge,**
λ,	**Wavelength**
$F(\lambda)$	**Incident photon flux density at wavelength λ,**
$r(\lambda)$	**Incident light loss due to the light absorption and reflection by conducting**
IPCE(λ)	**Incident monochromatic photon-to-electron conversion efficiency**
α	**Light absorption coefficient**
P	**Porosity**
P_m	**Maximum power output**
E	**Light intensity**
σ	***Conductivity***
R	***Resistance***
ϕ	***Volume fraction***
C_w	***Coating weight***
L	***Tack***
A	***Absorbtion***
ε	***Molar absorbivity***
T	***Transmission***
τ_n	***RC time constant***
C	***Chemical Capacitance***
φ_{inj}	***Quantum yield of charge injection***
η_{coll}	***Efficiency of collecting the injecting charge***

1. Introduction

In the 1970s ZnO crystals were sensitised with light absorbing molecules of chlorophyll inducing a photovoltaic effect [1]. However it wasn't until 1991 when Brian O'Regan and Michael Gratzel used colloidal TiO_2 sensitised with a ruthenium based dye to make a Dye Solar Cell (DSC) with an extremely large surface area (for light harvesting) and useable efficiencies [2]. Since then much scientific work has gone in to the development of these cells with breakthroughs such as metallic substrate based cells [3], low temperature processable devices [4] and large area modules all being made [5]. The chosen device architecture throughout the 20 years succeeding 1991 utilised a liquid electrolyte which had many challenges associated with it[6]. Recently there has been a resurgence of interest in DSCs with new architectures, suitable for mass production, being presented [7].

1.1 The Dye-Sensitised Solar Cell

DSCs are dissimilar to traditional types of solar cell in that the material used for light absorption is decoupled from that used for charge transport. This can be likened to photosynthesis and is indeed dubbed 'artificial photosynthesis'. In traditional solar cells one material is both the source of photogenerated electrons and is used for transportation and charge separation. This configuration means that recombination losses associated with electron and hole pairs become a limiting factor. When combined with the fact that DSC is a majority carrier device and the spatial separation of the holes further decreases recombination rates it means DSC has a wide range of materials and configuration available for their construction [5]. However three components are always common to a DSC:

- **Light Harvesting Material:** The TiO_2 originally used in 1991[2] has a wide band gap of 3.2eV, therefore only light in the UV portion of the spectrum can be used for photo-excitation. This lead Grätzel et. al to coat the surface of the TiO_2 in a monolayer of dye which has much larger absorption range in the visible region of the spectrum, greatly increasing the amount of light that can be used in photoelectric generation, shown in Figure 1.1

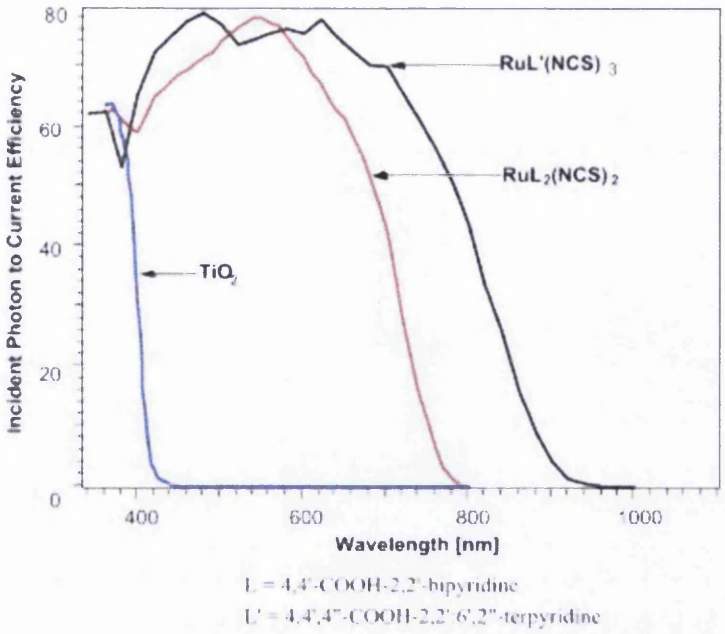

Figure 1.1. Photocurrent action spectra obtained with the N3 and the black dye as sensitizer andTiO_2 films [9] Copyright 2004 American Chemical Society

Several dyes have been developed with those based on a ruthenium complex, shown in Figure 1.2., being the most widely used (within liquid DSCs). Each dye has slightly different properties and are utilised so that they provide optimal cell performance through interaction with the other cell components, however all are intended to maximise light absorption.

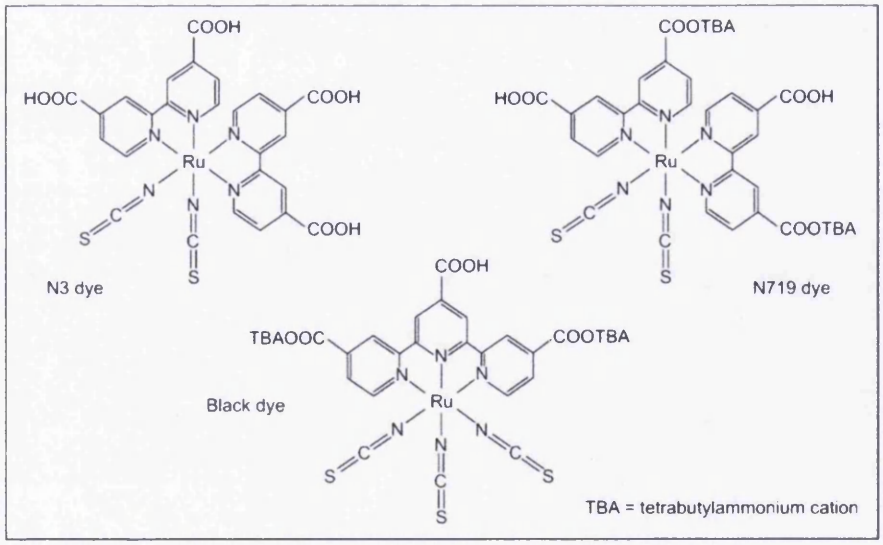

Figure 1.2. The chemical structure of a range of common ruthenium based dyes commonly used in DSCs [10] Copyright 2009 Platinum Metals Review

The carboxylate ligands attached to the Ruthenium complexes serve two purposes; first to anchor the dye molecule to the TiO_2 surface using bi-dentate coordination or ester bonding depending on the dye [11-15] and secondly the electronic interaction between the ligand and the conduction band (caused by the anchoring) results in an effective injection of photoexcited electron from the dye.

While the most common, Ru dyes are not the only sensitisers with porphyrins, phthalocyanines, organic and quantum sensitisers all displaying potential within DSC [16-19].

- **Redox Couple or Hole Transport Material (HTM):** The role of the redox couple or HTM is to provide the oxidised dye molecule with an electron. The most common redox couple is a liquid electrolyte based on the iodine/triiodide couple. Common iodides are LiI, NaI, KI, tetraalkylammonium iodide, and imidazolium-derivatives. These are then dissolved in non-protonic solvents such as acetonitrile, propionitrile, methoxyacetonitrile, propylene carbonate and combinations of them.

  A Liquid electrolyte poses a problem for cells in two respects, firstly the species is very aggressive and can corrode certain substrate materials, limiting the metals that can be used for substrates [20]. Secondly the liquid electrolyte poses problems when sealing as again the aggressive species limits the sealants that can be used. Ultimately polyolefin thermoplastics, some ionomers (such as Surlyn™), some epoxies and additive silicones [5] are the only materials available and even then the longevity of the seal is in question. Therefore there has been a move towards solid HTMs such as conducting polymers [21-22]. These will be discussed in more detail in Section 1.6.

- **Electron Transport Material**: The electron transport material layer is integral to the performance of DSSC and was one of the major advances in cell design. The layer must not only provide transport for the excited electron from the dye but also as a surface for the dye to be adsorbed onto. TiO_2 or titania has become the standard semiconductor for the electron transport layer since it shows an increased chemical stability over other semiconducting materials, is non-toxic and inexpensive and has a conduction band similar to the lowest unoccupied molecular orbital (LUMO) of the dye complexes. The size of individual particles of TiO_2 used are in the order of 10-

30nm which can lead to a TiO_2 having a high roughness factor - (Rf) >1000. This gives the TiO_2 film a very large surface area, [23], which is important since it will allow increased dye adsorption within the layer, increasing absorbance of light.

TiO_2 can form in three different structures, rutile, brookite and anatase, of which anatase is chosen for use in DSSC due to its preferential optical and electrical properties [24]. This is combined with the fact that anatase has a pyramid like structure with a low energy 101 plane on the exposed face [25], which increases the amount of dye the surface of the TiO_2 can adsorb [26].

The surface of the TiO_2 layer also provides an area for the reduction of the dye by the electrolyte and therefore must be porous enough to allow the electrolyte to diffuse through to all the adsorbed dye [27-29]. TiO_2 particles are pre-dispersed in a range of slips, pastes and colloids depending on the deposition method employed. As mentioned previously the TiO_2 particles must be sintered to form an electrical connection between the individual particles making an electrically linked network [30] decreasing the resistance of the layer. Sintering is usually carried out at around 400-500°C for a desired amount of time. Sintering has the dual purpose of also removing the binder in the paste and it is the removal of the binder that forms the mesoporous network. Low temperature processed TiO_2 pastes, as needed for polymer substrates or for energy saving, use solvents that will be removed at lower temperatures e.g. water [31].

1.2. Operating Principles

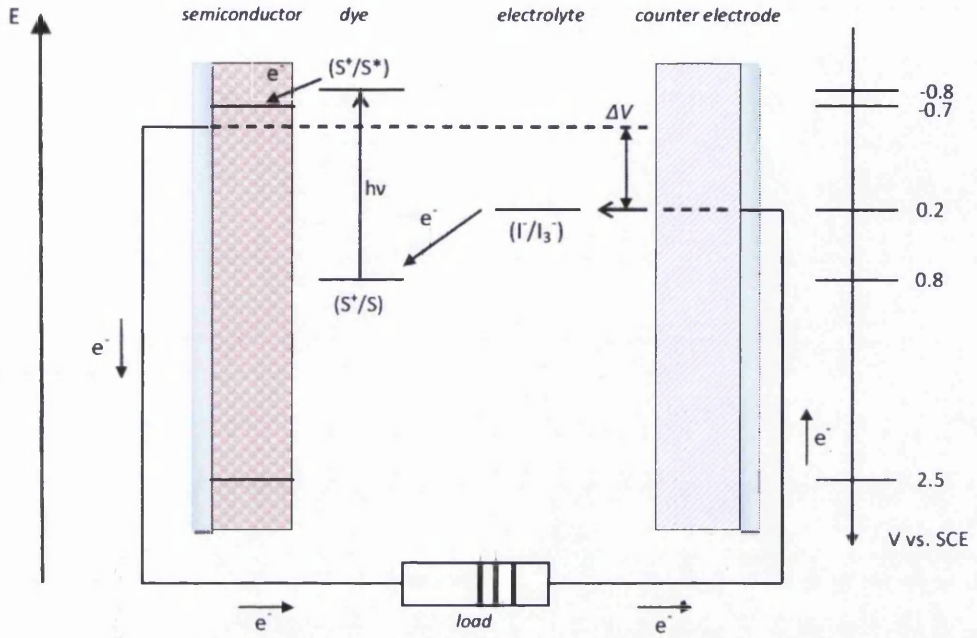

Figure 1.3: A schematic for the governing energy transfer principles for DSC [32] Copyright 1995 American Chemistry Society.

Figure 1.3 shows an example of the energy transfer principles for the original 1991 DSC architecture. In this set up it can be assumed that excitation of the dye is the starting point for photogeneration and occurs when photon flux is absorbed by the dye. This causes photoexcitation of an electron from the sensitiser's highest occupied molecular orbital (HOMO) to the lowest unoccupied molecular orbital (LUMO) due to a shift in electron density caused by the metal to ligand charge transfer (MLCT) [25, 33] Equation 1.1

$$S + h\nu \rightarrow S^* \qquad \text{(Eq 1.1)}$$

The LUMO is sufficiently negative with respect to the conduction band of the TiO_2 to provide the driving force for the energetically favourable injection of the electron into the conduction band of the TiO_2. Equation 1.2

$$S* \rightarrow S^+ + e^-(TiO_2) \qquad \text{(Eq 1.2)}$$

The injected electron then diffuses through the TiO_2 nanoparticles towards the back contact and ultimately is transferred to the external load.

Simultaneously the oxidised sensitising dye is reduced, the driving force again being the positive difference in energy redox potential and the HOMO in the sensitiser. This returns the sensitiser back to its ground state ready to absorb light again, Equation 1.3

$$S^+ + e^- \rightarrow S \qquad \text{(Eq 1.3)}$$

The holes then diffuse towards the counter electrode where they are re-reduced by an electron form the external circuit, via a platinum catalyst layer used from reducing the triiodide, Equation 1.4, and thus creating power generation without permanent chemical change of the cell components.

$$I_3^- + 2e^- \rightarrow 3I^- \qquad \text{(Eq 1.4)}$$

From these principles it can be seen that the energy difference between the HOMO and LUMO of the photosensitiser is analogous to the band gap of inorganic semiconductors and will be a major factor determining the photocurrent of the DSC. A larger photocurrent will be generated by a smaller HOMO-LUMO gap since the longer wavelengths of the solar spectrum can be utilised.

The voltage of the cell is determined by the energy gap between the Fermi level of a TiO_2 electrode and the redox potential of the I^-/I_3^- in the electrolyte [34].

It has been shown that the energy gap between the LUMO of the sensitiser and the conduction band of the TiO_2 (ΔE_1) and between the redox potential and HOMO of the sensitiser (ΔE_2) should be larger than 200mV to provide a sufficient driving force for efficient electron transfer [35].

The dynamics of the reaction have been shown in Figure 1.4 and it can be seen that electron injection and dye regeneration leading to photo-induced charge separation occur on a femto to nanosecond time scale.

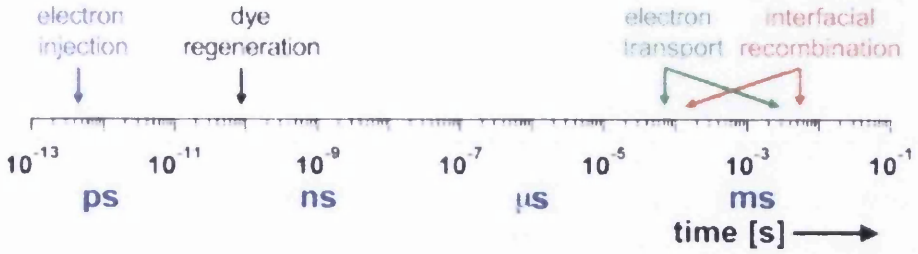

Figure 1.4. Difference in times for electron transfers occurring in DSSC operation [9] Copyright 2004 American Chemistry Society

It can be seen that electron transport through the film is relatively slow in comparison, as is the redox capture of the electron by the oxidized relay. This means that recombination of photo injected electrons in the TiO_2 to the tri-iodide must be extremely slow – something that has been put down to a low electrocatalytic activity of the TiO_2 which is not favourable for the reduction of tri-iodide ions. The reason that DSCs function so well is that electron injection and dye regeneration are faster than recombination.

1.3. Factors Affecting Cell Performance

1.3.1. Scattering Layers

One of the most important parameters of a DSC is how efficient it is at converting the incident light it receives into electricity. This is called the conversion efficiency of the DSC (η_{global}) and can be calculated from Equation 1.5.

$$\eta = \frac{J_{sc} \cdot V_{oc} \cdot FF}{P} \qquad \text{(Eq 1.5)}$$

Where J_{sc} is the cells current at short circuit conditions, V_{oc} is the voltage of the cell under open circuit conditions, FF (fill factor) is an ideality factor and P is the incident power. J_{sc} can further be defined as the integrated product of the incident photon flux density ($F(\lambda)$) and the cell's incident photon to converted electron (IPCE) over wavelengths used for light absorption by the dye [39], shown by Equation 1.6.

$$J_{sc}=\int qF(\lambda)[1-r(\lambda)]IPCE(\lambda)d\lambda$$

(Eq 1.6)

where q is the electron charge and $r(\lambda)$ is incident light loss and IPCE(λ) can be obtained through the Equation 1.7.

$$IPCE\ (\%) = \frac{\#\ electrons\ out}{\#\ photons\ in} \cdot 100 = \frac{Jsc\ /\ e}{P.\lambda\ /\ hc}$$

(Eq 1.7)

One way in which the efficiency of the cell can be improved is by improving the photo-response of the film to the longer wavelengths of light, in the red end of the spectrum. The low absorbance of the larger wavelengths is shown by Figure 1.5 where the N719 dye has high absorbance in the region 450nm to 550nm, resulting in a high IPCE for this region. The fact that the dye adsorption is maximal at 530nm leads to the complete extinction of the light within the photoactive film at this wavelength. The same is not true for the lower energy wavelengths of light in the red end of the spectrum where a significant part of the radiation will not be absorbed and will actually penetrate the layer [35].

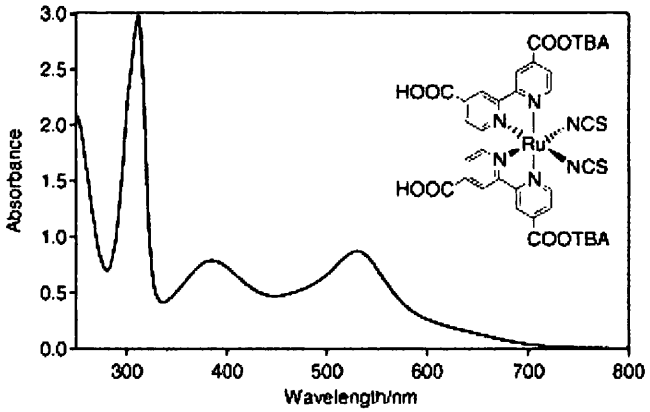

Figure 1.5. UV–Vis absorption spectrum of N719 in 1:1 acetonitrile and tert-butanol. And the structure of N719 [40] Copyright 2004 Elsevier.

The absorption of light with wavelengths greater than 580nm can be greatly improved by including larger scattering particles into the TiO_2 film. The larger particles cause multiple

reflections of light, increasing the path length of the photons inside the film and thus increasing the probability of interaction with a dye molecule [41]. Figure 1.6 shows the effect on the IPCE for a cell containing scattering layers compared with a cell that contains only small particles of TiO_2, showing a superior IPCE in the red region of the spectrum for the layer containing scattering particles.

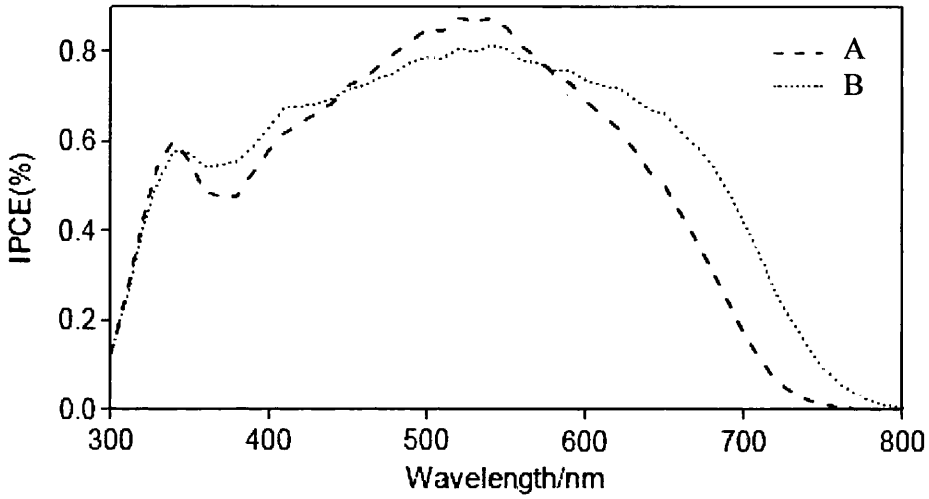

Figure 1.6. a)The influence on IPCE of a sensitised TiO_2 film containing 100% small evenly sized TiO_2 particles b) a film with a mixture of small TiO_2 particles and larger scattering TiO_2 particles [41] Copyright 1997 American Ceramics Society.

1.3.2. Illumination direction

Liquid DSC consisting of fluorine doped tin oxide coated glass as both the working and counter electrodes (Glass-Glass cells) allow incident light used for photo generation access from two different directions, the 'Forwards' illumination, where light enters normal to the working electrode first and then is absorbed by the dye sensitised TiO_2 electrode. Or 'reverse' illumination where light enters normal to the counter electrode travels through this and the Platinum (Pt) catalyst, through the electrolyte before finally being absorbed by the dye sensitised TiO_2 layer, as shown in Figure 1.7.

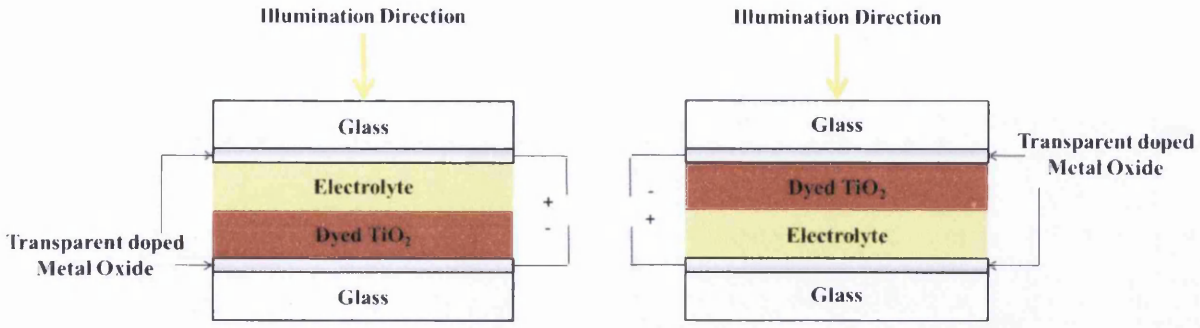

Figure 1.7. Schematic representation of (a) reverse illumination and (b) forwards illumination directions in glass-glass DSC.

Reverse illumination is less popular for DSC for a number of reasons with the main one being a conversion efficiency drop of ~24% when switching to reverse illumination [42]. However, when using a metal as the substrate the opacity of the metal does not allow for forwards illumination. One of the reasons as to why reverse illumination is detrimental to cell performance is that generation of current in the TiO_2 film is most efficient close to the back contact [43-44]. When in forwards illumination the first photons to be absorbed will be the ones with wavelengths that match the maximal absorption range of the dye. This absorption and excitation of the dye will happen close to the back contact. As a result the electrons that are injected into the semiconductor have a relatively short distance to travel till they reach the electrode and this decreases their chance of recombination with the HTM [45]. Following on from this, the larger wavelengths of light, in the red end of the spectrum, will travel further through the film and as a result will be absorbed at a distance further away from the electrode, resulting in higher losses through recombination and a lower IPCE for the wavelengths in this region. In reverse illumination, wavelengths of light with absorption coefficients close to the maximal of the dye will be absorbed at the furthest point from the back contact, and larger wavelengths closest to the electrode. As a result reverse illumination shows a lower IPCE for wavelengths of light with absorption coefficients similar to that of the specific dye due to high recombination losses but an increase in the IPCE in the red end of the spectrum [45]. This has been shown experimentally with a drop in J_{sc} [39, 42, 46]. The same has also been shown analytically for photovoltage [47] where it is dependent on the diffusion length (L) and the and the film thickness (d) Goméz et. al concluded that for forwards illumination photovoltage will drop due to recombination losses until a point at

which it remains constant. Whereas in reverse illumination there is a steady decrease as film thickness increases. Suggesting that with respect to film thickness in forwards illumination it should be optimised from a practical point of view, but in reverse it should be optimised form a performance perspective. While this is only a model it has corresponded well with practical results on the subject [48-50].

Another well documented reason for a drop in cell performance by reverse illumination is due to the fact that the light has to travel through more absorbing material before reaching the dye molecules. For example in the case of liquid DSC light must first travel through a Pt coated counter electrode whereas in forwards illumination light only travels through the FTO coated glass working electrode, as shown in Figure 1.7. Light reaching the TiO_2 film in forwards illumination will have losses associated with it by reflection and absorption of the FTO coated glass, however these will only account for around ~10% depending on the specific glass used. In reverse illumination however light scattering by the Pt catalyst and absorption by the electrolyte decreases the amount of light reaching the surface. The Pt catalyst can be assumed to affect all wavelengths equally and depending on the thickness and deposition method can account for *ca* 3% loss of light [42,46]. Additionally the electrolyte based on I^-/I_3^- has been shown to absorb a significant amount of light in the wavelength regions from 400 nm to 600 nm. The result on final cell performance caused by the additional absorbance and scattering of light means that a lower percentage of light illuminating the cell will be utilised by the active layer.

1.3.3. Porosity

The porosity of the TiO_2 film has been shown to play an important role in the overall performance of a DSC and was a major breakthrough with regards to getting cells that could reach the theoretical efficiency of the dyes [51-53]. There are two aspects to the film morphology, firstly the pore size and secondly the overall porosity. A highly porous film is one of the most important features dictating the performance characteristics of a cell and gives it huge advantages over a solid substrate in terms of surface area[9,54]. A decrease in porosity of the film has a detrimental effect on the performance of a cell due to the fact it is proportional to a decrease in surface area for adsorbed dye [54]. Since the light absorption coefficient α is proportional to the dye surface area [55] by the relationship shown in Equation 1.8 where v and z are materials constants depending on the dye and nanoparticle dimensions [41, 55]

$$\alpha = v(1 - P)(P+z) \qquad \text{(Eq 1.8)}$$

The small particles commonly used in the TiO_2 films have a high surface area and a high porosity, however the pore spacing within the film is small. A larger pore size is beneficial to the performance of a DSC since the larger pore size allows for easier penetration of the HTM through the structure [29]. This is again at the expense of a reduced surface area the dye can be absorbed on [55] leading to a lower absorbance of the film and as result, lower performance. Clearly an optimal level of porosity, pore size and surface area needs to be established to achieve maximum performance of the cell.

1.3.4 Surface Roughness

Early work on DSC suggested that cell performance could be optimised by control of pore size, thickness and interfacial surface area [56]. Later work on the subject found that high efficiencies could be obtained by combining a thin, high mobility redox couple with a 'rough' TiO_2 surface [57]. Further work on the subject has shown that cell performance was sensitive to the topography and the morphology of the sintered TiO_2 which is partly influenced by the starting substrate topography [58] and also showed that there was a decrease in V_{oc} due to an increased electron back reaction. As described in more detail in Section 1.4 metal substrates have a variable surface roughness, with many having a highly flat and reflective surface due to various pickling and cold rolling treatments [59]. While the high scattering can enhance cell performance [46] the decrease in surface area can be detrimental to the cell. In recent times work has been done to try and increase the surface area of the metal substrate by electrochemically roughening the surface [60]. The study showed that a 23.6% increase in surface area compared with lateral surface area increased J_{sc}, due to an enhanced electrical contact between TiO_2 and the larger area of the substrate. They also found no significant loss in V_{oc} and this was down to no significant electron back transfer in the interfaces tested.

1.4. Metal Cells

While glass has its benefits in terms of performance over other substrates it brings with it many drawbacks. One of the key disadvantages of glass is the high cost [50, 61] combined with the fact that glass is rigid and therefore not suitable for many applications in which flexibility is needed [46].

Substrates based on polymers have been investigated [21, 62-63] but they have, to date, produced poor efficiencies due to the requirement for low sintering temperature resulting in poor necking of the TiO_2 particles. The highest efficiency by an all plastic cell is 4.3% under 1 sun at the time of writing [33].

Work has been done using metal as an alternative to glass for working electrode and as the counter electrode with promising results [3,20,39,42,64]. Metal substrates have the advantage over glass, and to a greater extent polymeric substrates, as they have a low sheet resistance compared with the FTO coated glass cell [20,42,64-65] which is maintained after sintering unlike FTO glass in which the resistance increases post sinter [66]. This leads to a decrease in the series resistance of the cell and an increase in the fill factor [67] and can mean cells can be made larger without the serious resistance losses seen in glass cells. Combined with this metallic sheets can be used that are thin enough to make the cell flexible [33,46,64] with the weight saving and ease of shaping making them useful for many applications such as mobile phones, clothing, and portable power supplies.

Another advantage of metallic substrates is that their surfaces can be made highly reflective, which will reflect any wavelengths of light not already absorbed by the film, such as in the red end of the spectrum, back towards the porous film, providing the cell with an extra light source over the glass cell [42,46,66-67] This increases the Incident photon-to-current efficiency (IPCE) for the cell of the larger wavelengths of light, increasing the performance of the cell.

However metallic substrates do have disadvantages. The main problem is that cells fabricated using metal substrates have to be reverse illuminated due to the opacity of the metal. This has an associated efficiency loss as explained in Section 1.3.2. Another problem for metal substrate cells is their high recombination losses from the metal-electrolyte boundary, known as photocurrent leakage, [42,46,67-69] where the injected electron in the substrate reduces the electrolyte of an exposed surface resulting in the loss of that electron from the circuit. However the studies show that the losses caused by this type of

recombination can be minimised by use of a blocking layer such as TiO_2, SnO_x, SiO_x or combinations thereof [42,46,66] which give marked improvement in the short circuit current. A further difference between metal and glass cells is that the FTO layer on the glass has a higher surface area which provides a larger area for electrical contact [58]. This increase in electrical contact generates a shorter distance for electron diffusion, leading to a greater chance the electron will be injected to the substrate in turn minimising the losses from TiO_2 to the electrolyte. The surface profile of metal substrates can be variable and therefore the electrical contact will also be variable which can lead to a decrease in performance.

The type of metal used for the substrate also greatly affects the cell performance Metals such as Al, Ni and Co form a non-conducting oxide layers during high-temperature sintering processes and are not suitable unless their surfaces are covered with SnO_2 to protect against the oxidation [70]. Alloys such as Stainless Steel (SS) and metals such as Ti, Zn and W form a semi-conducting oxide layer on the surface which is needed in this type of cell construction. Corrosion of metallic substrates is also of great importance when considering a substrate for DSC. Work has been done to assess various metals resistance to corrosion caused by the liquid electrolyte commonly used in the cells [20,65]. The results have shown that StSt and Ti show the best resistance and are therefore the most suitable over other metals such as Cu. This combined with the above factors meant that Ti has become the main metal used for substrate materials used in liquid DSC. However less aggressive HTM such as polymeric solid state options shouldn't provide such a corrosion issue and should make other metallic substrates an option. One such option which becomes viable when the corrosive liquid electrolyte is removed is Electrolytic Chrome-Coated Steel (ECCS). This is a sheet steel which has an electrolytically deposited chromium / chrome oxide layer on the surface of the steel. Its advantages over many other metals include low surface roughness, high reflectivity, low cost and an anti-oxidation coating [71].

1.5. Zinc Oxides

ZnO in the wurtzite hexagonal phase II-VI is a wide-band-gap semiconductor that possesses an energy-band structure and physical properties similar to those of TiO_2. For this reason it has been used as an alternative to TiO_2 in DSC.

While ZnO has a higher electronic mobility than TiO_2 and a reduced recombination loss, conversion efficiencies of only 0.4–5.8% have been reported for ZnO based DSC, much lower than that of the 12.3% reported with TiO_2. Despite this studies into ZnO continue due

to the versatility offered in the forms of nanostructures that can be produced and due to the ease of crystallisation and anisotropic growth of ZnO.

Examples of these nanostructured forms of ZnO include nanoparticles, nanowires (or nanorods), nanotubes, nanobelts, nanosheets, and nanotips. The production of these structures can be achieved through sol–gel synthesis [72], hydrothermal/solvothermal growth, physical or chemical vapour deposition, low-temperature aqueous growth, chemical bath deposition, or electrochemical deposition.

Of the above methods a sol gel synthesis from chemical solutions to produce a nano-particulate film is the closest to the method currently used in TiO_2 solar cells and it is the simplest to produce. To date however low efficiencies of only 0.4-2.22% have been achieved using this method [73-75]. Methods for producing ZnO nanoparticles are commonly focused around precipitation of particulates from the liquid phase solutions containing zinc acetate and zinc nitrates. Variations in the procedure and concentrations used can lead to particles ranging in size and structure while remaining on the nanoscale [76-77].

While ZnO structures do have their advantages, they also have many limitations which contribute to the aforementioned lower efficiency. One of these limitations concerns the electron injection efficiency which determines how efficiently an oxide can accept an electron injected into it from a sensitizer [78]. For TiO_2 sensitised with Ru based dyes electron injection is dominated by a fast component on the femtosecond scale, whereas in ZnO it is dominated by a slower component on the picosecond scale, leading to an injection rate difference of two orders of magnitude. This discrepancy has been put down to the difference in the conduction bands of the oxides. While TiO_2 is primarily empty 3d orbitals, ZnO is composed of empty s and p orbitals and this leads to a difference in density of states and TiO_2 having a larger effective mass of conduction band electrons. Another theory that explains the low electron injection efficiency in terms of ZnO having intermediate states resulting in a slower step wise injection [79].

A further limitation for ZnO is the physical incompatibility with the ruthenium based dyes. The reason for this incompatibility can be explained by considering the charge on the surface of the ZnO when in a dye solution. ZnO has a point of zero charge = 9 so in a Ru based dye solution with an acidic pH of 5 the surface becomes positively charged. The protons adsorbed on the surface of the oxide attack the ZnO and lead to its dissolution. While the dissolution in itself is undesirable the main problems come from the fact that the dissolved Zn^{2+} forms agglomerates with the dye which adsorb onto the surface of the remaining oxide and retard the injection of an electron into the oxide from a sensitiser,

leading to a much lower overall conversion efficiency[78]. Work has recently shown that the growth of these agglomerates may be retarded by dyeing at an increased temperature [80].

ZnO has also been found to be beneficial in Solid State Dye Solar Cells (s-DSC) due to amongst other things it's high electron mobility [81-82]. s-DSC employ a solid HTM with the organic molecule Spiro-OMeTAD the most widely used, explained in more detail in Section 1.6. While Sol-Gel TiO_2 electrodes have shown great promise in s-DSC and have achieved efficiencies of 5.1% [83] the efficiency is still around only half that of the best performing liquid DSC. One of the main problems in s-DSC is the recombination from the semiconductor into the HTM. Since the electron transfer mechanism in Spiro-OMeTAD is a one electron transfer, as opposed to the complex set of reactions involved in the liquid I^-/I_3^- electrolyte, and the charge transport in the HTM is slower it leads to a limiting current in the cell.

Boucharef et al have shown that an s-DSC can be fabricated using an all ZnO mesoporous semiconductor film, however efficiencies were still low at ~0.5% [84]. This has been attributed to poor coupling of the ZnO with the reference dye N719 and its tendency to form Zn^{2+} dye agglomerates with the ZnO surface inhibiting charge injection. Therefore continued efforts are needed to ensure that ZnO can be used as a semiconductor in s-DSC.

Another way in which ZnO may prove itself beneficial in a s-DSC would be to employ it as a core-shell structure. This would add the effect of a blocking layer – as mention above, something that is critical to s-DSC operation. This may be TiO_2 with a ZnO shell, or vice-versa. MgO has already been used in this respect for s-DSC and has shown promise, creating cells with efficiencies of 4.7% [85].

Amongst the methods to produce zinc oxide for use in solar cells, most are based on zinc acetate and zinc chloride [87]. Zinc dross and waste zinc which is a by-product of galvanising steel sheet can be dissolved in the various acids to produce zinc acetate or chloride and therefore in theory also be used to create ZnO structures for DSC.

1.6. Hybrid Organic Photovoltaics (HOPV)

In the world of dye sensitised solar cells, those with liquid electrolytes are currently the most researched type of DSC and steps are being taken to industrialise them into a commercial product [88]. These cells offer many benefits such as the highest reported efficiency for a DSC along with the large amount of work that has gone into studying their operation and stability. However when considering the problems associated with the liquid electrolyte it is easy to see that replacing it with an alternative would be highly desirable. The liquid electrolyte itself is corrosive to a wide range of materials [89-90] which limits down the choice of material for the working electrode substrate, counter electrode, seals as well as having to protect the current collectors. The electrolyte is prone to leaking from the cells combined with the atmospheric components diffusing into the cell decrease lifetime substantially, an issue highlighted by disposable batteries which show short lifetimes and leakage [91-92].

This is before the problems which occur during the mass processing of the cells, including filling of the electrolyte, keeping volume consistent and handling of the material are taken into account. Thus far the electrolyte has really been the main factor in retarding the mass production of DSC and why the actual architecture of the cells hasn't changed significantly from the one made by Gratzel and O'Regan in 1991[2].

In theory the liquid electrolyte can be replaced with a solid state Hole Transport Medium (HTM) which would fulfil the job of the electrolyte and also negate many of their problems. This s-DSC is different to quasi-solid DSC which involves gelling of the liquid electrolyte. While gelling of the electrolyte has been shown to be beneficial by many groups it still shows macroscopic fluidity and in essence only delays the inevitable problems associated with the liquid electrolytes by slowing down the kinetics and therefore only true s-DSCs are being investigated within this work. The area of s-DSC is one which is becoming increasingly researched [88] with multiple variations being produced such that the defining lines between DSCs and Organic Photovoltaics are becoming blurred, leading to an emerging field in Hybrid Organic Photovoltaics (HOPV). As far back as 1995 Tennakone et al incorporated a CuI based solid state electrolyte into a DSC [93] and while showing great promise in terms of cell performance they do suffer from instability. Other s-DSCs incorporating CuSCN amongst other materials were tried and in 1997 polymeric HTMs were

used [91,94]. At present the highest efficiency and best performing stable HTM is the so called Spiro-OMeTAD, shown in Figure 1.8.

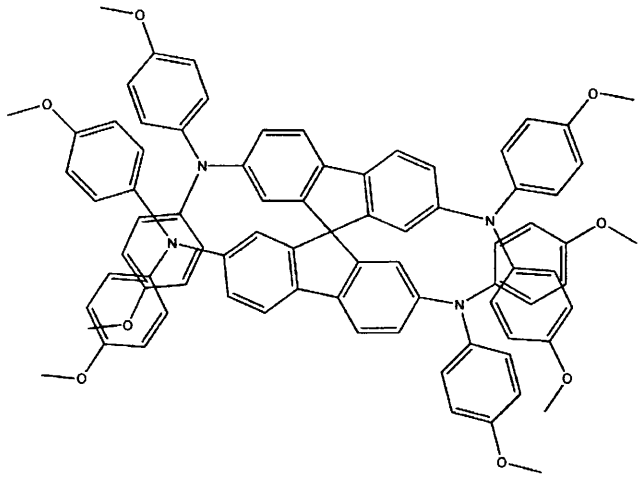

Figure 1.8. 2,2',7,7'-tetrakis(N,N-di-p-methoxyphenylamine)-9,0'-spirobifluorene (Spiro-OMeTAD) [95] Copyright 2000 EPFL.

This thesis uses Spiro-OMeTAD as a HTM exclusively and therefore the rest of this review will mainly concentrate on its use and operation. Figure 1.9 shows a schematic illustration of an s-DSC using Spiro-OMeTAD made on a doped tin oxide coated glass substrate. It can be seen when comparing an s-DSC with a liquid DSC (such as the one depicted in Figure 1.7) firstly the back contact is a metallic, in this case gold but almost always gold or silver. The opacity of this contact means that in the current state of art one electrode must be transparent (the working electrode) and therefore illumination can only occur from one direction. Figure 1.9 also shows a compact and unbroken TiO_2 layer which is essential to s-DSC performance as it stops recombination, discussed in more detail in Section 1.6.3. The height of the nanoporous TiO_2 layer is shown to be around 2μm thick, much thinner than the 12μm commonly used for liquid DSC, and this is required for adequate pore filling by the Spiro-OMeTAD, discussed further in Section 1.6.4.

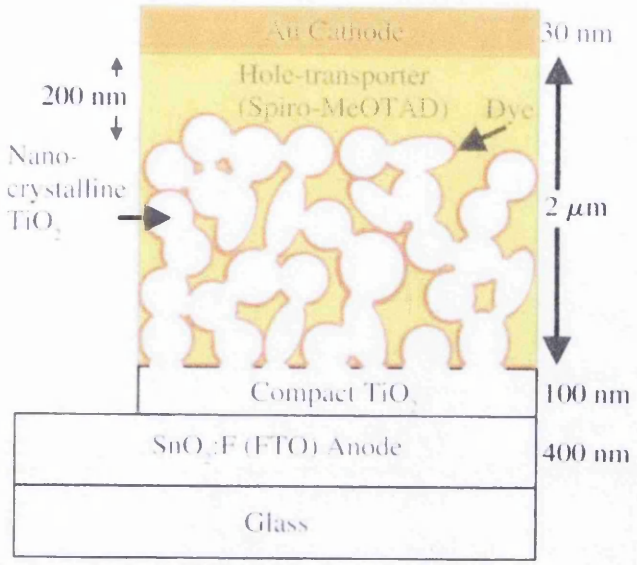

Figure 1.9. A schematic illustration of a solid state DSC [88] Copyright 2010 CRC Press

1.6.1. Spiro-OMeTAD Operation

The new field of research that contains organic electronics is an ever rapidly expanding area for study and possibilities. Understanding how these type of semiconductors actually transport charge through their solid mediums is a non-trivial task to understand and explain and as a result several different models have been put forward [96-97] with a high probability it may be a combination of three proposed theories: Polaron, Disorder and Trapping. The exact method of charge transportation is still an area which is being investigated and the precise mechanism, or at least primary mechanism has yet to be conclusively determined. The difficulty comes in the fact that many of the features which define one feature of charge transport mechanisms are also displayed by the other mechanisms making them hard to differentiate during measurement. Doping of the Spiro-OMeTAD to increase its conductivity, which is discussed in the next section, can be explained in relation to carrier trapping. This type of charge transfer involves the assumption that there are certain sites within the HTM that are below a certain energy level to be trapped and sites above to be free. The traps can be visualised as energy 'wells' where charge becomes trapped, therefore using this visualisation energy would be needed to de-trap the charge i.e. get out of the well, and move to the next trapping site and in this sense trapping is a temperature dependant mechanism. Through this mechanism of moving between trap sites the charge will eventually travel through the HTM and thus 'conduction' is achieved.

If Spiro-OMeTAD's role in DSC operation is now considered, remembering what happens in liquid cells, we can assume the following:

A charge is generated in the dye by photoexcitation which is then injected into the conduction band of the TiO_2 for transport to the external circuit. The dye is now left in an oxidised state and needs an electron, which it must receive from the HTM. The HTM injects an electron into the dye and the dye injects a hole into the HTM. The hole moves through the HTM in a series of hopping steps and finally reaches the back contact. Here it injects a hole into the back contact, and the back contact can inject an electron back into the HTM to start the process over again [95].

While it is important to remember that this is a simplistic view and in actual fact this type of process is happening many multiple times a second in normal cell operation, the more important thing to note is that the reduction of the dye, charge transport and reduction of the HTM is all a 1 electron/1 hole process. This is distinctly different from the multiple reactions involved in liquid electrolytes based on iodide/triiodide which involve intermediate species. This means that the driving force for the reduction of the dye can be lower, the redox potential of the HTM can be closer to the HOMO of the dye and ultimately the V_{oc} of the cell can be higher. This is summarised by Figure 1.10.

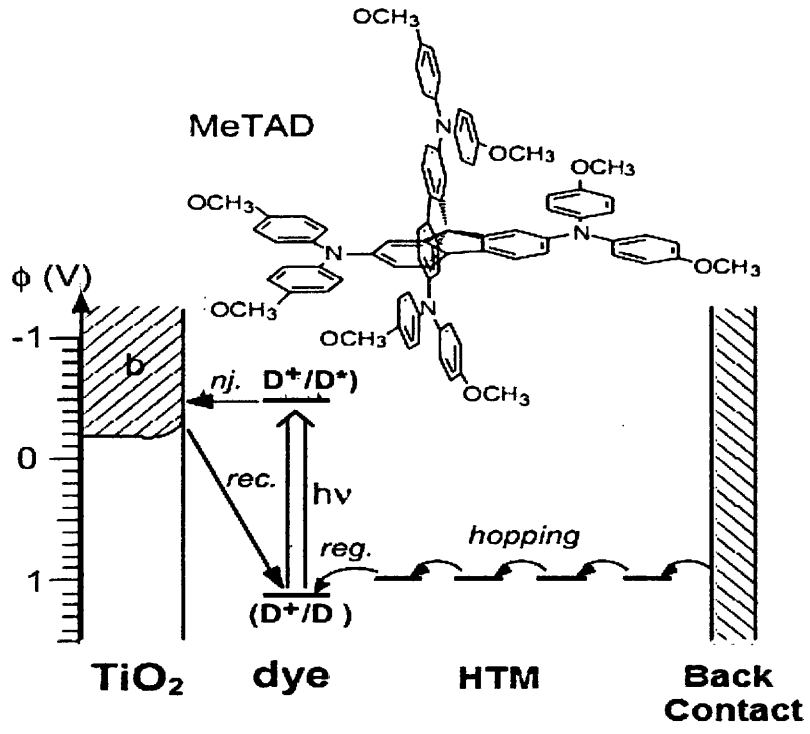

Figure 1.10. Energy Level diagram from a dye solar cell containing Spiro-OMeTAD [95] Copyright 2000 EPFL

Indeed it has been shown in Figure 1.11 cyclic voltammogram that the oxidation potential of Spiro-OMeTAD has two, one electron transfers at 818 and 932mV vs NHE which is very close to the HOMO level of dyes such as N719: ~950-980mV vs NHE [95]. This has the possibility of being brought even closer using different dyes.

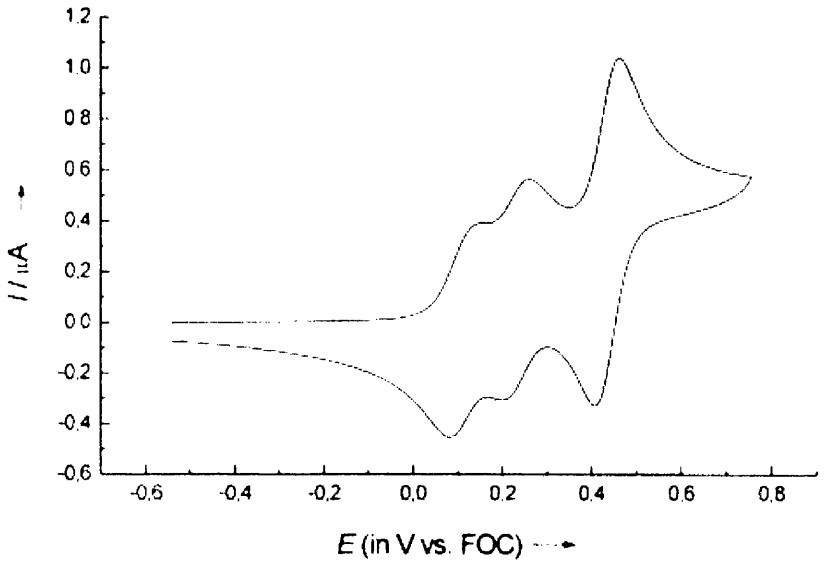

Figure 1.11. Cyclic Voltammagram of Spiro-OMeTAD [95] Copyright 2000 EPFL

1.6.2. Additives to Spiro-OMeTAD

As a HTM on its own Spiro-OMeTAD is a very poor conductor with a conductivity of $2.7x10^{-7}$ S cm^{-1} or 3.7Mohms/cm [98]. It is therefore essentially a non-conductor when used in a DSC and offers no benefit. To make it useful as a HTM it has been found that the addition of certain salts can lead to a large increase in conductivity [99]. One of the salts that has been well documented to increase conductivity is that of Lithium Bis(Trifluoromethanesulfonyl)Imide (LiTFSI). In one study the conductivity was shown to increase to $2.0x10^{-5}$ S cm^{-1} upon the addition of 12% LiTFSI, however it is not immediately obvious why this two order magnitude increase would occur. It has been shown through UV-Vis studies that the Spiro-OMeTAD+LiTFSI does not oxidise and therefore the idea that the charge density may be increased can be ruled out [84]. What does appear to happen is that the TFSI component creates an extrinsic amount of disorder within the HTM. This means that the coulomb traps mentioned before begin to overlap significantly. The potential barrier between the two overlapping trap sites is thus then reduced making so called hopping between sites

energetically easier. This would not necessarily increase the charge mobility but would increase the charge transports, as is shown by the increase in conductivity.

1.6.3. Recombination

In s-DSC hole transfer from the oxidized dye is on the nanosecond timescale, usually significantly faster than interception, making the charge recombination almost exclusively between electrons from the TiO_2 with holes in the HTM [6]. It is the same process that means the V_{oc} can be increased that also results in the increased recombination for Spiro-OMeTAD systems. As it is a one electron transfer process the charge recombination process of electron from the TiO_2 to the HTM is on the microsecond timescale as opposed to the millisecond process involved in iodide/triiodide[100]. Many methods to reduce the recombination rate have been investigated with one of the most convenient being the effect of additives into the HTM, the primary one of these being Li+ additions. It has been shown through transient absorption spectroscopy [101] that lithium additions in the form of LiTFSI act to slow down recombination. The proposed reason for this is due to the lithium being located close to the surface of the TiO_2, effectively screening the electrons in the TiO_2 and the holes in the HTM - similar to its effect in liquid electrolytes. This is obviously beneficial as LiTFSI was added already to increase charge transport. Tert-Butyl-Pyridine is another additive which can also slow down recombination kinetics as has been shown before and has the additional benefit that it can dissolve LiTFSI in the HTM casting solution before it is applied to the cells [102].

Numerous other ways have been shown to reduce the recombination such as different dyes [103-104], increasing dipole offset [105], coordination of ions to the dye backbone [106] and the use of different metal oxide coatings on the cells.

The other main method for recombination is between the working electrode contact and the Spiro-OMeTAD. The problem being that a key substrate in s-DSC is fluorine doped tin oxide coated glass. In liquid DSC this isn't a significant issue as the iodide/tiiodide has a strong overpotential at the SnO_2 interface, however, Spiro-OMeTAD forms a perfectly ohmic contact. Therefore formation of a device in which SnO_2 and Spiro-OMeTAD were contacting would lead to a large fraction of photogenerated charges in the SnO_2 recombining with the HTM leaving a largely inefficient device. It is therefore essential that a solid thin blocking layer of TiO_2 is coated onto the SnO_2 to inhibit any contact or an alternative to SnO_2 is used [95].

1.6.4. Pore Filling

One of the main issues with any device where a solid state electrolyte is trying to fully infiltrate a nanoporous structure would be that of complete pore filling. It was assumed from other studies that the thicker (~7μm) TiO_2 films needed for this would not be able to be 100% filled by a solid state HTM. However work done by Snaith et al shows that cells containing a film thickness up to 7.2 μm can show consistent current collection throughout the entire film, showing that the Spiro-OMeTAD penetrates throughout the whole film [107]. However in the same paper it also shows that while penetrating throughout the whole film the pores themselves will not be 100% filled (closer to 80%), but this is still enough for operation. The proposed mechanism of pore infiltration and filling is that the original solution, which contains 30% Spiro-OMeTAD in chlorobenzene, is cast upon a TiO_2 film and forms an excess pool of solution on top of the TiO_2. As the chlorobenzene begins to evaporate it leaves the top of this pool with a high concentration of Spiro-OMeTAD as opposed to a low one at the bottom of the TiO_2. This then sets up a concentration gradient and the solution supersaturates from further evaporation, driving Spiro-OMeTAD into the pores as shown by Figure 1.12.

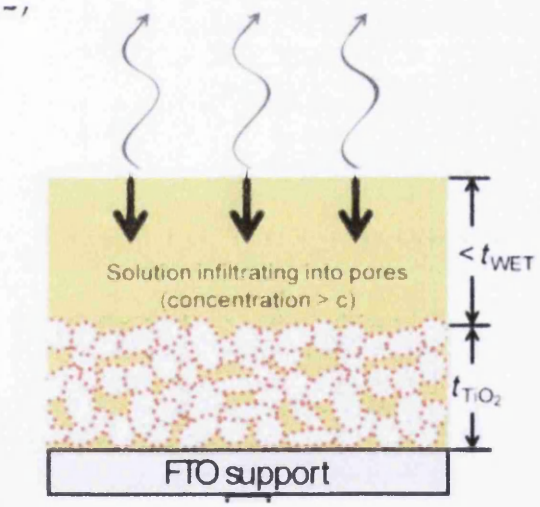

Figure 1.12. Mechanism of Spiro-OMeTAD infiltration into a mesoporous layer [108] Copyright 2010 Wiley.

While the above work was done via spin casting, which is often the employed method for the fabrication of test cells, the mechanism will mean that the deposition of a Spiro-OMeTAD solution will be applicable to other methods. Indeed it has already been shown that this type of materials can be doctor bladed into cells and still produce the same efficiency as

cells that have been spin coated [109]. However, it has shown that Spiro-OMeTAD will not fill a pore but rather will 'wet' to the surface of the TiO_2 [110-111]. The path length for a hole along the surface of the TiO_2 is then effectively increased and the probability of recombination increased. Therefore work into complete pore filling in thick films is still required.

1.6.5. Back contact

The back contact is the equivalent of the counter electrode in a liquid DSC. However unlike a liquid DSC the counter electrode doesn't have to act as a catalyst for reduction of the electrolyte. It must however provide an ohmic contact for effective current collection and also provide a large contact area with the top of the Spiro-OMeTAD within the cells. Due to these facts the most effective form of contact made so far is evaporated silver or gold contacts [84].

A few problems arise from this method of depositing back contacts. Docampo et al have shown that a phenomenon occurs that when complete devices are devoid of oxygen they fail to work [112]. The proposed mechanism that has been put forward is that there is contact made between the back contact spiking through the Spiro-OMeTAD at pinholes in the Spiro-OMeTAD overlayer and making contact with the TiO_2. When oxygen is present this forms a Schottky diode which acts to block a shunting path, however, when the cell is devoid of oxygen this barrier moves towards ohmic and creates a considerable shunting path leading to poor cells. One solution that was proposed was to add a wide band gap semiconductor such as Al_2O_3 on top of the TiO_2 thereby creating an effective barrier between the back contact and the TiO_2. This is essential for long term stability of the cells as an oxygen rich cell would lead to a lower lifetime of the organic compound.

The main problem with the back contacts as they are is that they have to be evaporated, which requires vacuum processing. This itself creates large technical challenges for large scale processing and also requires a significant capital outlay and therefore an alternative is ideally sought.

1.7. PEDOT

In 1977 Heeger, MacDiarmid and Shirakawa discovered electrically conducting polymers, this was the ignition for over 30 years of research worldwide into the subject. Out of the many different types of conducting polymers, poly(3,4-ethylenedioxythiophene) or PEDOT is currently the most widely used and the best in terms of conductivity, processability, transparency and stability. While the world of conducting materials is often split into metallic conductors, semiconductors and insulators conducting polymers bridge the gap between semi-conductors and into metallic conductors, seen in Figure 1.13 and are as such not clearly defined. PEDOTs are intrinsically conducting polymers, which differ distinctly from extrinsically conductive polymers which are insulating polymers loaded with a conducting medium of some kind, confusingly the term conducting polymer is used to describe both [113-114].

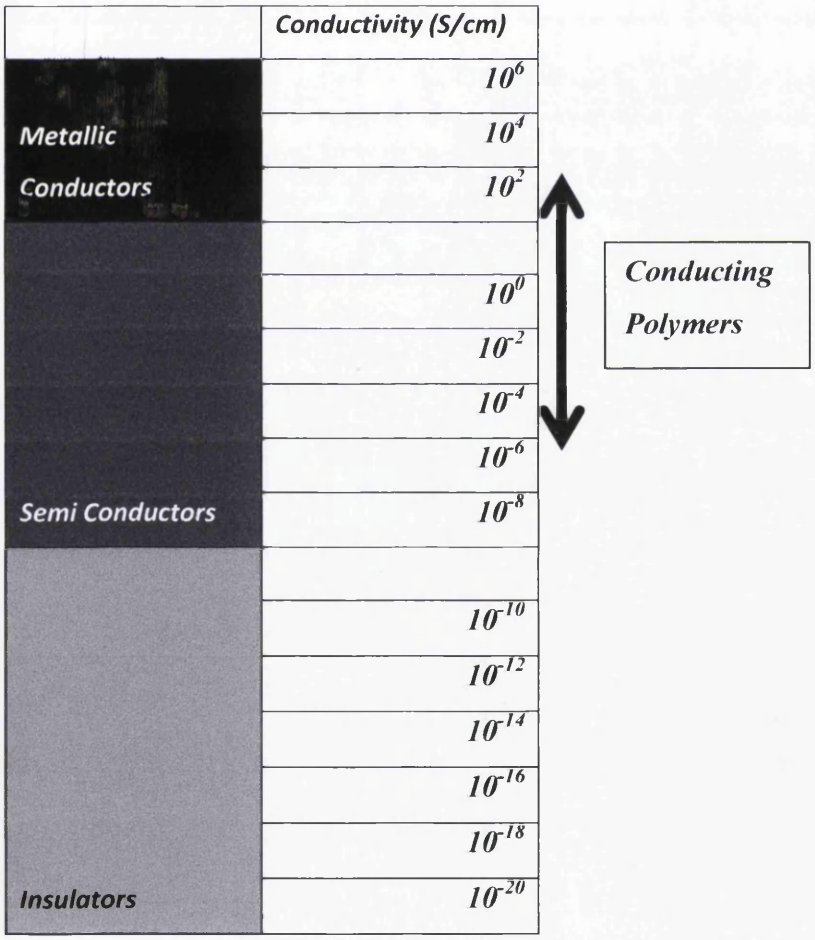

Figure 1.13. The range of conductivity between metallic conductors, semiconductors and insulators showing where conducting polymers sit within this range.

In insulating polymers σ bonds are formed by all the valance band electrons and as a result the band gap is very large hence, insulating. However in intrinsically conductive polymers typically a conjugated system is formed whereby along the polymer backbone the formation of a π system occurs. Carbon atoms along that backbone form three σ bonds. Subsequently the remaining p orbital engage with the π system allowing a delocalization of π electrons, if the carbon carbon bonds were of equal length then the delocalized electron would be found in a half filled band, leading to metallic conduction [115] however equal length carbon bonds would lead to an unstable structure and as a result the backbone takes the form of repeating units consisting of two closely spaced carbon atoms and two further apart. This means there is a completely filled π band followed by an empty π* band and as such pure conjugated polymers are themselves semiconductors. As such without any additional treatment pure conjugated polymers would have very low conductivity, but much like other semiconductors they can be 'doped' [117]. Unlike inorganic semiconductors the term doping refers not to the addition of an atom but a reduction or oxidation of the polymer thereby creating new electronic states rendering them conductive. Some important oxidising agents for PEDOT are: iron(III) chloride, Iron(III) tosylate and ammoniumperoxodisulfate [118] creating chloride, tetrachloroferrate, tosylate and sulfate as counter ions. Counter ions are present whenever there is oxidised PEDOT as they are essential for charge balancing and one of the big breakthroughs for PEDOT came with the addition of Poly(styrenesulfonate) (PSS) as a counter ion to form PEDOT:PSS in 1989 [119]. PSS itself is not a dopant, as it does not have an oxidative effect, it simply acts as a counter ion. Therefore EDOT is first polymerised and doped with persulphates like $K_2S_2O_8$ [119] before the addition of PSS as the counter ion. The sulphate ions can be later removed using an ion exchange resin to obtain pure PEDOT:PSS [120]. The real advantage that PSS gave to PEDOT was that the subsequent PEDOT:PSS molecule was found to give a stable microdispersion in water which was then processable by a wide range of techniques on a large scale. Techniques for deposition such as relief, flexo, gravure, offset, screen, inkjet and nozzle printing could then all be employed [121].

1.7.1. Secondary Doping

While primary doping is used to describe the action of oxidising or reducing the polymer chains, secondary doping defines an additive that further increases an already doped polymer by several orders of magnitude [122]. For PEDOT:PSS a range of chemicals can be added to the polymer to increase the conductivity which range from organic solvents, sugars,

polyols, ionic liquids, surfactants and salts [123-135] all of which increase the conductivity to a varying amount. Out of these two Diethylene Glycol (DEG) and Dimethyl Sulfoxide (DMSO) are shown to give the highest improvement in conductivity. This is combined with the fact that the conductivity enhancement is often (but not essential) found once the film is heated [123] and since both DEG and DMSO are removed completely when the film will be heated makes them the preferred choice at the time of printing. The reason for the increase in conductivity through secondary dopants has been the subject of much study [126,133,136-137]. X-ray diffraction was employed to study the structure of the PEDOT:PSS films with and without secondary dopants [138]. It was found that there was no change in the pattern produced between the two films and along with another study the change from amorphous to crystalline films was ruled out [139]. Instead several studies have seemed to suggest that the addition of high boiling point solvents, such as DEG and DMSO, changes the structure of the PEDOT:PSS into regions of more aggregated and uniform regions of PEDOT and PSS throughout the film [128-133]. AFM images also suggested an ordering process [136] and combined with the fact that it has been shown that pure PEDOT:PSS when deposited freezes into a non-equilibrium state [137] suggests the secondary dopants act in a similar manner to plasticisers [140]. This means that the presence of the high boiling point solvents keep the film from becoming 'frozen' long enough such that there is a thermodynamically driven ordering leaving them in a more thermodynamically favourable state [137]. Since it is the PEDOT region that does the conducting (PSS regions can be thought of as non-conducting) this ordering of the film can result in pathways of high conductivity as shown in Figure 1.14.

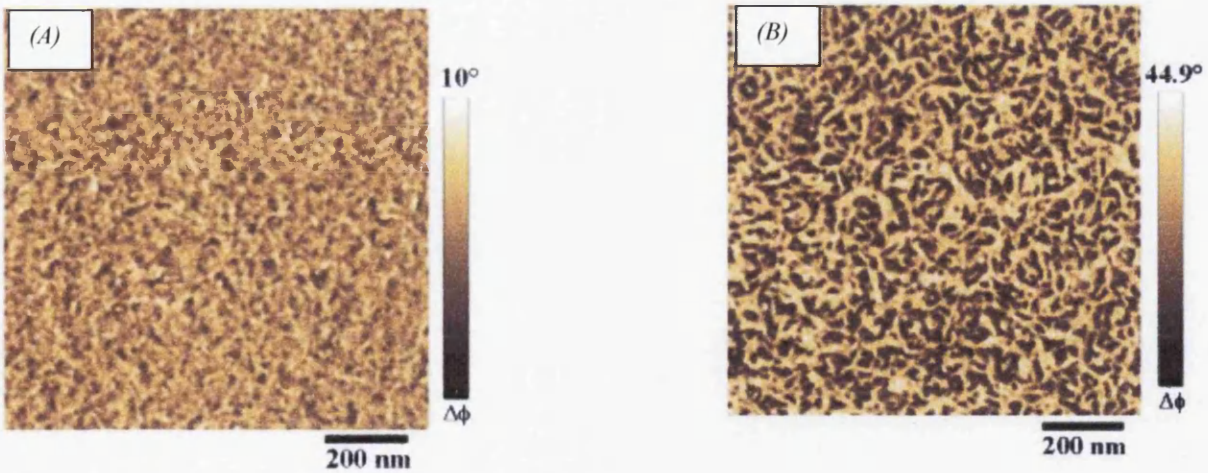

Figure 1.14. The difference in PEDOT (darker) and PSS (lighter) phases when DEG is not present (A) and present (B) in the wet PEDOT:PSS solution [136] Copyright 2006 American Chemistry Society.

1.7.2. Other Dispersion modifications

As well as for conductivity dispersions of PEDOT:PSS can be modified for many various different properties including surface tension, adhesive and mechanical properties, hardness and resistance to solvents. One such modification is binders and the role of binders is two-fold, one is to improve the adhesion of PEDOT:PSS to substrate layers and the other is to prevent cracks and maintain conductivity during thermoforming [141]. The most commonly used binders for this purpose are polyvinyl alcohol, polyesters and polyurethanes [141]. Most polymeric binders will soften when heated such that they can be thermoformed but will still be present in the final film, as a result they increase the non-conductive percentage within the film and ultimately decrease the conductivity [142] an example of this is shown in Figure 1.15.

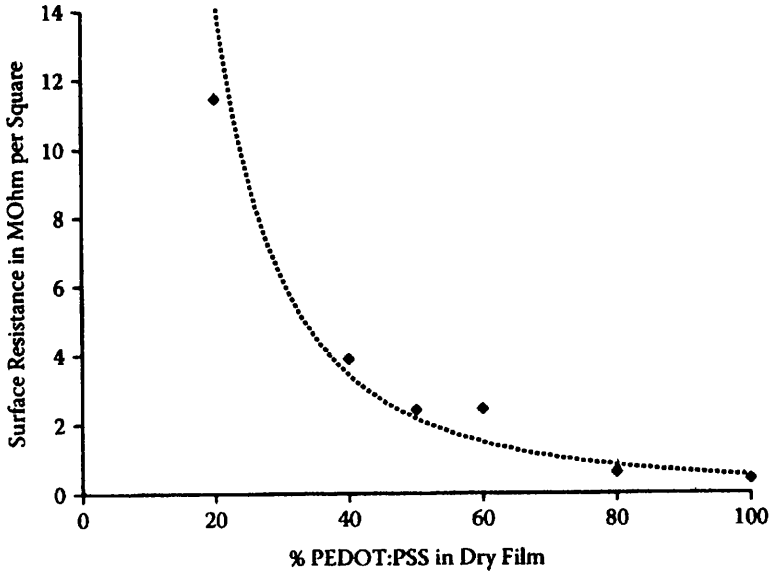

Figure 1.15. Change in surface resistance with the addition of polyurethane to PEDOT:PSS mix [143] Copyright 2011 CRC Press.

1.7.3. Surfactants and Solvents

Aqueous PEDOT:PSS has a surface tension that is within the region 65-71mN/m and is dependent on the amounts of PEDOT and PSS. This surface tension is too high to wet to surfaces of common substrates such as polyethylene tetraphthalate, polycarbonate and polyethylene. Water soluble low boiling point solvents have been chosen such as ethanol, 2-

propanol, methanol and 1-butanol and they are shown to decrease the surface tension but also as a side effect may decrease the dispersion stability and conductivity [143].

1.7.4. Transmission

As shown in Figure 1.16 PEDOT shows absorption within the red region of the spectrum, leading to PEDOT's characteristic blue colour. Due to the eye's sensitivity to a greenish hue the light blue coating of PEDOT offer and almost invisible coating. Another important consideration is the transmission as a function of film thickness. The thickness dictates the resistivity according to Equation 1.9 where σ^{-1} is the resistivity, R_{sq} is the sheet resistance and d is the layer thickness. While this means that increasing the film would give enhanced electrical properties for applications such as solar cells, OLEDS and Displays, light transmission is crucial.

$$\sigma^{-1} = R_{sq} \cdot d \qquad \text{(Eq 1.9)}$$

An example of how light transmission varies with film thickness is shown in Figure 1.16. Therefore a trade-off between the two needs to be reached leading to an optimum somewhere between the two parameters for these applications.

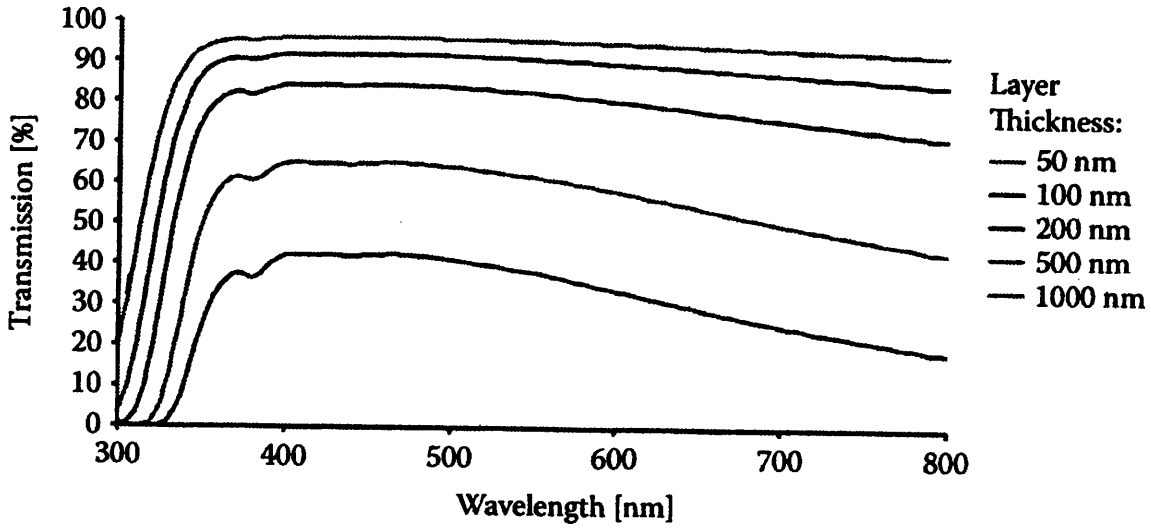

Figure 1.16. Transmission of PEDOT:PSS at various layer thickness [143] Copyright 2011 CRC Press.

1.7.5. PEDOT in DSC

Along with many other types of conducting polymer PEDOT has been suggested as a solid electrolyte within the cells. It was first tried by polymerising the EDOT monomer [144] in situ within the cell using Iron (III) as the oxidant and an applied electrical field [145]. Cells made using this method showed conversion efficiencies of only 2-3% [146] which is lower than that of the preferred solid electrolyte – Spiro-OMeTAD.

The other area PEDOT has been suggested for in DSC is for use as a replacement for the counter electrode in a liquid based DSC. As mentioned before the counter electrode consists of a transparent conducting layer, often FTO or ITO glass covered with a thin layer of platinum. This set up offers many disadvantages, such as the high-temperature or complex method used for the deposition of the platinum as well as the fact that it accounts for over half the cost of the cell as a whole. PEDOT was found to have a similar catalytic effect as the platinum [147] and a layer of PEDOT:PSS can substituted for the platinum within the cell [148]. Efficiencies of 5.81% were achieved in comparison to 5.66% reference cells, a result that seems very promising. PEDOT counter electrodes were also tried with gel electrolytes and a similar effect was observed [149].

1.7.6. Work Function

The work function is defined as the energy required to remove an electron from the highest filled level in the Fermi distribution of a solid into a vacuum [150]. The Work Function (WF) of the PEDOT plays an important role in s-DSC, much like the WF of the HTM must be above the HOMO of the dye the WF of the PEDOT must be above that of the HTM therefore promoting efficient hole transfer dynamics with driving force being the positive difference in energy levels as shown in Figure 1.17. Like the HTM and dye the energy levels should ideally be as close together whilst still maintaining sufficient driving force to obtain the highest possible voltage.

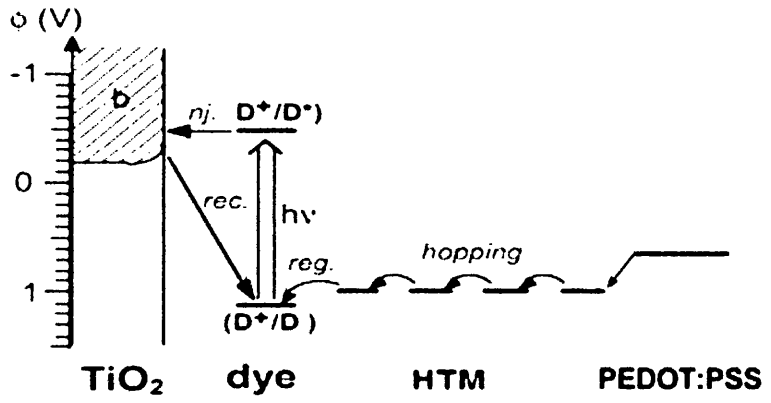

Figure 1.17. Energy Level diagram from a dye solar cell containing Spiro-OMeTAD and PEDOT:PSS [95] Copyright 2000 EPFL

However using the WF to predict which PEDOTs may be compatible with Spiro-OMeTAD will give a rough approximation. This is because the interface created between the two cannot simply be explained in terms of the Schottky-Mott model - a model often used to describe interfaces. This is due to the energy barrier of hole injection ΔE is not the difference of the ionisation potential and the work function. Indeed in one study while the Work Function varied by 0.9eV the hole injection barrier remained unchanged [151]. The phenomenon of ΔE being independent has been explained in terms of Fermi Level pinning [152-153]. Cationic species formed at the interface are believed to be counter balanced by the SO^{-3} groups creating a dipole, with the strength of this dipole scaling linearly with WF, and pinning occurs.

Another point to bear in mind is that the surface of PEDOT:PSS has been found to be enriched with PSS [154] which can increase the WF of the surface. In a study it was found that if the PSS region was removed via sputtering with Ar ions the WF could be reduced from 5.13eV to 4.75eV [155].

1.8. Pressure Sensitive Adhesives

The field of pressure sensitive adhesives (PSAs) is a large and increasingly diverse science. The first PSAs were used in medical applications from as early as 1845 and consisted of natural rubber and tackifier resin on cloth [156]. However, it is still hard to define what exactly a PSA is. The term pressure sensitive implies that pressure is needed for them to function, however this can range from adhesives used in touch blow labelling which require effectively no pressure right through to high pressures on coil coating lines. It has been noted that the German word for PSAs is Haftkleber which means an adhesive which adheres and differentiates between adhesion and an adhesive bond [157]. The term is often further confused when pressure sensitive products (PSPs), of which Cling Film is a classic example, are considered since they contain no separate adhesive layer yet still form pressure sensitive adhesion. One source separates PSPs from PSAs by describing PSAs as adhesives "which in dry form (solvent and water free) are aggressively and permanently tacky at room temperature and that firmly adhere to a variety of dissimilar surfaces upon the mere contact without the need of more than a finger or hand pressure, require no activation by water, solvent or heat"[158] (which is not applicable to most PSPs). One theme common to PSAs is that they are all viscoelastic in nature and therefore the rheological behaviour of each adhesive will have a bearing on their ultimate adhesive bond properties [159]. At a macro level the interaction of a PSA and the substrate it is adhering to is the result of a wetting and spreading process establishing surface area contact between the two. At a more fundamental level interfacial interaction is caused by forces such as van der Waals, H-bonding, acid-base and donor acceptor interactions [160-161]. The resultant 'pressure sensitivity' these physical and chemical interactions form is common to all PSAs but the ways in which they can be achieved are vastly different. PSA can differ in their chemical compositions, with common varieties being silicones, natural rubbers, block copolymers, polyisobutene and acrylics, as well as the additives, binders, tackifier, fillers, resins and many more before carrier substrate, deposition conditions, application and lifetime are even considered [162]. What this ultimately shows is that there is a lot of scope for variation and development within the field for a material that still has the eventual goal of being called a PSA.

1.8.1. Pressure Sensitive Adhesive - Tack

Exactly how a PSA adheres to another substrate is a subject that is complex, dependant on many factors, different for different materials set and as such could not possibly be covered within the scope of this thesis. The bonding has several different elements to it such as the wetting of the PSA, the chemical interactions and viscoelastic deformation upon removal [159] and as such there are many different methods to measure and define a PSA's properties [163]. One such property is called Tack, which is described as the ability of a viscoelastic macromolecular compound to build up an instantaneous bond by pronounced viscous flow, which behaves elastically by debonding [164]. The less pressure that is required to form a bond and the stronger the bond that is formed results in a higher Tack value for a PSA. Control of tack is essential in many bonding processes. Too great a tack may cause nearly as many problems as too low of a tack [165]. Some PSAs, such as those found on masking tapes, do not have instantaneous tack and need pressure to be applied before adhesion is achieved, these types of products have a special type of tack called application tack [164]. In addition to this some PSAs are designed to stick to surfaces that are slightly moist (such as ones used in medical applications) and their tack has to be characterised using wet-tack testing where the surface of the tester is covered in water[166]. For the most part though PSA's Tack measure two steps: the bond formation and bond separation, which is done using one of three standard measurements:

- Polyken – Involves bringing a flat probe in contact with the PSA at a controlled rate, contact pressure and dwell time and the force required to break that bond is measured [167]. This test is an extension and more controlled version of the thumbtack measurement where the tester would press their thumb onto a PSA and then judge the tack based on the sensation they felt.[168]
- Loop Tack – Is a measure of the force required to remove a standard adhesive-coated film loop from a standard stainless steel plate after short contact of the test strip with the steel plate in the absence of pressure.[169]
- Rolling Ball – A stainless steel ball is allowed to run down a slope from a point down an inclined plane onto the adhesive tape; the distance travelled along the sample is measured in centimetres [170]. This test is unusual in that a lower value travelled by the ball indicates a PSA of higher tack.

The Polyken and Loop simulate real bond formation conditions whereas the Rolling Ball Tack (RBT) measures the tack under different conditions and is sensitive to TCAs of low coating weights (a measure of the amount of TCA on a surface) [164]. All the tests are dependent on the carrier substrate and testing material in which standard conditions are often defined.

Some of the factors that can influence the Tack of a PSA are the adhesive used, contact load, dwell time, adhered temperature, humidity, and the adhesive's flow characteristics [171]. In addition to this tack only occurs once the coating weight of an adhesive is above a certain threshold which allows the PSA to have sufficient enough viscoelastic response. During debonding for example it has been suggested that the PSA forms fibrils such that they dissipate a large amount of deformation energy, increasing the PSA's bond strength [172], if the PSA film is too thin the formation and deformation of these fibrils is too low and the bond strength is also low.

As suggested before, Tack is only one measurement of a PSA's properties (the others commonly being shear and peel strength) however it is highly indicative of how the PSA will behave and the bond it will form in contact with substrates. It is therefore a good measure of the usefulness of a PSA.

1.8.2. Acrylic Emulsion

As mentioned in the Section 1.8 there are broad categories of PSAs based on their chemical compositions. Of these, Acrylic based PSAs have the distinct advantage over almost all other types in that they are inherently tacky, colourless polymers that are resistant to oxidation, discolouration and loss of tack[162]. Silicone based PSAs can outperform Acrylic PSAs in many of those respects, however acrylic has the distinct advantage over silicone of being much lower in cost [162]. Use of acrylics as PSAs has been known as far back as 1928 and can be used without the need for additional compounding or formulation as a homopolymer [173]. However homopolymers rarely possess all the desired properties for a PSA and therefore a copolymer is usually used. These are often prepared from acrylic esters with vinyl unsaturated monomers in varying amounts to obtain the desired properties by solution or emulsion polymerization [162]. Compared with solution, emulsion polymerisation is heterogeneous and involves water, monomers and initiators with the addition of emulsifiers buffers and possibly a seed latex. In a typical process the emulsifier is added to water and the monomer introduced to form an oil-in-water emulsion with particle sizes in the range of 1-10μm [162, 174]. A similar but more rapid process called mini-emulsion uses sonication to

produce particles which are in the size range of 50-500nm [175]. The 'base' polymer emulsion then has additional components added to it (such as tackyfying resin, cross-linker) along with final solids content and viscosity to make a product with specific properties. Unlike solution processed PSAs, emulsion based ones have the particulate nature of the film still present when dried [176]. An example of this remaining structure can be seen in Figure 1.18 in a cross section of an acrylic emulsion PSA where the boundary areas of the former polymer particles can clearly be seen.

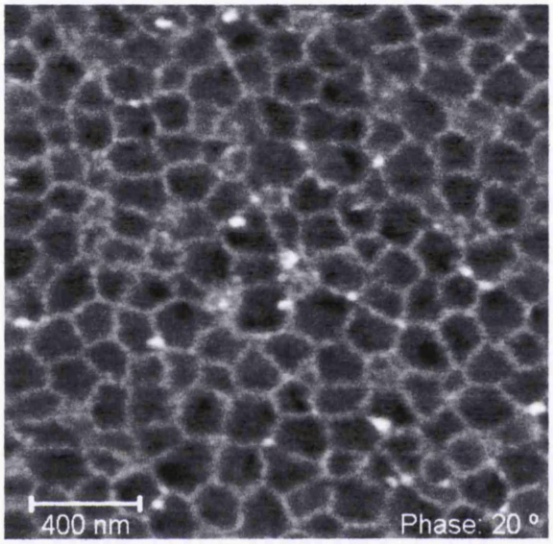

Figure 1.18. Film structure of a mono-modal dispersion acrylic emulsion pressure sensitive adhesive seen in an AFM tapping mode picture: dark areas= soft, bright = hard phases [176] Copyright 2007 Pressure Sensitive Tapes Council

As a result the adhesion of these films is always lower than that of their solution counterparts. However emulsion polymerisation dominates commercial production due to its ease of handling and formulation, high molecular weights and high versatility. In addition to this their water-based, non-toxic, non-flammable nature has seen their use and popularity rise as the demand for more environmentally friendly products has grown [177].

1.9. Conducting Adhesives

The past decade has seen a growth in the demand for conductive adhesives for many different applications. These range from LCD screens [178], smart windows [179], OLEDS [180] and solar cells [181] and such adhesives include particle loaded adhesives, gelled electrolytes, thin layers and multiple layers with different charge characteristics respectively. Due to such a broad range of materials coming under the umbrella of conductive adhesive this section deals with only ones that have properties relevant to this thesis. Those properties are; transparency, applicable to traditional coating methods, a high conductivity especially in the Z axis as well as maintaining substantial adhesive qualities.

1.9.1. Anisotropic Conducting Adhesives (ACA)

These adhesives are so called anisotropic as they only conduct in one direction - perpendicular to the plane of the adhesive when applied as a film – or Z axis. They usually comprise of a mix of an insulating adhesive and a conducting particle – metallic or metallic coated. [178]. With the particle size being equivalent to that of the final film thickness when sandwiched between two conducting films an electrical pathway is made through the particles shown in Figure 1.19.

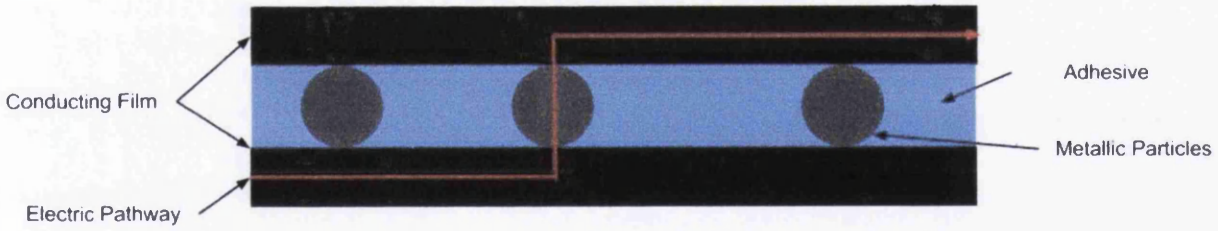

Figure 1.19. A cross section diagram of an ACA showing the electric pathway.

As there is no contact between the particles there is no conduction in the x and y directions simply in the Z. The particles used in the films are themselves metallic in nature and are opaque, however if the adhesive portion is of a high transparency then the particles will only serve to block an amount of light proportional to their concentration. If this concentration is low enough, usually around 10 vol.% then the films are deemed to have high enough light transmission to be classed as transparent (there will also be a factor of light diffraction around particles which will also be taken into account).

Work initially started on ACAs back in the 70s and the product was quickly taken to market by companies such as Nippon, Hitachi and Sony and since by 3M, Loctite and Delo as well as others. As there is a wide variety of different applications for ACAs many different products have been produced with varying parameters. Almost every type of polymer adhesive can and has been used in an ACA but currently the two most commonly used are those based on epoxies and those based on acrylates [182].

The two most common metals used in ACAs are silver and nickel and out of the two silver is most often used for its superior conductivity and chemical stability [182]. Unlike other good conductors, such as copper, which form non-conductive oxides over time when exposed to moisture and heat, the oxides of silver show high conductivity. Silver also benefits from being able to be formed into a wide range of sizes and shapes with relative ease such as; spheres, flakes, nanowires and porous particles [182-183]. Nickel on the other hand retains its conductivity due to its resistance to oxide growth but is a harder material to process into desired shapes. However nickel does find applications in ACAs due to its resistance to deformation under pressure and also its lower cost compared to silver. Both materials suit themselves well to coating of non-metallic particles, such as glass microspheres, which are being used more readily within ACAs [184]. Metal coated non-metallic particles not only have the advantage that they use much less metal than particles of pure metal keeping cost down but they can also be made very spherical and to within a narrow size distribution - both qualities beneficial to ACAs . Other fillers include gold and carbon, however these tend to be limited to high end applications (space, military) or low end applications (shielding) respectively [182,185].

1.9.2. Isotropic Conducting Adhesives and Percolation Theory

Unlike anisotropic conducting adhesives isotropic conducting adhesives (ICA) can be made that will conduct in the x, y and z axis equal. Isotropic conductivity can be achieved in composite materials (such ICAs) by using a network of conducting particles, such as silver, copper and nickel, which span out in all directions of a matrix equally. However for an ICA to achieve conductivity from one point to another there must be a connecting chain of conducting particles linking each point. As shown in Figure 1.20.a if the loading of the particles within the matrix is too low no connection is made from A to B, the point in which the particle loading becomes great enough to form a spanning network, Figure 1.20.b, there is the first connection from A to B and as the particle loading is increased Figure 1.20.c the amount of pathways increased.

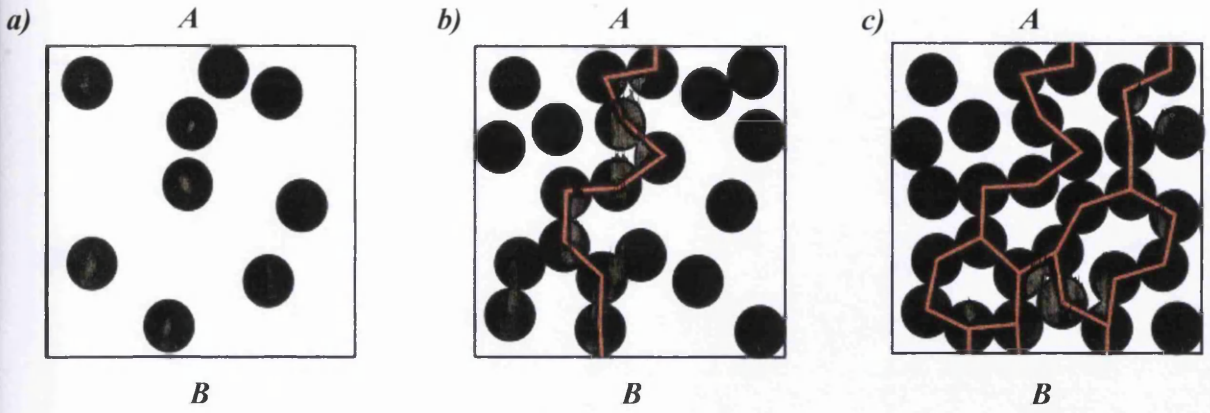

Figure 1.20. Schematic showing conducting particles (black circles) within a matrix (white space within the square) at a loading a) too low to form a conducting pathway between points A and B b) at the point which the load is great enough to form the first conducting pathway (red line) between A and B and c) a loading above that shown in b where there are many conductive pathways formed in 2-dimensions

This scenario is modelled using percolation theory and the situation shown in Figure 1.20.b is known as the critical percolation threshold and is the point at which a continuous spanning network is formed [186]. Percolation was first suggested in 1957 [187] and is an expansive field of maths in its own right, being used to described many real world phenomena such as the spread of wildfire and social networks[188]. At its most basic level it describes when randomly distributed spherical phases within a matrix of another phase reach a density such that they form clusters which span from one bounding edge of the matrix to the another bounding edge and how the spanning clusters grow as the density increases in 2-D [186] (Figure 1.20.c). However percolation theory has also to be used in more complex ways such as in 3-D and also using different geometry phases such as honeycombs and elongated structures such as sticks and rectangles [189].

In the case of ICAs above the percolation threshold there will be three distinct phases: The adhesive matrix, isolated electrically conducting particles (e.g. silver) and electrically conducting particles forming spanning clusters. It is only the last of these that will provide any conduction and therefore by varying the amount of conducting particles an ICA contains will vary its conductivity isotropically (assuming randomly distributed particles within the matrix) [190]. The electrical conductivity of such an ICA would increase its bulk d.c conductivity (g_e) as the volume fraction (ϕ) of the conducting particles occupied within the ICA according to a power law shown by Equation 1.10. [190].

$$g_e(\phi) \propto (\phi - \phi_c)^{\mu} \quad \text{(Eq. 1.10)}$$

where the critical exponent μ has been calculated to be = 1.94 for random 3-D networks and 1.33 for 2-D [186]. ϕ_c is the minimum volume fraction needed to form a spanning cluster in the ICA know as the percolation threshold which is 0.18 for spheres in 3-D[191].

The bulk conductivity (G_{film}) of an ICA is therefore expected to follow Equation 1.11;

$$G_{film}(\phi) = K(\phi - \phi_c)^{\mu} \quad \text{(Eq. 1.11)}$$

where K is an arbitrary scaling factor.

What this also means for ICAs is that the particles do not have to be comparable to the film thickness (as in ACAs) but can consist of many small conducting particles to form the conducting pathways and this may incur cost savings as well as additional transparency.

1.9.3. Conducting Polymer Adhesives

While other conducting adhesives focus on additions of metallic particles and inorganic salts there has been relatively little work done on using conducting polymers and even less on transparent conducting adhesives. Initial work in the area was done as early as 1995 looking at polymer blends of polyaniline (PANI) and epoxy for use as an anti-static film [192] as well as a corrosion inhibitor [193]. Work continued over the next 15 years with many papers using PANI and different polymers such as Polycarbonate [194] Poly(vinyl alcohol) [195] and Poly(ethyleneoxide) (PEO)[196]. With particular interest being paid to a blend of PANI-camphorsulfonic acid/poly(methyl methacrylate) (PANI-CSA/PMMA) which showed low sheet resistances of 100 Ω/□ and transmittance of ~70% between 475 and 675 nm [197-198]. This was put down to a combination of very low percolation threshold and interpenetrating network of fibrillar, crystalline PANI within the PMMA matrix [199]. Recently a paper was published regarding the use of PANI with different blend of epoxies and solvents for the potential use as adhesives [200]. It was concluded that the type of epoxy used for the blend dictated the percolation threshold of the final film, proposing that this was

due to a high aspect ratio forming conducting pathways. It was also suggest that that solvent plays a crucial role in the final film physical and electrical properties for the same reasons.

PEDOT:PSS has had less attempts made at being blended with polymers for the purpose of adhesion than that of PANI but is starting to gain more attention. As mentioned in the section 2.1.2 PEDOTs have been blended with binders for the purpose of retaining electrical conductivity during subsequent thermoforming. Indeed PEDOT:PSS has successfully been blended with Polyvinyl alcohol and PEO to form conducting films, where conductivity was achieved at a low PEDOT:PSS concentration due to the phase segregation of the PEDOT:PSS by the crystalline PEO meaning the film had more conducting pathways [201]. Heraeus Clevios™ commercially produce a film designed to be coated onto surfaces and undergo post forming, but it does not provide adhesive properties to another surface [202]. There have been two key approaches to modify PEDOT solutions in such a way that they become both adhesive and conductive, each way maintaining a level of transparency. The first was by the addition d-Sorbitol, within a PEDOT:PSS solution itself and also thermally deposited on top as a thin (10nm) layer [180]. This paper notes that the thermally deposited layer was the most controllable. The d-Sorbitol layer provides enough mechanical force to bond the two substrates as it acts as a hot melt adhesive with a melting point of ~100°C but is of a thin enough nature that it does not interfere with electrical conductivity. In this work they also make a polymer light emitting diode (PLED, often called an OLED). While it doesn't give exact details of the transparency it can be seen from the promising results they obtained for the PLED (and pictures given) that the transparency must be high.

The second approach has been to mix graphene oxide (GO) into the PEDOT:PSS solution for the intention of making laminated tandem solar cells [203]. It has previously been reported that a shift from a benzenoid to quinoid ground states can increase conductivity [204] and the GO in the aqueous solution appears to make this transition. In addition to this the structure moves to a well aligned fibril like structure which could not only aid an increase in conductivity but may also be the reason for the tacky like qualities of the film.

1.10. Electroluminescent lamps

There are now a range of options for flexible printed light emitting devices with the two most dominate options being: the relatively mature technology of Electroluminescent (EL) and the emerging Organic Light Emitting Diodes (OLEDs). While the two technologies both emit light they differ in the way the emission is produced: OLED devices by the principle of injection of electrons and holes near a p-n junction to emit light whereas EL devices emit light by the acceleration of electrons in a high electric field causing excitation by impact [205]. More specifically EL lamps often use phosor powders commonly composed of ZnS doped with other materials such as Mn or Cu. The doping materials create defects which act to concentrate applied electric fields meaning applied fields of 1 - 10 V/mm can create local fields > 100 V/mm. The high local electric field then induces tunneling of holes from one end and electrons from the other. The holes are trapped on copper recombination centers and upon reversal of fields, the emitted electrons recombine with the trapped holes to produce light as shown in Figure 1.21.

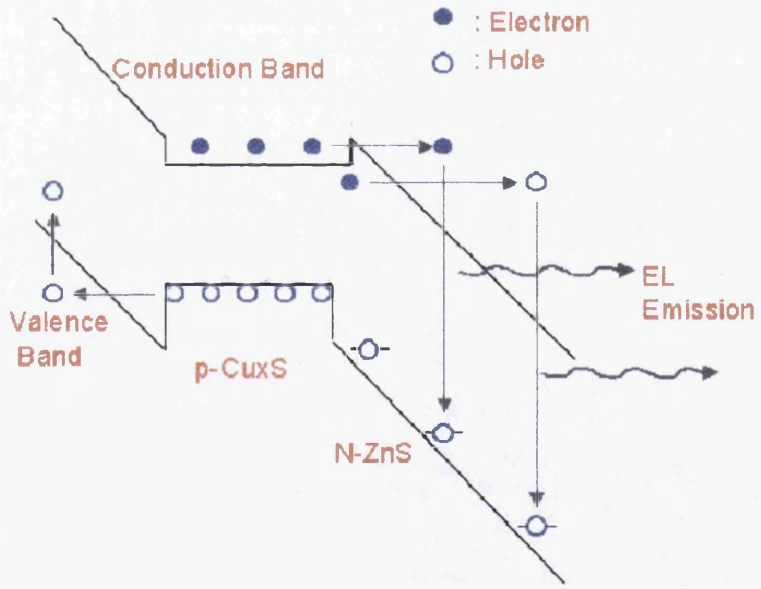

Figure 1.21. Energy level diagram of an electroluminescent emission of phosopor powder doped with CuS. Copyright Gdansk University.

This principle of operation gives them some fundamental disadvantages over OLEDs, such as high operation voltage, lower operational lifetime and limited brightness. However EL is now considered a mature technology and with its properties widely reported [206-207],

ease of processing and insensitivity to the environment over OLEDs makes them a more viable option for applications such as LCD backlighting [208].

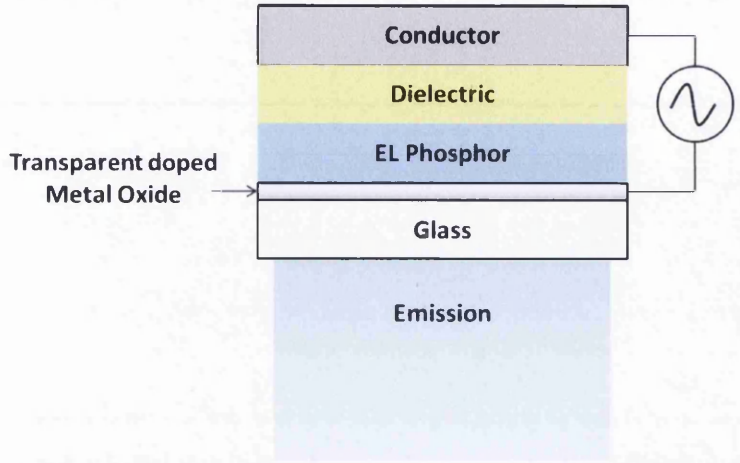

Figure 1.22. Cross section schematic of a conventional bottom emission EL device.

A basic cross-section of a typical inorganic electroluminescent lamp can be seen in Figure 1.22. The EL device consists of several layers where a phosphor layer, which has phosphor particles embedded within a dielectric is deposited onto transparent conductor and then has a dielectric and a conductor sequentially coated on top of it. The device is capacitive in nature and as a result uses high AC driving voltage for its operation. Electrons from the interface between the phosphor and the dielectric or the bulk states of the phosphor are accelerated by the electric field caused by the high AC voltage and then impact, exciting luminescent centres which in turn generate light. The classic phosphor material used is ZnS doped with Mn however other materials such as SrS:Ce and (Ca,Sr)GazS4:Ce have been suggested for their colour enhancement.

With EL being a mature technology many companies offer of the shelf EL materials which can be coated in a variety of different ways.

1.11. Near Infrared Radiation Curing

The near-infrared region (NIR) of the electromagnetic spectrum is situated between the visible and the infrared at a wavelength of 780 nm to 2500 nm, Figure 1.22. Typically in commercial NIR ovens the emitters (lamps) peak at around 1000 nm.

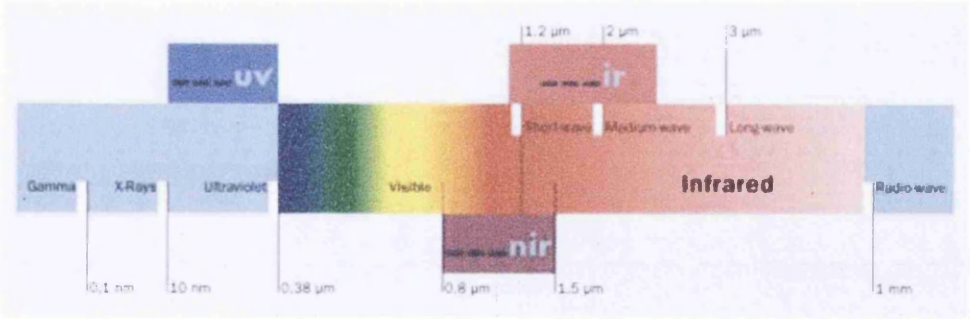

Figure 1.23. NIR band within the electromagnetic spectrum [209] Copyright 2009 Adphos.

In this region the radiation excites combinations and overtones of molecular vibrations which are forbidden by the selection rules of quantum mechanics [210]. This means that the molar absorptivity is typically small in this part of the electromagnetic spectrum with the consequence that many polymer compounds do not have a strong absorbance and so do not heat up easily when irradiated with such short wave IR. NIR therefore has the potential to selectively heat and dry a material with a strong absorbance in this part of the spectrum and its inherent energy density would enable high speeds, whilst any material without a strong NIR absorbance will allow penetration of the radiation through it thus avoiding damage. NIR also has been shown to have ultrafast processing speeds, being capable of 200 m min^{-1} line speeds when curing paints on steel substrates [211], sintering silver inks on PET substrates[212] and for rapid sintering of titania particles on steel and titanium surfaces for dye-sensitized solar cells (DSCs)[213].

1.12. Conclusions and aims for thesis

Next generation low-cost printable opto-electronic devices, such as s-DSCs and EL lamps, represent exciting and rapidly growing scientific fields with several developments being made in recent years. There is massive potential for devices of this nature to be applied on a large industrial scale however first several important challenges must be overcome. One of the main issues is the use of an evaporated metallic contact or at the least a contact that contains expensive metals such as Ag or Au which are not viable options for large area applications. In recent years the advent and widespread use of conducting polymers such as PEDOT:PSS has offered an alternative contact which can be both fully printed and transparent. PEDOT's in particular still present a problem if applied directly to many opto-electronic devices containing sensitive organic material since the solvents and temperatures used during their processing can damage the layers. In combination with this the conductivities of PEDOT:PSS still aren't comparable to metallic conductors so without significant modification and alteration their use in opto-electronic devices is still limited.

Conductive adhesives is an ever growing area of interest and are finding applications in a wide range of tradition electronic devices, replacing solder to much such devices more flexible. The adhesives usually consist of a conducting phases within a non-conducting adhesive phase leaving the conductivity dictated by percolation theory. Conductive adhesives represent an interesting concept for use in opto-electronic devices as they could potentially be used to connect devices to layer of higher conductivity (for large area current extraction), avoiding the potentially damaging direct deposition of the layer onto the device.

Recently NIR curing has shown to have massive potential in the reduction of both time and energy input when processing wet deposited layers such as paints and inks. These are both important energetic and financial considerations for the processing of any large area coatings. Similarly ZnO is gaining interest over other semiconductor materials, such as titania, due to its low temperature and energy saving processing. However the performance of devices such as DSCs made with ZnO have not yet managed to match that of those made with titania.

This work aims to advance the field of photovoltaics by creating for the first time an s-DSC on metal using a transparent conducting adhesive to contact a transparent electrode. In doing so creating the world's first vacuum free, ITO free, silver free, all printed roll-to-roll compatible solid state dye sensitised solar cell (culminating in Chapter 7). However to achieve this was not straight forward and a number of challenges needed to be overcome.

Firstly a transparent conducting adhesive (TCA) that was compatible with the device architecture had to be developed. **Chapter 3** describes how the TCA was developed from a series of trials and how ultimately an acrylic based pressure sensitive adhesive came out as the most viable. The chapter then describes how the various properties of conductivity, tack and transparency of the material change with varying PEDOT:PSS concentration and film thickness. It doing so it was discovered that the volume fraction of PEDOT:PSS needed in the dry film to achieve conductivity (critical percolation threshold) was close to 0.0078. The fact that it was so low shows that there was some ordering to the PEDOT:PSS within the TCA providing benefits to the cost, transparency and tack of the film.

The TCA was then cast onto a printed grid carrier substrate and adhered to the top of a conventional s-DSC, however these cells showed very low currents owing to the Spiro-OMeTAD's poor lateral conductivity. As a result it was decided that a material with higher lateral conductivity (but maintaining transparency) was needed on top of the Spiro-OMeTAD as a contact layer. This layer was required to be compatible with R2R deposition and with the TCA material. For this PEDOT:PSS was the obvious choice however owing to the fact that the PEDOT:PSS is a waterborne solution and needs to be cured at 120°C and Spiro-OMeTAD is moisture sensitive and s-DSCs are temperature sensitive some challenges for depositing and curing spiro-OMeTAD need to be overcome first.

Chapter 4 deals with how orthogonal solvents such as IPA and Ethanol were added to the PEDOT:PSS solution to decrease the % of water it contained due to its potential impact on the Spiro-OMeTAD. However the % of PEDOT:PSS would also decrease (as would the final film thickness) and the film structure and ultimately conductivity might have also been affected and therefore the this impact was also investigated. It was found through a series of tests that the conductivity wasn't appreciatively changed and that a ratio as high as 1:1:1 PEDOT:PSS to Ethanol to IPA could be used. To combat the use of 120°C for the curing of the PEDOT:PSS evaporation drying using high convection hot air was used. This ensured that the films could be dried but that their temperature remained below 60°C.

To take this a step further **Chapter 5** deals with the NIR curing of the PEDOT:PSS This was attempted to speed up the curing making it more compatible with roll-to-roll processing and it was found that the curing time could be reduced from 240 seconds down to 2 seconds without any significant change in the resistivity of the film. The TCA used PEDOT:PSS and therefore could also be cured by NIR in a matter of seconds. The use of these developments with the PEDOT:PSS and the use of the TCA within the s-DSC film can be found in Chapter 7 where it was found that a combination of PEDOT:PSS mixed in the ratio 4:1:1 with ethanol and IPA and dried by forced evaporation along with a TCA made with a volume fraction of 0.0175 and film thickness of 37μm gave an s-DSC with comparable efficiencies to ones will an evaporated silver back contact. This then paved the way for an s-DSC to be constructed on a metallic substrate using all of the prior developments. The NIR curing of the PEDOT:PSS could not be utilised in this instance as it still heated the cells as a whole to undesirable temperatures but the development may still have uses in other opto-electronic devices.

Even with the use of a TCA the s-DSC still has a high temperature step when 450°C is used to sinter the TiO_2 and eliminating this step by using zinc oxide, which has the potential to be sintered at lower temperatures, was investigated. ***Chapter 6*** electrochemically investigates how sintering ZnO at lower temperatures impacts on the performance of liquid based DSCs through a range of transient and EIS techniques. This showed that ZnO films sintered at temperatures of 250°C had the potential to be used in DSC technology.

The technology developments in chapters 3-6 are brought together in **Chapter 7** to demonstrate a how they can be practically used an the impact they have on a solid state dye sensitised solar cell made on a metallic substrate that is processed without the need for vacuum, ITO or silver that can be printed roll-to-roll on a metallic substrate.

Finally to prove the TCAs potential in other opto-electronic devices (other than s-DSC), EL lamps, which are charge based devices and also emit not receive light of their operation, were fabricated and trialled with the TCA as described in **Chapter 8**. This showed that not only could conventional based devices made with FTO glass be fabricated with a TCA instead of a silver paint but that the cells could also be made on aluminium substrate,

reducing cost. The TCA conformed to the phosphor powder and enabled a high emission from the lamp dependant on the tack, conductivity and transparency of the TCA.

1.13. References

[1] H. Tributsch, *Photochemistry and Photobiology*, **16**(4), 261, (1972).

[2] B. O'Regan, M. Grätzel, *Nature*, **353**, 737 (1991).

[3] T. Meyer, A. Meyer, D. Ginestoux , *Proc. SPIE-Int. Soc. Opt. Eng.*, **4465,** 13, (2002).

[4] T. Miyasaka, Y. Kijitori, *J.Electrochem. Soc.*, **151**(11), 1767, (2004).

[5] G. Tulloch, *J. Photochem. Photobiol. A : Chem.*, **164,** 209, (2004).

[6] H. Snaith, L. Schmidt-Mende, *Adv. Mater.* **19**, 3187, (2007).

[7] B. Hardin, H. Snaith, M. McGehee, *Nature Photonics*, **6**,162 (2012).

[8] M. Grätzel, *J. Photochem. and Photobiol. C: Photochem. Rev.*, **4**(2), 145, (2003).

[9] M. Grätzel, *J. Photochem. and Photobiol. A: Chem.*, **164**(1), 3, (2004).

[10] M. Ryan, *Platinum Metals Rev.*, **53**(4), 216 (2009).

[11] M. Nazeeruddin, R. Splivallo, P. Liska, P. Comte, M. Grätzel, *Chem. Commun.*, 1456 (2003).

[12] R. Argazzi, C. Bignozzi, T. Heimer, F. Castellano, G. Meyer, *Inorg. Chem.*, **33**, 5741 (1994).

[13] K. Finnie, J. Bartlett, J. Woolfrey, *Langmuir*, **14**, 2744, (1998).

[14] M. Nazeeruddin, M. Amirnasr, P. Comte, J. Machay, A. McQuillan, R. Houriet, M. Grätzel, *Langmuir*, **16**, 8525, (2000).

[15] K. Murakoshi. G. Kano, Y. Wada, S. Yanagida, H. Miyazaki, M. Matsumoto., *J. Electroanal. Chem.*, **396**, 27, (1995).

[16] A. Kay, M. Grätzel, *J. Phys. Chem.*, **97**(23), 6272, (1993).

[17] M. Garcia-Iglesias, J. Yum, R. Humphry-Baker, S. Zakeeruddin, P. Pechy, P. Vazquez, E. Palomares, M. Grätzel, M. Nazeeruddin, T. Torres, *Chem. Sci.*, **2**(6), 1145, (2011).

[18] N. Cai, S-J. Moon, L. Cevey-Ha, T. Moehl, R. Humphry-Baker, P. Wang, S. Zakeeruddin, M. Grätzel, *Nano Letters*, **11**(4), 1452, (2011).

[19] P. Santra, P. Kamat, *J. of the American Chemical Society*, **134**(5), 2508, (2012).

[20] T. Ma, X. Fang, M. Akiyama, K. Inoue, H. Noma, E. Abe, *J. Electroanal. Chem.*, **574**, 77, (2004).

[21] F. Pichot, J. Pitts, B. Gregg, *Langmuir*, **16**, 5626, (2000).

[22] S. Haque, E. Palomares, H. Upadhyaya, L. Otley, R. Potter, A. Holmes, J. Durrant, *Chem. Commun.*, 3008, (2003).

[23] T. Allen, *Particle Size Measurement*, Chapman & Hall, (1993).

[24] M. Hoffmann, S. Martin, W. Choi, D. Bahnemann, *Chem. Rev.*, **95**, 69, (1995).

[25] M Gratzel, *Inorg. Chem.*, **44**, 6841, (2005).

[26] N. Park, J. Van de Lagematt , A. Frank, *J. Phys. Chem. B.*, **104**, 8989, (2000).

[27] L. Hu, S. Dai, J. Weng, S. Xiao, Y. Sui, Y. Huang, S. Chen, F. Kong, X. Pan, L. Liang, K. Wang, *Phys. Chem. B.*, **111**, 358, (2007).

[28] G. Kron, U. Rau, K. Taretto, M. Durr, T. Miteva, J. Werner, *Proceedings of 3rd World Conference*, **1**, 133, (2003).

[29] J. Wienke, J. Kroon, P. Sommeling, R. Kindermann, M. Späth, J. Van Roosmalen, W. Sinke, *ECN*, (1997).

[30] P. Sommeling, M. Späth, J. Kroon, R. Kinderman, J. Van Roosmalen, *ECN*, (2000).

[31] T. Miyasaka, M. Ikegami, Y. Kijitori, *J. Electrochem. Soc.*, **154**, A455 (2007).

[32] A. Hagfeldt, M. Grätzel, *Chemical Reviews*, **95**(1), 49, (1995).

[33] V. Zardetto, F. Di Giacomo, D. Garcia-Alonso, W. Keuning, M. Creatore, C. Mazzuca, A. Reale, A. Di Carlo, T. Brown, Adv Eng Mater, 2013

[34] D. Cahen, G. Hodes, M. Grätzel, *J. Phys. Chem. B.*, **104**(9), 2053, (2000).

[35] K. Kalyanasundaram, M. Grätzel, *Coord. Chem. Rev.*, **77**, 347, (1998).

[36] M. Nazeeruddin, A. Kay, I. Rodicio, R. Humphry-Baker, E. Müller, P. Liska, N. Vlachopoulos, M. Grätzel. *J. Am. Chem. Soc.*, **115**, 6382, (1993.

[37] G. Redmond, D. Fitzmaurice, *D. J. Phys. Chem.*, **97**, 1426, (1993).

[38] Y. Tachibana, K. Hara, K. Sayama, H. Arakawa, *Chem. Mater.*, **14**, 2527, (2002).

[39] S. Ito, N. Ha, N. Rothenberger, P. Liska, P. Comte, S Zakeeruddin, P. Pechy, M. Nazeeruddin, M. Gratzel, *Chem Commun.*, 4004, (2006).

[40] Z. Wang, H. Kawauchi, T. Kashima, H. Arakawa, *Coordination Chemistry Reviews.*, **248**(13), 1381, (2004).

[41] C. Barbe, F. Arendse, P. Comte, M. Jirousek, F. Lenzmann, V. Shklover, M. Grätzel, *Am. Ceram. Soc.*, **80**, 3157, (1997).

[42] J. Hyeok, P. Yongseok, J. Ho-Gyeong, Y. Seung-Yup-Lee, M. Gu-Kang, *Jrnal of The Elctrochel Scty.*, **155**, 145, (2008).

[43] A. Hagfeldt, U. Bjorksten, S. Lindquist, *Sol. Energy Mater. Sol. Cells*, **27**, 293, (1992).

[44] N. Alonso-Vante, J. Nierengarten, J. Sauvage, *J. Chem. Soc., Dalton Trans.*, **11**, 1649, (1994).

[45] H. Lindstorm, H. Rensmo, S. Sdergren, A. Solbrand, S Lindquist, *J. Phys. Chem.*, **100**, 3084, (1996).

[46] M. Kang, N. Park, K. Ryu, S. Chang, K. Kim, *Solar Energy Materials and Solar Cells*, **90**, 574, (2006).

[47] R. Gomez, P. Salvador, *Solar Energy Materials & Solar Cells*, **88**, 377, (2005).

[48] K. Hara, T. Horiguchi, T. Kinoshita, K. Sayama, H. Sugihara, H. Arakawa, *Sol. Energy Mater. Sol. Cells*, **64**, 115, (2000).

[49] S. Ito, T. Kitamura, Y. Wada, S. Yanagida, *Sol. Energy Mater. Sol. Cells*, **76**, 3, (2003).

[50] H. Greijer, L. Karlson, S. Lindquist, A. Hagfeldt, *Renewable Energy*, **23**, 27, (2003).

[51] M. Dürr, A. Schmid, M. Obermaier, A. Yasuda, G. Nelles, *J. Phys. Chem. A*, **109**, 3967, (2005).

[52] D. Zhao, T. Peng, L. Lu, P. Cai, P. Jiang, Z. Bian, *J. Phys. Chem. C*, **112**, 8486, (2008).

[53] S. Uchida, R. Chiba, M. Tomiha, N. Masaki, Shirai, *M.Electrochemistry*, **70**, 418, (2002).

[54] N. Meng-Ni, M. Leung, *Solar Energy Materials & Solar Cells*, **90**, 1331, (2006).

[55] Y. Saito, S. Kambe, T. Kitamura, Y. Wada, S. Yanagida, *Sol. Energy Mater. Sol. Cells*, **83**, 1, (2004).

[56] A. Arango, S. Carter, P. Brock, *Appl. Phys. Lett.*, **74**, 1698, (1999).

[57] A. Breeze, Z. Schlesinger, S. Carter, P. Brock, *P J Phys. Rev. B*, **64**, 125, (2001).

[58] H. Al-Dmour, D. Taylor, J. Cambridge, *J. Phys. D: Appl. Phys.*, **40**, 5034, (2007).

[59] A. Tamba, N. Azzerri, *J. Appl. Electrochem.*, **2**, 175, (1972).

[60] Y. Ho-Gyeong, J. Yongseok, K. Jongdae, B. Byeong-Soo, K. Gu, *App Phys Lett.*, **93**, 133311, (2008).

[61] G. Smestad, C. Bignozzi, R. Argazzi, *Sol. Energy Mater. Sol.Cells*, **32**, 259, (1994).

[62] N. Park, G. Schlichthörl, J. Van de Lagemaat, H. Cheong, A. Mascarcnhas, A. Frank, *J. Phys. Chem. B*, **103**, 3308, (1999).

[63] D. Zhang, T. Yoshida, H. Minoura, *Chem. Lett.*, **31**, 874, (2002).

[64] X. Fang, T. Ma, M. Akiyamaa, G. Guana, S. Tsunematsua, E. Abe, *Thin Solid Films*, **472**, 242, (2005).

[65] M. Toivola, F. Ahlskog, P. Lund, *Solar Energy Materials & Solar Cells*, **90**, 2881, (2006).

[66] Y. Jun, J. Kim, M. Kang, *Solar Energy Materials & Solar Cells*, **91**, 779, (2007).

[67] K. Onoda, S. Ngamsinlapasathian, T. Fujieda, S. Yoshikawa, *SEE*, 21, (2006).

[68] K. Onoda, S. Ngamsinlapasathian, T. Fujieda, S. Yoshikawa, *Solar Energy Materials & Solar Cells*, **91**, 1176, (2007).

[69] K. Miettunen, J. Halme, M. Toivola, P. Lund, *J. Phys. Chem. C*, **112**, 4011, (2008).

[70] M. Kang, N. Park, S. Kwang, H. Soon, K. Kim, *Chem. Lett.*, **34**, 804, (2005).

[71] http://www.tinplate.com.tw/Frame/tfs.htm

[72] M. Vafaee, M. Ghamsari, *Mater. Lett.*, **61**, 3265, (2007).

[73] S. Rani, P. Suri, P. Shishodia, R. Mehra, *Sol. Energ. Mat. Sol. C*, **92**, 1639, (2008).

[74] G. Redmond, D. Fitzmaurice, M. Graetzel, *Chem. Mater.*, **6**, 686, (1994).

[75] L. Zeng, S. Dai, W. Xu, K. Wang, *Plasma Sci. Tech.*, **8**, 172, (2006).

[76] L. Spanhel, M. Anderson, J. Am, *Chem. Soc.*, **113**, 2826, (1991).

[77] K. Keis, L. Vayssieres, H. Rensmo, S. Lindquist, A. Hagfeldt, *J. Electrochem. Soc.*, **148**, A149, (2001).

[78] H. Horiuchi, R. Katoh, K. Hara, M. Yanagida, S. Murata, H. Arakawa, M. Tachiya, *J. Phys Chem B*, **107**(11), 2570, (2003).

[79] A. Furube, R. Katoh, K. Hara, S. Murata, H. Arakawa, M. Tachiya, *J. Phys.Chem. B*, **107**, 4162, (2003).

[80] R. Zhang, J. Pan, E. Briggs, M. Thrash, L. Kerr, *Sol. Energ. Mat. Sol. C*, **92**, 425, (2008).

[81] K. Tennakone, G. Kumara, I. Kottegoda, V. Perera, *Chem. Commun.*, **1**, 15, (1999).

[82] K. Keis, E. Magnusson, H. Lindstrom, S. Lindquist, A. Hagfeldt, *Sol. Energy Mater. Sol. Cells*, **73**, 51, (2002).

[83] H. Snaith, A. Moule, C. Klein, K. Meerholz, R. Friend, M. Grätzel, *Nano. Lett.* **7**, 3372, (2007).

[84] M. Boucharef, C. Bin, M. Boumaza, M. Colas, H. Snaith, B. Ratier, J. Bouclé, *Nanotech.*, **21**, 205203, (2010).

[85] G. Kumara, M. Okuya, K. Murakami, S. Kaneko, V. Jayaweera, K. Tennakone, *J. Photochem. Photobiol. A*, **164**, 183, (2004).

[86] S. Roh, R. Mane, S. Min, W. Lee, C. Lokhande, S. Han, Appl. Phy. Lett., 89, 253512, (2006).

[87] Q. Zhang, C. Dandeneau, X. Zhou, G. Cao, Adv. Mater., 21, 4087, (2009).

[88] K. Kalyanasundaram, Dye Sensitized Solar Cells, CRC Press, (2010).

[89] K. Miettunen, X. Ruan, T. Saukkonen, J. Halme, M. Toivola, H. Guangsheng, P. Lund, *J. Electrochem. Soc.*, **157**(6), B814, (2010).

[90] G. Reynolds, T. Watson, G. Williams, D. Worsley, *ECS Transactions*, **33**(17), 129 (2011).

[91] U. Bach, D. Lupo, P. Comte, J. Moser, F. Weissortel, J. Salbeck, H. Spreitzer, M. Grätzel, *Nature*, **395**, 583 (1998).

[92] J. Wu, S. Hao, Z. Lan, J. Lin, M. Huang, Y. Huang, *Adv. Funct. Mater.*, **17**, 264, (2007).

[93] K. Tennakone, G. Humara, A. Kumarasinghe, K. Wijayantha, P. Sirimanne, *Semiconduct. Sci. Technol.*, **10**, 1689, (1995).

[94] K. Murakoshi, R. Kogure, Y. Wada, S. Yanagida, *Chemistry Letters*, **5**, 471, (1997).

[95] U. Bach, Thesis no. 2187, EPFL, (2000).

[96] H. Bassler, *Phil. Mag. B*, **50**, 347, (1984).

[97] H. Bässler, P.M. Borsenberger, R. Perry, *J. Polym. Sci. B: Polym. Phys.*, **32**, 1677, (1994).

[98] H. Snaith, M. GrätzeL, *Appl. Phys. Lett.* **89**, 262114, (2006).

[99] K. Karlsson, Thesis no. 892, Uppsala University (2011).

[100] J. Krüger, R. Plass, M. Grätzel, P. Cameron, L. Peter, *J. Phys. Chem. B*, **107**, 7536, (2003).

[101] J. Kruger, R. Plass, L. Cevey, M. Piccirelli. M. Gratzel, U. Bach, *Appl. Phys. Lett.*, **79**(13), 2085, (2001)

[102] F. Fabregat-Santiago, *J. Am. Chem. Soc.*, **131,** 588 (2009)

[103] P. Bonhôte, J. Moser, R. Humphry-Baker, N. Vlachopoulos, S. Zakeeruddin, L. Walder, M. Grätzel, *J. Am. Chem. Soc.* **121,** 1324 (1999).

[104] S. Haque, S. Handa, K. Peter, E. Palomares, M. Thelakkat, J. R. Durrant, *Angew. Chem. Int. Ed.* **44,** 5740, (2005).

[105] R. Marcus, N. Sutin, *Biochim. Biophys. Acta* **811,** 265, (1985).

[106] H. Snaith, S. Zakeeruddin, L. Schmidt-Mende, C. Klein, M. Grätzel, *Angew. Chem. Int. Ed.* **44,** 6413, (2005).

[107] H. Snaith, R. Humphrybaker, P. Chen, I. Cesar, M. Grätzel, *Nanotech.*, **19,** 424003, (2008).

[108] I. Ding, N. Tetreault, J. Brillet, B. Hardin, E. Smith, S. Rosenthal, F. Sauvage, M. Gratzel, M. McGehee, *Adv. Funct. Mater.* **19**, 2431, (2009).

[109] I. Ding, J. Melas-Kyriazi, N. Cevey-Ha, K. Chittibabu, S. Zakeeruddin, M. Grätzel, M. McGehee, *Org. Electron.* **11,** 1217 (2010).

[110] L. Schmidt-Mende, M. Grätzel, *Thin Solid Films,* **500,** 296, (2006).

[111] J. Kroeze, N. Hirata, L. Schmidt-Mende, C. Orizu, S. Ogier, K. Carr, M. Grätzel, J. Durrant, *Adv. Funct. Mater.* **16,** 1832, (2006).

[112] P. Docampo, H. Snaith, *Nanotechnology,* **22,** 225403, (2011).

[113] W. Feast, *Handbook of Conducting Polymers*, Marcel Dekker (1986)

[114] R. Hanselmann, *Elektrisch leitfahige Polymere. Thieme ROEMPP Online. www.roempp.com,* (2008)

[115] A. Heeger, *J. Phys. Chem. B.,* **105**(36), 8475, (2001).

[116] S. Curran, *Handbook of Organic Conducting Molecules and Polymers*, John Wiley and Sons (1997).

[117] S. Curran, *Handbook of Organic Conducting Molecules and Polymers*, John Wiley and Sons, (1997).

[118] L. Groenendaal, F. Jonas, D. Freitag, H. Pielartzik, J. Reynolds, *Adv. Mater.* **12**, 481, (2000).

[119] F. Jonas, EP 440957 8 Feb 1990

[120] F. Jonas, EP 752454 3 July 1995

[121] T. Tachikawa, N. Itoh, S. Handa, D. Aoki, and T. Miyake. *SID proceeding,* **34,** 1280, (2005).

[122] A.MacDiarmid, A. Epstein, *Synth. Met.* **65**(2), 103, (1994).

[123] F. Jonas, EP 686662 6 May 1994.

[124] B. Martin, N. Nikolov, S. Pollack, A. Saprigin, R. Shashidhar, F. Zhang, P. Heiney, *Synth. Met.* **142**(2), 187, (2004).

[125] J. Kim, J. Jung, D. Lee, J. Joo, *Synth. Met.* **126**(2), 311, (2002).

[126] J. Ouyang, C. Chu, F. Chen, Q. Xu, Y. Yang,, *Adv Funct Mater.*, **15**(2), 203, (2005).

[127] W. Kim, A. Makinen, N. Nikolov, R. Shashidhar, H. Kim, Z. Kafafi, *Appl Phys Lett.*, **80**(20), 3844, (2002).

[128] S. Timpanaro, M. Kemerink, F. Touwslager, M. De Kok, S. Schrader, *Chem Phys Lett.*, **394**(4), (2004).

[129] M. Satoshi, Y. Kazuyoshi, N. Hiromichi, A. Toshika, N. Mitsuaki, *J. P.*, **6**, 204704, (2006).

[130] F. Louwet, L. Groenendaal, J. Dhaen, J. Manca, J. Van Luppen, E. Verdonck, L. Leenders, *Synth. Met.*, **135**(1), 115, (2003).

[131] H. Yasushi, M. Yasushi, Y. Kazuyoshi, N. Hiromichi, A. Toshika, J. P. **27**, 328276, (2005)

[132] B. Fan, B. Mei, J. Ouyang, *Macromolecules*, **41**(16), 5971, (2008).

[133] S. Jönsson, J. Birgerson, X. Crispin, G. Greczynski, W. Osikowicz, A. Van der Gon, W. Salaneck, M. Fahlman, *Synth. Met.*, **139**(1), 1, (2003).

[134] M. Döbbelin, R. Marcilla, M. Salsamendi, C. Pozo-Gonzalo, P. Carrasco, J. Pomposo, D. Mecerreyes, *Chem. Mater.*, **19**(9), 2147, (2007).

[135] Y. Xia, J. Ouyang, *Macromolecules*, **42**(12), 4141, (2009).

[136] X. Crispin, F. Jakobsson, A. Crispin, P. Grim, A. Volodin, M. Van der Auweraer, W. Salaneck, M. Berggren, *Chem. Mater.*, **18**(18), 4354, (2006).

[137] A. Nardes, R. Janssen, M. Kemerink, *Adv. Funct. Mater.*, **18,** 865, (2008).

[138] J. Kim, J. Jung, D. Lee, J. Joo. *Synth. Met.*, **126**(2), 311, (2002).

[139] B. Martin, N. Nikolov, S. Pollack, A. Saprigin, R. Shashidhar, F. Zhang, P. Heiney, *Synth. Met.*, **142**(1) 187, (2004).

[140] S. Ghosh, O. Inganas, *Synth. Met.*, **121**(1), 1321, (2001)

[141] H. Müller, D. Schultze, F. Jonas, K. Lerch, H. Weber, EP, 821025 (1996).

[142] X. Ding, H. Yang, C. Wu, L. Chen, *Dianzi Yuanjian Yu Cailiao*, **23**(7), 38, (2004).

[143] A.Elschner, *PEDOT principles and applications of an intrinsically conductive polymer*, CRC Press, (2011).

[144] Y. Saito, T. Kitamura, Y. Wada, S. Yanagida, *Synth. Met.*, **131**(1), 185, (2002).

[145] J. Xia, S. Yanagida, *Solar Energy*, **84**(11), 1888, (2009).

[146] R.Meerheim, K. Walzer, M. Pfeiffer, K. Leo, *Appl. Phys. Lett.*, **89**, 061111, (2006).

[147] S.Reineke, F. Lindner, G. Schwartz, N. Seidler, K. Walzer, B. Lüssem, K. Leo, *Nature*, **459**, 234, (2009).

[148] J.Chen, H.Wei, K. Ho, *Sol. Energy Mater. Sol. Cells*, **91**, 1472, (2007).

[149] M.Biancardo, K. West, F. Krebs, *J. Photochem. Photobiol.*, **187**, 395, (2007).

[150] C. Kittel, *Introduction to Solid State Physics 8th Edition*, Wiley, (2004).

[151] N.Koch, A. Elschner, J. Rabe, R. Johnson, *Adv. Mater.*, **17**, 330, (2005).

[152] C. Tengstedt, W. Osikowicz, W. Salaneck, I. Parker, C. Hsu, M. Fahlman, *Appl. Phys. Lett.*, **88**, 053502 (2006).

[153] N. Koch, A. Vollmer, *Appl. Phys. Lett.*, **89**, 162107, (2006).

[154] G. Greczynski, T. Kugler, W. Salaneck, *Thin Solid Films*, **354**(1), 129, (1999).

[155] J.Hwang, F. Amy, A. Kahn, *Org. Electron.*, **7**, 387, (2006).

[156] R. Jordan, *Adhäsion*, **1**, 17, (1987).

[157] I. Benedeck, *Developments in Pressure-Sensitive Products,* Taylor & Francis, (2006).

[158] Pressure Sensitive Tape Council Glossary, http://www.ptsc.org/technical/glossary.php~glossary

[159] I. Benedek, M.Feldstein, *Fundamentals of Pressure Sensitivity*, CRC Press, (2009).

[160] R. Good, M. Chaundry, C. Van Oss, *Fundamentals of Adhesion*, Plenum Press (1991).

[161] M. Chaundry, *Mater. Sci. Eng.*, **16**, 97, (1996).

[162] I. Benedek, M. Feldstein, *Technology of Pressure-Sensitive Adhesives and Products*, CRC Press Taylor & Francis Group, (2009)

[163] D. Lim, H. Kim, *Theoretical Aspects*, VSP, Utrecht, (2006).

[164] I. Benedek, M. Feldstein, *Applications of pressure-sensitive products*, CRC Press Taylor & Francis Group (2009).

[165] B. Duncan, L. Lay, A. Olusanya, R. Roberts, S. Abbott, *7th Int. Conf. Adhion. Adhsiv.*, UK, 313, (1999).

[166] Label, *Labels*, **2**, 98, (1997).

[167] P. Hammond, *ASTM Bulletin*, **360**(5), 123.

[168] L. Williams, Master of Science Thesis, Department of Civil and Environmental Engineering, Virginia Tech, Blacksburg, Virginia, (2000).

[169] ASTM D6195 - 03 Standard Test Methods for Loop Tack, ASTM International, PA, (2011).

[170] Pressure Sensitive Tape Council, *Test Methods For Pressure Sensitive Adhesive Tapes*, Northbrook, IL, (2000).

[171] F. Hu, A. Olusanya, L. Lay, J. Urquhart, L. Crocker, *Report 8, Project PAJ1, NPL Report CMMT(B),* 129, National Physical Laboratory, Teddington, UK, (1998).

[172] A. Zosel, *Int. J. Adhion. and Adhsive.*, **18**, 265, (1998).

[173] W. Bauer, German Patent 575,327, Rohm & Haas, (1933).

[174] W. Smith, R. Ewart, *J. Chem. Phys.*, **16**, 592, (1948).

[175] J. Asua, *Prog. Polym. Sci.*, **27**, 1283 (2002).

[176] C. Beyers, S. Kirsch, P. Schocker, D. Urban, PSTC 30th Ann. Tech. Conf. FL. USA, (2007).

[177]http://www.acs.org/content/acs/en/education/whatischemistry/landmarks/acrylicemulsion.html

[178] H. Kristiansen, J. Liu, *Polym. Elect. Pack. Proceedings*, 223, (1997).

[179] W.Wixwat, *Appl. Sci.*, London, 461, (1990).

[180] J. Ouyang, Y. Yang, *Adv. Mater.*, **18**, 2141, (2006).

[181] M. Granström, K. Petritsch, A. Arias, A. Lux, M. Andersson, R. Friend, *Nature,* **395**, 257, (1998).

[182] J. Liu, *Conductive Adheisves for Eletronics Packaging*, Elect Pub LTD, (1999).

[183] Y. Shimada, Inter. Symp. *Adv. Pack Mater.* 336, (2000)

[184] Y. Shimada, Inter. Symp. *Adv. Pack Mater.* 343, (2000)

[185] C. Kooring, D. Riphagen, *Electro. Sci. and Tech.*, **7**, 69, (1980).

[186] D. Stauffer, *Introduction to Percolation Theory,* Taylor & Francis, (1985).

[187] S. Broadbent, J. Hammersley, *Proceedings of the Cambridge Philosophical Society* ***53,*** 629, (1957).

[188] Y. Chen, G. Paul, R. Cohen, S. Havlin, S. Borgatti, F. Liljeros, H. Stanley, *Physica A,* **378**, 11, (2007).

[189] G. Pike, C. Seager, *I. Phys. Rev. B.,* **10,** 1421, (1974).

[190] M. Sahimi, *Applications of Percolation Theory,* Taylor and Francis, (1994).

[191] M.J. Powell, *Phys. Rev. B*, **20,** 4194, (1979).

[192] J. Peltola, Y. Cao, P. Smith, *Adhesives Age*, **18**, 374, (1995).

[193] A.Talo, P. Passiniemi, O. Forsen, S. Ylasaari, *Synth. Met.*, **85**(1), 1333, (1997).

[194] W. Lee, Y. Kim, S. Kaang, *Synth. Met.*, **113**,(3), 237, (2000).

[195] A. Pud, N. Ogurtsov, A. Korzhenko, G. Shapoval, *Prog. in Polym. Sci.*, **28**(12), 1701, (2003).

[196] B.Vincent, J. Waterson, *J. Chem. Soc., Chem. Commun.*, **9**, 683, (1990).

[197] Y. Cao, G. Treacy, P. Smith, A. Heeger, *Appl. Phys. Lett.*, **60**(22), 2711, (1992).

[198] Y. Cao, G. Treacy, P. Smith, A. Heeger, *Synt. Met.*, **57**(1), 3526, (1993).

[199] C. Yang, Y. Cao, P. Smith, A. Heeger, *Synth. Met.*, **53**(3), 293, (1993).

[200] S. Desvergne, A.Gasse, A. Pron, *Journ. Appl. Polm. Sci.*, **120**(4), 1965, (2011).

[201] A. Hopkins, J. Reynolds, *Macromol.,* **33,** 5221, (2000).

[202] Clevios, FPVA 2010217, Data Sheet

[203] V. Tung, J. Kim, L. Cote, J. Huang, *J. Am. Chem. Soc.*, **133**(24), 9262, (2011).

[204] J.Ouyang, Q. Xua, C. Chua, Y. Yanga, G. Lib, J. Shinar, *Polymer*, **45**, 8443, (2004).

[205] R. Mauch, *Applied Surface Science*, **92**, 586, (1996).

[206] B. Allieri, S. Peruzzi, L. Antonini, A. Speghini, M. Bettinelli, D. Consolinia, G. Dotti, L. Depero, *Journal of Alloys and Compounds*, **341**, 79, (2002).

[207] M. Ciez, S. Nowak, W. Zaraska, Z. Porada, *Opto-Electronics Review*, **15**(3), 159, (2007).

[208] K. Hecker, ed., 2009 OEA Roadmap – 3rd edition 2009, VDMA

[209] http://www.adphos.de/functionality_of_NIR_technology.html

[210] C. Banwell, *Fundamentals of Molecular Spectroscopy 2nd ed.,* McGraw-Hill, London, (1972).

[211] R. Knischka, U. Lehmann, U. Stadler, M. Mamak, J. Benkhoff, *Prog. Org. Coat.*, **64,** 171, (2009).

[212] M. Cherrington, T. Claypole, D. Deganello, I. Mabbett, T.M. Watson, D. Worsley, *J. Mat. Chem.*, **21,** 7562, (2011).

[213] T. Watson, I. Mabbett, H. Wang, L. Peter, D. Worsley, *Prog. Photov. Res. App.*, **19**(4), 482, (2011).

2. Experimental Procedures

2.1. Manufacture of a Transparent Conductive Adhesive (TCA)

TCAs are made and their properties investigated in Chapter 3, they are then used in fabrication of s-DSCs and EL lamps in Chapters 7 and 8 respectively. In addition to this the rapid curing of the TCA is investigated in Chapter 5.

To fabricate the TCA a commercially available PEDOT:PSS blend (EL-P3145 AGFA) and an acrylic based emulsion PSA (F46 Stycobond) were mixed in wet quantities relating to the amount of each being present in the final dried film. The PEDOT:PSS and PSA wet solution have a solids content quoted at 0.8 and 60% respectively and a density of $1g/cm^3$ [1-2]. Therefore to calculate the mass needed to obtain the necessary volume fractions Equation 2.1 can be used.

$$M_{PP} = \frac{\phi \cdot M_{PSA} \cdot \rho_{PP}}{(1 - \phi) \cdot \rho_{PSA}} \qquad \text{(Eq. 2.1)}$$

Where M_{pp} is the mass of PEDOT:PSS in the final dry TCA film

=

(Weight of wet solution PEDOT:PSS x % solids content of PEDOT:PSS in the wet solution)

i.e. in the case of EL-P4135 if 1g of wet solution was used in the TCA fabrication M_{pp} = (1 x 0.8) = 0.8g.

Similarly M_{psa} is the mass of PSA in the final dry TCA film

=

(Weight of wet PSA solution x % solids content of PSA in the wet solution.)

ϕ is the volume fraction of PEDOT:PSS in the final dry TCA film and ρ_{PP} and ρ_{PSA} are the density of PEDOT:PSS and PSA.

To investigate how the parameters of a TCA changed as the volume fraction of PEDOT:PSS changed within the final dry film the amount of wet PEDOT:PSS solution added to the initial mix was varied to give volume fractions of 0.0065 to 0.0200 in the dry film. Table 2.1 shows these values, calculated using Equation 2.1.

Table 2.1: Showing the volume fraction (ϕ) and the mass of PEDOT:PSS in the dry TCA film and the volume of wet PEDOT:PSS and PSA that needs to be mixed to achieve this ϕ

ϕ	**Volume of wet PSA solution (ml)**	M_{pp} (g)	**Volume of wet PEDOT:PSS solution (ml)**
0.0065	1.00000	0.00393	0.49069
0.0070	1.00000	0.00423	0.52870
0.0075	1.00000	0.00453	0.56675
0.0080	1.00000	0.00484	0.60484
0.0085	1.00000	0.00514	0.64297
0.0090	1.00000	0.00545	0.68113
0.0100	1.00000	0.00606	0.75758
0.0125	1.00000	0.00760	0.94937
0.0150	1.00000	0.00914	1.14213
0.0175	1.00000	0.01069	1.33588
0.0200	1.00000	0.01225	1.53061

The two constitutes were mixed for 5 minutes in a pestle and mortar resulting in a visually homogeneous blend shown in Figure 2.1.

Figure 2.1. Wet blend of PSA (Styccobond F46) and PEDOT:PSS (Agfa EL-P3145)

The wet solutions were then vacuum degassed for 1 minute before being tape cast using Scotch Tape™ as a height guide (tape height 180μm unless otherwise stated) . These were then cured at 60°C for 15minutes followed by 130°C for 5minutes in a standard convection oven, an example of this is shown in Figure 2.2.

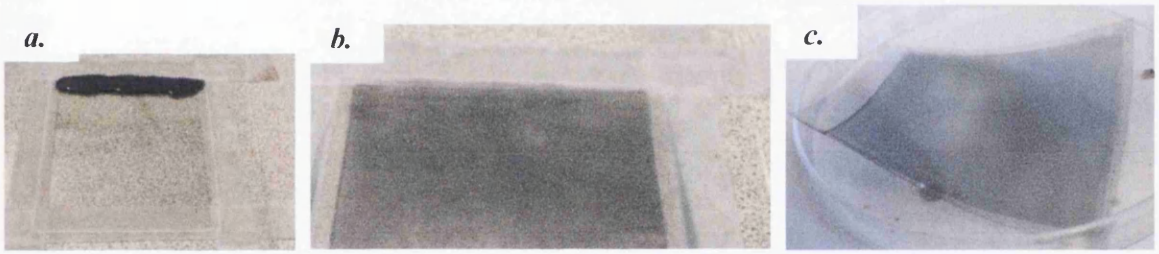

Figure 2.2. A TCA a) Before being cast b) after casting an c) after curing

To investigate how the final TCA parameters were affected by changes in dry film thickness, wet films of TCA were tape cast onto soda glass at heights of 45, 90, 135, 180, 225, 270, 315, 360μm and cured as described above. Films were tested using a four point probe method and a source meter (Keithley 2400) described in more detail in Section 2.7.1.

2.1.1. Fabrication of a TCA-laminate

To increase the potential application of the TCA it can be cast upon a transparent conducting sheet material and cured to form a "TCA-laminate" that can be applied at room temperature using hand pressure only. To do this first a transparent sheet material is needed and for this thesis a product called Epimesh 300™ (Epigem) was used which consists of a

current collecting square nickel grid (line width 5μm, pitch 300μm) embedded in a transparent PET film and quoted at 1.2 Ohms/square [3]. It is not believed that Epimesh 300™ specifically is crucial to the TCA-laminate's operation and indeed other transparent sheet materials may be used in its placed. It was selected however as it is an example of an indium tin oxide (ITO) free flexible transparent sheet material that has been processed without a vacuum. Furthermore it was one of the best performing, in terms of transparency and conductivity sheet materials at the time of experimentation. A wet solution TCA was prepared as described in Section 2.1 and then bar coated onto the Epimesh 300™, nominally this layer had a PEDOT:PSS volume fraction of 0.0175 and wet film thickness of 90μm microns unless stated otherwise.

This was then subjected to a 60°C heat treatment for fifteen minutes to remove any low boiling point solvents. The temperature is then increased to 120°C for five minutes to remove the higher boiling solvents.

After curing and cooling the resulting structure was then referred to as a TCA-laminate. This could then be applied to surfaces/devices at room temperature using only finger pressure such that the TCA component is in mechanical and electrical contact.

2.2 Preparation of PEDOT:PSS solutions and films with additional solvents

To make samples of PEDOT:PSS that had a lower water percentage that were more compatible with moisture sensitive layers additional solvents in their initial wet mix a solution of EL-P3145 (EL-P 3145 from AGFA GmbH) had varying amounts of solvent added to the wet PEDOT:PSS solution. In the case of PEDOT:PSS, ethanol and IPA additions are denoted as follows, 4:1:1 indicates 4 parts PEDOT:PSS solution 1 part ethanol 1 part IPA by volume. This mix was then tape cast onto standard soda glass slides using Scotch magic tape as a height guide to give a 45μm wet film thickness. The samples were then dried in an oven for 5minutes at a temperature of 130°C as per the manufacturers' recommendations. The dried films then had 4x1-mm wide line contacts at 1.5mm separation sputtered onto the surface using a Quorum 150T as electrical contacts and their conductivity measured as described in Section 2.7.1.

2.2.1 Evaporative Curing

Films were also cured using an evaporative cure, to achieve this first a 2.5cm wide glass slide had silver contacts deposited onto the surface with a 1cm wide gap in the middle using a Quorum 150T as electrical contacts which would be used to measure the resistance of the curing PEDOT:PSS. A width of 0.5cm either side of this gap was then masked off using magic tape. Wet PEDOT:PSS (EL-P3145) was then cast upon the exposed silver and the gap, as shown in Figure 2.3.

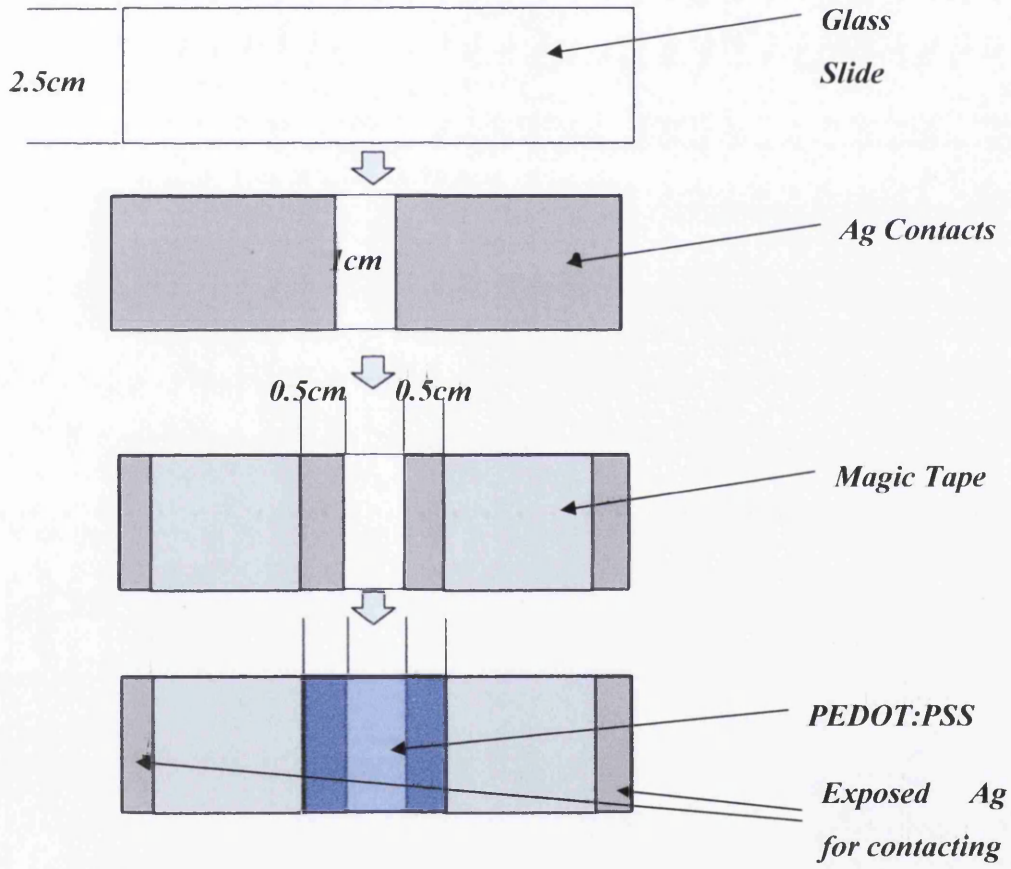

Figure 2.3. A schematic of the deposition build-up of a slide used for testing the cure of PEDOT:PSS under hot air convection.

This slide was then connected to a Keithly 2400 source meter at the exposed Ag (Figure 2.3) and the resistance measured between the two. The slide then had a thermocouple affixed to the underside, below the gap in the Ag contacts and was held under a hot air dryer,

Remmington 200, at a 10cm distance on full power such that the airflow was perpendicular to the sample as shown in Figure 2.4. The temperature witnessed by the films was measured along with the film resistance as a function of time and then plotted

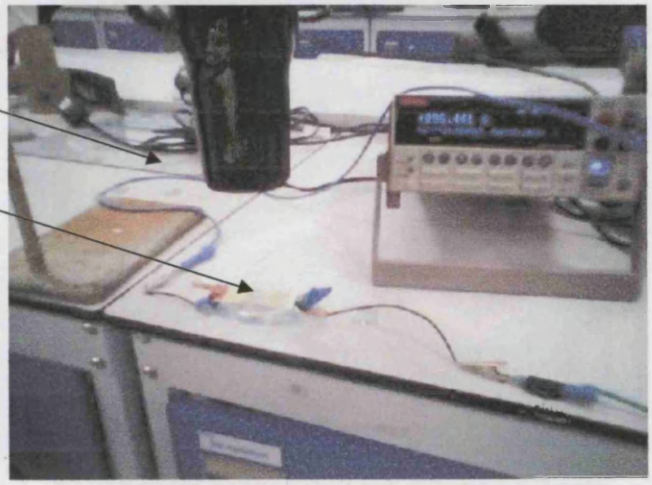

Figure 2.4. Experimental set up for measuring the temperature and resistance as a function of time for a PEDOT:PSS film cured using hot air convection evaporation.

This procedure was also recorded using a TIM 160 IR camera calibrated using a sample of cured PEDOT:PSS. The temperature can then be recorded at any point in the recorded frame and duration of the video using the TIM Connect software.

2.3 NIR Curing

Unless otherwise stated samples of PEDOT:PSS for NIR curing were prepared by tape casting a 25mm x 60mm strip of commercially available PEDOT:PSS solution (EL-P 3145 from AGFA GmbH) onto PET substrate (Melinex ST505 175μm from DuPont Teijin Films) producing a wet film thickness of 45μm using Scotch Tape™ as a height guide.

For a TCA cured using NIR a volume fraction of 0.0175 and a wet film cast height of 180μm (using multiple layers of Scotch Tape™ as a height guide) mounted on a soda glass substrate of thickness 3mm was used (as described in Section 2.1).

The PEDOT:PSS was then subjected to two different curing methods; six HB-NIR near-infrared emitters (Adphos NIR/IR Coil lab LV2) shown in Figure 2.5 and a conventional hot-air oven (Heraeus Vacutherm).

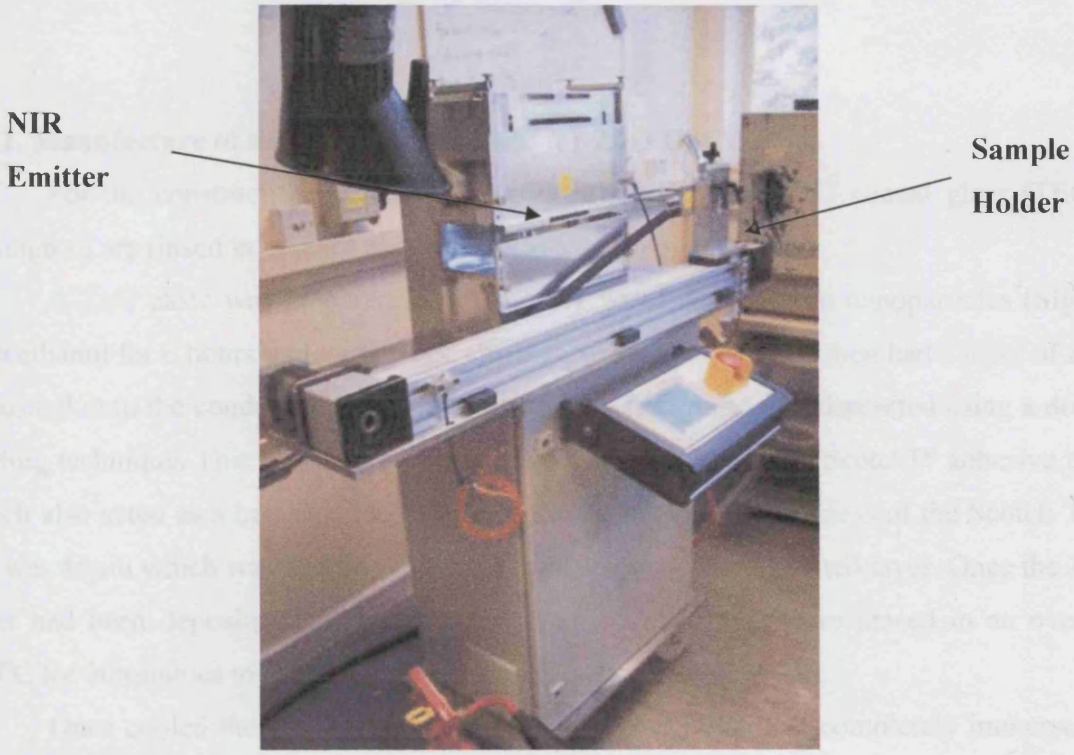

Figure 2.5. Adphos NIR/IR Coil lab LV2 curing unit

NIR heating was achieved by moving the sample holder under the NIR emitter at varying speeds at pre-set power levels. This allowed the exposure times to vary from 1.4 to 2.2 seconds. Conventional hot air oven samples were dried at a temperature of 140°C for between 60 and 300 seconds for the PEDOT:PSS and the two step curing method outlined in Section 2.1 for the TCA. Both sets of samples were otherwise subjected to atmospheric conditions during drying. After cooling to room temperature the sheet resistance of the samples was measured using a four-point probe (Keithley source meter) explained in Section2.7.1.

Samples exiting the NIR lamp were also recorded using the TIM 160 IR camera as described in Section 2.2.1.

2.4. Manufacture of a Liquid Dye Solar Cell

2.4.1. Manufacture of the working electrode for ZnO DSCs

For the construction of the working electrode strips of FTO coated glass (TEC-7, Pilkington) are rinsed in ethanol and then cut to a width of 2.5cm.

A ZnO paste was prepared by mixing 1:1 wt of ZnO <50nm nanoparticles (Sigma) with ethanol for 6 hours under magnetic stirring. Strips of FTO glass then had a layer of ZnO deposited onto the conducting side of the glass. The ZnO paste was deposited using a doctor blading technique. This involved masking the edge of the strip with Scotch™ adhesive tape, which also acted as a height guide for the deposited layer. The thickness of the Scotch Tape ™ was 45μm which was then the subsequent thickness of the deposited layer. Once the ZnO layer had been deposited the tape was removed and the strips were placed in an oven at 450°C for 30minitues to allow the ZnO particles to sinter (Figure 2.6).

Once cooled the strips were then placed in a Petri dish and completely immersed in 0.3mM N719 dye, purchased from Dyesol. This consisted of cis-bis(isothiocyanato)bis(2,2'-bipyridyl-4,4'-dicarboxylato)-ruthenium(II)bis-tetrabutylammonium in ethanol:dH_2O(1:1 vol:vol). The strips were then left in the dye solution in the absence of light for 16-20 hours to allow the dye to be adsorbed onto the ZnO surface (Figure 2.6).

After dyeing the strips were removed from the solution and excess dye was removed using ethanol. The strips were then blown using air to remove the ethanol. Once dry the strips were cut into 1.5cm x 2.5cm cells. The dyed ZnO was then scratched, using a glass coverslip, into 1cm^2 areas.

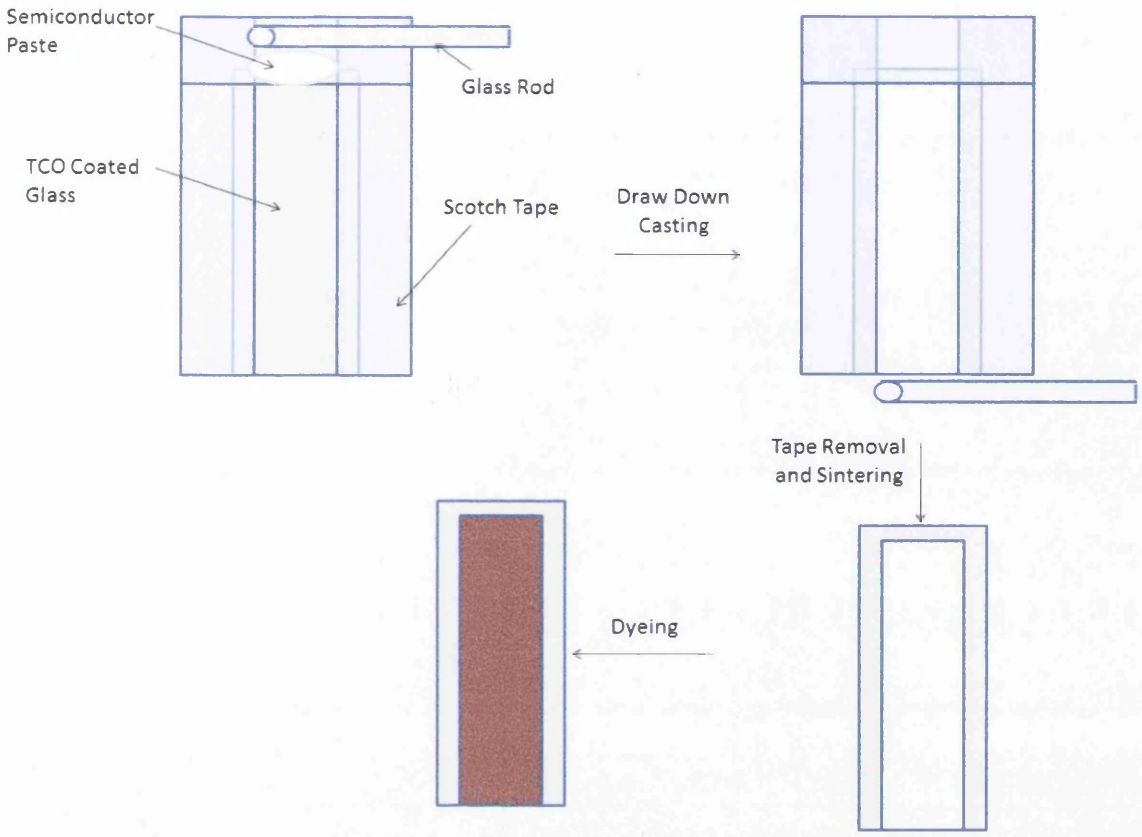

Figure 2.6. Fabrication of a working electrode used in a DSC

2.4.2. Fabrication of the Counter Electrode

Counter electrodes were constructed using FTO coated glass cut to the same 1.5cm x 2.5cm dimensions as the working electrode using the same method and were rinsed in ethanol after cutting. After cutting the cells had a 0.5mm hole drilled in them using a tungsten carbide drill bit. After drilling the cells were then washed first with a solution of water and detergent, then rinsed with de-ionised water and finally washed with ethanol and blown dry using compressed nitrogen. The cells then had a layer of 5mM chloroplatinic acid (Sigma-Aldrich) in isopropyl alcohol (IPA) deposited onto the surface of them, using the wetting effect of the surface to create a thin layer on the glass. The electrodes were then heated in an oven at 400°C for 30mins to form a thin layer of platinum.

2.4.3. Cell Construction

To seal the counter electrode to the working electrode a square gasket of 30µm Surlyn™ was placed between the two electrodes and heat applied via a hot plate below and pressure applied manually using a ceramic tool from above. Once cooled the space between

the two electrodes was filled by vacuum injecting via the drilled hole in the counter electrode with the electrolyte solution of 0.1M LiI, 0.6M tetrabutyl ammonium iodine (TBAI), 0.5M 4-tert butylpyridine (4-TBP) and 0.1M I_2 in 3-methoxypropionitrile (MPN).

Once filled, excess electrolyte was removed from the surface with a paper towel, allowing the hole to be sealed using a piece of Surlyn™ and a microscope coverslip.

Finally the cells had bus bars applied to the exposed edges of the cell using silver paint and the cells contacted with the I-V testing equipment. A finished cell schematic is shown in Figure 2.7.

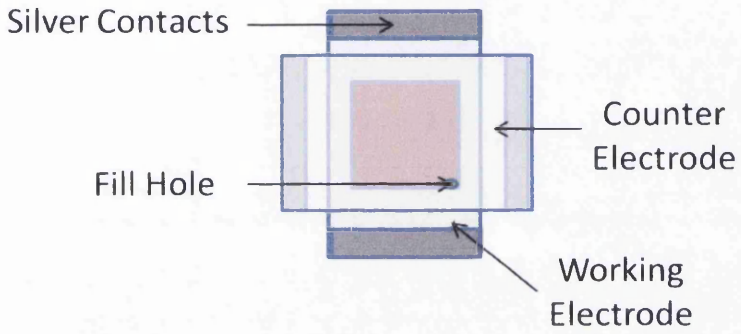

Figure 2.7. A schematic of a finished liquid DSC

2.5. Fabrication of solid state Dye Solar Cells

2.5.1. Fabrication of the Working Electrode

ECCS and FTO glass had a layer of non-porous TiO_2 deposited as a blocking layer by a spray-pyrolysis process. This involved a spray gun apparatus and a solution of titanium precursor. The precursor solution used was 0.2 M titanium diisopropoxide bis(acetylacetonate) in ethanol (TAA = 364.26 g/mol) (Sigma Aldrich). One layer of this solution was then sprayed using compressed nitrogen and passed over the substrate at a distance of 15cm, while the substrate is heated by a hotplate to 250°C. The temperature was then increased to 450°C and 19 subsequent deposition procedures were performed sequentially at 10 second intervals. The resulting layer is a dense dielectric TiO_2 with a

coating thickness between 40 nm and 100 nm. TiO_2 paste (Dyesol's DSL 18NRT) diluted with ethanol (60:40 vol%) was then bar cast at 45μm, ramped to 450°C over a 30minute period and held there for a further 30 minutes to give a dry film thickness (DFT) of 1.6 microns (mesoporous TiO_2). The sensitising dye D102 (Mitsubishi Dyes) is dissolved in an acetonitrile and tert-Butanol solution at 0.5mM and the mesoporous TiO_2 is then submerged in this solution for 60 minutes at room temperature, followed by rinsing, to produce the working electrode.

2.5.2. Hole Transport Layer

Spiro-OMeTAD (Lumtec) was dissolved in chloro-benzene at 200mg/ml and 20mM LiTFSI (Sigma-Aldrich) solution in acetonitrile and 22μL of tBP was added . The Spiro-OMeTAD was applied to the TiO_2 via spin coating. Excess solution was applied to the surface of the TiO_2, left for 60seconds and then spin coated for 30seconds at 500-1000rpm. This lead to to infiltration of the TiO_2 and a capping layer above the TiO_2 of 200-450nm.

2.5.3. Backside Contact

The cells were contacted using either evaporated metallic contacts or the TCA-laminate (Section 2.1.1). For cells with metallic back contacts a $1cm^2$ contact of Ag or Au was deposited onto the Spiro-OMeTAD layer (Figure 2.8(a)) using a Quorum Tech 150T desktop evaporator to achieve layers of 200nm (Ag) and 5nm (Au). Cells contacted using a TCA-laminate first had a solution of PEDOT:PSS (AGFA EL-P-3145) mixed with ethanol and isopropanol in a 4:1:1 ratio bar-coated as a 45 μm wet film onto the Spiro-OMeTAD surface. The PEDOT:PSS layers were subsequently dried by hot air impingement in a dust-free environment for 7.5 minutes (Section 2.2.1). A TCA-laminate was fabricated in the way described in Section 2.1.1 with a $1cm^2$ area of TCA and an excess area of Epimesh 300™ such that it could be contacted using crocodile clips. This formed a TCA-laminate which was then applied onto the PEDOT:PSS surface of the s-DSC using hand pressure Figure 2.8b.

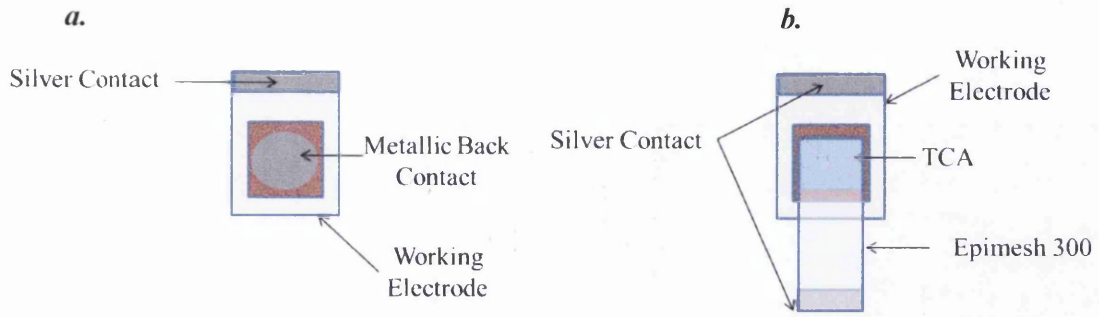

Figure 2.8. Schematic of s-DSC made using a) evaporated metallic back contacts b) TCA and grid laminate.

2.6 Fabrication of Electroluminescent Devices

Conventional EL devices were fabricated by bar casting a 45μm wet film thickness each of phosphor - dielctric -silver ink (8152B and 8153 Luxprint, DuPont) onto a piece of FTO coated glass (Tec-7, NSG-Pilkington) with drying at 140°C between consecutive depositions.

The TCA devices were prepared in the same way as conventional devices only the layer succession was dielectric – phosphor – TCA-laminate, applied using hand pressure, with no additional heating step instead of the silver ink. As an example of a cheap and readily available substrate aluminium sheet (A-14, Q-Panel) was also used which was swapped directly for FTO glass during construction. A schematic of the TCA-Laminate devices is shown in Figure 2.9. Active lamp area in all devices was $1cm^2$.

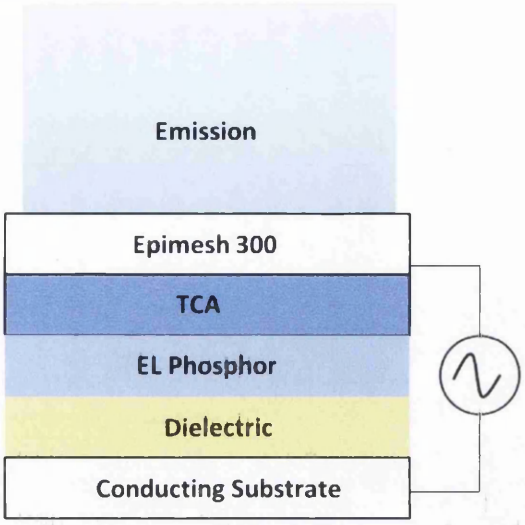

Figure 2.9. Cross-section schematic of a top emission electroluminescent device using a TCA-Laminate.

Lamps were driven by a sinusoidal voltage produced by an EL specific power supply (LM30, Light & Motion) with the excitation frequency fixed at 400 Hz and applied voltages of 75, 100, 125 and 140VAC. Luminescence was measured using a spectrophotometer in emission mode (Spectrolino, Gretag-Macbeth) with a spot size of 4mm. The output luminescence of the conventional lamp was then taken to be 100% and all other measured lamp outputs were then calculated as a percentage of the output of conventional EL lamps, i.e. if a lamp had a luminescence half that of the conventional lamps its output would be quoted as 50%

2.7. Electrical and Electrochemical Characterisation

2.7.1. Contact resistance measurements

To measure the specific contact resistance of a TCA and Ag contacts a slightly modified Transfer Length Method (TLM) [4] was employed which aims to resolve the Resistance of a film into its constituent parts. Here, strips of silver with the same area are deposited onto a piece of soda glass at increasing distances. A 1cm wide strip of TCA is then deposited onto another piece of glass and the two bought into contact as shown in Figure 2.10.

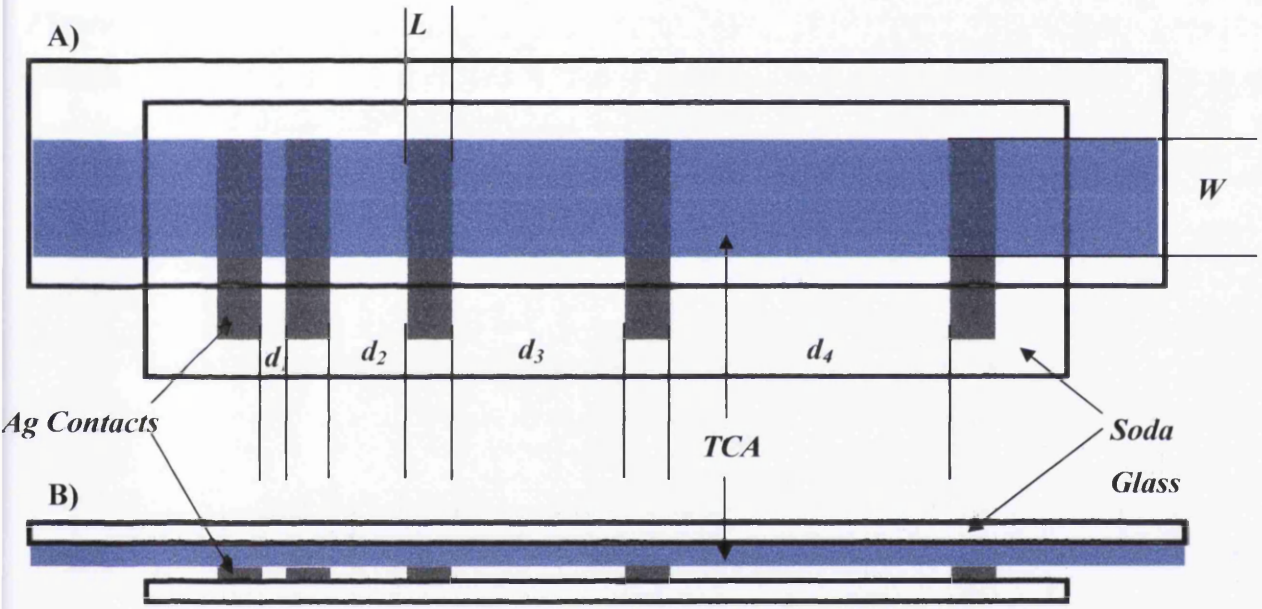

Figure 2.10. Schematic of a TLM set up of silver contacts and TCA from A) top down view and B) a side on view.

Where L is the contact length, W the width and d is the separation distance.

A current is then applied to the outer contacts and the voltage measured between the strips. The Resistance can then be calculated and plotted as a function of Resistance vs separation distance as shown in Figure 2.11.

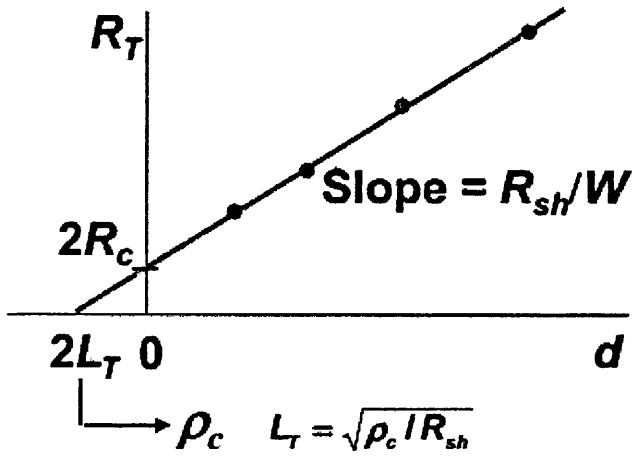

Figure 2.11. An ideal plot for Resistance vs separation distance from a TLM [5] Copyright Gatech.

The data can be extrapolated such that $d = 0$ and then the Resistance is purely made up from the contact resistance (x2 as there are two contacts). Division by 2 leaves the Resistance, and multiplication by LW obtains the specific contact resistivity (ρ_c), in ohm.cm^2, according to Equation 2.2.

$$R_c = \frac{\rho_c}{LW} \qquad \text{(Eq. 2.2)}$$

For this experiment $L = 0.5$cm and $W = 1.0$cm.

2.7.2. Conductivity Measurements

To measure the conductivity of the materials such as the TCA and PEDOT:PSS a Kelvin four point probe method was used. First the dried films on non-conducting soda glass had 4x1-mm wide line contacts at 1.5mm separation sputtered onto the surface using a Quorum 150T as electrical contacts and shown in Figure 2.12

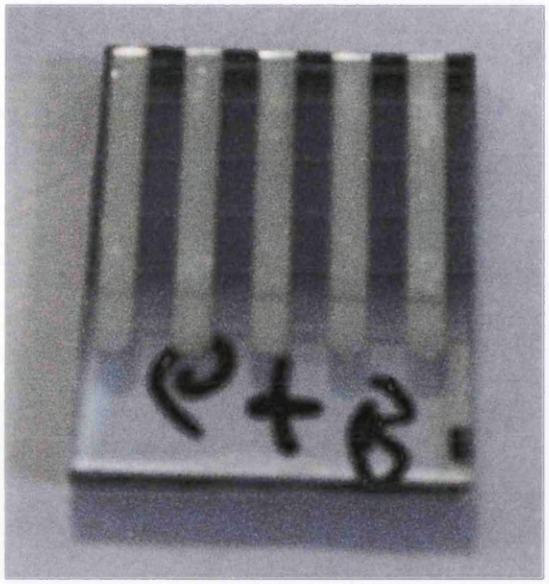

Figure 2.4. A sample of PEDOT:PSS with silver metal electrodes evaporated on the surface used for a 4-point probe measurement.

Samples had their height measured using a Dektak 150 Profilometer. The voltage was measured between the two inner contacts as a constant current is passed between the outer two using a Keithley source meter. The conductivity σ (S/cm) can then be calculated using Equation 2.3

$$\sigma = \left[\frac{V}{I} \cdot \frac{w.t}{s}\right]^{-1} \qquad \text{(Eq 2.3)}$$

Where V is the voltage difference, w is the width of the film, t is the film thickness, I is the applied current and s is the electrode separation.

2.7.3. Cell Testing

Unless otherwise stated the cells were tested for their I-V response on the day of fabrication. I-V testing was carried out using a Oriel Sol3A solar simulator and a Keithley 2400 source meter shown in Figure 2.11.

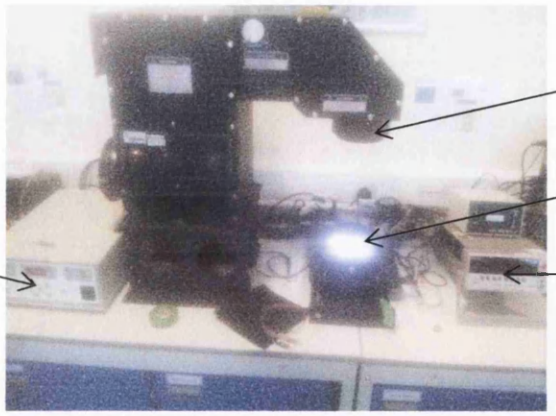

Figure 2.11. Newport Sol3A Solar Simulator

It is certified to IEC 60904-9 Edition 2 (2007), JIS C 8912, and ASTM E 927-05 standards for spectral match, non-uniformity of irradiance, and temporal instability of irradiance. Measurements were carried out at an irradiance of 1 Sun. Before testing the lamp had to be adjusted to ensure a 1 sun emission. This was done by calibrating the lamps emission to 1.00 ± 0.01 Sun using the NREL certified secondary standard silicon reference cell. The cells were tested ensuring that every cell was at room temperature and had a clean surface when placed in the test chamber. The cells were then tested at 0.009V increments from their J_{sc} to V_{oc} and the results plotted as an J-V curve with efficiencies and fill factors calculated using Equations 3.4 and 3.5.

$$P_{max} = V_{oc} \times I_{sc} \times FF \qquad \text{(Eq 3.4)}$$

$$FF = \frac{V_m I_m}{V_{oc} I_{sc}} = \frac{P_m}{V_{oc} \times I_{sc}} = \frac{\eta \times A_c \times E}{V_{oc} \times I_{sc}} \qquad \text{(Eq 3.5)}$$

2.7.5. Electrochemical Impedance Spectroscopy (EIS) Measurements

Impedance spectroscopy measurements were carried out on Gamry Reference 600 Potentiostat/Galvanostat/ZRA using ZPlot software. Cells were measured in a two electrode set-up in the dark and held at a potentials of -0.54 -0.78 V in 0.04 V increments. AC amplitude was ± 10 mV with a frequency range of 20 kHz to 0.1 Hz

2.7.6. Transient Measurements

Transient photovoltage decay measurements were made at open circuit. The bias light was provided by a custom made bank of 20 x 1 Watt, white LEDs. A given steady state V_{oc} value was obtained by altering the bias light intensity and upon reaching steady state, a pulse was provided by 1 x 1 Watt, red LED. The resultant small increase in voltage and exponential decay back to the steady state gives the recombination lifetime, τ which is determined by fitting a single exponential function to the voltage decay data.

2.7.7. Incident Photon to Current Efficiency (IPCE) Measurements

IPCE measurements were carried out using a QEX10 from PV measurements between 300nm and 1000nm.

2.8. Optical and Physical Characterisation

2.8.1. UV-Vis Measurements

The optical characteristics of the cell components were determined at various stages of the cell fabrication using a UV-Vis spectrophotometer (Perkin Elmer Lambda 750S). This measured the UV-Vis absorption spectrum of the cells and gave the data as a function of absorbance or transmission against wavelength.

2.8.2. Thermogravimetric Analysis (TGA)

TGA measurements were carried out using Perkin Elmer TGA. This was conducted by depositing 20mg of material in a crucible which was then heated at a rate of 10°C/minute and the change in weight recorded.

2.8.3. Tack Measurements

To test the adhesive nature of the films they were tested using an ASTM D3121 rolling ball tack standard which aims to simulate the capacity of the adhesive to bond with the surface of another material upon brief contact under virtually no pressure. To do this an 11.1mm diameter steel ball is rolled down a plane with a length of 18cm and an incline of 21°30' onto a strip of adhesive 25mm wide. The distance the ball travels along the strip is then measured using a ruler. The rolling ball tack testing equipment is shown in Figure 2.12.

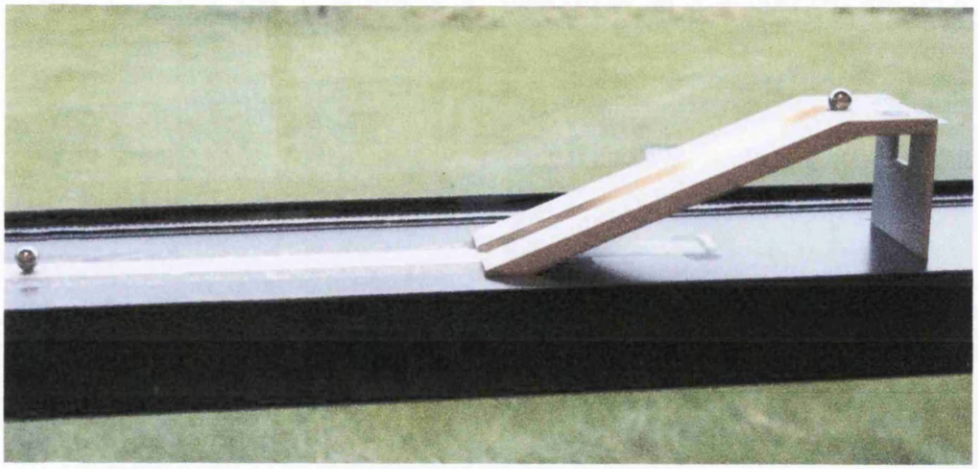

Figure 2.12. ASTM D3121 rolling ball tack tester

2.8.4. Profilometery Measurements

Surface profile measurements were carried out using a Dektak D150 with a 12.5μm stylus.

2.9. References

[1] Internal correspondence from AGFA GmbH Belgium, April 2012

[2] http://www.f-ball.co.uk/documents/safety/Styccobond%20F46%20iss%2011.pdf

[3] http://epigem.co.uk/products/optical-film/epimesh-300s

[4] HH. Berger, *Sol-Sta Elec*, **15**(2), 145, (1972)

[5] http://users.ece.gatech.edu/~alan/ECE4813/Lectures/Lecture4ContactResistance.pdf

3. An All Organic Transparent Conductive Adhesive for use in Opto-Electronic Devices

3.1. Introduction

As described in Section 1.12 the main motivation of this thesis is to develop an s-DSC on a metal substrate for subsequent incorporation into a roll-to-roll fabrication process. Due to the opacity of the metal, to enable this the Spiro-OMeTAD/hole transport material needs to be contacted by a transparent conducting layer. PEDOT:PSS is continually gaining interest as a transparent conducting layer and while it is a better conductor than Spiro-OMeTAD (240Ω/□) it has a still significantly higher sheet resistance than other s-DSC back contacts, such as evaporated Ag (1.3 Ω/□) and Ag nanowires (4.5 Ω/□) and also higher than a typical FTO working electrode resistance (7 Ω/□) [1]. It would therefore dominate the series resistance and would not be ideal for charge extraction over a large area on its own. One of the main advantages that PEDOT:PSS has over the evaporated metallic conductors is that it is transparent. The problem of metallic conductors being opaque can be overcome by forming the metal into a grid, whereby light transmission is then proportional to the coverage of the grid. If the grid is in contact with a PEDOT:PSS layer then the conductance of the total area of grid and PEDOT:PSS becomes an average of the two individual conductivities. Therefore by altering the thickness and spacing of metallic gridlines on a PEDOT:PSS layer a maxima can be found between sheet resistance and transparency - increasing the conductivity of the PEDOT:PSS at the expense of a small loss in transmission (in an ideal scenario). A metallic grid and PEDOT:PSS combination could be incorporated into or onto a s-DSC in a number of ways but within the context of the roll to roll manufacture of this work two ways have been selected (Figure 3.1):

a) Print a grid directly onto a PEDOT:PSS layer on top of the s-DSC
b) Produce a grid on a transparent substrate and then make this mechanically and electrically in contact with the s-DSC layers.

a)

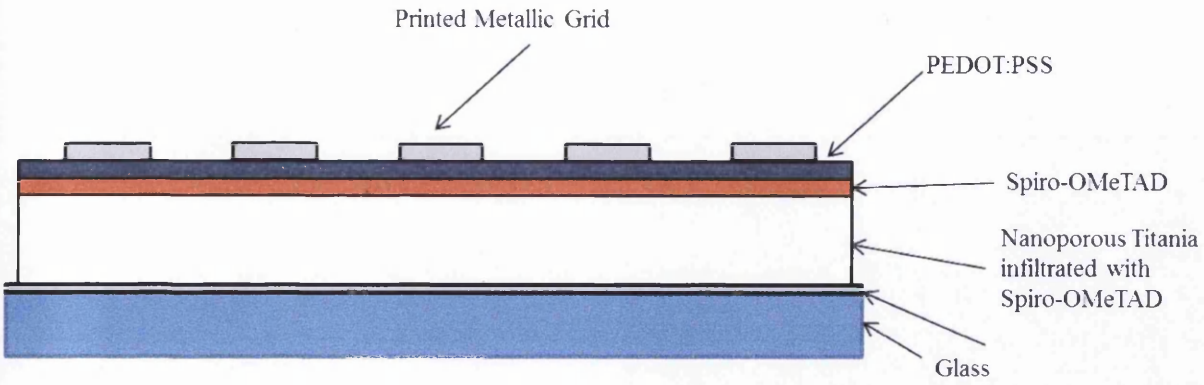

b)

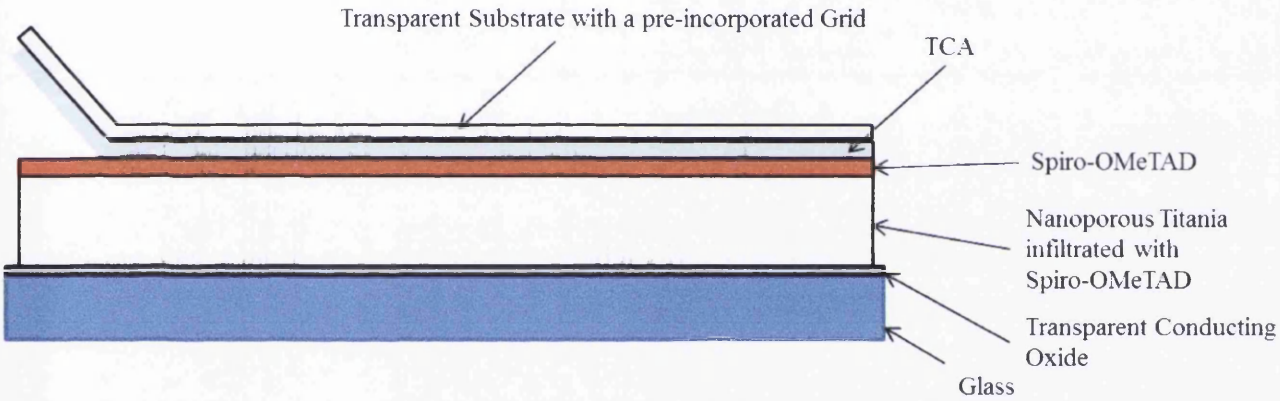

Figure 3.1. Cross sectional schematic of a s-DSC made with a) A top metallic grid printed directly onto the PEDOT:PSS and b) a pre deposited grid on a transparent sheet and then contacted electrically and mechanically with the Spiro-OMeTAD layer using a conducting laminate.

The latter option is usually referred to as lamination, where multilayer materials are manufactured together for overall improved properties [2]; a laminate unites two materials, in this case the grid on the transparent sheet and the Spiro-OMeTAD. While initially printing directly on the PEDOT:PSS would seem the obvious and easiest option, there is some advantages to the laminate option for someone wishing to manufacture this kind of device, outlined below:

- The processes can be performed separately. During continuous processing involving multi layers some layers may take longer to process (deposit, cure anneal etc.) than others and therefore their line speed would differ. To run different processes with vastly different line speeds often incurs significant space and cost problems. By separating the processes the overall manufacturing flow can be coordinated and bottlenecks can be avoided.
- Specialty grids cannot always be produced in-house by any given manufacturer and not on every kind of substrate. This is often due to IP, patents, expensive specialised equipment and processes unique to that substrate. The laminate process then allows a manufacturer to buy in a pre-produced grid and then apply it in-house.
- The grid is produced on a substrate that can not only provide a platform but may also serve a dual purpose of integrating other functional layers e.g. UV screening, moisture barrier.
- The curing of metal grids onto polymer substrates may not be feasible within the timescale required for the production of the device, rendering the option uneconomical to a manufacturer.

To enable light penetration, the laminate must be transparent and conductive, however for robustness and durability it must also provide a mechanical bond between the grid and the PEDOT:PSS layer. Low temperature processing is essential for protection of the Spiro-OMeTAD layer (discussed more in Chapter 4) therefore a hot lamination process has not been included within the scope of this work. As a result the low temperature bonding must be achieved chemically or via pressure using an adhesive and this introduces the term Transparent Conductive Adhesive (TCA). There are few materials that provide the role of a TCA (covered in Section 1.9) and those that do include two or more phases. Subsequently for the scope of this work one distinct category of TCA has been selected: Dual-Phase polymer; where a transparent conducting polymer provides the electrical connection and a polymer adhesive provides the mechanical bond.

Therefore, the overall aim of this chapter is to develop a TCA material that is transparent, electrically conducting and adhesive in nature that can be adhered without the need of heat, for use in opto-electric devices temperature sensitive in nature.

3.2. Experimental

Experimentation was carried out as described in Section 2.1. Initial compatibility results were conducted by hand mixing equal volumes of the adhesives and PEDOT:PSS solutions. Compatible adhesives were then assessed and used further. For all subsequent TCAs the materials used were a PEDOT:PSS (EL-P3145, AGFA) and an acrylic emulsion pressure sensitive adhesive (PSA) (F46, Styccobond).

For conductivity measurements a standard 4 point probe measurement was used by evaporating contacts onto the surface of the TCA as described in Section 2.1 with conductivity measurements done using the method outlined in Section 2.7.2 and contact resistance measurements done using the TLM method outlined in Section 2.7.1.

Optical transparency measurements were conducted using a Perkin Elmer Lambda 750s with a 60 mm integrating sphere as outlined in Section 2.8.1. Height measurements of the samples were conducted using a Dektak D150 Profilometer.

Tack was measured using the rolling ball tack (RBT) as per ASTM D3121 standard as outlined in Section 2.8.3.

3.3. Results and Discussion

3.3.1. Initial TCA Trials To Assess Different Adhesives and PEDOT:PSS Formulations

For the conducting polymer phase PEDOT:PSS was the obvious choice as it is the best performing and cheapest transparent conducing polymer at the time of writing. The TCA as a whole needed to be compatible with processing techniques such as screen printing and bar casting therefore the commercially available EL-P3145 PEDOT:PSS was selected as it had already been formulated for screen printing (and bar casting) giving it an advantage over others. The first step was then to find an adhesive that was compatible with PEDOT:PSS such that the two could be mixed, cast and cured without problems such as macroscopic separation of the two materials, curing of one of the materials upon mixing and bubbling or other defects formed during curing [3-4]. The field of adhesives is considered a mature technology with many different categories of adhesive, differing in their chemical composition, curing method and adhesion mechanism, combined with subcategories and manufacturer variations [5]. As

such rigorous testing of every adhesive is well beyond the scope of this work. Therefore a commercially available adhesive was selected from each of the 7 broad categories of adhesive and a trial based on a process of elimination was carried out by mixing, casting and curing the adhesives and rejecting those that incurred any issues, such as bubbling and separation as mentioned above. The results are summarised in Table 3.1.

Table 3.1: The different types of adhesives tested and observations on compatibility

Type of Adhesive	Product Name	Notes
Epoxy	Loctite Double Bubble	When pre-mixed with either of the two parts it would be near miscible but still tended to separate out into phases of epoxy and PEDOT:PSS
UVCure Cyanoacrylate	SuperGlue Glass adhesive	Formed into distinct clusters of PEDOT:PSS and Adhesive
PVA	EVO-Stik	Miscible when mixed and didn't initiate curing. Post heating the sample remained mixed but showed constant bubbling
Silicone	Bond Loc RTV Neutral Silicone	Adhesive cured instantly when mixed
Nitrile Rubber	Bostik All Purpose	Adhesive cured instantly when mixed
Acrylic Pressure Sensitive Adhesive	Styccobond F46	Miscible when mixed. If heated at a low temperature first and then a high temperature a fully cured film with no bubbles was formed
UV Cure Pressure Sensitive Adhesive	Devcon Tru Bond 3000	Mixed initially but very quickly reverted back to two phases. Curing under UV and heated needed and hard to balance.

Table 3.1 shows that most of the adhesives were not compatible with the waterborne PEDOT:PSS solutions. Figure 3.2 shows the samples and illustrates the inherent problems related to compatibility. For the silicone and nitrile rubber the problem is obvious as the addition of water initiated the curing rendering a cured adhesive matrix and uncured PEDOT:PSS.

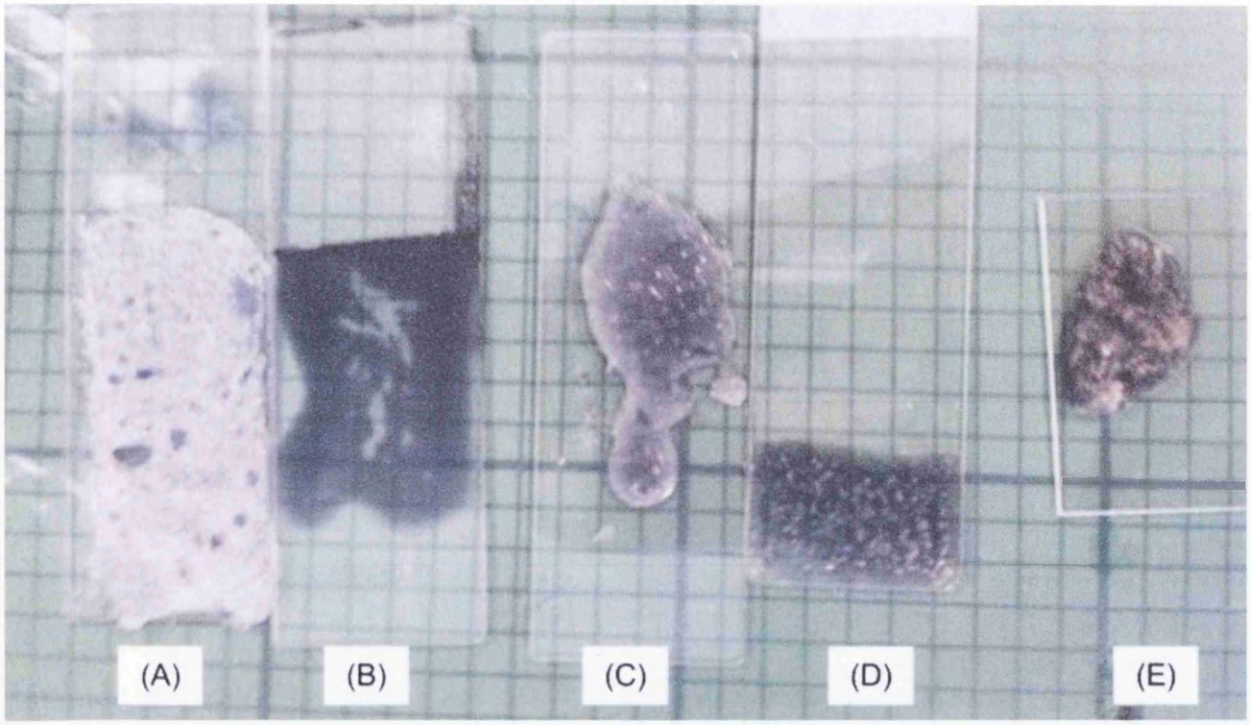

Figure 3.2: Attempts at mixing PEDOT:PSS with (A) Silicone (B) UV cure PSA (C) UV cured cyanoacrylate (D) PVA (E) Nitrile rubber adhesives

The UV cured cyanoacrylate and PSA were interesting in that they initially seemed to mix well but then with time showed segregation of the phases. This can clearly be seen in Figure 3.3. It could be argued that this isn't an issue if these blends were cast and cured soon after mixing however problems also arose when trying to cure these as the adhesive required UV and the PEDOT:PSS required heat (at different rates), balancing the two curing regimes as the phases separated proved difficult. These types of adhesive have not been ruled out completely but for the context of this work they were deemed unsuitable.

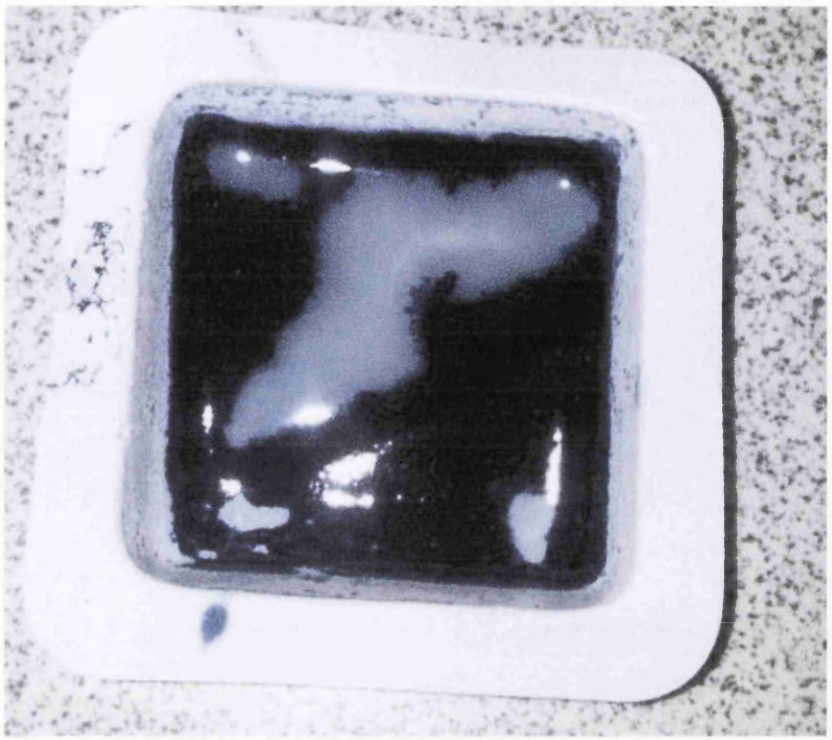

Figure 3.3: UV cure PSA Devcon Trubond and PEDOT:PSS 24hrs after mixing.

The epoxy adhesive mixed together well but separated during curing. Both the PSA and the regular PVA adhesives mixed well, which is expected as they are both waterborne dispersions like the PEDOT:PSS. The phases didn't separate out when they were cast and cured, however a solid matrix is formed first during curing which traps in high boiling point solvents leading to bubble defects. Two things need to happen during curing, water from the PEDOT:PSS solutions and the adhesive phase needs to be driven off and then the high boiling points (within the PEDOT:PSS solution) need to be driven off. With this in mind a two phase cure and dry was then chosen, with a lower temperature of 60-80°C (to evaporate the water) and then the sample held at 120°C to drive off the high boiling point solvents. The same issue always arose with the PVA that when the water was driven off the PVA tended to form a solid matrix with the high boiling point solvents still inside, when then heated to 120°C the trapped solvents then led to bubbling of the solid PVA. Bypassing the initial low temperature step did not negate the problem but actually made the bubbling worse as a skin formed which then trapped water and high boiling point solvents leading to additional bubbling. The issue of possible solvent entrapment combined with the issues that may arise when trying to cure the PVA between two non-porous sheets (as would happen in a laminate) where no solvent can escape meant that PVA was also deemed unsuitable. The acrylic emulsion PSA –PEDOT:PSS mix on the other hand did not show this type of bubbling when

held at the lower temperature for 15 minutes and then the higher temperature for 5 minutes (bubbling was seen if just one higher temperature was used) due to the PSA forming a more porous matrix when cured (discussed in section 5.4.2 in more detail) which then allows the high boiling point solvents a free path to be removed. Given that a PSA would also be ideally suited for a low temperature laminating procedure, acrylic based PSA's were selected for further study.

3.2.2. Origin of Conductivity and its relationship to PEDOT:PSS Volume Fraction

While it mixed, cast and cured well it was not immediately obvious whether the mix of acrylic PSA and PEDOT:PSS would be electrically conducting and if it was, how the conductivity would change as the amount of PEDOT:PSS was changed.

Figure 3.4 shows the electrical conductivity as a function of the volume fraction (ϕ) of PEDOT:PSS within the dry TCA film calculated as shown in Section 2.1. It can be seen that at ϕ of 0.006, 0.0065, 0.007 and 0.0075 the TCA exhibits no conductivity. At 0.008 the TCA shows an extremely low conductivity of 4.68×10^{-4} S/cm followed by a rapid increase for the subsequent ϕ consistent with a power law.

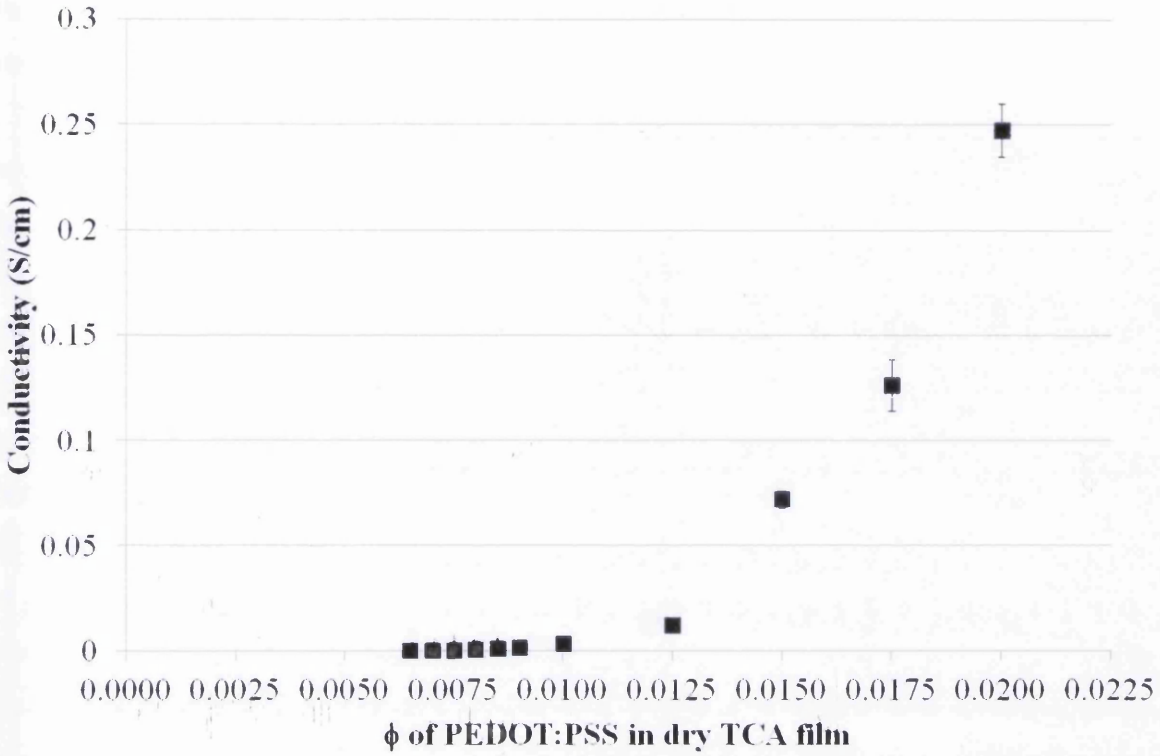

Figure 3.4. Change in bulk conductivity with the change in volume fraction (ϕ) of PEDOT:PSS in the dry TCA film.

This data shows that the TCA follows percolation theory (see Section 1.9.2) whereby below a certain volume fraction, in this case 0.0075, there are no conductive pathways made by the PEDOT:PSS through the non-conducting matrix. After this point the conductivity increases according to a power law function shown in Equation 3.1 [6].

$$G_{film}(\phi) = K(\phi - \phi_c)^{\mu} \qquad \text{(Eq. 3.1)}$$

Where $G_{film}(\phi)$ is the conductivity of a film of given volume fraction of conducting phase, (ϕ) is the conducting phase volume fraction, (ϕ_c) is the Critical Percolation Threshold, μ = a theoretical value calculated for different dimensioned networks.

The second thing this data shows is that the percolation threshold must lie between 0.0075 and 0.0080. This means that the critical percolation threshold must be considerably lower than for spheres randomly orientated in a 3-D network, which has a theoretical value of 0.18 [7]. This low ϕ_c shows that the PEDOT:PSS within the PSA does not exist as discreet

spheres that eventually join together to form spanning networks but instead must have extended geometry such as discs, cylinders or wires with a high aspect ratio that then overlap to form a spanning network. The reason the PEDOT:PSS does this is due to a similar phenomenon that was observed when PEDOT:PSS was added to polyethylene oxide (PEO). The crystalline nature of the PEO forced phase separation and left the PEDOT:PSS to concentrate interspherulitically[8]. This meant that the PEDOT:PSS did not form randomly distributed phases but rather had an ordered structure resulting in the onset of conductivity occurring much lower. In a PSA with an emulsion structure a proportion of the volume will be occupied by the particles inherent to the emulsion (as explained in Section 1.8.2). Therefore when mixed with PEDOT:PSS the emulsion particles would limit the space the PEDOT:PSS could occupy in a given volume leading to not a random distribution of phases but rather an orientation of PEDOT:PSS between particles. This will have the effect of lowering the concentration needed for a spanning conducting network to occur, shown schematically in Figure 3.5.

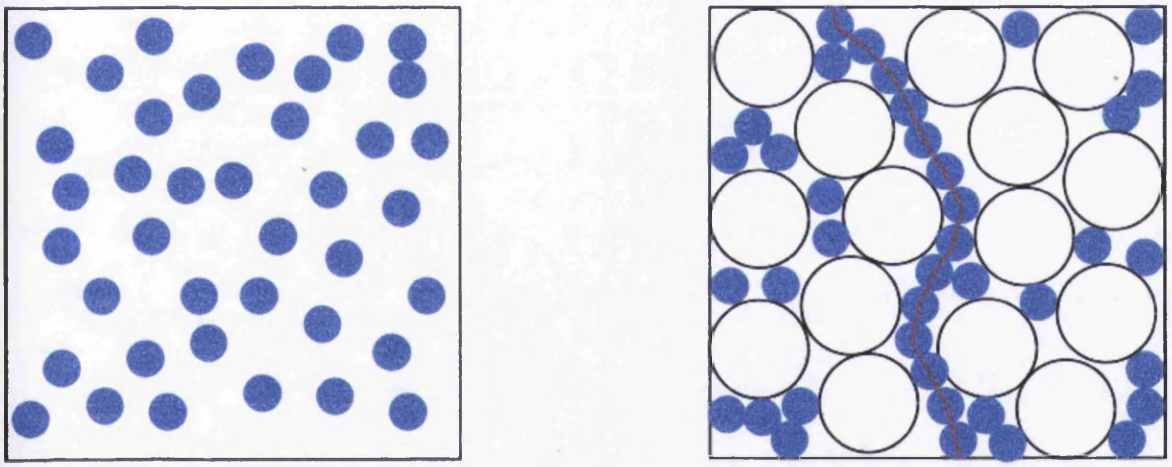

Figure 3.5. Schematic of: a) randomly distributed PEDOT:PSS phases (blue circles) that do not form a spanning network within a matrix and b) PEDOT:PSS of the same concentration forming a spanning network when the matrix has a particulate structure (as found in an acrylic emulsion) which the PEDOT:PSS phases are excluded from (white circles).

The image in Figure 3.6 shows a section of TCA that has been cryo-sliced and then imaged using AFM in tapping phase mode. The image shows a packed particle structure, almost honeycomb in nature, with a particle diameter of 150nm, which is in line with the structure of an acrylic emulsion PSA (shown in Figure 1.18). It can further be seen that there

are illuminated regions at the boundaries of these particles that are 60nm in diameter (Figure 3.6b). The illuminated regions represent harder phases where the AFM tip has bounced rather than struck the material (in tapping mode) creating a positive phase lag. PSA by its nature will be softer than the PEDOT:PSS so these regions are defined as PEDOT:PSS. This then shows that the PEDOT:PSS phases are indeed ordering themselves between the particles within the PSA structure and are not randomly orientated phases, explaining why the percolation threshold for the TCA is so low. This also confirms a dual phases polymer structure within the TCA where the PEDOT:PSS and PSA are still discrete phases, as opposed to altering one of the constituents chemically or forming a copolymer.

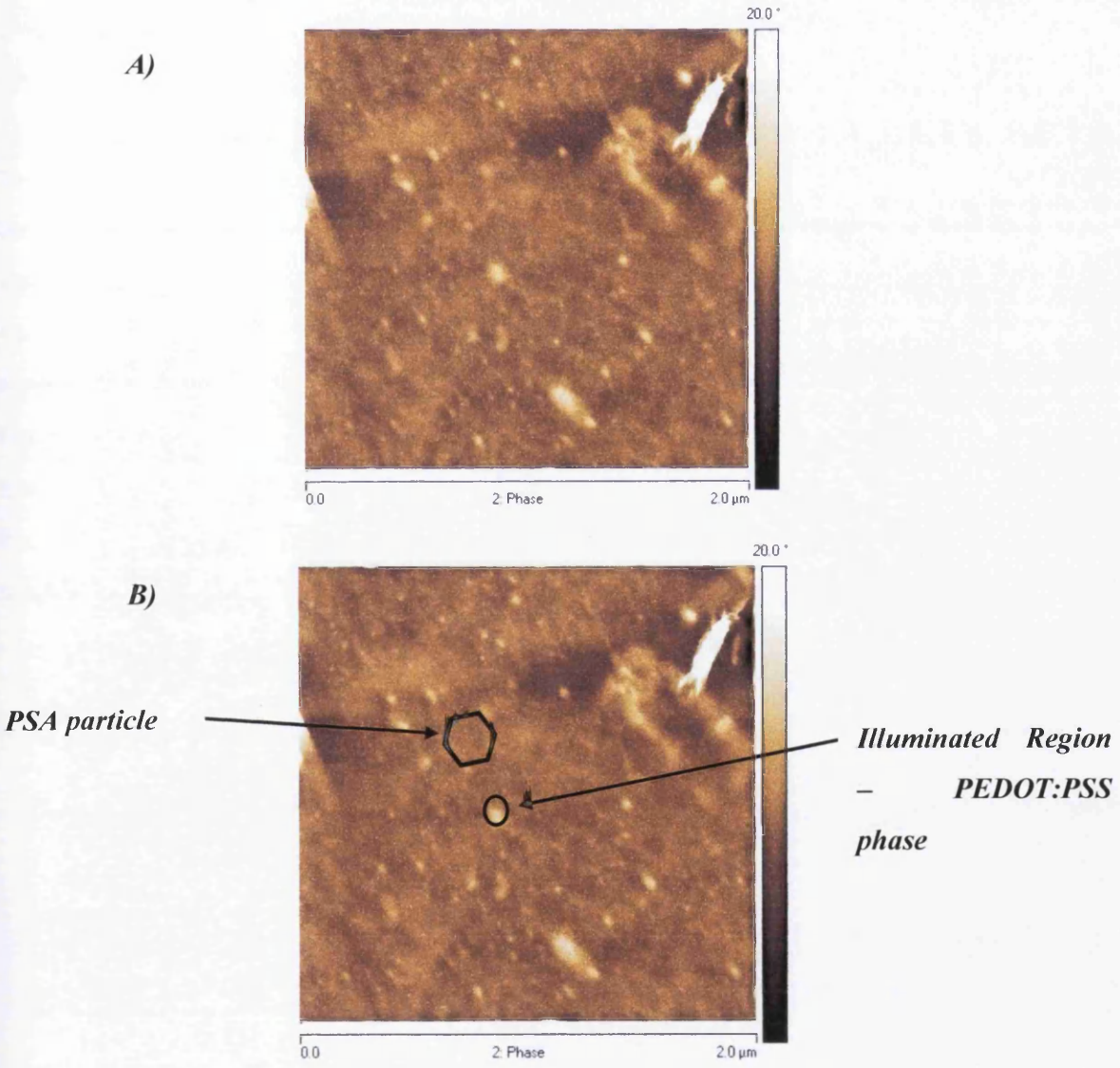

Figure 3.6. AFM phase images of A) cryo-sliced section of a TCA with 0.0175 PEDOT:PSS volume fraction and B) annotated to highlight the PSA particle and PEDOT:PSS phases.

The volume fraction is also similar to what has been observed before where Ag nanowires overlapped to form a spanning network at concentrations much lower than spherical particles in 2-D [9] which can be modelled in 2-D using sticks [10]. This result is significant as it means that the TCA can conduct when the volume fraction of the PEDOT:PSS is exceptionally low which means that compared with Ag nanowires, which have also been suggested as an alternative back contact in s-DSCs in low concentrations[1], the TCA will have a cost saving as PEDOT:PSS is cheaper than Ag per gram. Significantly it also indicates that a conductive adhesive with a high degree of transparency could be fabricated whilst maintaining a tack sufficient enough for it to be used as a transparent electrode in opto-electronic devices (as described in Sections 3.2.5 and 3.2.6) [11] .

Ag nanowire films have been suggested to be closer to 2-D networks than 3-D [9] therefore to determine the network dimensions and ultimately calculate the exact ϕ_c. Logs can be taken of G_{film} and (ϕ - ϕ_c) and plotted in Figure 3.7. It is known that the ϕ_c must lie between 0.0075 and 0.008 and it is also know that μ from Equation 3.1 will be 1.33 when the network is 2-D and 1.94 when 3-D [12]. Figure 3.7 shows that when the value of μ (the slope) is fixed at 1.33 for a 2-D network the value of ϕ_c must be 0.00876 which does not lie between 0.0075 and 0.008 and indicates that this TCA does not represent a 2-D network. For the 3-D line with the μ value set to 1.94 the ϕ_c is 0.00786 confirming that the PEDOT:PSS forms a spanning 3-D network with a percolation threshold of 0.00786 or PEDOT:PSS concentration in the dry film of 0.00786

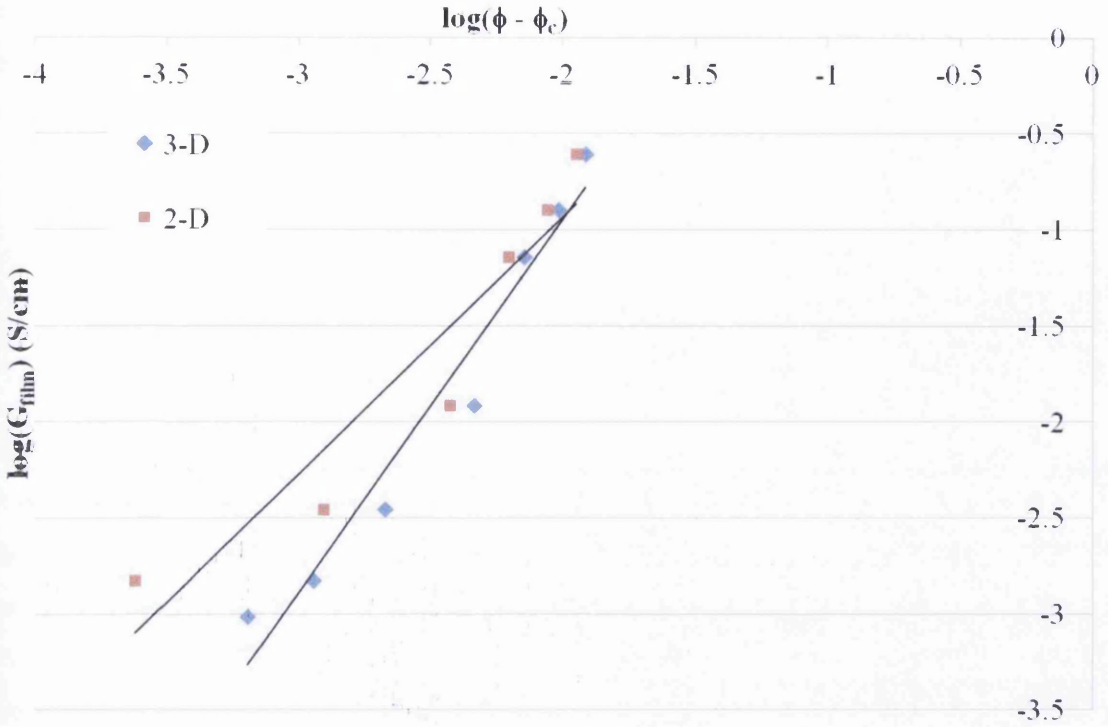

Figure 3.7. Change in the $\log(G_{film})$ and the $\log(\phi - \phi_c)$ in TCA films of varying PEDOT:PSS volume fraction with μ (slope) set to 1.94 for 3-D networks and 1.33 for 2-D.

This is in line with previous studies of PEDOT:PSS mixed with other non-conducting materials including PEO, polyurethane and cellulose which have all found trends described by percolation theory [8, 13-14]. One important point to notice from a practical point of view is that when going from ϕ of 0.008 to 0.02 the conductivity of the TCA changes by 3 orders of magnitude and this has implications for maintaining strict material preparation given the sensitivity of this product for commercial production.

As a comparison another PEDOT:PSS solution (PH1000 plus 5% Dimethyl Sulfoxide, Heuraeus) with a higher quoted conductivity of 850 S/cm (if used just as PEDOT:PSS), 10x that of the EL-P3145 PEDOT:PSS, was also mixed with the PSA using the method described in Section 2.1. The PH1000 PEDOT:PSS has a solids content of 1.3% and therefore to achieve a final PEDOT:PSS ϕ in the dry TCA film of 0.0175, 0.822g was added per 1g of PSA in the wet mix (see Section 3.1 for more details). Table 3.2 shows a comparison of the TCAs and their conductivity.

Table 3.2. Conductivity of a TCA films fabricated with different PEDOT:PSSs and the properties of the films.

PEDOT:PSS used	Quoted Conductivity of PEDOT:PSS before mixing with PSA (S/cm)	ϕ in dry TCA film	Film Thickness (μm)	Measured Conductivity (S/cm)
EL-P3145	80	0.0175	45	0.139 ±0.00042
PH1000	850	0.0175	51	0.145 ±0.00022

It can be seen from the measured conductivity values in Table 3.2 that the conductivity of the TCA does not change significantly even when a PEDOT:PSS of 10x higher original conductivity is used. What this highlights is that within this volume fraction range the structure of the PEDOT:PSS film that provides enhanced conductivity when used unadulterated will be broken apart once it is mixed with a PSA. This holds true if the PEDOT:PSS phases are seen as discreet particles, as the conductivity of the TCA will depend only on how many and the length of the spanning clusters formed which is in turn dependent on the amount of PEDOT:PSS phases (or in the case the volume fraction) present. If this is equal for two TCAs the conductivity should be roughly equal. Any change in conductivity could be explained by a difference in the size and shape of the PEDOT:PSS particle phases. This means that even PEDOT:PSS of a higher conductivity grade will give the same conductivity once the volume fraction is taken into account, This could have cost saving implications suggesting that a basic or 'lower grade' and ultimately cheaper PEDOT:PSS could be used in the formulation of a TCA.

3.2.3. The geometry of PEDOT:PSS within the TCA and surface outcropping

One assumption is that the PEDOT:PSS will outcrop at the surface and that the outcrop frequency will be indicative of an equal to the bulk distribution however it is important that this is quantified and confirmed. The importance of outcrops of PEDOT:PSS on the surface of the TCA and how they occur is significant as they will be the only sites for electrical contact and as a result vitally important to the electrical performance of the TCA. In a device such as a s-DSC they are sites for current collection and therefore their area and separation need to be quantified in order to ultimately optimise device performance.

The AFM micrographs of the surface of a TCA in Figures 3.8.a-e firstly show the same dual phase structure seen in Figure 3.6 indicating that the surface is indicative of the bulk (again the illuminated regions represent regions of PEDOT:PSS).

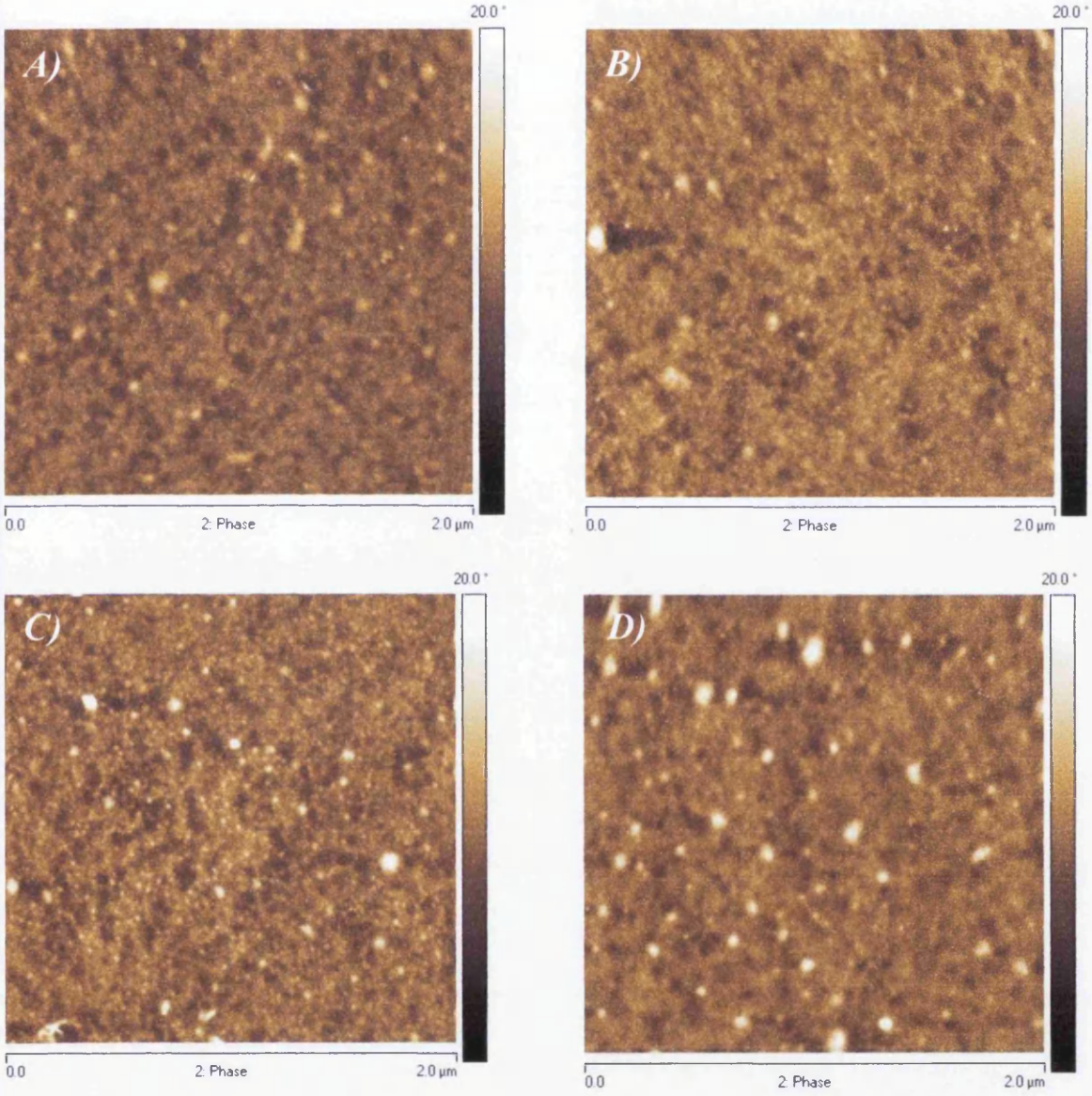

Figure 3.8. AFM phase images of the surface of a PSA with A) No PEDOT:PSS present, B) 0.0125 PEDOT:PSS TCA C) 0.0175 PEDOT:PSS TCA and D) 0.0200 ϕ PEDOT:PSS TCA. The illuminated regions are harder in nature and therefore regions of PEDOT:PSS in a PSA matrix.

The PEDOT:PSS regions increase from no additions in the PSA only sample (Figure 3.8.a) through to the TCA containing ϕ 0.0200 PEDOT:PSS (Figure 3.8.e). Figure 3.8 also shows that their spacing decreases from an average of ~1μm to ~300nm as the PEDOT:PSS content is increased from 0.0125 to 0.0200. To see if the surface is representative of the bulk of the TCA as a whole then a simple model can be applied shown in Figure 3.9. A TCA with a PEDOT:PSS ϕ of 0.02 is used as an example, which has a PEDOT:PSS outcrop diameter of 60nm and an average spacing of 300nm (360nm centre to centre) derived from image analysis of figure 3.8(d).

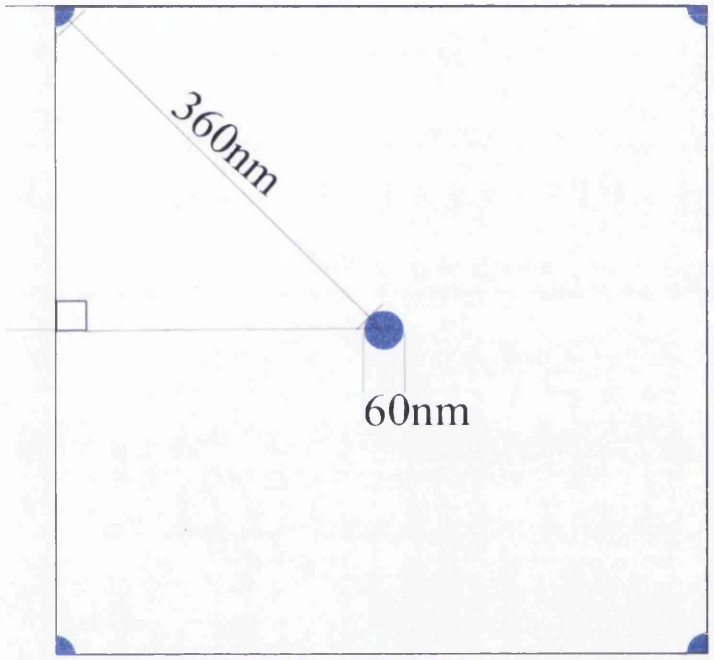

Figure 3.9. A Simple model showing the outcrops of 60nm diameter PEDOT:PSS (blue circles) evenly spaced within a TCA such that each outcrop is no more than 300nm from another outcrop (360nm centre to centre). A square area includes two complete outcrops.

Using the centre to centre spacing diagonal in the square as a hypotenuse of a right angle triangle each side of the square can be found to equal 509.1nm. The area of two outcrops divided by the area of the square leaves the percentage area of the outcrops. In this case that would be:

$5656\ nm^2 / 259{,}200nm^2 = 0.0218$

This is within error equal to the volume fraction of the PEDOT:PSS of the TCA and shows that the surface outcrops are representative of the volume fraction of PEDOT:PSS in the dry film. This gives evidence that the PEDOT:PSS is indeed evenly distributed throughout the dry TCA film in the z-axis (film thickness).

The second point to note is that the outcrop is a circle and the diameter remains relatively constant at 60nm for all the TCAs containing PEDOT:PSS. This shows that increasing the PEDOT:PSS volume fraction simply decreases the spacing of the outcrops, or to put it another way the PEDOT:PSS networks in the TCA become denser but their dimensions remain relatively unchanged as the volume fraction of PEDOT:PSS increases. This can be explained when considering the spacing between the particles of the PSA in Figure 3.6. A simple cubic packing structure of four 150nm diameter particles, such as the one shown in Figure 3.10, using the hypotenuse leaves a pore size large enough to fit a circular particle of 62nm. As the particles in the emulsion are constant for all TCAs the size of the PEDOT:PSS phases would remain relatively constant provided adequate and even mixing of the TCA.

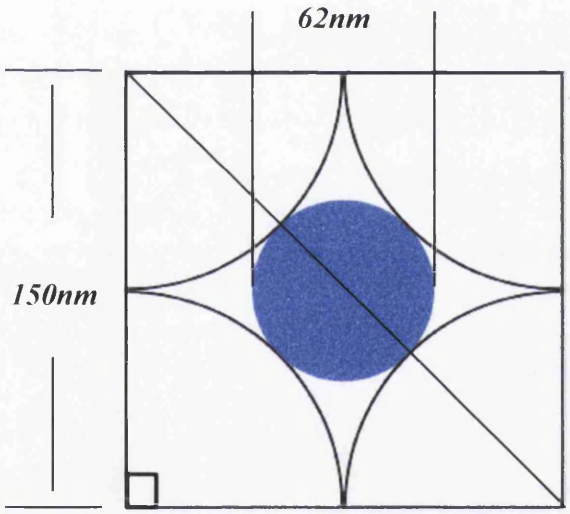

Figure 3.10. Cubic packing of spherical particles with a diameter of 150nm with a pore size large enough for a 62nm spherical particle representing a PEDOT:PSS phase (blue particle) within a PSA emulsion (white particles).

However cubic packing isn't the only way particles can be packed and also the PEDOT:PSS phases always being spherical (rather than filling the pore space entirely) suggests there are other factors influencing the PEDOT:PSS geometry and distribution. One such factor could be the fact that the PSS molecule has a different affinity for water and OH

group and compounded by the hydrophobicity of the PEDOT molecule could lead to the PEDOT:PSS forming micellular or core shell structures/particles of their own, as suggested previously [16]. This would mean the PEDOT:PSS phases would tend towards spherical particles of a relatively consistent size over this small range of volume fractions, however further work would be needed to confirm this.

3.2.4 Dry TCA Film Height and its Relationship to Conductivity

A key variable that has an impact on TCA performance is the layer thickness, aside from other parameters such as transparency and tack the film height may affect the conductivity as well. In the previous section it was seen that increasing the PEDOT:PSS volume fraction increases the conductivity according to a power law. The wet solution of PEDOT:PSS contains more solvent than the PSA, 99.2 and 40% respectively. Therefore a wet film at a given cast height will contain more solvent (and less solids) the higher its PEDOT:PSS volume fraction compared to the PSA, this would ultimately result in a thinner dry film. This is shown by Table 3.3, as the ϕ of PEDOT:PSS in the TCA is increased by adding proportionally more PEDOT:PSS in the wet mix, the dry film height decreases for a fixed wet cast height of 180μm. It is also noteworthy that the theoretical film thickness - calculated by assuming that the dry film height for a given wet cast height will be proportional to the % solids within the wet solution (i.e. if the solid percentage was 50% the dry film height would be half the wet cast height), shows a good correlation with the measured dry film height and is a useful approximation for predicting dry film thickness when considering TCA production and applications.

Table 3.3 Weight of PSA and PEDOT:PSS needed to make the respective PEDOT:PSS volume fraction (ϕ) in a dry film. Also displayed is the solvent % in the wet mix, theoretical dry film height and measured film height at 180μm.

ϕ of PEDOT:PSS in dry film	Weight of PSA solution needed (g)	Weight of PEDOT:PSS solution needed (g)	Percentage Weight of Solvent in wet TCA (%)	Theoretical Dry Film Thickness of a 180μm wet cast height (μm)	Measured Dry Film Thickness (μm)
0.0065	1.00	0.49	59.49	74.95	73.00
0.0070	1.00	0.53	60.47	71.15	70.00
0.0075	1.00	0.57	61.41	69.45	67.00
0.0080	1.00	0.60	62.31	67.84	66.00
0.0085	1.00	0.64	63.17	66.30	65.00
0.0090	1.00	0.68	63.99	64.83	63.00
0.0100	1.00	0.76	65.52	62.07	60.00
0.0125	1.00	0.95	68.83	56.10	57.00
0.0150	1.00	1.14	71.53	51.24	49.00
0.0175	1.00	1.33	73.82	47.12	45.00
0.0200	1.00	1.53	75.77	43.62	40.00

While the bulk conductivity values used in Section 3.2.2 take into account the dry film height in their calculation this would assume isotropic behavior within the film.

Therefore, to investigate how the film height affects conductivity samples were cast at increasing 45μm wet film thickness. Subsequently their dry film thickness and conductivity were measured and their bulk conductivity calculated as shown in Figure 3.11.

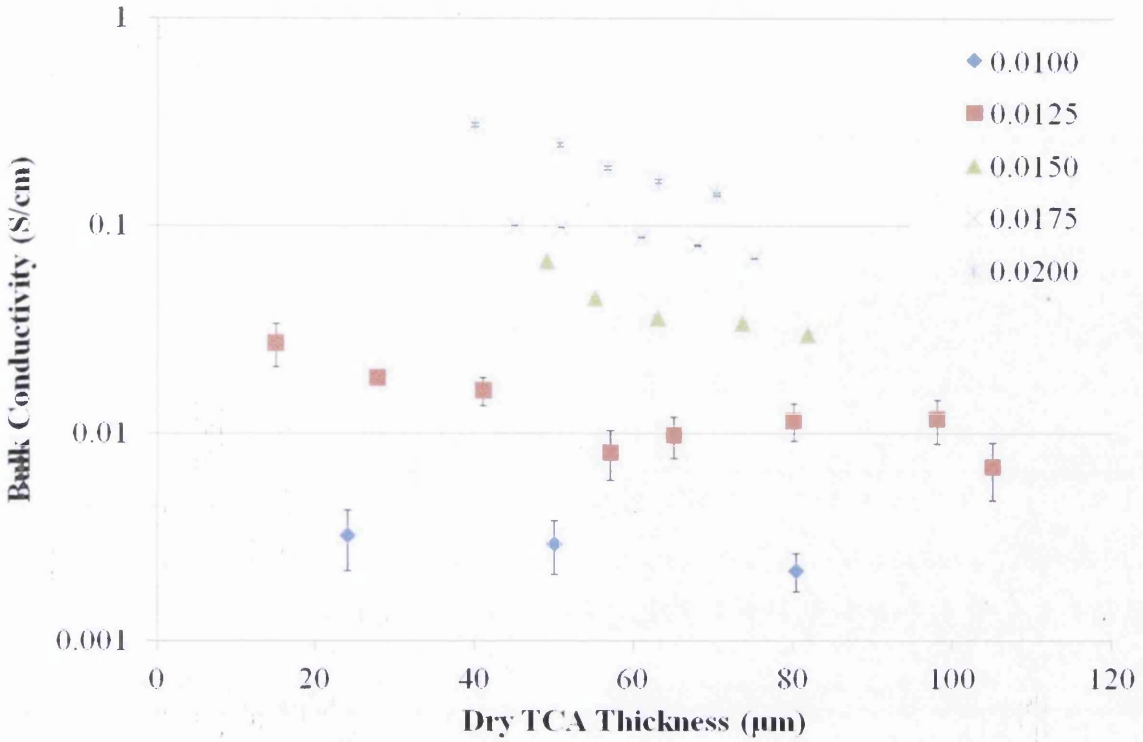

Figure 3.11. A semi log plot of conductivity Vs dry film thickness for TCAs made with 0.0100 to 0.0200 PEDOT:PSS ϕ at varying dry film thickness. Averages of 4 samples and 4 repeat measurements on each per data point.

In Figure 3.11 we can see that there is a general trend for the bulk conductivity to decrease as the film height increases for all samples. The films do actually decrease their measured Resistance values as the film height increases, however the rate is not uniform to the height increase. This means that as the film thickness increases the Resistance of the film doesn't drop proportionally and since the dried film height is taken into account in the conductivity calculation (as shown in Equation 2.3) this leads to the overall decrease in bulk conductivity. The decrease appears from this data to be linear with the relationship shown in Equation 3.2.

$$G_{film}(\phi) = -sC_w + d \qquad \text{(Eq. 3.2)}$$

Where $G_{film}(\phi)$ is the conductivity of a film with a certain volume fraction of conducting PEDOT:PSS in the dry TCA film. C_w is the coating weight which in this case is interchangeable with the dry TCA film thickness. s and d are both constants dependant on the materials used for the TCA and the volume fraction of PEDOT:PSS within the film.

Initially it could be suggested that the change in conductivity could be caused by inhomogeneous distribution of the PEDOT:PSS throughout the vertical height of the film (z-axis), with more PEDOT:PSS located towards the base worsening the conductivity measured as the film thickness increases (since this measurement is taken at the surface). However it can be seen from Figure 3.12 that when the Ag line are printed onto the substrate and then the 0.00125 TCA coated over it, the measured bulk conductivity shows exactly the same trend as when the Ag lines are evaporated onto the surface. If there had been inhomogeneous distribution in the vertical axis these lines would be opposite, diverging as the film thickness increased. The discrepancy in conductivity between the two measurements has been attributed to the different silver used (printed not evaporated) and its contact made with the TCA and with the measuring probes. This confirms the results shown in Section 3.2.3 which suggest (from the AFM results) that PEDOT:PSS is homogeneously distributed throughout the film thickness.

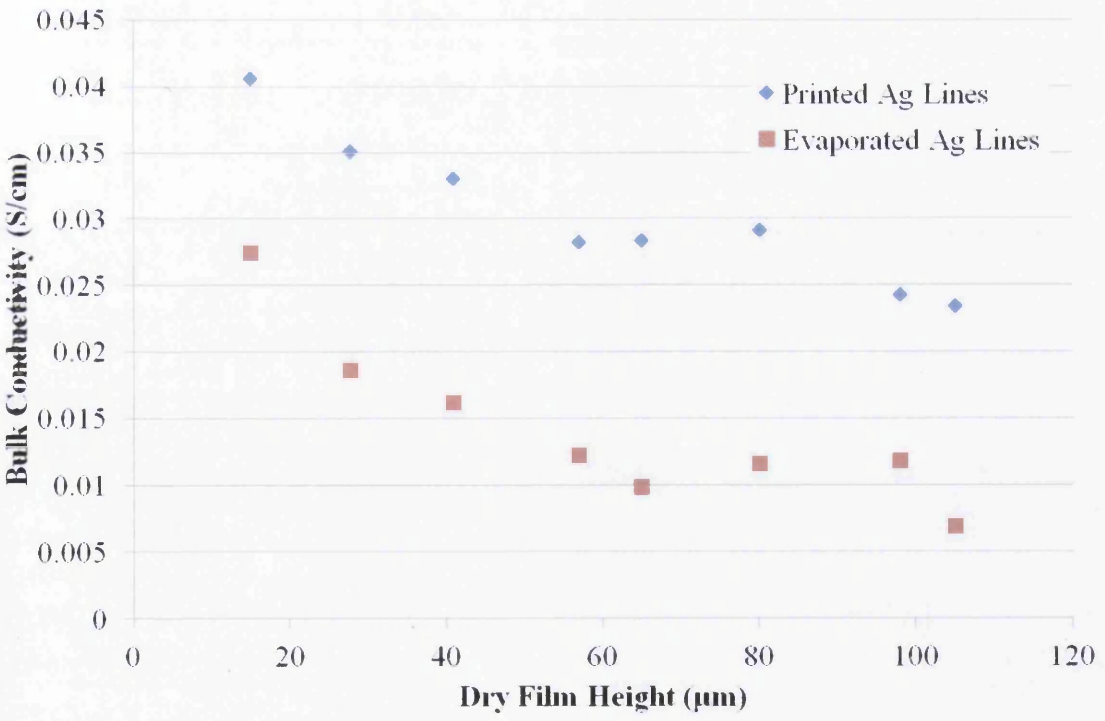

Figure 3.12. Variation in conductivity of a PEDOT-Laminate containing a ϕ 0.00125 PEDOT:PSS at different dry film heights measured with Ag lines evaporated on the surface and printed Ag below the PEDOT-Laminate.

An obvious reason for the discrepancy would simply be error in the conductivity measurement which is carried through to all the samples. This highlights problems with the four point probe technique as you can still get conduction through the silver contacts and then contact resistance becomes an issue. Another scenario for the change in conductivity with film thickness could be one that has been suggested before in wholly PEDOT:PSS films, that the lateral conductivity is greater than the horizontal conductivity [16-17]. This due to the shrinkage of the PEDOT:PSS gel particles in the vertical direction as the PEDOT:PSS solution dries leaving disc like shapes and PSS rich lamella running parallel to the substrate surface [16]. This anisotropic conductivity is consistent with what is occurring in the TCA where conductivity is greater in the direction parallel to the substrate. The mechanism of this anisotropic behaviour is shown schematically in Figure 3.13.

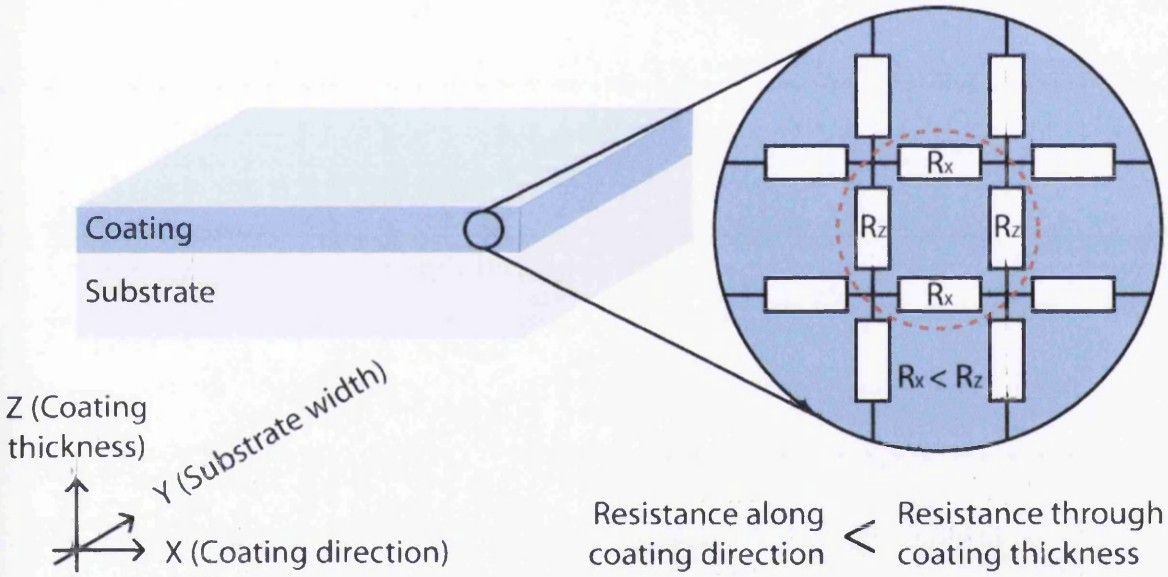

Figure 3.13. Schematic through a bar cast TCA showing that the resistance in a direction parallel to the substrate (x or y) is lower than in the coating thickness (y).

As well as the shrinkage of the PEDOT:PSS regions during curing of the TCA the anisotropic distribution of the PEDOT:PSS could be caused by the casting direction. Evidence against this are the circular outcrops observed in Figure 3.8 as one would expect a more elongated or ellipsoid shape in the casting direction, however it doesn't rule out that there may be a more macroscopic factors in the PEDOT:PSS distribution and further work would be needed to quantify this.

To see if the percolation theory still holds true when the change in bulk conductivity at different cast heights is taken into account averages of the bulk conductivity of each ϕ PEDOT:PSS from the data in Figure 3.11 can be taken. This can then plotted against the PEDOT:PSS volume fraction, as shown in Figure 3.14, which shows that despite the anisotropic behaviour the change in conductivity still increases according to a power law. Figure 3.15 shows the same average data but logs are again taken of G_{film} and (ϕ - ϕ_c) in order to determine the ϕ_c and an average value of ϕ_c = 0.00763 is obtained with μ = 1.94 for 3dimensions (compared with ϕ_c = 0.00786 found in Section 3.2.2). Therefore the ultimate percolation threshold will vary depending on the cast height used although not significantly.

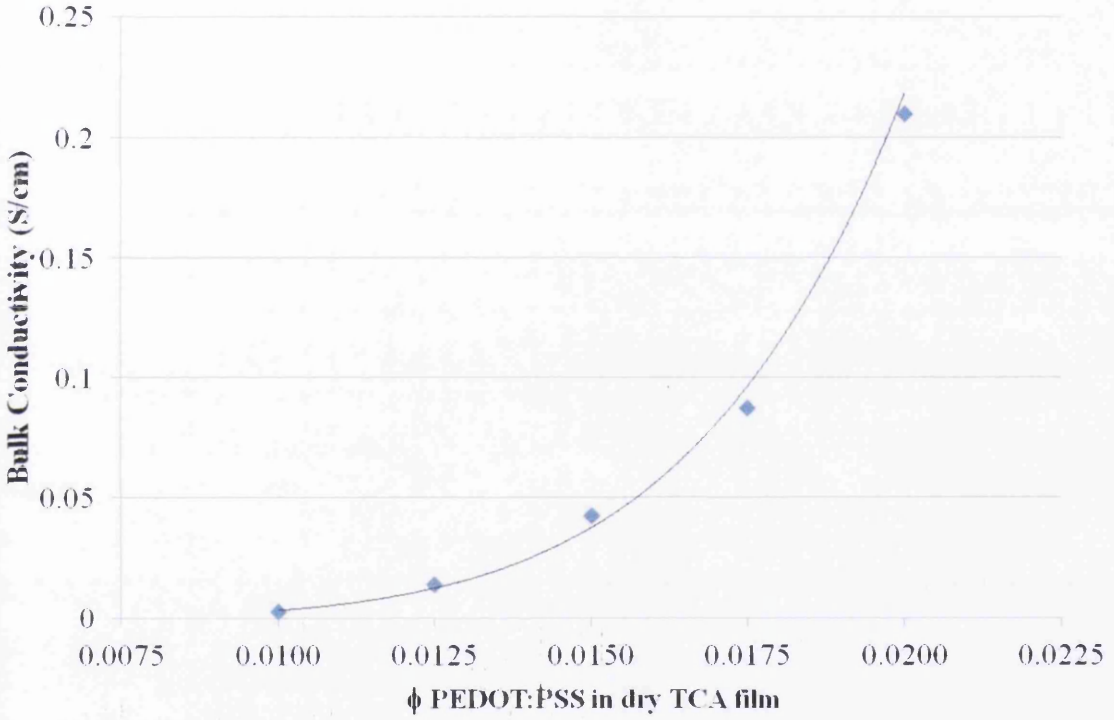

Figure 3.14. Change in Bulk Conductivity for films of varying ϕ PEDOT:PSS in dry TCA film. Each data point is an average of TCAs of a certain ϕ PEDOT:PSS at different cast heights.

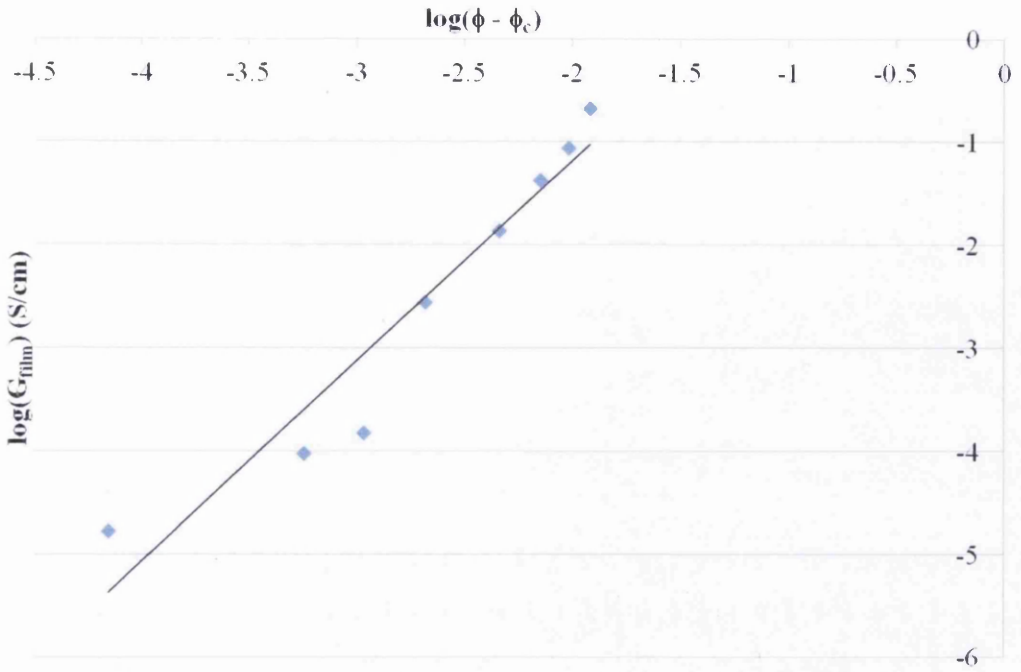

Figure 3.15. The change in the log(G_{film}) and the log($\phi - \phi_c$) in PEDOT:PSS TCA films

3.2.5. Film Tack as a function of Coating Weight

The tack of the film is vitally important to the applications of the material. PEDOT:PSS has been mixed with other polymers previously but it is the tack of the TCA material that sets it apart and increases its potential applications. The tack of the film is what will keep the non-adhesive regions of PEDOT:PSS in mechanical and electrical contact with surrounding layers.

To investigate how the adhesive alone behaved before PEDOT:PSS additions were made the cast film height of pure PSA was varied and the tack measured after curing using a rolling ball tack test (RBT). From this test a value for the distance the ball has travelled is obtained which is called the 'Tack', (between 5-25cm for common tapes) where the lower the number means the greater the tack or more adhesive the film (see Section 1.8.1), the results of this are presented in Figure 3.16.

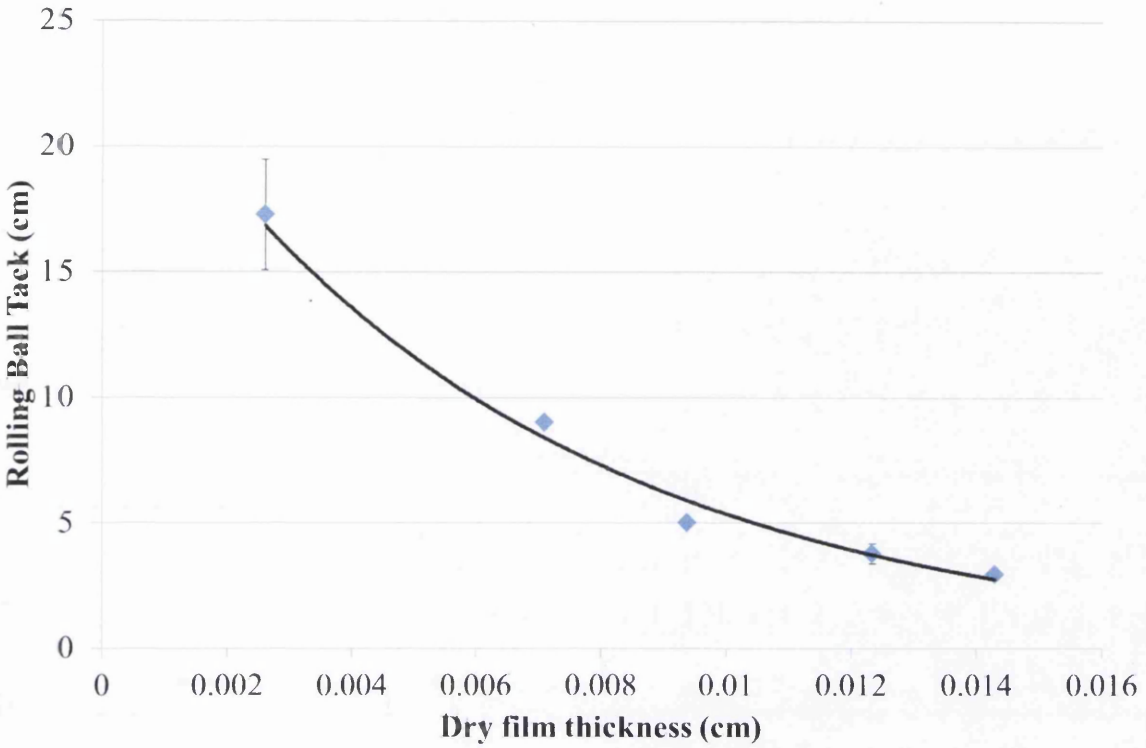

Figure 3.16. The change in Rolling Ball Tack as a function of change in film thickness for PSA. A lower value on the Y axis indicates a greater tack. Averages of 4 samples and 4 repeat measurements on each per data point

Figure 3.14 shows how the Tack changes as a function of dry film thickness for the pressure sensitive adhesive alone. It can be seen that the curve formed by the PSA without any PEDOT:PSS in the RBT test shows an apparent exponential increase in tack (decrease in the value obtained from rolling ball tack distance) as the thickness increases. The thickness is proportional to the coating weight (C_w), which has been found previously in the field [11]. In this regime the coating can be summarised by Equation 3.3.

$$L = \beta e^{\alpha C_w} \qquad \text{(Eq 3.3)}$$

Where L is the Rolling Ball Tack and α is a value that refers to the nature of the adhesive shown by the steepness of the curve and β is the extrapolated y-intercept. α and β are inherent properties of the adhesive and are important as they will be affected by the addition of PEDOT:PSS and the way they are affected could give indication of how the adhesive nature of a TCA could be improved. In an ideal adhesive α should be 0 and the

adhesion of a film shouldn't depend on coating weight [11]. However in the real world this is never the case and how the adhesion (in this measurement shown by the tack) varies with respect to the coating weight will be dependent on the nature of the adhesive itself (some adhesives vary their tack less with coating weight, some more so). β is a function of the parameters influencing adhesive contact made when considering the surface only, shown by the y intercept of the graph where the coating thickness is equal to 0. In reality at this point the β value would be ∞ and therefore the extrapolated value for β is merely indicative of how the adhesive behaves at low coating weights. As the coating weight decreases the surface properties proportionally have a larger influence than the bulk, indeed one could imagine a situation where an adhesive film has a thickness infinitely close to but not equal to 0 that is essentially only 'surface' and no bulk, and in this situation it is only the surface properties of the film that will be influencing the Tack.

To investigate how the adhesive behaved when PEDOT:PSS is added (to create a TCA) various PEDOT:PSS volume fractions with PSA were made with different cast heights and the tack measured using RBT. The results are shown in Figure 3.17 and the corresponding β and α values from exponential trend lines fitted to the data are shown in Table 3.4.

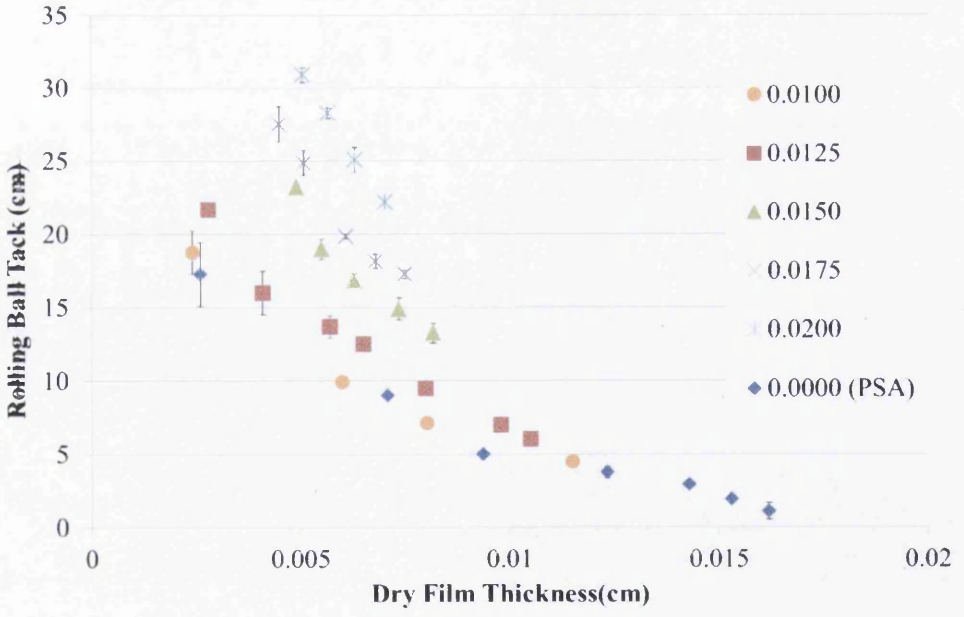

Figure 3.17 Variation in tack for a given cast height of TCA films made using 0.0100-0.0200 PEDOT:PSS ϕ A PSA with no PEDOT:PSS added is also shown as an example. Data points are the average of 4 samples with each measurement repeated 4 times.

Table 3.4. Values of β and α obtained from the exponential trend lines fitted to data in Figure 3.15 using the relationship in Equation 3.3.

PEDOT:PSS ϕ in dry film	β	α
0.0000	25.16	-154.60
0.0100	26.28	-156.70
0.0125	37.80	-158.80
0.0150	47.25	-159.70
0.0175	56.52	-163.80
0.0200	94.96	-169.80

It can be seen from Table 3.4 that the β value increases from 25.16 to 94.96 for 0 to 0.02 volume fraction PEDOT:PSS respectively. This is in line with what has been previously suggested the β value is with regards to an adhesives peel strength that it is dependent on the parameters influencing contact build-up between the adhesive and the surface it is adhering to [11]. Therefore the decrease in the β value from Table 3.4 indicates that the overall contact build-up is lower for films containing increasing PEDOT:PSS content. This is to be expected as the addition of the non-adhesive PEDOT:PSS into a PSA matrix means there will be a lower overall surface area of adhesive and therefore the tack will decreases below that of the PSA alone. As shown in Table 3.4 the α values tend towards a more negative value of -169.80 at 0.0200 PEDOT:PSS volume fraction compared with -154.60 for pure PSA. Since the α values in Table 3.4 tend towards a more negative value (and the steepness of the curve increase) at higher PEDOT:PSS volume fractions it shows that as the film thickness is increased the tack of the TCA tends towards that of the PSA. What α and β ultimately show is that adding the non-adhesive PEDOT:PSS causes less of an effect on the tack in thicker coatings and is more influential to the surface properties of the film at lower coating weights. This is in line with what has been found previously that tack values obtained from RBT are sensitive to the coating weight and also that the surface conditions have more influence than the bulk at lower coating weights [6]. Both β and α follow polynomial distributions with respect to the PEDOT:PSS content as shown by Equations 3.4 and 3.5.

$$\beta = i\phi^2 - j\phi + l \quad \text{(Eq 3.4)}$$

$$\alpha = m\phi^2 + n\phi - p \quad \text{(Eq 3.5)}$$

Where i, j, m, n, p and l are all constants dependant on the TCA constituent materials used.

3.2.6. Analysis of the optical characteristics of a TCA film

The TCA presented here has applications within opto-electric devices and could potentially used as a film where light is either generated by the device and transmitted through the TCA (electroluminescent lamp) or used by the device and is received through (a solar cell). Therefore the optical behaviour of the film must be analysed and quantified to determine optimal behaviour.

To identify TCA transmission in the visible spectrum samples of 0.0150 and 0.0200 volume fraction PEDOT:PSS TCA (with similar dry film thicknesses) were fabricated and their transmission measured using UV-Vis spectroscopy along a sample of pure PSA. The results of this can be seen in Figure 3.18. Additionally to see how the absorbance varies with increasing film thickness and varying PEDOT:PSS volume fractions TCA films were fabricated at varying dry film thicknesses and volume fractions between 0.0100 – 0.0200 and their absorbance measured at the wavelength of 530nm (figure 3.19). This wavelength was selected as it lies in the middle of the visible spectrum, where most opto-electric devices operate and therefore will be indicative of it their performance in such a device.

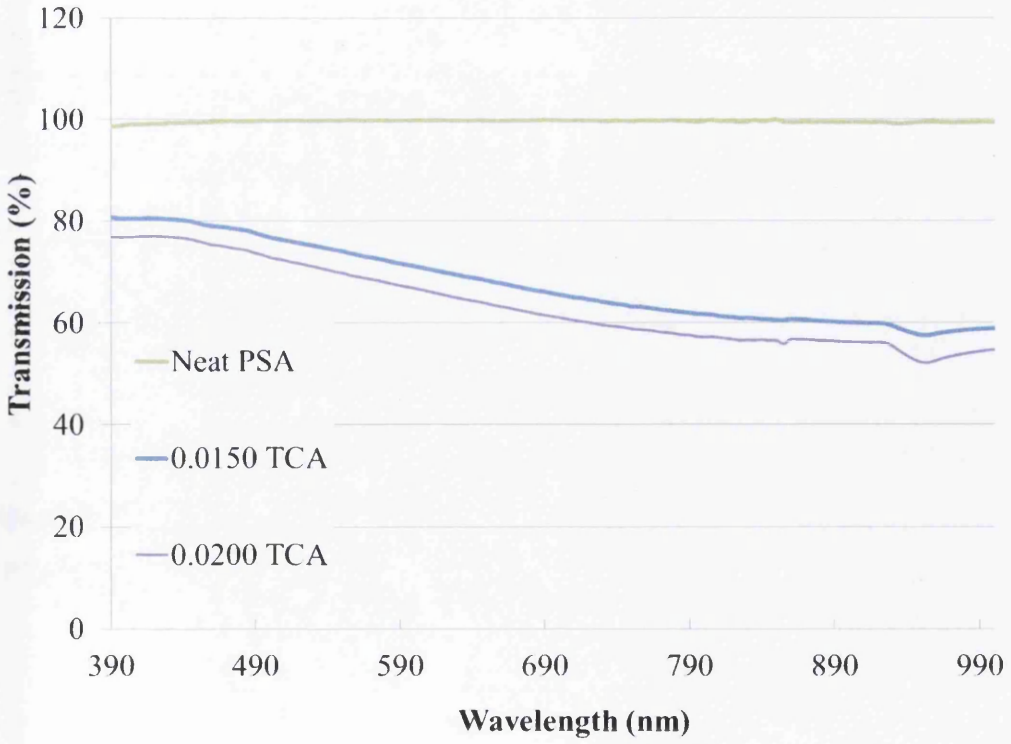

Figure 3.18. UV-Vis transmission spectrum for TCA film with a 0.0150 PEDOT:PSS volume fraction TCA with a dry film thickness of 49μm, a 0.0200 PEDOT:PSS volume fraction with a dry film thickness of 49μm on a glass substrate and a film of neat PSA with a dry film thickness of 48μm.

Figure 3.18 shows the transmission spectrum of a 0.0150 and a 0.0200 TCA which shows the decrease in transmission characteristic of PEDOT:PSS. Furthermore PEDOT:PSS transmission decreases as the PEDOT:PSS ϕ is increased along the range of wavelengths. Figure 3.18 also demonstrates how little the PSA absorbs since its transmission is nearly identical to the glass substrate it was applied to. This further confirms that the main absorbance of the TCA film will be from the PEDOT:PSS, further increasing as the ϕ increases.

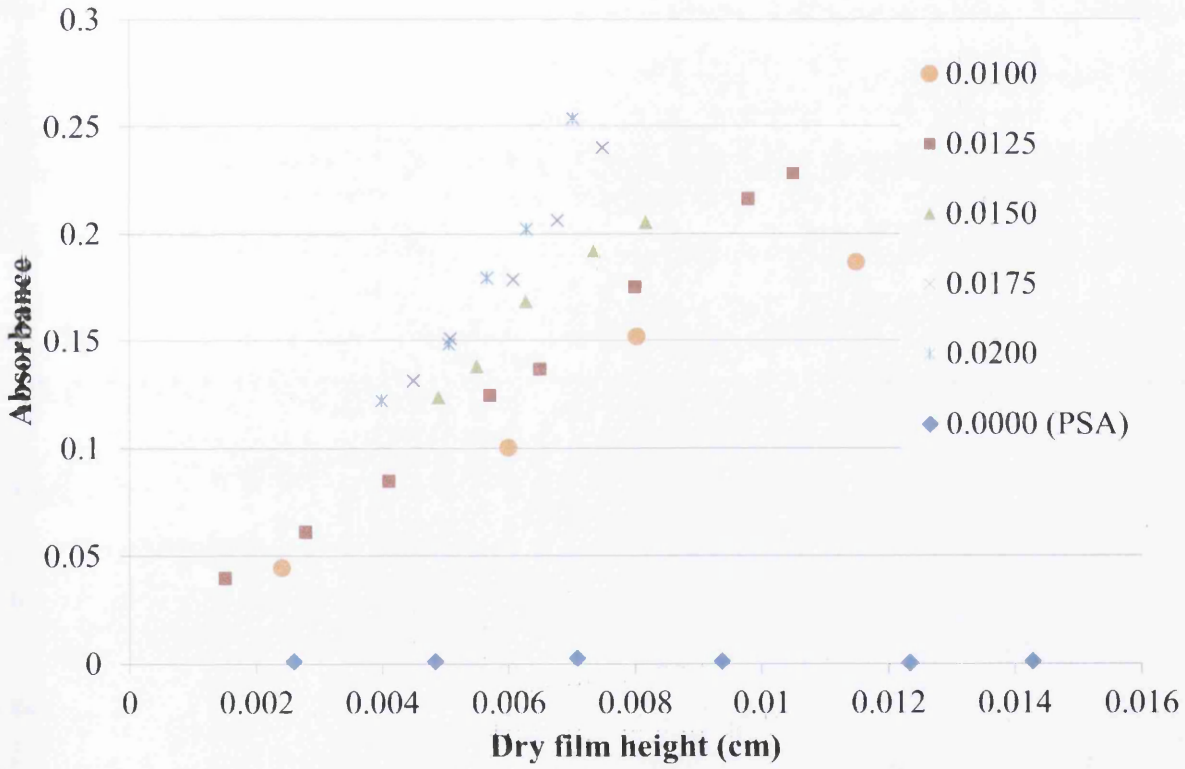

Figure 3.19. Relationship between dry film height and absorbance of TCA films of varying ϕ PEDOT:PSS at 530nm wavelength. Average of 3 samples per data point.

When observing the values for the absorbance at 530nm for a given dry film height in varying ϕ PEDOT:PSS, shown in Figure 3.19, it can be seen that when comparing the absorbance as a factor of the film thickness for a given volume fraction the relationship is linear. This is in line with what has been found previously that as the PEDOT:PSS film thickness increases the transmission decreases [18]. It also indicates that increasing the PEDOT:PSS content will lead to less light being allowed through in a linear fashion as will increasing the TCA film thickness.

Figure 3.19 also shows the PSA absorbance as a function of increasing film thickness at 530nm. It can clearly be seen that PSA has almost no absorption at 530nm, with A<0.003 even when the dry film height is increased from 15-105μm.

The linear relationship of absorbance of the TCA shown by the data in Figure 3.19 can be described by the relationship shown in Equation 3.6.

$$A = \varepsilon C_w \phi \qquad \text{(Eq 3.6)}$$

Where ε a constant, C_w is the film thickness and ϕ is the volume fraction of PEDOT:PSS in the dry TCA film.

This is a similar relationship to the Beer-Lambert law used to relate the absorbance of light to the properties of a material through which the light is travelling [19] shown by Equation 3.7.

$$A = \varepsilon bc \qquad \text{(Eq 3.7)}$$

Where ε is the molar absorptivity, **b** is the path length and **c** is the concentration.

A can be linked to Transmission, **T**, by equation 3.8

$$A = 2 - \log_{10} \%T \qquad \text{(Eq 3.8)}$$

This is not unexpected since the PEDOT:PSS phases in a polymer of high transparency in the visible region (PSA) can be thought of as a solution. The path length is then proportional to the film thickness and the concentration of the volume fraction of the

PEDOT:PSS in the TCA. It is useful to know this relationship when considering the application of this TCA as the absorbance for a desired TCA thickness and PEDOT:PSS volume fraction could be predicted without the need for trials and measurement. One thing to bear in mind is that the Beer lambert law does not hold true for samples of high concentration, due to the fact that molecules in close proximity will have electrostatic interactions changing the absorptivity coefficient [20], and would need to be considered for TCAs with a higher volume fraction of PEDOT:PSS

3.2.7. The relationship between Conductivity, Tack and Absorbance

As has been shown in the previous sections of this chapter the various properties of conductivity, tack and absorbance follow trends relating to the film thickness (coating weight) and PEDOT:PSS volume fraction in the dried TCA film and therefore their values can be predicted. Being able to predict properties of the TCA is important for commercial applications of the TCA for three reasons:

- If a specific TCA property is required e.g. conductivity, the coating weight and volume fraction that would give this value can be selected avoiding experimental trials.
- The predicted values can act as a benchmark such that if a TCA is fabricated and the values differ from those predicted it may indicate an issue with the processing, deposition or curing of the TCA.
- The trends observed here are inherent and indicative to the mechanisms of how this mix of TCA conducts, absorb light and adhere. If different trends were observed for different blends of conducting phase and adhesive this may quickly indicate they conducting/adhering/absorbing light through different mechanisms which may lead to the discovery and development of TCA mix with more desirable properties.

As has been shown in the previous sections of this chapter the properties of conductivity, tack and absorbance are influenced by the ϕ of PEDOT:PSS in the dry film and the dry film height by Equations 3.1 and 3.2 for conductivity, Equation 3.3 for tack and

Equation 3.6 for absorbance. Table 3.5 summarises how (within the range investigated here) the PEDOT:PSS and dry film height affect the three variables.

Table 3.5. Increase (up arrow) or decrease (down arrow) in conductivity, tack and absorbance of a TCA film with either increasing PEDOT:PSS ϕ or dry film thickness.

	Conductivity	Tack	Absorbance
Increase in PEDOT:PSS ϕ	↑	↓	↑
Increase in Dry film Thickness	↓	↑	↑

The three properties and two variables can be linked and summarised by Equation 3.9.

$$G_{film}(\phi) = f\frac{A\phi}{Tack\ Cw} \qquad \text{(Eq 3.9)}$$

Equation 3.9 shows that there is a relationship between the properties and the variables of the TCA, ultimate performance of the TCA will always be a trade-off between the three parameters and optimisation will depend upon which is the crucial factor desired. However this relationship will only hold true for a TCA made within this range and these thicknesses as at higher ϕ and increased or decreased thicknesses the relationships will vary.

3.2.8. The Stability of a PEDOT:PSS and Acrylic Emulsion TCA

Opto-electric devices that this TCA may be incorporated into such as s-DSC may require lifetimes of up to 25 years and therefore the stability of the TCA over a long period is critical to device performance. While not rigorous standardised testing the stability of the TCA and influence on the conductivity over a period was investigated using samples that had been left uncovered in ambient conditions in the dark for 5750 hrs. It has been shown previously that silver contacts (as used in this investigation) are stable in contact with PEDOT:PSS and therefore should not contribute to any changes observed[21]. Figure 3.20

shows the change in conductivity of 0.00125 ϕ PEDOT:PSS samples at different dry film thickness over 5750 hrs in ambient air, what can be seen is that the conductivity actually increases for all samples. Since it is know that both PEDOT:PSS and PSAs are [18,22], it is possible that water in the TCA matrix due to ambient absorption will provide additional pathways of conduction and marginally increase conductivity.

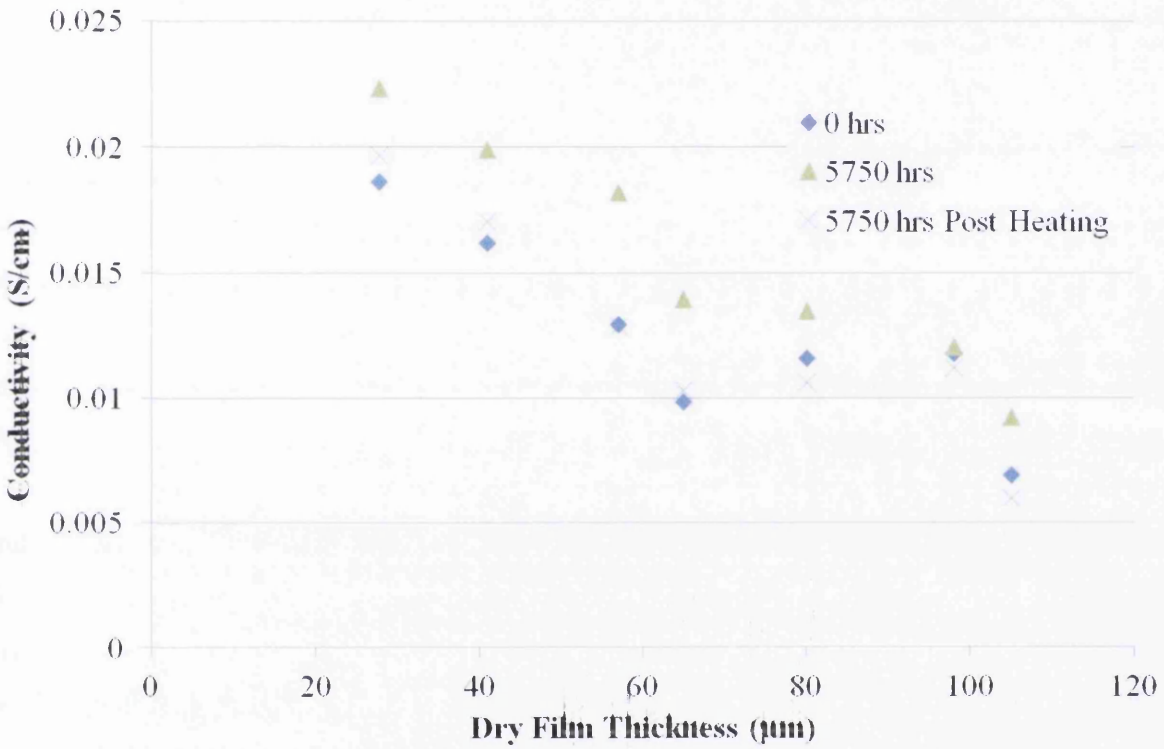

Figure 3.20. Change in conductivity of 1.25% PEDOT:PSS TCA samples of differing heights post manufacture, after an additional 5750hrs under ambient conditions in the dark and after a subsequent 30 minute 120°C heating step. Average of 3 samples and 4 repeat measurements per data point.

In order to test this influence, the aged films were subsequently heated at 120°C for 30minutes to remove the absorbed water. The samples conductivity subsequently reduced to near the original conductivity. This is a significant finding as it demonstrates that water ingress does occur in the TCA and that it has an influence on conductivity. The original conductivity of the TCA can be recovered upon removal of the water with heating. Further work is now needed to test the stability under other conditions such as increased humidity and UV exposure for extended periods of time.

3.2.9. Quantifying the Contact Resistance of a TCA with Respect to Conductivity and Tack

While the bulk conductivity is a good metric for quantifying the conductivity of the TCA another important factor to consider is the contact resistance that may exist between a TCA and a opto-electric device. That is, the resistance that occurs at the interface of the two layers. Such devices will have an inherent series resistance and the contact resistance between TCA and the other active layers will contribute to this series resistance (as will the contact resistance between the surface it is adhering to and any underlying material) and too high a series resistance can limit how well the device can perform. Therefore quantifying how the contact resistance behaves with respect to PEDOT:PSS ϕ and film thickness is important for device optimisation. The contact resistance was measured by depositing the TCA onto increasingly spaced strips of Ag and measuring the voltage between the strips under constant load and extrapolating the data to the y-intercept, this is then used for calculating the contact resistance as explained in Section 2.7.1

The interaction of the TCA with the surface of the silver contacts will be complex and consist of many factors that affect the contact resistance. Two significant factors are the number of contact sites and the tackiness of the film. The amount of contact sites was investigated by varying the volume fraction (ϕ) of PEDOT:PSS which will increase its area on the surface of the TCA (results shown in Table 3.6 and Figure 3.21).

Table 3.6. Measured values of resistance at varying distance for different ϕ PEDOT:PSS in dried TCA films, the Y intercept from a graph of distance vs resistance and the specific contact resistivity.

ϕ PEDOT:PSS in dry film		Ag Line Spacing 0.5 cm	1.5 cm	3 cm	5.5 cm	Y intercept	Contact resistance (Ohms.cm^2)
0.0085	Average (ohms)	400000	500000	700000	1000000	150000	37500
	StDev (ohms)	4400	9600	13000	20000		
0.0090	Average (ohms)	89000	150000	220000	700000	31656	7914
	StDev (ohms)	1500.00	2800.00	3900.00	15000.00		
0.0100	Average (ohms)	10000	90000	130000	190000	17577	4394
	StDev (ohms)	190	1800	2500	4000		
0.0125	Average (ohms)	2900	6100	11000	18000	1571	392
	StDev (ohms)	29	120	250	400		
0.0150	Average (ohms)	1200	2100	3300	4900	948	237
	StDev (ohms)	22	40	58	98		
0.0175	Average (ohms)	900	1100	5200	6800	104	26
	StDev (ohms)	21	21	110	150		

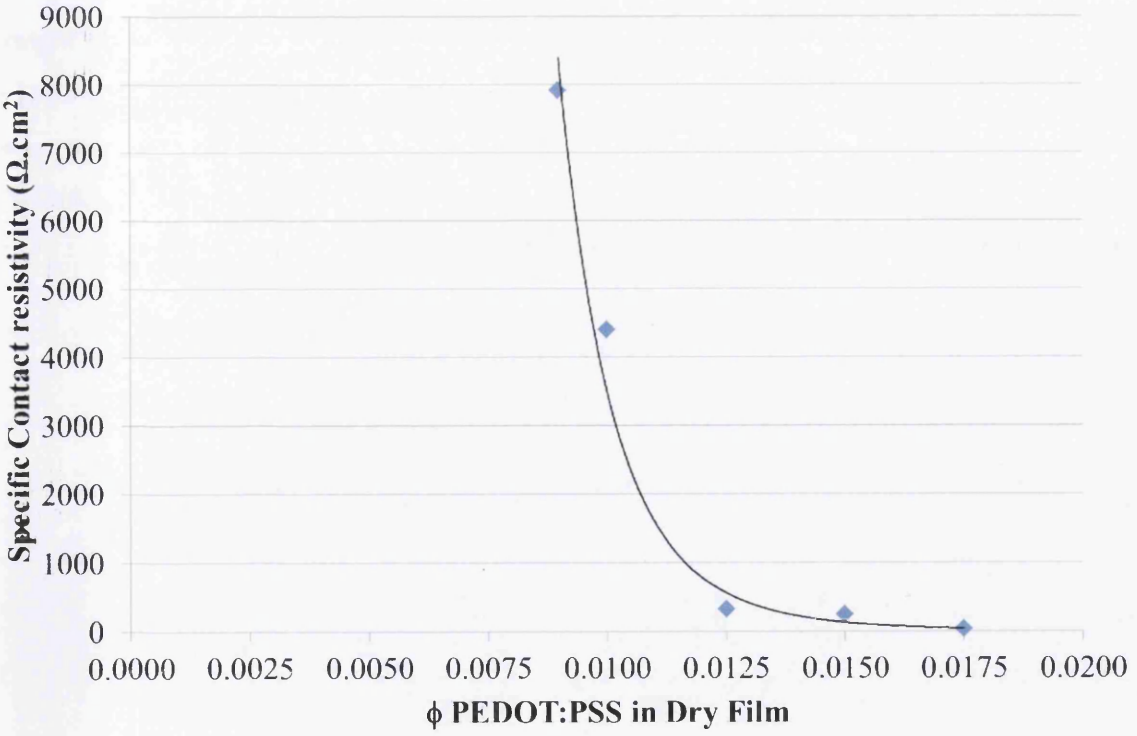

Figure 3.21. Change in contact resistance with a change in ϕ PEDOT:PSS a dry film TCA

It can be seen from Figure 3.21 and Table 3.6 that when the contact resistance from each TCA sample is plotted against the ϕ PEDOT:PSS within the dry films the contact resistance decreases from 7.9 $k\Omega.cm^2$ at 0.0090 ϕ to only 26 $\Omega.cm^2$ at 0.0175 ϕ according to a power law function. The 0.0200 ϕ sample was not included in Figure 3.21 as the tack was not sufficient enough to make a constant contact once pressure was removed, making the contact resistance impossible to measure.

This is in accordance with the result found for the bulk conductivity in Section 3.2.2 that the PEDOT:PSS on the surface is indicative of the PEDOT:PSS contained within the film and that the total amount of PEDOT:PSS on the surface is critical to the contact resistance.

While the adhesive portion of the surface doesn't contribute directly to electrical conduction it does provide an adhesive force between the films which will keep the PEDOT:PSS regions in contact with the film even when pressure is removed. The data in Table 3.7 and the graph in Figure 3.22 shows how the contact resistance changes when the tack of the TCA increases (shown by a decrease in the RBT value) (a change in tack is brought about through varying film thickness, as shown in Section 3.2.5, for the 0.0125 ϕ PEDOT:PSS). The TCA with a dry film thickness of 15µm could not be included in this data set as the films did not remain in contact when the pressure was removed as a result of insufficient tack, the same as in Figure 3.21

Table 3.7. Measured values of resistance at varying distance for a 0.0125 ϕ PEDOT:PSS in dried TCA film at different dry film heights, the Y intercept from a graph of distance vs resistance and contact resistance of a 0.5 x 1 cm area. Average of 3 samples with 3 repeat measurements per data point.

Dry film height (μm)	Tack (cm)		Ag Line Spacing 0.5 cm	1.5 cm	3 cm	5.5 cm	Y intercept	Contact resistance (Ohms.cm^2)
28	22	Average (ohms)	61000	68000	72000	-	59895	1497
		StDev (ohms)	84	76	120	-		
41	16	Average (ohms)	3250	7050	12800	-	1331	332
		StDev (ohms)	40	100	170	-		
57	14	Average (ohms)	2900	6100	11000	-	1263	315
		StDev (ohms)	45	88	120	-		
65	13	Average (ohms)	2000	5200	10500	15550	1181	295
		StDev (ohms)	36	100	180	158.6735		
80	10	Average (ohms)	1350	3900	5650	10300	836	209
		StDev (ohms)	19	57	88	130		
98	7	Average (ohms)	1100	3400	5800	-	771	192
		StDev (ohms)	14	40	59	-		

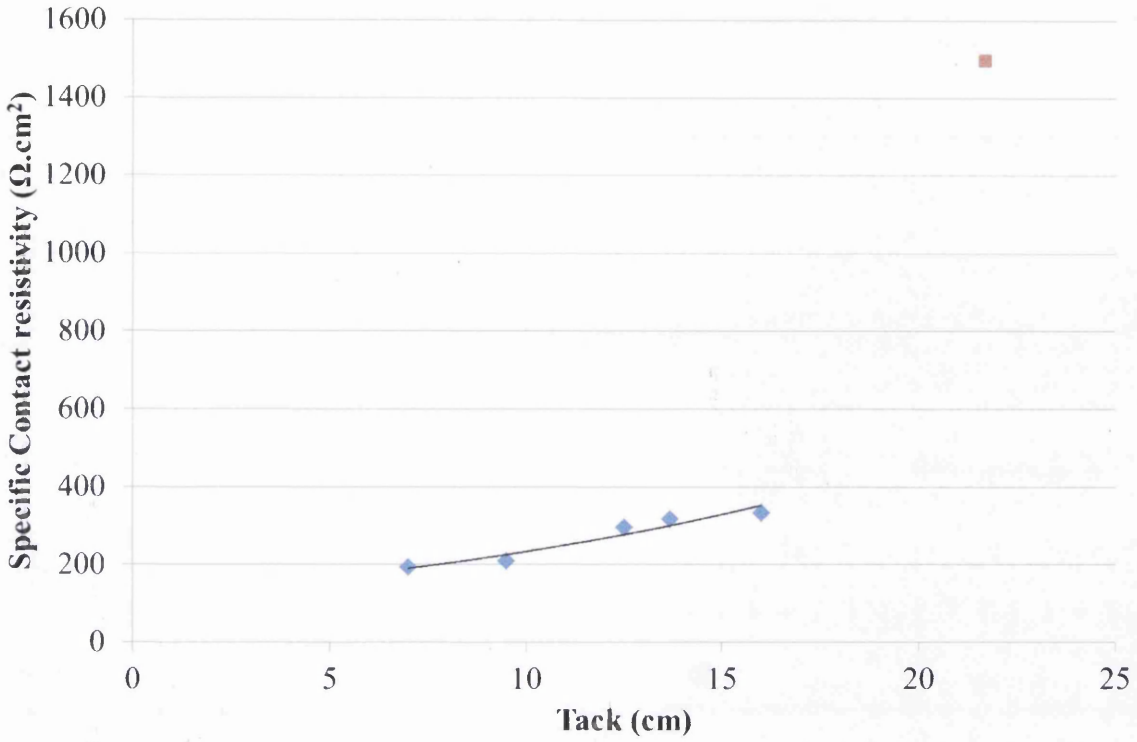

Figure 3.22. Change in contact resistance as the tack of 0.0125 ϕ PEDOT:PSS TCA is varied. A sample with a Tack of 22cm is shown but not included on the graph for reference but not included in the trend line analysis

The TCA with a 28µm dry film height and Rolling Ball Tack value of 22cm has been shown on the graph however it has not been included in the trend line analysis as the tack was not sufficient enough to cause contact between the whole area of the contact strips meaning the comparison between this data point and the rest in the set was not valid. However, it has been included in order to illustrate that the tack within the film must be sufficient in order to make permanent contact with the whole area of the film once pressure is removed, otherwise large areas of the TCA may not be in contact with the active layers leading to sub-optimal connectivity. While this has not been explicitly researched within this scope of this work, it can be said that the critical point must lie somewhere between tack values of 21.74 - 22.73cm for this TCA and ϕ PEDOT:PSS and this would differ for alternative ϕ PEDOT:PSS and PSA combinations.. The trend for the remaining values can be seen to exponentially decrease from 295Ω to 192Ω as the tack increased from 22.73 to 7.14cm.

This illustrates that the tack of the film is important not only to establish and maintain a pressure free contact but also that the contact resistance decreases as the tack increases.

While it is true that the tack (not just ϕ) also changes for the data shown in Figure 3.21 the reason for the decreased contact resistance cannot be attributed to the tack (as in Figure 3.22). This is because the effect is the opposite, as shown in Figure 3.23. As the tack increases the contact resistance increases although the trend is not so clearly defined for this data. This shows that while the tack will have an influence on the contact resistance when changing the ϕ of the PEDOT:PSS, the dominant factor will be the amount of surface sites of PEDOT:PSS and shows that bulk conductivity will be indicative of contact resistance.

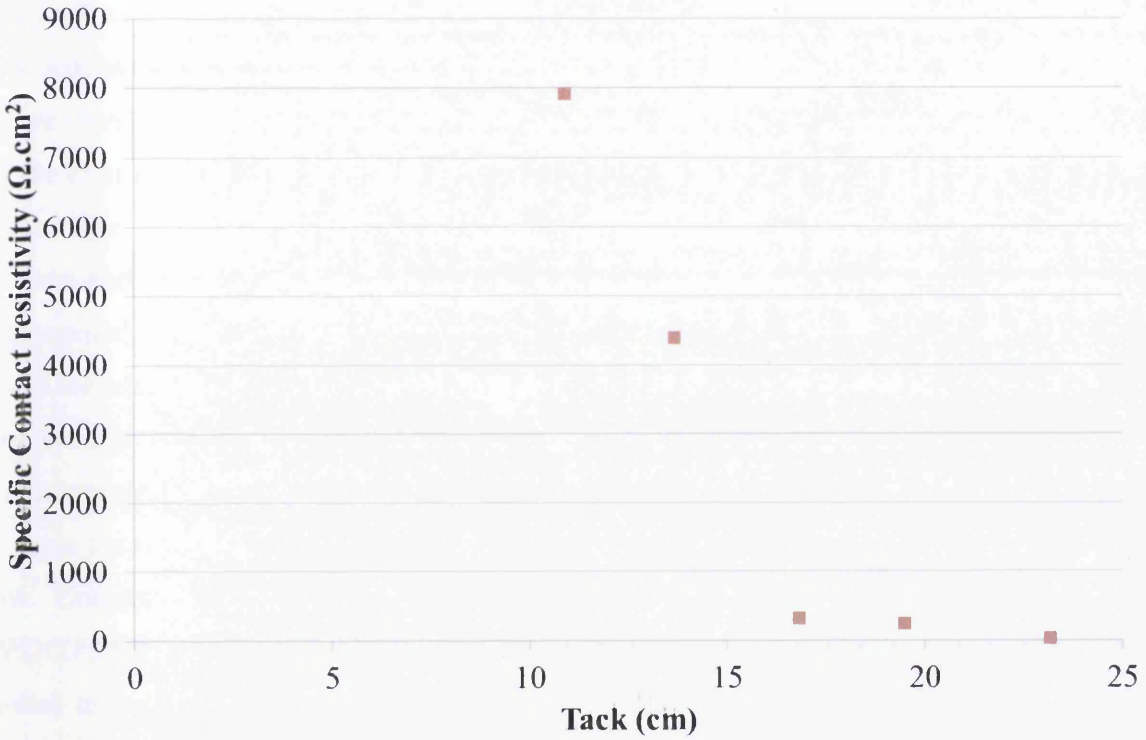

Figure 3.23. The change in contact resistance with decrease in tack (increase in rolling ball tack value) caused varying the ϕ of PEDOT:PSS is changed within a TCA film.

However this is only true down to a crucial ϕ threshold whereby the tack becomes so low (through a combination of reduced film height and decreased amount of non-adhesive material at the surface) that the film no longer makes adhesive contact and the contact resistance essentially goes to infinity. This is true for the previously mentioned 0.0200 ϕ PEDOT:PSS sample which would not make adhesive contact once pressure was removed as its tack lay below the critical threshold.

3.3. Conclusions

A dual phase polymer has been presented in which the two main constituents are PEDOT:PSS and an acrylic emulsion pressure sensitive adhesive. This enables the key properties of both polymers to be combined in the film rendering it conductive and adhesive. When the volume fraction of the PEDOT:PSS is increased the film behaved according to percolation theory where a critical percolation threshold can be defined followed by a power law increase in conductivity. However the very low volume fraction at which this threshold is reached indicates that the geometry of the PEDOT:PSS phases are not discreet spheres but rather elongated structures with a high aspect ratio. When the PEDOT:PSS volume fraction of the film is kept constant and the height varied the conductivity actually decreases due to anisotropic conductivity within the film, indicating that the PEDOT:PSS phases are elongated in the x and y axis rather than the z. The adhesive nature of the films can be categorised by an exponential increase as the film thickness increases. The volume fraction of PEDOT:PSS in the films also plays a role in the adhesive nature as a film of a given height with a higher volume fraction of PEDOT:PSS has less tack than one with a lower volume fraction. The transparency as a function of PEDOT:PSS within the final film is linear within the low volume fraction region following a similar relationship to one described by the Beer-Lambert law. Contact resistance is linked to tack and conductivity with the volume fraction of PEDOT:PSS within the film having a large influence on the contact resistivity, which is linked to bulk conductivity. It was shown that the TCA films were stable over 5000hrs in ambient conditions, with water ingression being the only issue.

This material has been named a Transparent Conductive Adhesive and has applications within a wide range of plastic electronics especially where contact is needed with temperature and moisture sensitive layers. This includes hybrid organic photovoltaics (HOPV), organic photovoltaics (OPV) organic light-emitting diodes (OLED), and Electroluminescent (EL). It also has potential as a replacement for lead solder in electronic contacts within organic circuits.

3.4. References

[1] B. Hardin, W. Gaynor, I-K. Ding, S. Rim, P. Peumans, M. McGehee, *Org. Electron.*, **12,** 875, (2011).

[2] lamination. (n.d.) *Collins English Dictionary – Complete and Unabridged.* (2003).

[3] http://pc.dupont.com/dpc/en/US/html/visitor/s/trouble/PDSG_Home.html

[4] Building and Construction Authority, *6. Common Defects,* (2010)

[5] I. Benedek, M. Feldstein, *Technology of Pressure-Sensitive Adhesives and Products*, CRC Press Taylor & Francis Group, (2009)

[6] M. Sahimi, *Applications of Percolation Theory,* Taylor and Francis, (1994).

[7] M.J. Powell, *Phys. Rev. B*, **20,** 4194, (1979).

[8] A. Hopkins and J. Reynolds, *Macromol.,* **33,** 5221, (2000).

[9] A. Madaria, A. Kumar, F. Ishikawa, C. Zhou, *Nano. Res.,* **3,** 564, (2010).

[10] G. Pike, C. Seager, *I. Phys. Rev. B.,* **10,** 1421, (1974).

[11] I. Benedeck, *Developments in pressure-sensitive products,* Taylor & Francis, New York (2006).

[12] D. Stauffer, *Introduction to Percolation Theory,* Taylor & Francis, (1985).

[13] H. Randriamahazaka, F. Vidal, P. Dassonville, C. Chevrot, D. Teyssie, *Synth. Met.*, **128,** 197, (2002).

[14] M. Åkerfeldt, M. Strååt, P. Walkenström, *Text. Res. J.,* **83**(6), 618, (2013).

[15] T. Takano, H. Masunaga, A. Fujiwara, H. Okuzaki, T. Sasaki, *Macromol.*, **45**(9), 3859, (2012).

[16] A. Nardes, M. Kemerink, R. Janssen, J. Bastiaansen, N. Kiggen, B. Langeveld, A. van Breeman, M. de Kok, *Adv. Mater.,* **19**(9), 1196, (2007).

[17] A. Nardes, M. Kemerink, R. Janssen, *Phys. Rev. B.* **76,** 0085208/1, (2007).

[18] A.Elschner, *PEDOT principles and applications of an intrinsically conductive polymer*, CRC Press, (2011).

[19] J. Ingle, S. Crouch, *Spectrochemical Analysis*, Prentice Hall New Jersey, (1988).

[20] D. Skoog, D. West, F. Holler, S. Crouch, *Fundamentals of Analytical Chemistry 8th Ed.*, Cengage Learning, (2003).

[21] A. Elschner, H.C. Starck Clevious GmbH, *Unpublished Result,* (2008).

[22] Y-Y. Lu, M. Crandell, R. Koppes. U.S. patent 6,048,611 (2000).

4. Selection, optimisation and processing of PEDOT:PSS as an interlayer for lateral conductivity in a s-DSC

4.1. Introduction

At present s-DSC is currently produced exclusively on glass. The counter electrode usually consists of an opaque layer of evaporated silver or gold which provides excellent contact to the Spiro-OMeTAD layer as well as good lateral conduction for charge extraction and mirror like properties of light reflection [1], see Figure 4.1.

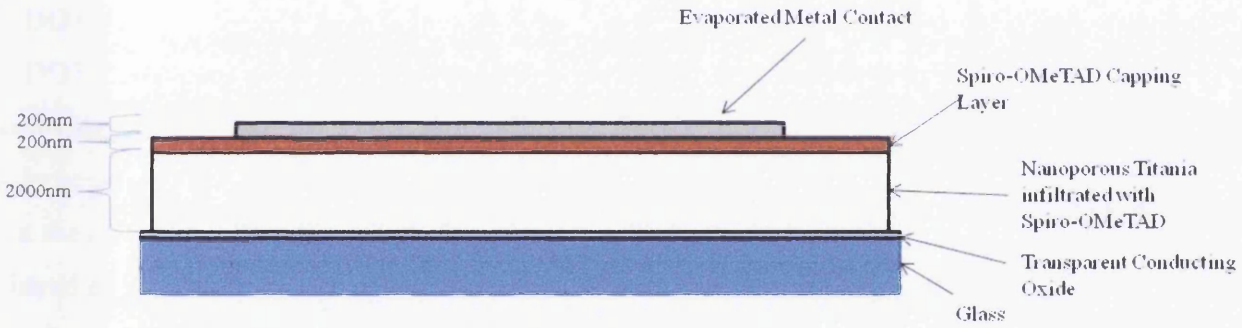

Figure 4.1: Schematic cross section of a conventional s-DSC made on glass with an evaporated silver contact.

This configuration is acceptable when the cell substrate is glass as illumination can enter the cell from the working electrode side, however, when the substrate of the cell is metal, illumination comes from the counter electrode side and the opaque silver will allow no light transmission into the cell. Attempts have been made at developing a counter electrode for cells on metal using a thin layer of gold (25nm) such that light transmission of 90% can be achieved [2]. Whilst this enables cells with efficiencies of 1.8% at 0.16cm^2, gold at this thickness has poor lateral conductivity leading to poor charge extraction and the efficiency drops to 0.05% when the cell size is increased to 1cm^2 [3]. An additional disadvantage is that it still involves a relatively slow and costly vacuum process and gold is inherently expensive.

Developing an alternative to thin gold is a necessary requirement for large scale roll to roll processing of S-DSC.

As was seen in Chapter 3 the TCA only has certain sites on the surface where current collection occurs (PEDOT:PSS locations on the surface of the TCA) and since Spiro-OMeTAD only has a low conductivity ($2.0x10^{-5}$ S cm^{-1}) it will provide little lateral conduction. Therefore a material with higher conductivity is needed to aid current collection. A PEDOT:PSS interlayer appears to be a viable alternative in this case, it provides a combination of transparency, lateral conductivity and easy processing. However PEDOT:PSS in its current commercial formulation is not without its challenges. In Section 1.4.1 it was seen that the main constituents of PEDOT:PSS solutions are PEDOT, PSS, solvents (usually water and/or propylene glycol) high boiling point solvents (such as ethylene glycol and dimethyl sulfoxide). The last of these two provide potential problems when used in s-DSC. It was found that PEDOT:PSS when applied directly caused the Spiro-OMeTAD to de-laminate from whatever substrate it may be adhered to. In this current scenario water in the PEDOT:PSS causes the Spiro-OMeTAD to de-laminate from the mesoporous titania. PEDOT:PSS is then exposed to the titania forming a shunting pathway (in addition to removing the dye from the surface of the titania). To avoid Spiro-OMeTAD delamination orthogonal solvents such as ethanol and IPA were used in sufficient quantities with the water that the de-lamination effect is negligible. PEDOT:PSS itself does not readily mix with either ethanol or IPA therefore the objective is to find a combination of solvents that will lead to a consistent film with maximum conductivity that will provide minimal de-lamination.

In addition to delamination a further problem is that the high-boiling point solvents within the PEDOT:PSS solution need to be removed at temperatures of approximately 120°C [4]. At temperatures around 120°C Spiro-OMeTAD with additives (LiTFSI and tBP) was found to begin to crystallise and this change from an amorphous state could lead to a reduction in its intimate contact with the dye [5]. Therefore an alternative heating process (to achieve 120°C) was needed. Two methods are proposed; forced evaporation and light (NIR) curing (Chapter 5). In evaporation the kinetic energy of particles based near the surface of a liquid can overcome intermolecular forces and can escape leading to a vaporisation of a liquid at a temperature below its boiling point [6]. The rate of evaporation of PEDOT:PSS solutions under ambient conditions is far too slow and therefore the rate needs to be increased, hence the term "forced evaporation". If we assume pressure, intermolecular forces, density of the liquid and the surface area needed to evaporate are all fixed in our scenario then the other factors that affect the rate of evaporation are concentration of substance in the

air, flow rate of air over the surface and temperature. The first two of these are closely linked, a high flow rate of air in an open system will reduce the concentration of the vaporised high-boiling point solvents at the surface, decreasing the boundary layer and increasing the rate of evaporation [6]. Temperature is proportional to kinetic energy and therefore the higher the temperature the faster the rate of evaporation. Therefore a system with a high flow rate of hot air has been proposed for an increased rate of removal of the high-boiling point solvents at a temperature below the crystallisation point of Spiro-OMeTAD.

It is also worth noting that while the work in this chapter has been done so a TCA can be used with s-DSCs it can also be applied to the use of printed grid as contacts on opto-electronic devices.

To summarise this chapter sets out to:

a) Be able to apply a PEDOT:PSS interlayer on top of a s-DSC containing Spiro-OMeTAD so that a conductive pathway can be found between conducting phases when a TCA is applied to such a cell.
b) Find a combination of solvents and ratios that inhibit Spiro-OMeTAD delamination long enough for all the solvents to be removed from the PEDOT:PSS whilst maintaining layer conductivity
c) Develop and test a high flow rate hot air system for forced air evaporation of a wet PEDOT:PSS film at temperatures below 100°C

4.2. Experimental Procedures

Film preparation and conductivity testing of PEDOT:PSS at various dilutions was carried out as described in Section 2.2 whereby PEDOT:PSS was mixed with varying amounts of ethanol and IPA such that the amount of each was denoted by (PEDOT:PSS):ethanol:IPA e.g. 1:1:1 indicated 1 parts PEDOT:PSS solution 1 part ethanol 1 part IPA by volume. To measure the conductivity of the PEDOT:PSS films once dry, films had 4 1-mm wide line contacts at 1.5mm separation sputtered onto the surface using a Quorum 150T as electrical contacts and their conductivity measured in the same way as described in Section 2.7.1.

Samples to be oven cured were heated to 120°C in a convection oven for 5 minutes and samples to be cured by evaporation were held under a hot air dryer as detailed in section 2.2.1 measure the resistance change shown in figure 2.3.

4.3. Results and Discussion

4.3.1. Selecting an appropriate PEDOT:PSS for incorporation as an interlayer s-DSC

Due to the versatility of the PEDOT a wide range of solutions and formulations containing PEDOT (commonly with the anion PSS) can be made. Some formulations are low conductivity to stop static charge building, some for hole injection and some for lateral electric conductivity. The latter has increased conductivity over the other types of PEDOT, usually in the 10-900 S/cm. For this work a lateral conductivity of at least 40 S/cm has been deemed the minimum conductivity due to the conductivity of other materials used in the DSC stack as outlined in Section 1.12. Many different types of PEDOT were obtained and the standard oven cure applied to see which PEDOTs showed the necessary conductivity, displayed in Table 4.1.

Table 4.1: The various properties of selected PEDOT containing solutions

Manufacturer	Type	Label	PEDOT Content (vol%)	Conductivity Enhancer	Conductivity (S/cm)
AGFA	PEDOT:PSS in H_2O	A054	0.54%	Diethylene Glycol	0.1
AGFA	PEDOT:PSS in H_2O	A130	1.30%	Diethylene Glycol	1.9
AGFA	Neutral PEDOT:PSS	AN11	1.10%	Diethylene Glycol	0.09
TDA	Lauryl Terminated PEDOT:PEG	TLT	0.80%	P-toluenesulfonate (dopant)	31.75
Heuraeus	PEDOT:PSS high conductivity grade	HHC	1.3%	Dimethyl Sulfoxide	850
AGFA	PEDOT:PSS with 70% propylene glycol for screen printing	ASP	0.80%	Diethylene Glycol	80

From Table 4.1 above it can clearly be seen that the Heraeus HHC and the AGFA ASP are the two with the highest conductivity, showing a significant increase from the AGFA A054 PEDOT:PSS. The AGFA ASP PEDOT:PSS (Agfa EL-P3145 ASP) has a large amount of its water replaced with propylene glycol to increase its viscosity enabling it to be easily bar cast and unlike all water based PEDOT:PSS'. Therefore due ease of processing it was selected for further experimentation over the Heuraeus HHC, despite the HHC having a higher conductivity, as processability was deemed a more important factor when considering the scale up of these devices.

4.3.3. Addition of solvents to decrease water and high boiling point solvent content percentage

As explained in Section 3.1 the water and propylene glycol constituents will delaminate Spiro-OMeTAD, which could be detrimental to s-DSC cell performance, whereas ethanol and IPA will not. Therefore, by adding ethanol and IPA into the wet PEDOT:PSS solution the ratio of propylene glycol and water to PEDOT:PSS is decreased, the amount that water and propylene glycol will be in contact with the Spiro-OMeTAD decreases and the overall delamination will decrease. However the effects of adding ethanol and IPA to the solution in terms of ultimate performance is unknown and could cause the conductivity drop to below 40 S/cm. Also adding ethanol and IPA won't only decrease the water and propylene glycol vol% but it will also reduce the PEDOT:PSS solids vol% content. For reference theoretical solids contents of the solutions once mixed with ethanol and IPA can be seen in table 4.2. While it is true that solutions with higher ethanol and IPA contents will produce thinner films (and therefore be able to carry less electrical load) the bulk conductivity is calculated relative to the film thickness and therefore thickness should not be a major influencing factor, rather, being influenced by the effect the solvents themselves have. To test the influence of solvent additions, ethanol and IPA were added to the PEDOT:PSS as described in Section 2.2, using the notation PEDOT:PSS:Ethanol:IPA ratio, and the effect on conductivity measured. The results of these experiments can be seen in table 4.3 and figure 4.2.

Table 4.2. Theoretical change in solids content as a factor of dilution for PEDOT:PSS

Ratio of PEDOT Solution:Ethanol:IPA	PEDOT:PSS Content in wet solution(%)
Original	0.80
4:1:1	0.53
3:1:1	0.48
2:1:1	0.40
1:1:1	0.27

Table 4.3. Change in height and conductivity of the diluted and original undiluted PEDOT:PSS samples

Ratio of PEDOT Solution:Ethanol:IPA	Dry Film Thickness (μm)	Conductivity (S/cm)	StDev
Original	1006	44.21	5.43
4:1:1	453	63.43	6.32
3:1:1	384	80.34	7.32
2:1:1	354	55.26	8.21
1:1:1	174	47.91	4.35

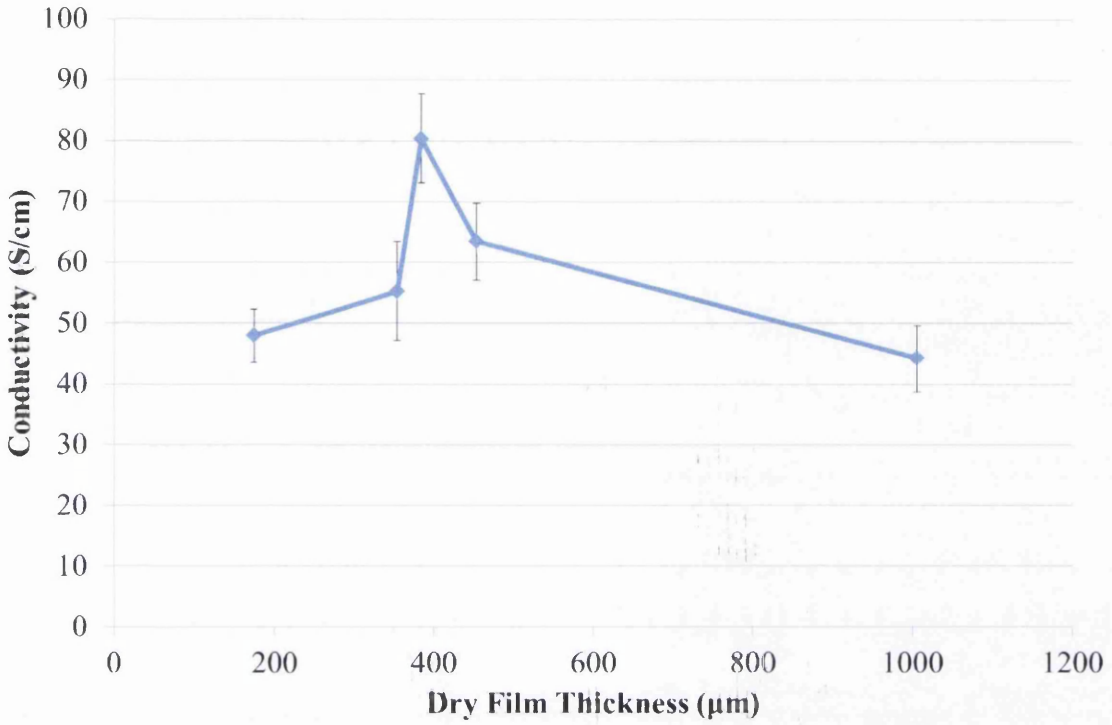

Figure 4.2: Change in conductivity as a function of dry film thickness for diluted PEDOT:PSS.

When looking at the trend and the values for the conductivity seen in Table 4.3 and Figure 4.2 it can be seen that initially there is a rise in conductivity towards the 3:1:1 sample followed by a fall. The height however follows a logical decrease the more dilute the sample. The reason for the rise and fall in conductivity is not initially clear. There are two effects that may have happened: the addition of the solvents altered the size of the PEDOT and PSS phases or it altered their distribution. This leads to three possibilities: firstly since PEDOT shows more solubility for alcohols [7] than the PSS molecule the introduction of ethanol and IPA creates more segregation between the phases leading to larger phases in the final film, increasing conductivity. Secondly, the films become progressively thinner while the current load is kept constant so the conductivity would appear to drop as the films ability to handle the load decreases. Thirdly, since ethanol and IPA will be removed first during curing this may lead to a differing distribution of the phases through the thickness of the film. A combination of all factors is also a possibility.

AFM imaging can be used to determine the phase separation of the PEDOT and PSS in the final film, however the cause for the change in conductivity is not the focus of this

investigation and therefore the work was not undertaken. This work was conducted to investigate whether by adding the solvents ethanol and IPA to the original wet solution of PEDOT:PSS it still behaved as a conductor or more specifically that it maintained its conductivity above 40 S/cm. This was proven as evidence in Figure 4.2.

4.3.4. Forced evaporation for a reduced temperature cure

As outlined in Section 3.1 so as not to damage other constituents in devices utilising PEDOT:PSS, such as s-DSC, by the 120°C cure temperature conventionally used, forced evaporation is proposed as an alternative to convection heating to remove the solvents. To investigate this an experiment was set up as outlined in Section 2.2.1 by taking a sample of wet PEDOT:PSS deposited on two silver contacts (on a microscope slide) and dried under a high flow hot air and the temperature and the resistance measured and logged as a function of time. Figure 4.3 shows the change in resistivity of PEDOT:PSS and how the temperature fluctuates under high flow rate hot air. The graph displays Resistance rather than the resistivity or conductivity as the measuring of film height during curing was beyond the scope of this experiment or indeed not necessary, once dry film thickness can be taken and used in the calculation of the conductivity for comparison between films.

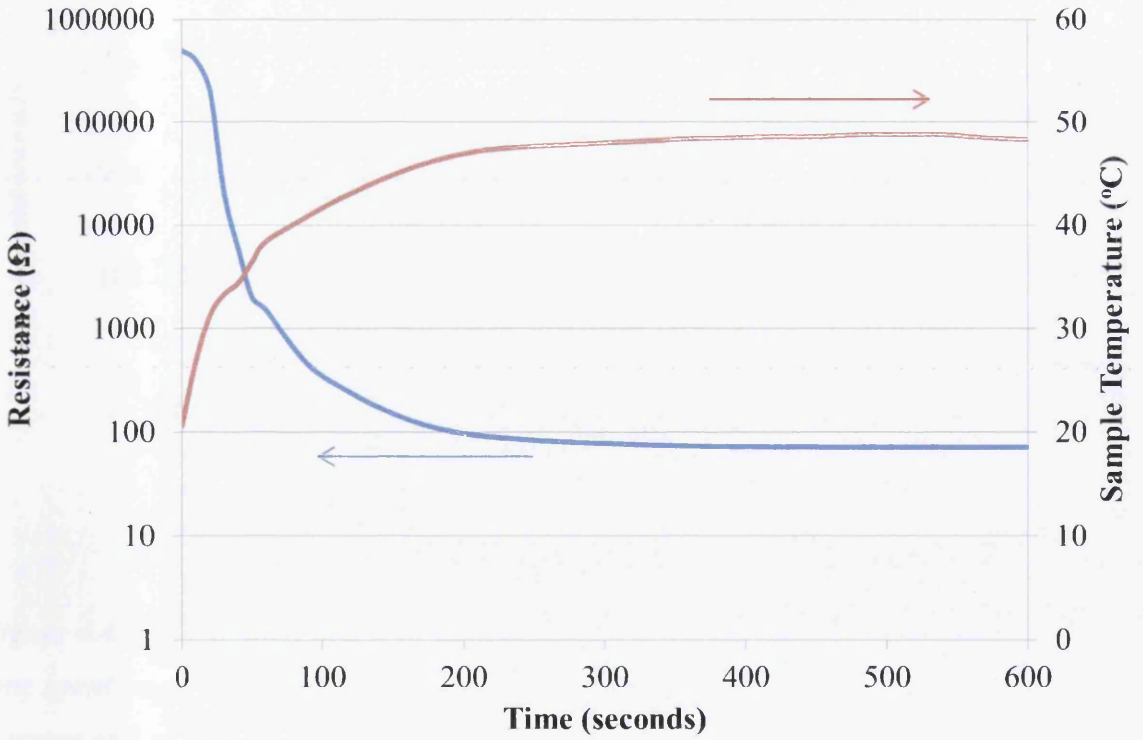

Figure 4.3. Change in Resistance, shown on a log-scale, and temperature as a function of time spent under hot-air drying for PEDOT:PSS. Average of 3 samples per curve.

It can be seen in Figures 4.3 that the resistance initially drops incredibly quickly such that within the first few minutes the PEDOT:PSS is within 10% of its final resistance. When looking at the temperature in Figure 4.3 it can be seen that it increases such that the temperature is 90% of it's maximum within the first few minutes. Two important points can be noted when comparing the temperature of the sample and the resistivity; firstly the rate of decrease in resistivity is proportional to the rate of increase in temperature. Or put another way, the rate of PEDOT:PSS curing is proportional to the rate at which energy is applied to the system (as might be expected). Secondly if the rate at which energy is supplied is increased then the rate of curing would also be increased. This fits in well with the theory of evaporation in that if we increase the rate of flow of air and the temperature the rate of evaporation would increase. To prove the same experiment was conducted (as obtained the data in Figure 4.3) however this time a dryer with a higher air flow rate was used and the results can be seen in Figure 4.4.

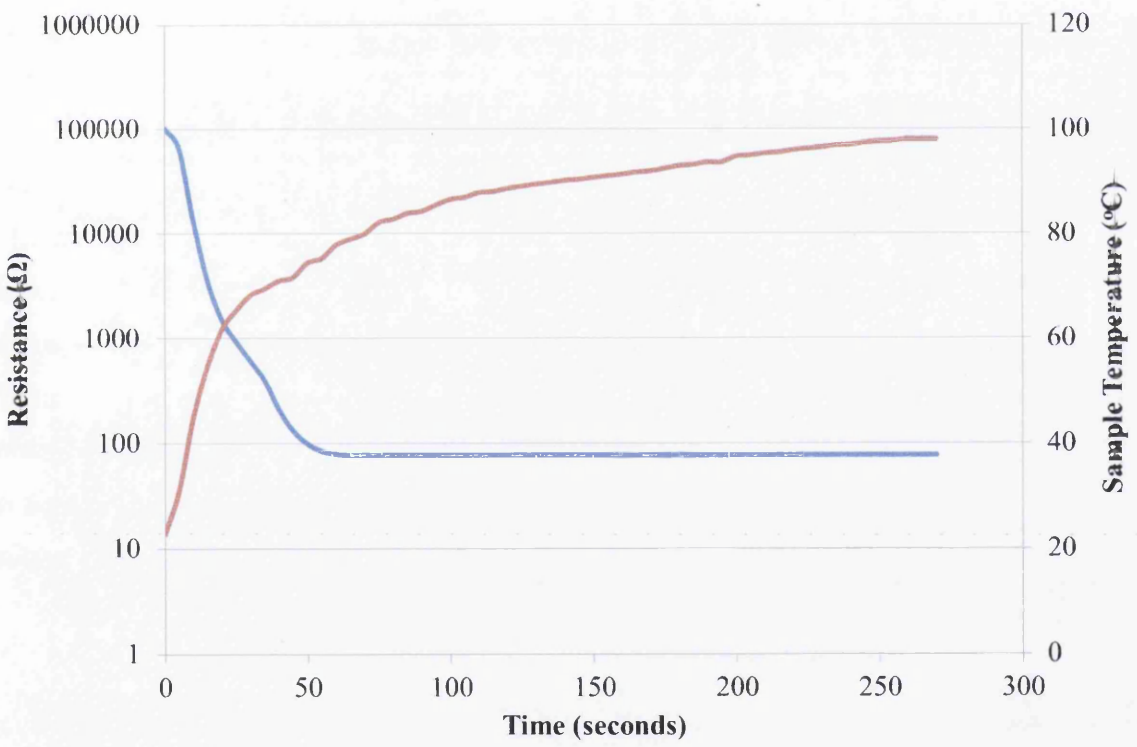

Figure 4.4. Change in Resistance, shown on a log-scale, and temperature as a function of time spent under hot-air dryer with a higher flow rate and temperature for PEDOT:PSS. Average of 3 samples per curve.

It can be seen that the sample in Figure 4.4 reaches its minimum resistance at about 65 seconds whereas the sample in Figure 4.3 was nearer the 570 seconds mark. It is also shown that the sample dried with the higher temperature and air flow reached a higher overall temperature, of 98.1°C compared with 55.3°C for lower airflow and temperature.

Increasing the rate at which this PEDOT:PSS or any other PEDOT:PSS cures has obvious beneficial effects for mass production involving PEDOT:PSS as it would mean line speeds could increase and oven lengths could decrease thereby increasing throughput and decreasing cost respectively. The other objective of curing the PEDOTs by alternative methods is to reduce processing temperatures. It can be seen from Figure 4.3 that the samples do not go above 60°C. Even a sample of metal held under the hot air flow reaches equilibrium at 60°C. Equilibrium is reached when the rate of heat removal from a substrate is equal to the heat being absorbed and can therefore be controlled by the temperature of the air and its flow rate. Increasing this too much will change the equilibrium point, as highlighted by the data presented in Figure 4.4 when air flow and temperature were higher. If it was increased further, while drying would be achieved in less time it could subsequently push the substrate temperature above the desired limit of the Spiro-OMeTAD.

Another way the time to cure could be decreased is by increasing the ratio of lower boiling point solvents content through the addition of ethanol and IPA. As shown in Section 3.3.2 the addition of these even up to a 1:1:1 dilution (PEDOT:PSS solution:ethanol:IPA) still shows a conductivity above 40 S/cm. Ethanol and IPA both have boiling point lower than that of water and propylene glycol and as a result should be removed first. Figure 4.5 shows Thermo Gravimetric Analysis (TGA) derivative results for samples prepared with varying solvent content. It can be seen that for a PEDOT:PSS sample with no solvent addition there is no significant change in weight around 80°C, followed by a continuous removal of mass till around 170°C when the rate of mass being removed slows to a plateau.

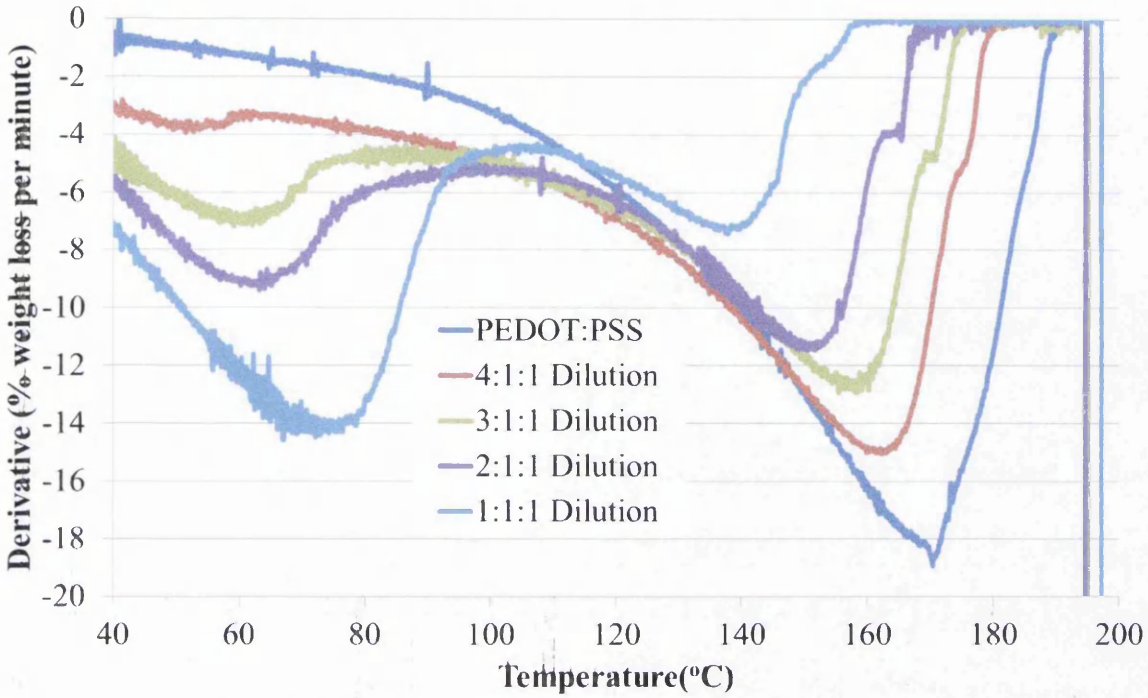

Figure 4.5. Derivative change in weight per minute as a function of temperature for PEDOT:PSS and diluted PEDOT:PSS samples heated at a rate of 10°C a minute.

It can be seen that for the 4:1:1 dilution there is mass being removed at around 80°C which increases for 3:1:1, 2:1:1 and 1:1:1 PEDOT:PSS dilutions. This can clearly be attributed to the increasing IPA and ethanol content. Correspondingly less mass is removed at higher temperatures showing its proportion in the initial solution is less in the dilute solutions. The higher temperature mass removal corresponds to a small amount of water and the majority being propylene glycol. It can be seen that the point at which no more mass is removed (the PEDOT:PSS's dry point) is at increasingly lower temperatures for more diluted samples. This shows that samples containing a higher proportion of solvent can be dried using a lower energy input. Therefore a diluted PEDOT:PSS sample should take less time to dry than a less diluted one if subject to the same evaporation curing conditions.

It can be seen from Figure 4.6 and Figure 4.7 that when increasingly diluted PEDOT:PSS samples were subject to the same evaporation curing conditions to those shown in Figure 4.3 the time until complete cure decreased with increasing dilution, ranging from 280 to 600 seconds for the 1:1:1 dilution and PEDOT:PSS respectively. This shows that faster drying can be achieved by increasing amounts of solvents that are removed at lower temperatures with less energy input such as ethanol and IPA. This occurs because for the

same energy input (high flow rate hot air) the constituents as a whole require less energy to evaporate and therefore drying is achieved sooner.

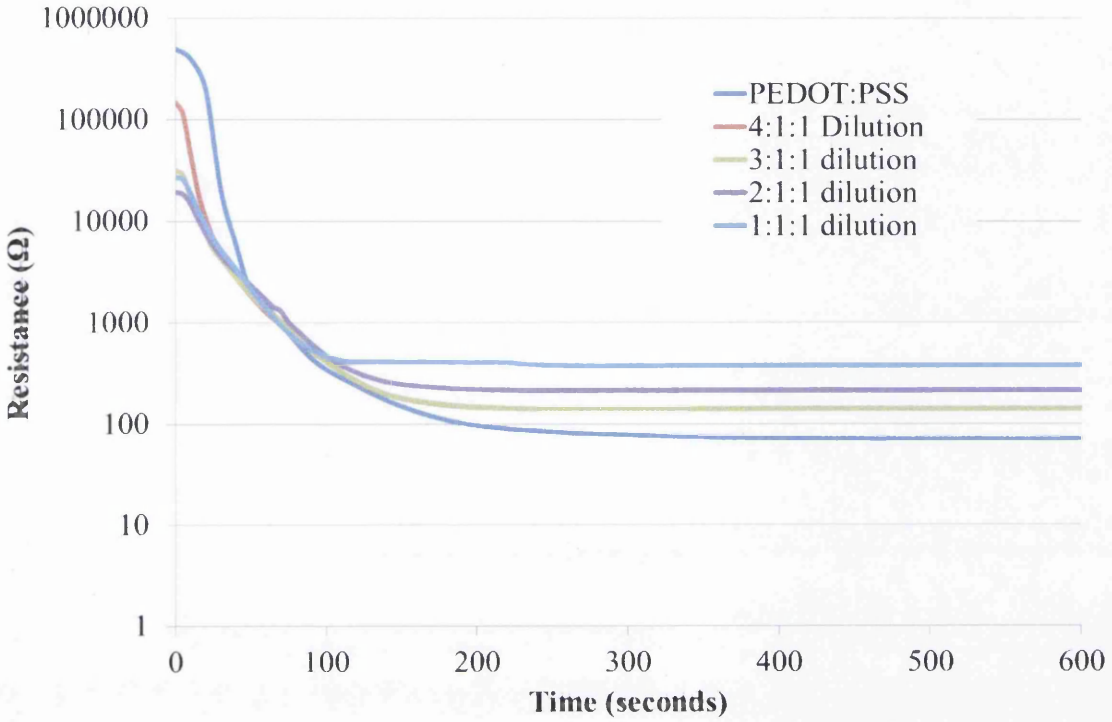

Figure 4.6. Change in Resistance, shown on a log-scale as a function of time spent under hot-air drying for PEDOT:PSS and PEDOT:PSS dilutions. Average of 3 samples per curve.

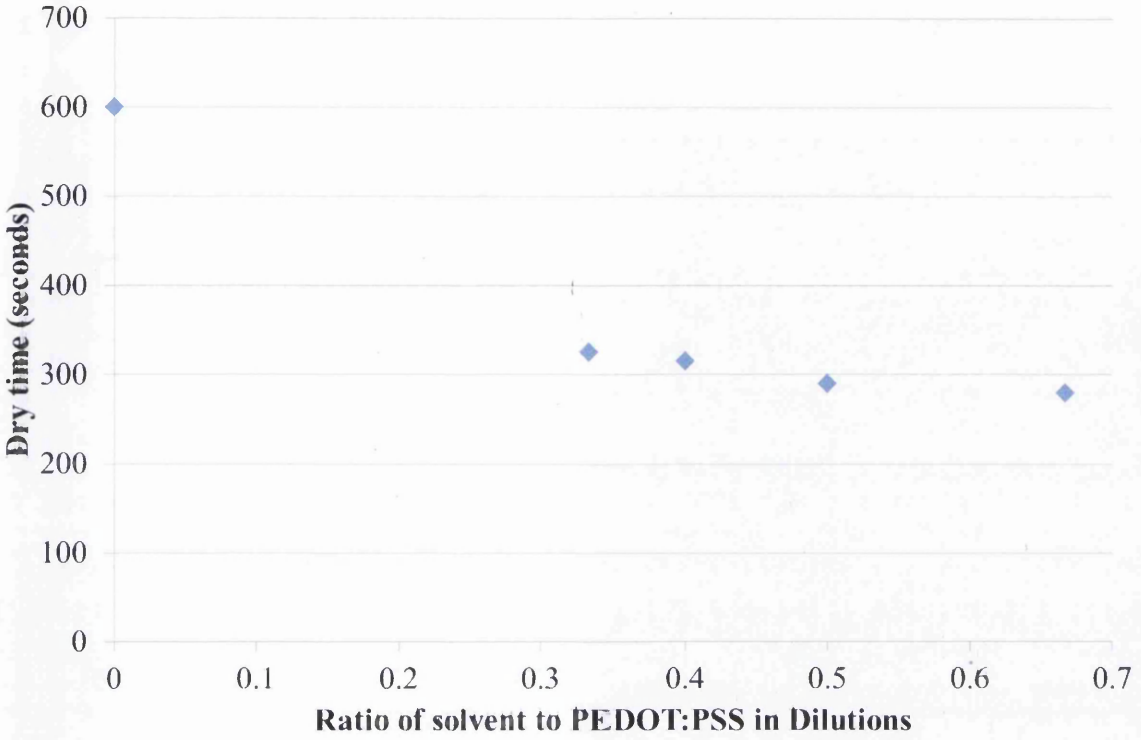

Figure 4.7. Time till dry for PEDOT:PSS and dilutions of PEDOT:PSS dried using hot air drying method from the data presented in Figure 4.6.

When all the solvent is removed the PEDOT and PSS phases will be in their closest proximity possible. As a result this cure point will coincide with the lowest Resistance of the film and where the Resistance plateaus. Once the film is at this point the dry film height can be measured and the conductivity calculated. The calculated conductivities can be seen in Figure 4.8 and for reference the film heights, sample dilutions and conductivities can be seen in Table 4.4. They indicate that when the solvents are added there appears to be no linear trend in conductivity with dilution in ethanol and IPA.

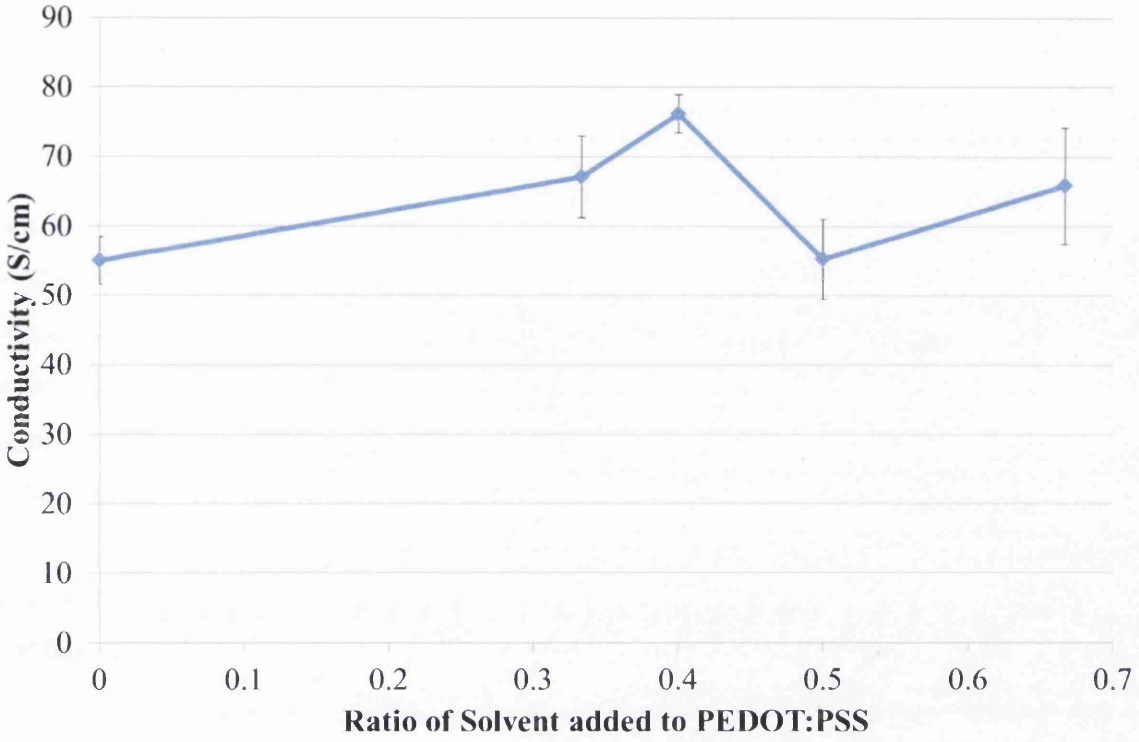

Figure 4.8. Change in conductivity as a function of ratio of PEDOT:PSS to solvent cured for films cured by hot air drying.

Table 4.4. Change in height and conductivity of samples of PEDOT:PSS, and dilutions with ethanol and IPA dried under hot air drying.

Sample	Dry Film Thickness (nm)	Conductivity S/cm	StDev
PEDOT:PSS	936	55.02	3.45
4:1:1	453	62.59	5.87
3:1:1	384	73.74	2.76
2:1:1	337	55.24	5.76
1:1:1	174	61.26	8.34

When the values in Table 4.4 are compared with those in Table 4.3 it can be seen that while this is not an identical measurements the values are at least within the same order of magnitude range. This indicates that the samples cured via this method are similar to those cured in an oven, all conductivities are above 40 S/cm and therefore evaporation curing is an acceptable technique. This is confirmed by results in Table 4.5 which show the variation in the weight of the samples before and after curing and shows that the two are essentially the same, highlighting that all solvent will still be removed by evaporation at temperatures below the boiling points.

Table 4.5. Difference in weight before and after curing of oven and evaporation heating methods for PEDOT:PSS

	Wet PEDOT:PSS weight (g)	**Dry PEDOT:PSS weight (g)**	**Difference between Wet and Dry films (%)**
Oven	0.02170	0.00017	0.78
Evaporation	0.01860	0.00015	0.81

4.3.5. In Situ Determination of PEDOT:PSS Cured point.

In Section 3.3.3 the cure point of the PEDOT:PSS was determined by the point at which the lowest resistance was measured. Determination of the exact cured point is crucial during manufacturing; if the PEDOT:PSS is dried too long energy and time is wasted, if it is not long enough solvent will still be present within the film which will have knock on effects for subsequent layers and final film properties. While the dry/cured point does coincide with it's maximum conductivity, this is measured using a contact method and this may not be suitable for in-situ monitoring when fabricating sensitive devices. Thermal Imaging has the potential to be utilized as a non-contact in-situ measurement to determine the cured/dried point of the PEDOT:PSS by relating it to its emissivity since a material's emissivity can change whether a material is wet or dry[8]. To assess the use of thermal imaging the

PEDOT:PSS was dried using the same setup as the results obtained in Figure 4.3. The experiments were then also filmed with a thermal imaging camera, the data from this filming is shown in Figure 4.9.

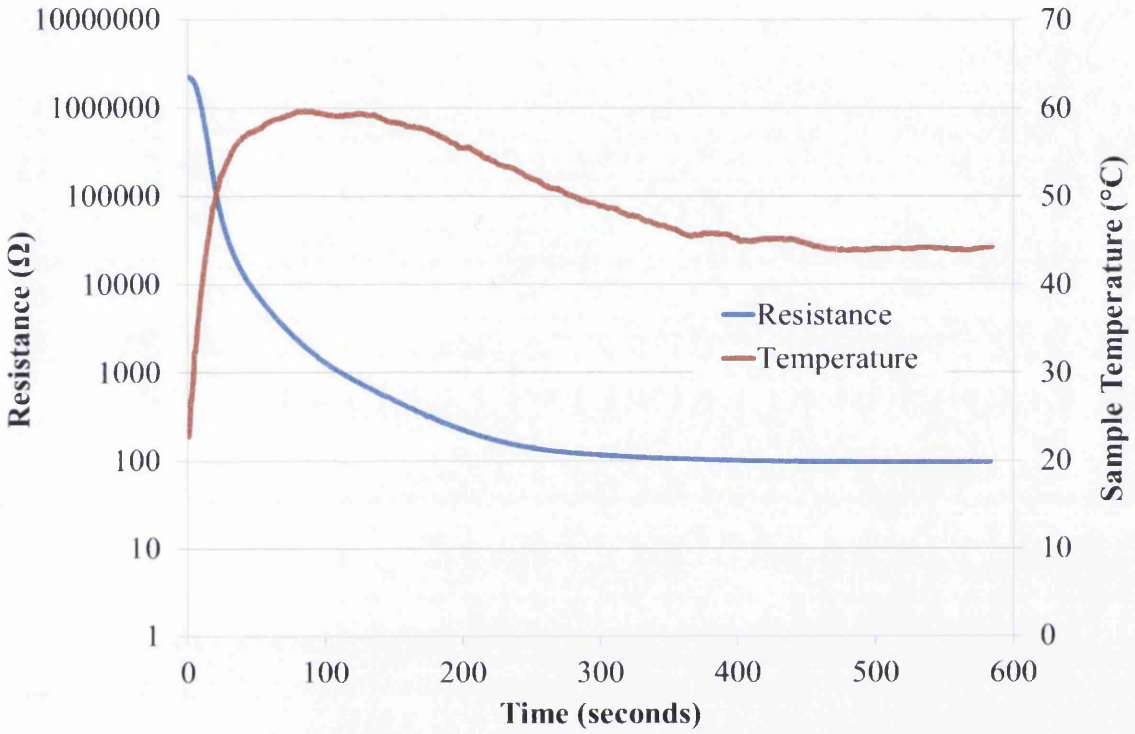

Figure 4.9. Change in Resistance, shown on a log-scale, and temperature as a function of time spent under hot-air dryer and temperature for PEDOT:PSS measured using Thermal Imaging.

It can be seen that initially the temperature increases to a maximum point and then begins to decrease until 560 seconds and then increases only marginally after this. Figure 4.10 shows the image from the thermal camera at 560 where the resistance and temperature of the sample can be seen.

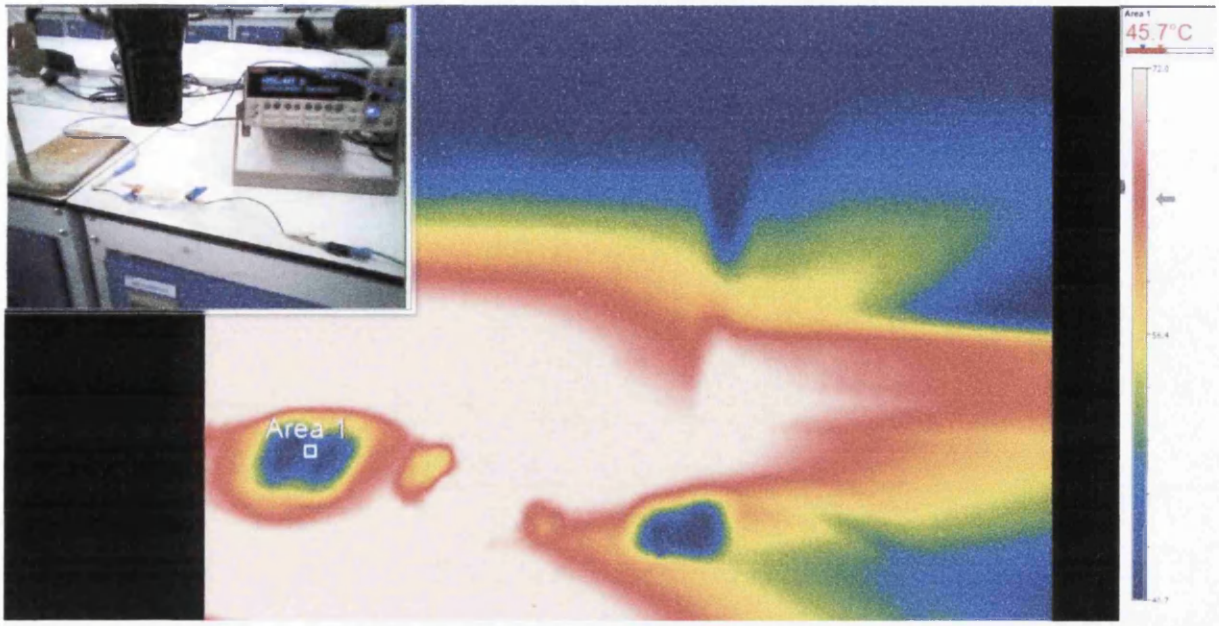

Figure 4.10 Screen grab from a video of the PEDOT:PSS (Area 1) being cured by a hairdryer, recorded using a thermal imaging camera. The inset shows the visible camera recording.

At first this drop in temperature seems to be illogical since the sample is still being supplied energy from the hot air dryer at the same rate (solvent removal is unlikely the cause). The emissivity the PEDOT:PSS (EL-P3145) wet is 0.79 whereas dry it is 0.45. Since the camera calculates the temperature from a previously measured material specific emissivity value and the radiation given off by the sample, when the emissivity changes the temperature also appears to change.

From the same experiment the resistance as a function of time was measured, shown on the second y-axis in Figure 4.9. It can be seen that the temperature drops and the resistance also drops until 560 seconds. After 560 seconds the temperature begins to rise again and the resistance plateaus showing how the Thermal Imaging can be used to determine the dry point and its correlation with the maximum resistance. It can also be seen that the results from the Thermal imaging camera show a good correlation to the results obtained from the thermocouple used in Figure 4.3 which shows this method is viable for in-situ measurement for a PEDOT:PSS film.

4.4. Conclusions

It has been shown that the addition of solvent to a PEDOT:PSS solution affects firstly the final film height and secondly the conductivity. The change in conductivity appears to be unrelated to the solvent used in this study (although there may be certain solvents which affect the conductivity not tested in this study). It was also shown that curing of the PEDOT:PSS can be achieved using high convection air drying (forced evaporation). This means that the temperatures can be kept lower than for conventional oven curing and as a result PEDOT:PSS solutions can be cured at temperatures not exceeding 60°C. The exact point at which the PEDOT:PSS becomes cured can be shown by its change in emissivity as inferred from measurements by IR cameras. This offers a method of In-situ monitoring of PEDOT:PSS curing when coated on, for example, a roll-to-roll processing line. The addition of lower (than water) boiling point solvents and a high convection air dryer was then used in combination to show that films of PEDOT:PSS could be cured under 60°C at decreasing times with increasing solvent. This is significant since it paves the way for PEDOT:PSS to be coated onto films or devices that are sensitive to the water contained in the PEDOT:PSS solution and to high temperatures needed to cure the conventional PEDOT:PSS.

4.5. References

[1] H. Snaith, A. Moule, C. Klein, K. Meerholz, R. Friend, M. Grätzel, *Nano. Lett.* **7**, 3372, (2007).

[2] I. Bruder, BASF Ludwigshafen, Unpublished Result, (2012)

[3] Konarka, WO 20120/107795 A1, 23 Sept (2010).

[4] Agfa, Unpublished Processing Guide, (2012)

[5] I-K. Ding, Thesis, Stanford University, (2011)

[6] M. Silberberg, *Chemistry (4th edition ed.).* New York: McGraw-Hill. (2006).

[7] J. Choi, J. Jeon, Y. Ko, Y. Park, S. Kim, J. Yim, *Thin. Sol. Films,* **517**(13), 3645, (2009).

[8] A. Moropoulou, N. Avdelidis, M. Koui, I. Tzevelekos, *J. Therm. Int.,* **10**(3), 115, (2000).

5. Ultrafast curing of PEDOT:PSS and PEDOT:PSS containing TCA films.

5.1. Introduction

As stated in Chapter 4, for PEDOT:PSS to be used in temperature sensitive opto-electronic devices such as s-DSCs the PEDOT:PSS layer needs to be cured in such a way that device temperature is kept below a temperature which may be detrimental to the device. While evaporative curing proved to be successful in this respect it took take over 9 minutes to cure the undiluted PEDOT:PSS sample. As such, drying times to get good conductivity are typically a minimum of 2-4 minutes which then makes the convection oven a very costly capital item [1]. An alternative method for curing the PEDOT:PSS would be to use rapid radiative heating, whereby the PEDOT:PSS solution or the underlying substrate would absorb the radiation causing highly specific directional heating.

Near Infrared Radiation (NIR) has previously been used to selectively heat and dry materials that have strong absorbance in the NIR part of the spectrum such as silver inks, titania and platinum [2-5]. It could therefore potentially be used to cure a PEDOT:PSS layer in-situ on an opto-electronic device such as an s-DSC without damaging other temperature sensitive layers within the cell. The inherent energy density of NIR would enable a fast cure and ultimately a high line speed, giving added benefit to the mass production of these types of devices. This may have an added benefit in the case of s-DSCs that the water and propylene glycol solvents in PEDOT:PSS solutions de-laminate the Spiro-OMeTAD layer. The disadvantage of a high processing speed could be that, as stated in the Section 1.7.1, there wouldn't be sufficient time for an ordering of the phases within the PEDOT:PSS to take place to a more thermodynamically favorable and highly conductive state [6]. High boiling point solvents are included in the solution such that they stop the PEDOT:PSS structure becoming frozen long enough however if these solvents are removed too quickly there will not be sufficient time for re-ordering and the point of the high-boiling point solvents is negated. Currently the time scale for the reordering has not been documented.

Since the TCA shown in Chapter 3 also contains PEDOT:PSS NIR curing may also be a viable option to reduce time and cost during its fabrication having implications when the scale up of this material is considered.

5.2 Experimental

NIR drying of the PEDOT:PSS was carried out as explained in Section 2.3 using undiluted PEDOT:PSS (EL-P3145, Agfa). This allowed the exposure times to be varied from 1.4 to 2.2 seconds. All films had a wet cast height of 45μm. To initially test if a film was cured the sample had an ethanol soaked swab run over the surface, if material was removed it was deduced that these settings were not sufficient to cause a cure.

Once the films were deemed cured testing of the films was carried out as described in Section 2.3 and Section 2.7.2. It is important to recognise that the NIR method represents a significant power saving as well as speed increase. At full power the NIR operates at 25kW (for a few seconds) whereas the conventional oven is on continuously at 1.3kW.

5.3. Results and Discussion

5.3.1. NIR curing of PEDOT:PSS for rapid processing

Figure 5.1 shows the % Transmission UV-Vis-NIR spectrum of the bare PET film as well as the PEDOT:PSS solution used in this study in both a wet and dry film condition recorded using a Perkin Elmer Lambda 750s with a 60 mm integrating sphere. Also shown on the graph is the region in which the NIR has a peak emission, 800-1300nm (shaded). It can be seen that PET shows near 90% transmission at 1000nm (the output maximum of the lamps) whereas the wet PEDOT:PSS film shows 80% and the dry 70%. This is a significant difference considering that the film thickness is 175μm, 45.0μm and 0.93μm for the PET, PEDOT:PSS wet and dry respectively. This measurement leads to the likely conclusion that the thicker PET will remain relatively unaffected when exposed to the NIR. Absorption and heating will therefore primarily be concentrated in the PEDOT:PSS with increased heating occurring as the film dries.

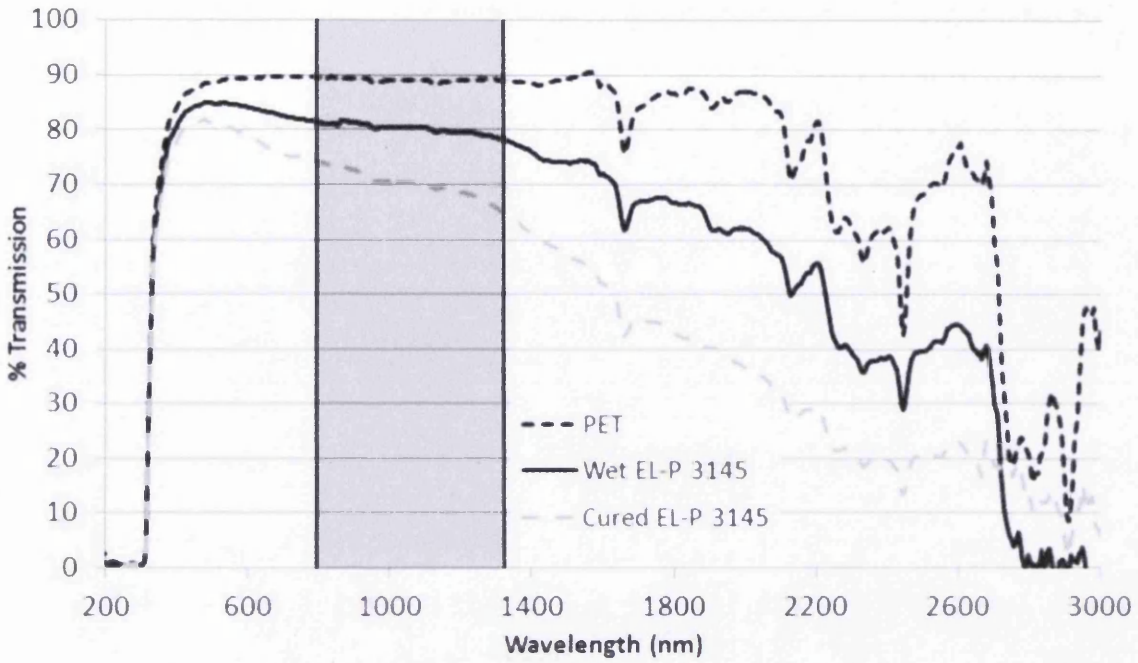

Figure 5.1. UV/VIS/NIR Spectrum of PET (black dashed 175 μm thick) and EL-P 3145 PEDOT:PSS (wet (black 45 μm thick) and dry (grey 0.93 μm thick) spectra are displayed. The grey shaded area indicates the region of peak NIR emission for the fast heating method described.

It is clear that the dry PEDOT:PSS film has the highest NIR absorbance (Figure 5.1) and is by far the thinnest layer and so has the highest extinction coefficient for NIR absorbance. The relative extinction coefficients at 1000 nm (the maximum of the lamp output for NIR) for the three materials are as follows; PET (1), wet PEDOT:PSS (8.3) and dry PEDOT:PSS (690). Obviously as the film is dried and the conducting polymer network forms the NIR absorbance will increase and the rate of drying accelerate. This appears to lead to highly effective drying on the PET substrate since energy absorbance is increasingly focussed in the active layer. A consequence of this focussed absorption is that any further NIR absorption after the initial drying phase is likely to further heat the active layer not just damaging the PEDOT:PSS but also the underlying PET. The importance of carefully controlling the PEDOT:PSS absorption is evidenced visually in Figure 5.2. When a PEDOT:PSS coated PET was subjected to one NIR treatment the PEDOT:PSS cured causing minimal damage to the PET substrate; after a second pass through the oven for a cured sample under identical treatment the heat generated by the absorption of the PEDOT:PSS was enough to melt the underlying PET substrate, as seen in Figure 5.2. To highlight this effect an

uncoated piece of PET substrate was run in parallel to the coated sample and showed no damage after multiple NIR heat treatments.

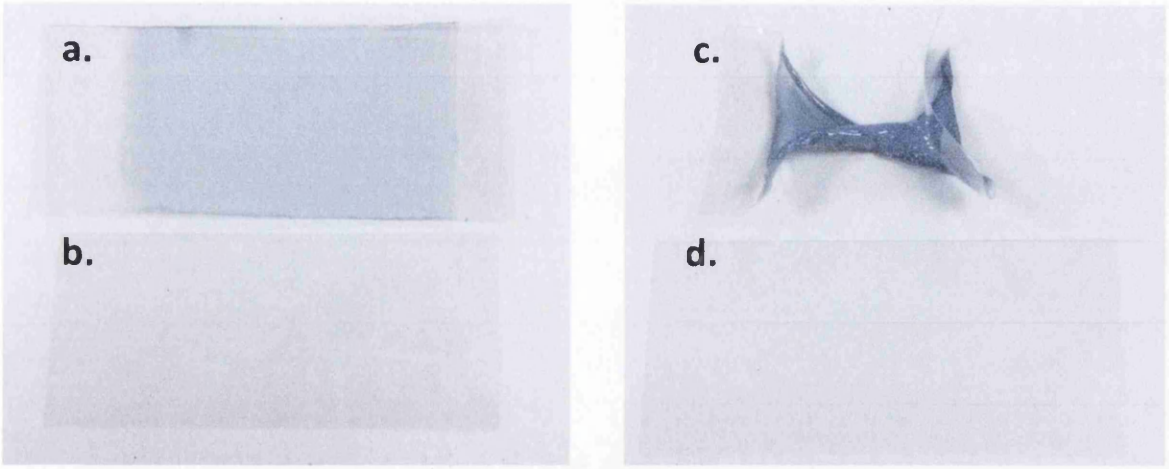

Figure 5.2. Images of (a.) PET sheet coated with PEDOT:PSS after 1 NIR treatment (b.) uncoated PET sheet subjected to the same single NIR treatment (c.) sample (a). subjected to another identical NIR treatment and (d.) sample (b). subjected to multiple NIR treatments. (sheets 11.5 x 5 cm)

It is clear from Figure 5.2 (b) that excess energy input can damage the PET causing it to wrinkle up and is a direct result of the 690:1 ratio of extinction coefficients at the lamp maximum output of 1000 nm. This possible damage to the substrate manifesting itself from heat transfer from the PEDOT:PSS was mitigated in two ways. Firstly the rapid nature of the process is such that the heating phase is significantly shorter than hot air treatment with a maximum exposure of just 2 seconds. This allows less time for substrate degradation to occur. A second feature is that a modified sample stage was used. The use of a PTFE sample block instead of the standard metal unit meant that any NIR radiation penetrating the PET film did not lead to undesirable rapid heating of the sample stage which would otherwise ultimately lead to thermal damage of the PET. If this process were to be scaled up the same effect could be achieved using cooled and coated rollers or sample holders which were reflective of the NIR energy. This is an extremely important feature of this form of direct sample heating; in order to avoid undesirable heating of the instrument hardware and ensure local heating careful consideration must be given to materials selection of oven components and sample carriers.

Figure 5.3 shows a comparison of sheet resistance values following heat treatment between the two drying processes; hot-air oven at 130°C and NIR. An important feature of the data displayed is how rapidly the resistivity of samples drops with time. The critical difference between both methods is the total time for curing and conductivity development which is up to two orders of magnitude quicker for NIR; it is for this reason the data is shown on a logarithmic scale for illustration. Table 5.1 displays the data and scatter in values determined for repeated sample preparation to demonstrate the reproducibility of the curing conditions.

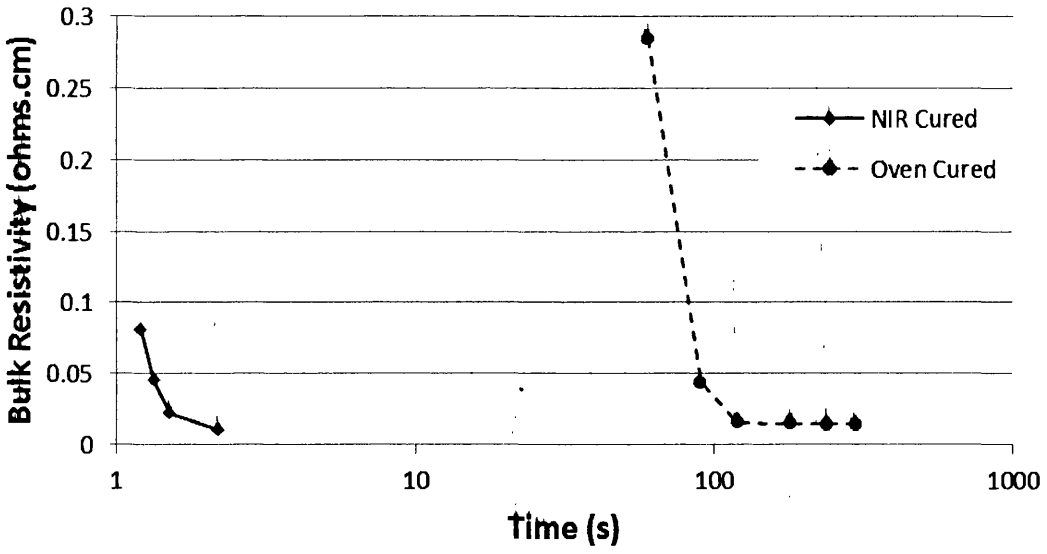

Figure5.3. Bulk resistivity of PEDOT:PSS films verses log dwell time for the two different heating methods.

Table 5.1. Comparison between headline bulk resistivity and process time.

Method	Drying time / s (NIR power)	Bulk Resistivity / Ω.cm	
Oven			± 0.006
130°C	60	0.284	
	90	0.044	± 0.004
	120	0.015	± 0.002
	180	0.015	± 0.001
	240	0.014	± 0.001
	300	0.014	± 0.002
NIR	1.20 (50%)	0.080	± 0.004
	1.33 (48%)	0.046	± 0.004
	1.50 (45%)	0.022	± 0.004
	2.00 (36%)	0.011	± 0.003

Both methods show a decrease in resistivity as drying time increases and for the oven cured method this highlights a transition between under-dried (non-conducting) and fully dried (conducting). For the NIR samples note that the power setting and exposure times were both changed. The aim of this was to allow the same energy input to be delivered to the samples during the exposure. In previous work [4,5] we have demonstrated that the substrate (a metal or FTO coated glass) would heat up and then drive off organic compounds and sinter particles. In this system a different approach is at play since it is the drying layer itself that is absorbing the energy. In the case of the NIR here it is distinct to the previous work where broadly faster heating caused faster sintering as here the same energy input too quickly gives a conducting film but with poor properties in the main due to pin-holing as will be detailed below.

Figure 5.4 shows AFM height scan images of the PEDOT:PSS surfaces highlighting the surface and topological changes occurring. The corresponding Z-range (maximum peak to valley height) gathered from the AFM images is shown in table 5.2 It can be seen that the 300 second oven cured sample Fig. 5.4a and the PEDOT:PSS cured by NIR at the lowest speed (and subsequently lowest power), 11m/min, Fig. 5.4b show similar surfaces corresponding to their similar resistivity as shown in table 5.1. As the NIR exposure time is lowered (and power increased accordingly) the surfaces change and the height between the peaks and valleys increases as it moves towards 1.2 seconds as shown by Fig. 5.4e. The images clearly

show a surface morphology change which we have additionally attempted to quantify on a larger scale across the samples using surface roughness measurements, also detailed in Table 5.2, performed on a Dektak profilometer (across a 1mm length). This data shows that the faster heating rates lead to a significantly roughened surface at the nanometre and micron scale, which we believe is related to solvent boil and cracking. This is a phenomenon whereby the coating in a partial state of cure has entrapped solvent which when it boils bursts out of the coating surface leading to a crater, pinhole or surface crack all of which will increase resistance. The sample treated in a conventional oven treatment is very much smoother. An aspect that will be explored in further work is the extent to which the roughness induced may affect the performance of thin film devices.

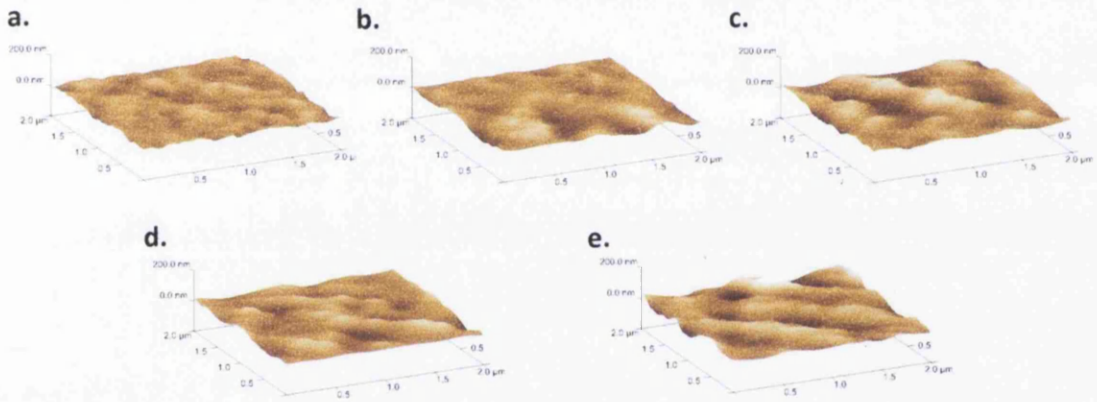

Figure 5.4. AFM Height Scan images of PEDOT:PSS surface cured by a. conventional oven at 130°C for 300 seconds, b. NIR oven for 2.18 seconds c. 1.5 seconds d.1.33 seconds e.1.2 seconds.

Table 5.2: Values of the surface roughness of PEDOT/PSS films dried at different rates in the NIR oven and in a conventional oven.

Exposure time / s	Power / %	Z-Range from AFM / nm	Ra from profilometry / nm
1.2	50	154.0 ±6	236 ±6
1.33	48	93.5 ±2	211 ±6
1.5	45	85.8 ±4	190 ±4
2.00	36	70.9 ±1	169 ±5
240 *	NA	62.5 ±2	72 ±2

*oven dried sample at 130°C for 300 seconds as a comparison

The proposed method for the drying of the PEDOT:PSS solutions is as follows: The PEDOT:PSS particles absorb the high energy density NIR radiation resulting in overtones of molecular vibrations within the coating itself leading to desirable thermal agitation and consequential heating. This localised heat drives off the solvent blends until the film is rendered dry. When the heating rate is too great and the escape of solvent is too rapid the final film will appear cracked, and this defect at the microscopic level is what leads to a loss in conductivity as the curing time is decreased. These results show that there is a limit to NIR curing in which conductivity starts to get sacrificed for increased throughput. An interesting observation is that the NIR dried films (2s) have better conductivity than those cured in a conventional oven for 240 s which either indicates a better interconnectivity of the phases or perhaps a reduction in possibly damaging oxidation. Further work is in progress to examine the effects of curing in different atmospheres.

5.3.2. Rapid curing of a TCA using NIR

In the Section 3.2.1 it was shown that the curing of the TCA took 15 minutes at a lower temperature, a ramp to a higher temperature and then 5 minutes at that higher temperature, equating to 22 minutes in all. As shown in Section 4.4.4 PEDOT:PSS can be dried using NIR in seconds as opposed to minutes. Since the TCA also contains PEDOT:PSS and would absorb NIR, shown in Figure 5.5, curing the TCA with NIR was also considered as a means to reducing the curing time.

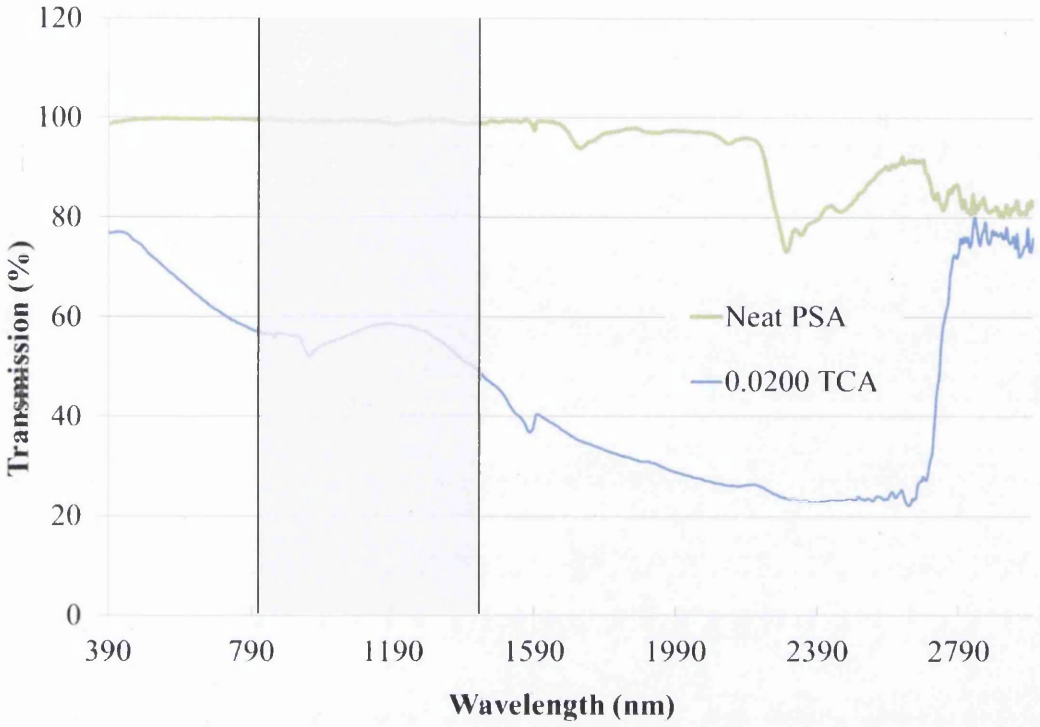

Figure 5.5. UV-Vis transmission spectrum for a TCA film with a 0.0200 PEDOT:PSS ϕ TCA with a dry film thickness of 50μm and a film of neat PSA with a dry film thickness of 48μm. The grey shaded area indicates the region of peak NIR emission.

This could have large implications on the processing of this material since curing times could be reduced as well as oven temperature length leading to overall energy and cost savings. One thing that would have to be borne in mind is that the TCA is a two-step curing process (as opposed to the PEDOT:PSS which was one) and therefore would need a two stage curing under the NIR lamps to first remove the water and then secondly to remove the higher boiling point solvents without causing any bubbling or film damage.

The Transmission profile of the wet elements of the TCA at 1000nm can be seen in Figure 5.6 along with a dried PSA film. It can be seen that the wet PEDOT:PSS will absorb much more than the wet PSA and therefore will account for the majority of heat generated within the film. Also when comparing the dried and wet PSA films it can be seen that the PSA tends towards nearly 100% transparency at 1000nm suggesting that most of the absorption is done by the water contained within the film.

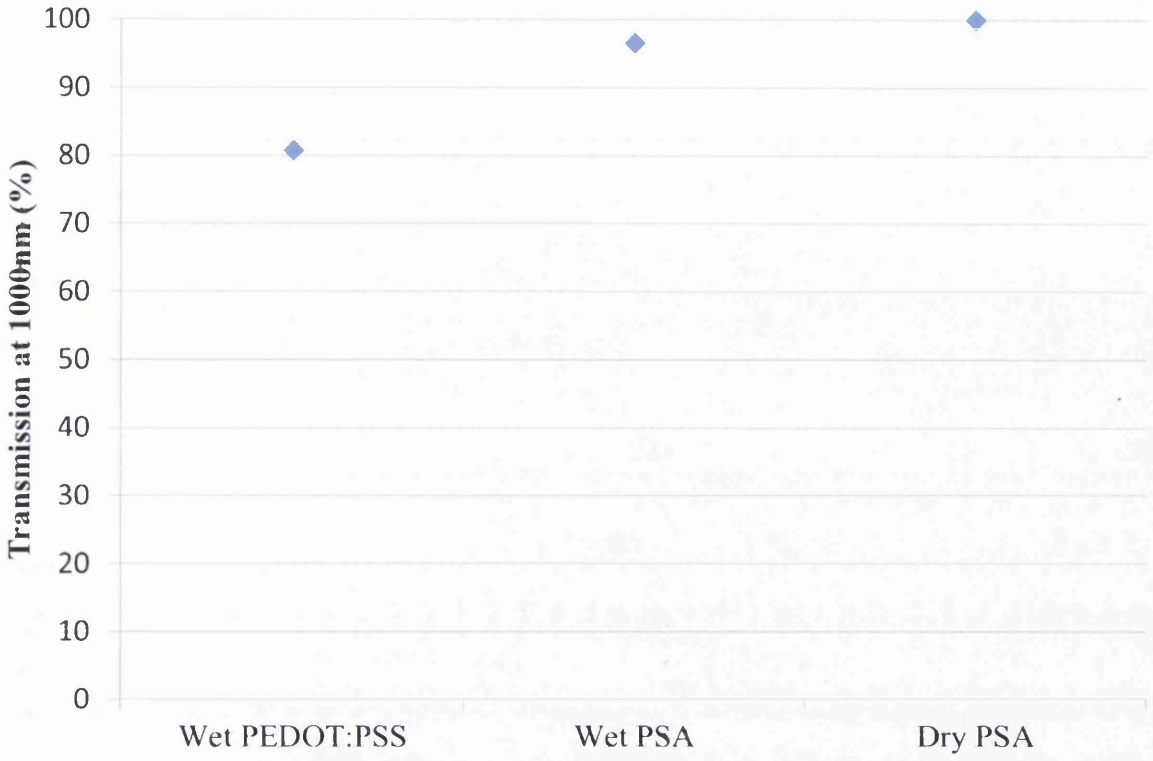

Figure 5.6. Transmission at 1000nm of Wet PEDOT:PSS (EL-P3145) and wet and dried PSA.

Therefore once the water is removed any further absorption of the NIR and heating as a result of it will mostly be done by the PEDOT:PSS. A 0.0200 ϕ PEDOT:PSS TCA was selected with a dry film height of 50μm as a representative TCA, trial and error was initially used to determine the correct settings for the drying of the film. It could be seen visually that when a sample was undercured the film was still wet, and when a sample was sample became overcured it appeared brown/burnt. In addition, other issues that occurred during processing was a cracking of the glass substrate, indicating too high a temperature and a bubbling of the film indicating entrapped solvent as described in Section 5.3. Therefore the drying steps that appeared to produce the best results entailed a two-step process; an initial first pass under the lamp with a lower power intensity of 80% followed by a second at 100% both at the same speed with a 1 second interval between passes. The speed range that lead to an appropriate level of drying was between 15m.min and 9.5m.min, with 15m.min 11m.min and 9.5m.min equaling exposure time to the lamp of two steps of 1.60, 1.18 and 2.53 seconds each respectively (slower speeds than this resulted in undercured samples). The first pass was intended to remove the water from the film and the second pass to remove the high boiling

point solvents from the PEDOT:PSS solution. The results for the conductivity of the films dried at different rates can be seen in Figure 5.7 using a semi log plot. The oven dried film shows a conductivity of 0.24 S/cm when dried for 1320 seconds in total and the NIR results show 0.19 S/cm, 0.17 S/cm and 0.15 S/cm for 1.60, 2.18 and 2.53 second dries respectively (two passes). This result shows that the TCA can be dried by NIR on a timescale a factor of 1000 quicker than a conventional oven dry.

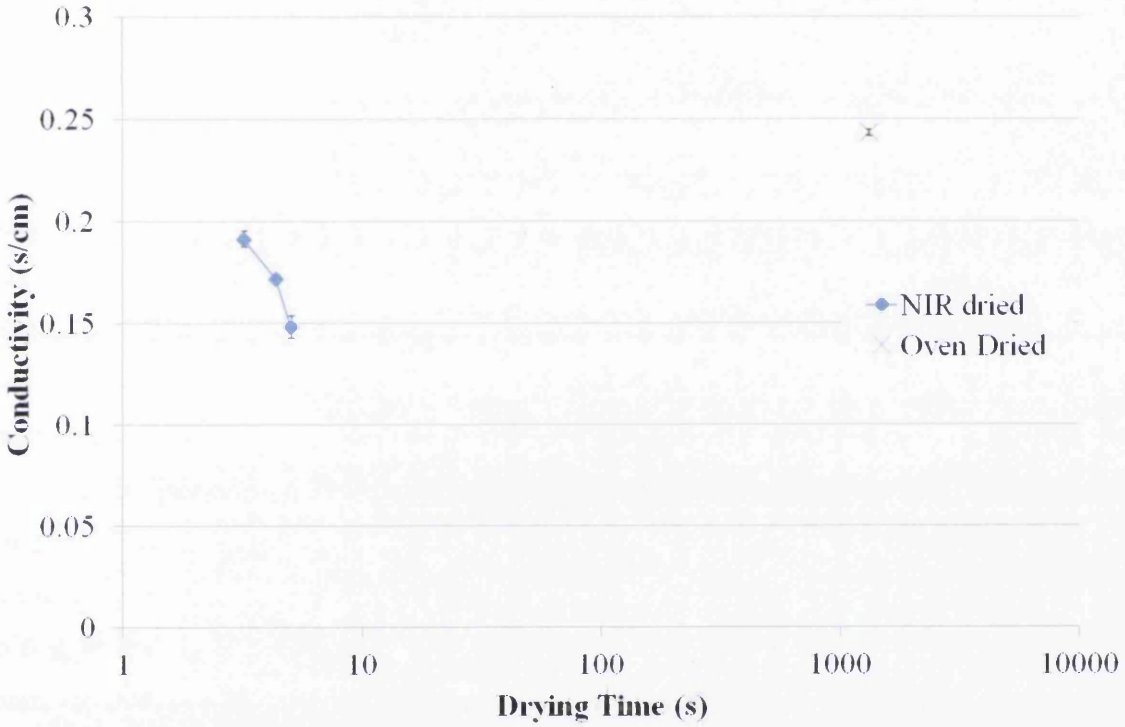

Figure 5.7. Semi log plot showing the change in conductivity as a function of drying time for NIR and Oven dried 0.0200 PEDOT:PSS ϕ TCA. Average of 3 samples and 3 repeat measurements per data point.

All the NIR cured samples show a lower conductivity than the oven cured sample despite all the samples being identical apart from their curing conditions. Therefore the discrepancy must come from the NIR curing stage and could be attributed to one of the following:

1. PEDOT:PSS damage
2. Void formation
3. Ostwald ripening

Discussed in more detail below:

1. During NIR curing (in this set up) the amount of energy the lamp is releasing is help constant but the temperature of the sample is unregulated, in an oven cure the opposite is true. Therefore during curing in the NIR a sample has the possibility to go above a temperature which may be damaging to the PEDOT:PSS in the TCA (and ultimately its conductivity) whereas in an oven it cannot. Further evidence that the samples may have gone above a damaging temperature during curing which can be seen in Figure 5.7 when comparing just the NIR samples. At a slower speeds in the NIR the samples will continue to be exposed to the NIR radiation even after the solvent surrounding the PEDOT:PSS has reached a temperature sufficient to evaporate. This extra energy input will have nowhere to dissipate apart from the sample and PEDOT:PSS itself therefore causing even greater heat damage to the PEDOT:PSS reducing conductivity. To prove this further work would be needed to deduce the temperature at which PEDOT:PSS began to be damaged at during an oven cure and NIR curing where the temperature was kept below this temperature conducted and the conductivity results then compared.

2. Another reason the difference in conductivity between the NIR and oven cured samples is that either the rate of temperature increase is too great or, like in point 1, the temperature is allowed to get too high resulting in the solvent being removed too quickly or boiling of the solvents, leaving voids. The voids leave some PEDOT:PSS particles further apart and not in contact, similar to that found in pure PEDOT:PSS in Section3.2.2. Again further evidence for void formation from NIR curing can be seen when observing the trend within the NIR cured samples where slower line speeds to have a lower conductivity (possibly as a result of more voids) which can be explained at thus: There is a lag time between subsequent passes where the samples pass out from under the NIR oven, the line reverses and then the travels back towards the NIR oven. During this lag time the samples aren't directly exposed to the NIR but are still very much warm. In the samples with the quicker line speed the sample will pass out the NIR exposure with solvent still remaining in the sample and the remaining energy within the sample will be dissipated when the sample is out of exposure to the lamp by evaporating the last of the solvent. In the slower line speeds they are subject to NIR for longer and this energy build up can cause the solvent temperature to rise to a level where it begins to boil, leaving voids within the material. This not only lowers the conductivity of the film as a whole but also would increase the transmission as the particles are now not as concentrated within the film shown in Figure 5.8. The oven cured

sample shows a lower transmission than all the NIR samples which could be a result of the fewest voids explaining why it has the highest conductivity.

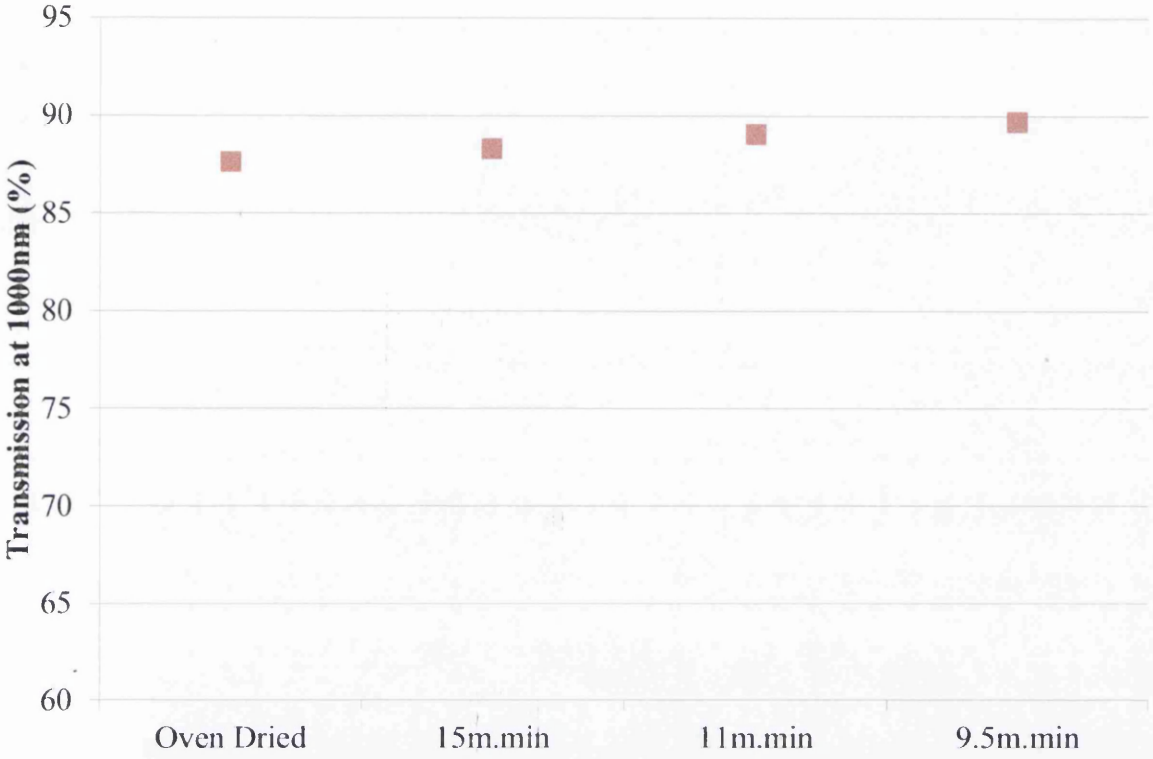

Figure 5.8: Showing the transmission at 1000nm of 50μm thick 0.0200 PEDOT:PSS ϕ TCA film dried via Oven and NIR methods of different NIR line speeds.

3. Acrylic based PSAs are known to have surfactants within their formulation [7] one of these is Alkyl Polyglycolether Sulphate. Surfactants are known to be able to form micelle structures or similar structures under the right conditions [8]. No such structures are seen on an SEM of sample of unaltered PSA as shown in Figure 5.9a. However when propylene glycol is added a variety of structures are formed on the surface, seen in Figure 5.9b and magnified in Figure 5.9c. EDX analyses of these structures (Figure 5.9d) show them to be sulphur containing indicating they are formed by the sulphur containing surfactant. Micelles form once a critical concentration is reached and therefore by adding the propylene glycol there will be more solvent for the surfactant to be mobile in and affords more time during curing in which the micelle structures can form. Since propylene glycol is one of the main constituents of the PEDOT:PSS formulation used here, when this is mixed with the PSA to make the TCA and cured in the oven it can be seen that these structures are also prevalent, Figure 5.9e. However, on an identical TCA cured in the NIR no such structures can be seen

Figure 5.9f. This shows that the speed of the NIR curing limits the formation of structures formed by a diffusion process. The PEDOT:PSS network in the TCA will still be mobile while the film is solvent and would behave similar to the micelles. If allowed a long time to cure (as would be provided by oven curing) Ostwald Ripening could lead to the diffusion of larger networks of PEDOT:PSS being formed, increasing conductivity. Longer times under the NIR (slower line speeds) would cure the TCA quicker, allowing less time for the PEDOT:PSS to be mobile and diffusion to occur leaving smaller and more isolated regions.

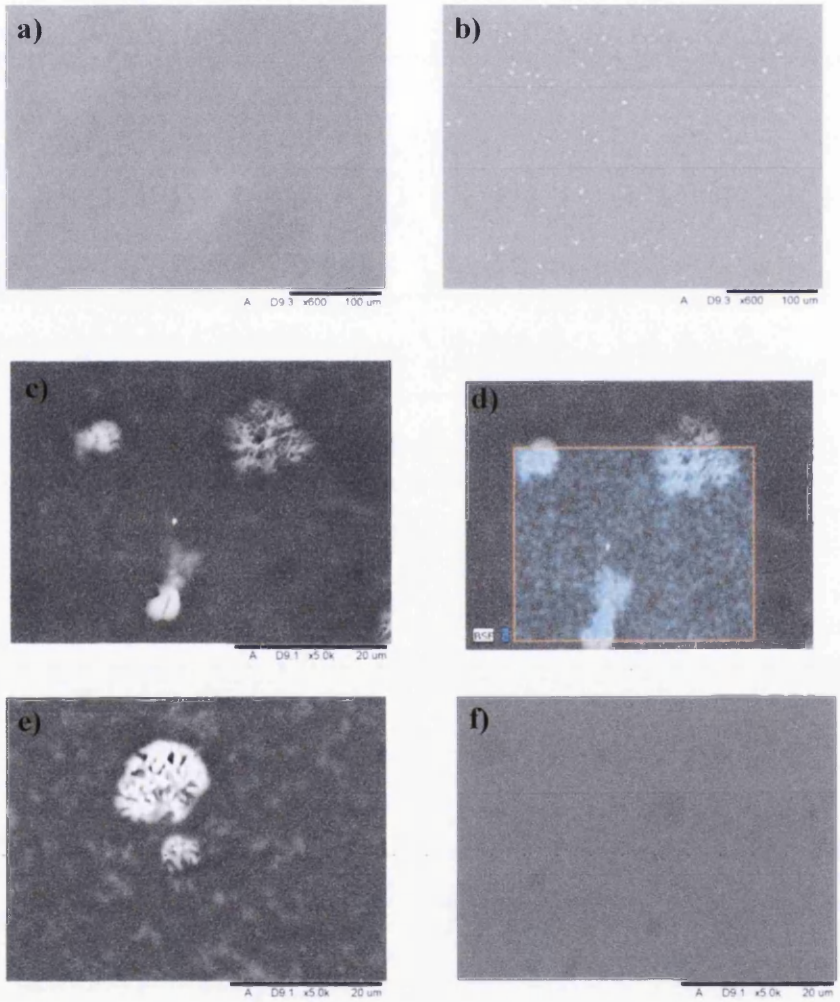

Figure 5.9. SEM micrographs of the surfaces of a) PSA b) PSA with a 30% Propylene Glycol addition, bright regions are micelles c) image b but magnified onto a micelle d) EDX analysis of image c for the element Sulphur, e) A 0.0200 PEDOT:PSS ϕ TCA oven cured and f) A 0.0200 PEDOT:PSS ϕ TCA TCA NIR cured at 11m.min.

In reality it is most likely a combination of the three mechanisms and further work would be needed to explain and categorize the effect conclusively. However what is apparent is that the effect is not that significant when in comparison to the time and cost saving an NIR curing step could provide.

5.4. Conclusions

This initial study shows that NIR can be used as an effective alternative to the drying of PEDOT:PSS solutions giving directly comparable conductive coatings to convection oven dried methods in a fraction of the time. The cause of this heating has been attributed to the absorbance of PEDOT:PSS within the peak emission of the NIR emitter leading to heating and removal of the solvents. The PET substrate does not absorb as significantly in this region and therefore remains undamaged unless the heating is applied for long enough that the PEDOT:PSS heats up beyond the melting temperature of the substrate polymer. The loss of conductivity as the rate of NIR heating is increased is attributed to cracking defects left in the film by solvent boil representing a limit to the speed the samples can be cured at. However this still leaves the potential for this NIR heating step; considering a 200 metre per minute process the minimum conventional oven size would be almost 500 metres, however with an NIR oven this could be reduced to less than 7 metres representing both a considerable capital and energy saving potential.

It has also been shown that the TCA can be dried using an NIR method. The drying time must still be completed in two steps as with a conventional dry to avoid excessive bubbling. The drying time can be reduced from 22 minutes down to 4 seconds without significant loss in the transmission or conductivity. Longer exposure times leads to worse conductivity due to boiling of the solvents causing bubbling, damage to the PEDOT:PSS or insufficient PEDOT:PSS networks. Work is now underway to characterise NIR curing impact on the TCAs adhesive properties.

5.5. References

[1] J. Perelaer, P. Smith, D. Mager, D. Soltman, S. Volkman, J. Korvink, U. Schubert, *J. Mater. Chem.* **20,** 8446, (2010).

[2] M. Cherrington, T. Claypole, D. Deganello, I. Mabbett, T.M. Watson, D. Worsley, *J. Mat. Chem.,* **21,** 7562, (2011).

[3] T.M. Watson, I. Mabbett, H. Wang, L.M. Peter and D. Worsley, *Prog in Photov: Res and App*, **19**(4) 482-486 (2011).

[4] M.J. Carnie, C. Charbonneau, P.R.F. Barnes, M.L. Davies, I. Mabbett, T.M. Watson, B.C. O'Regan, and D.A. Worsley, J. Mat. Chem. A, **6**, 2225-2230 (2013)

[5] C. Charbonneau, K. Hooper, M.J. Carnie, J.R. Searle, B. Philip, D. Wragg, T.M. Watson and D.A. Worsley, Prog in Photov, 2013 in press (doi: 10.1002/pip.2368)

[6] A. Nardes, R. Janssen, M. Kemerink, *Adv. Funct. Mater.,* **18,** 865, (2008).

[7] http://www.flints.co.uk/pdffiles/treadfast_108.pdf

[8] G. Hartley, *Aqueous Solutions of Paraffin Chain Salts, A Study in Micelle Formation,* Hermann & Cie, Paris, (1936).

6. Electrochemical Analysis for the Realisation of Low Temperature Processed ZnO Dye Solar Cells

6.1. Introduction

As mentioned in previous chapters reduced temperature processing has many benefits for the industrial production of DSC, such as the reduced energy cost of producing the cells and its compatibility with conventional paint ovens. While **Chapter 3** developed a low temperature top contact and **Chapter 4** a low temperature processing method for a PEDOT:PSS interlayer, the TiO_2 fin a s-DSC still represents a high temperature processing step and a disadvantage from a large scale processing point of view. Zinc Oxide is a promising alternative porous semiconducting oxide electrode to TiO_2 for use within dye sensitised solar cells (DSC) due to its benefit of versatility of structures, low material cost and increased electron mobility but often at the cost of decreased performance [1-2]. Recently a breakthrough was made with the dyeing of ZnO cells which allowed the performance to be increased [3]. By including water in the dyeing process the ZnO surface was not attacked by the Ru based dyes and subsequently cells fabricated not only had a higher performance but also a higher reproducibility. Here we present a study into the processing of ZnO films at temperatures far lower than for conventional TiO_2 sintering and investigate how the lower temperatures influence the performance and electrochemical parameters within the cell.

Electrochemical techniques, namely, Electrochemical Impedance Spectroscopy (EIS) and IV measurements have been employed here to demonstrate that nanoparticulate ZnO cells can be processed at temperatures of 200°C or lower using conventional oven sintering techniques. EIS has been shown to be a powerful tool for the characterization of DSC Devices and IV measurements are a standard for characterization of all photovoltaic devices [4].

Recently EIS, amongst other electrochemical techniques, has been used to show the change in nanoparticulate ZnO films as a function of varying sintering temperature [5-6]. The studies used N719 and also nanoparticulate films as employed in this work. Within the study it was highlighted that ZnO increases crystallinity, decreases surface defects and decreases surface area as the temperature increased.

6.2. Experimental

ZnO liquid DSCs were fabricated according to the method outlined in Section 2.4. IV testing of complete devices was carried out as described in Section 2.7.3. Dye desorption measurements were done by first immersing the sintered ZnO photoanodes in a solution of N719 Dye in a 1:1 vol mix of Ethanol and de-ionised water as shown in previous work [3]. The dye was then desorbed from the photoanodes by immersing them in 20ml of 0.1M NaOH and the subsequent solution analysed using UV-Vis. EIS measurements were carried out as described in Section 2.7.5 and transient photovoltage decay as in Section 2.7.6.

6.3. Results and Discussion

6.2.1. Dye Desorption

To investigate the impact the impact sintering had on the surface area of the mesoporous ZnO film (and ultimately the amount of dye a film could adsorb) a conventional dye desorption method was used. The results of the dye-desorption experiment at various sintering temperatures can be seen in Figure 6.1. As the sintering temperature increases, the amount of dye adsorbed to the ZnO film decreases.

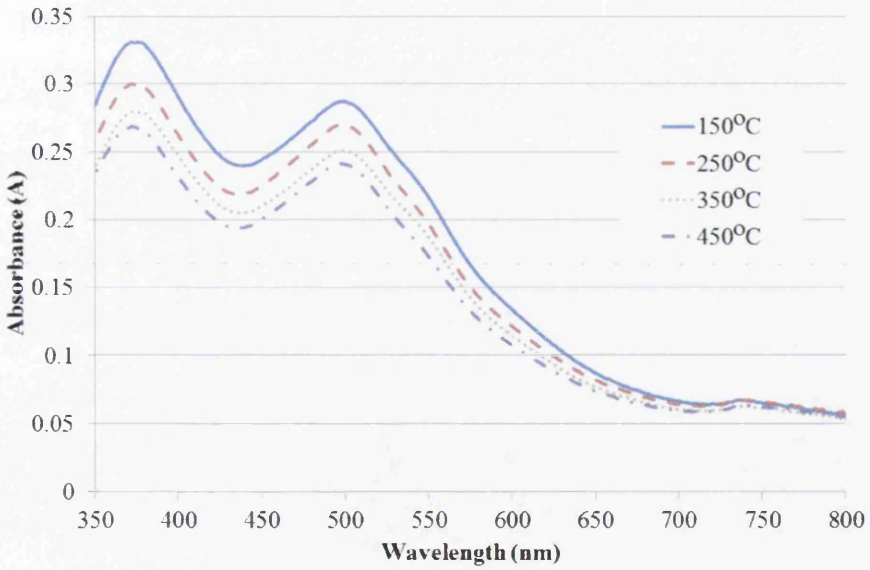

Figure 6.1. Change in absorbance as a function of wavelength of dye desorbed from the surface of ZnO films sintered at temperatures from 150-450°C. Average of 5 cells

Dye uptake is a good indicator for the surface area of the films, Figure 6.1 suggests that as sintering temperature is increased the surface area available for dye uptake is decreased.

As all the films went through the same dyeing process this means the absorbance is indicative of the surface area of the films covered by dye. The reduction in the amount of adsorbed dye could be caused by two things: the increased temperature induces necking and sintering between particles, reducing surface area or that pore size would decrease leading to less dye being able to reach the surfaces located within smaller pores. Both these effects are caused by increased levels of sintering and both would lead to a decrease in active area of the ZnO surface.

6.2.2. Charge Transfer Resistance

It has been shown by Bisquert et al that electron lifetimes (τ_n), the change transfer resistance R_{ct} and the chemical capacitance at the ZnO:electrolyte interface (C_{CC}) giving an RC time constant (Equation 6.1.) can all be calculated from Nyquist plots of EIS data [7].

$$\tau_n = R_{ct}C_{CC} \qquad \text{(Eq. 6.1)}$$

Figure 6.2 shows the change in the Rct (which is also referred to as the recombination resistance) as a function of bias voltage used in the EIS experiments, for cells with different sintering temperatures.

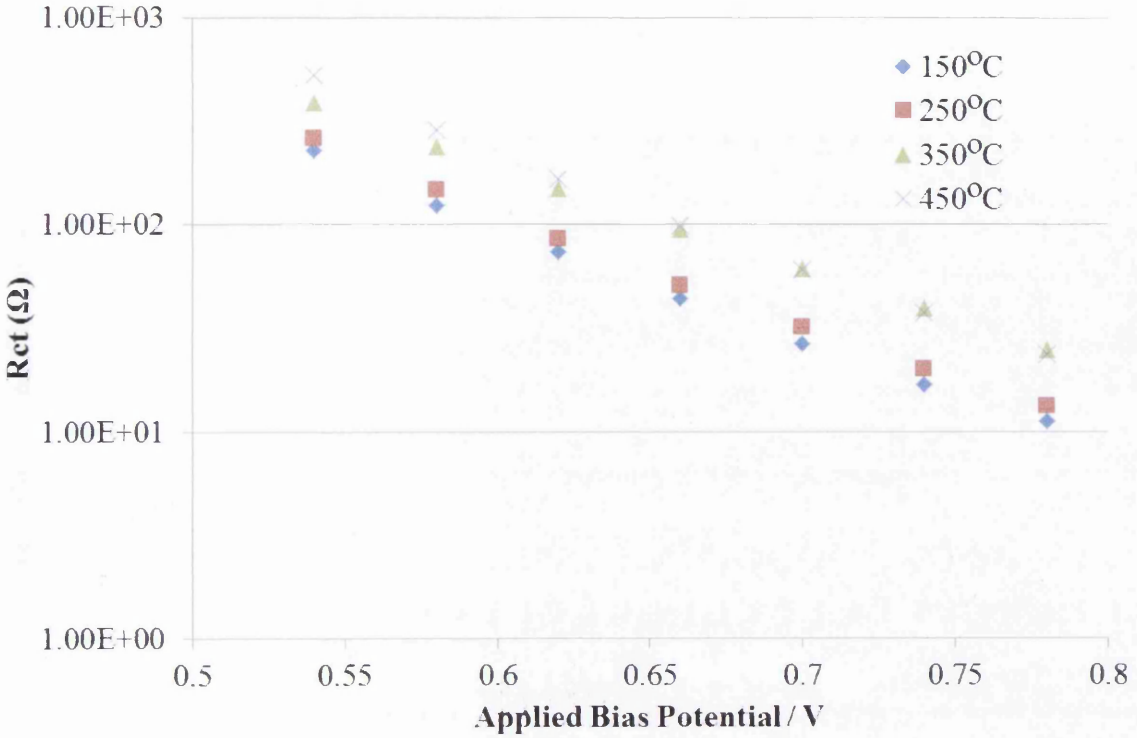

Figure 6.2. Change in R_{ct} as the Applied Bias Potential in the EIS measurement changes for complete DSC made with ZnO films sintered between 150-450°C. Average of 5 cells per data point.

It can be seen that cells made with ZnO films sintered at 150°C showed the lowest R_{ct} which subsequently increased for cells at 250°C, 350°C and 450°C. As has been shown before an increase in sintering between particles leads to an enlarged crystal size and therefore a longer electron transport distance and R_{ct}[8]. This shows that cells sintered at lower temperatures still have a large amount of surface defects, probably as a result of the manufacturing process of the ZnO nanoparticles, and these are decreased by increasing temperature.

Figure 6.3 reciprocates the trend from the R_{ct} values in Figure 6.2 as when the sintering temperature is increased there is a trend for increased recombination lifetimes. As the recombination lifetime shows how quickly the charge within the cell decays the longer the electron transport distance the longer the predicted electron lifetime with increased crystal size (found with increased sintering temperature) as has been highlighted in previous studies [5].

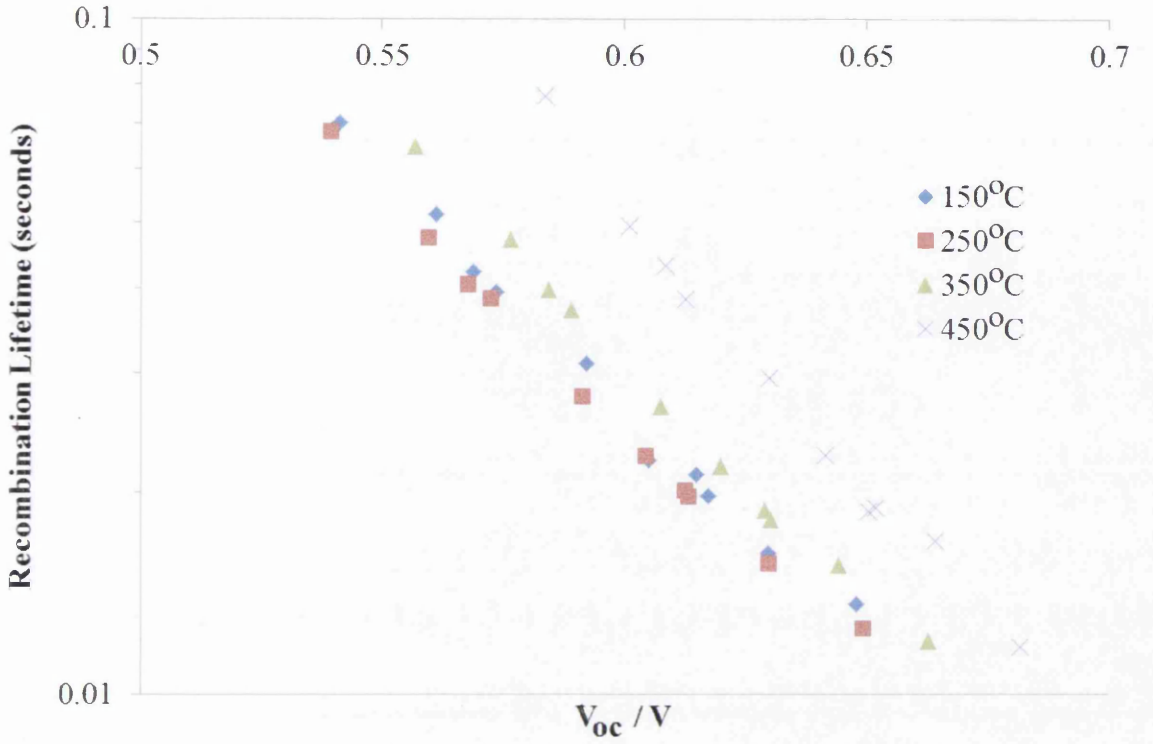

Figure 6.3. Change in recombination lifetime as the V_{oc} obtained from the transient measurements changes for full DSC made with ZnO sintered at varying temperatures. Average of 5 cells per data point.

6.2.3. Transport Resistance

The transport resistance R_t as shown by Fabregat-Santiago et al. can be determined from the EIS data of cells analysed using a transmission line model [9]. Figure 6.4 shows how the transport resistance as a factor of applied bias voltage as the ZnO films sintering temperature was changed. It can be seen that there is initially a rise in the R_t from 150°C to 250°C followed by a decrease from 350°C to 450°C.

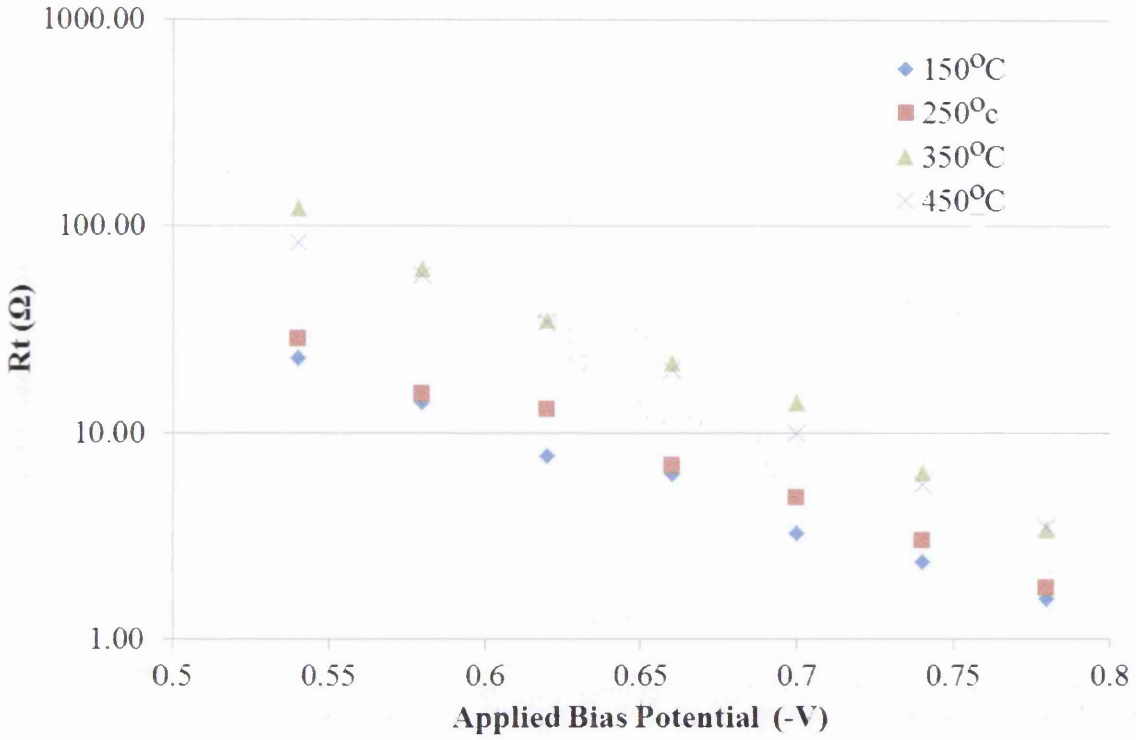

Figure 6.4. Change in R_t as the Applied Bias Potential in the EIS measurement changes for complete DSC made with ZnO films sintered between 150-450°C. Average of 5 cells per data point.

At first this seems counterintuitive as the more sintered films should have better connections and a lower R_t. However what may be occurring is that in the 150°C to 350°C regime the transport is dominated by the surface states, involving fast trapping and de-trapping kinetics. As the ZnO particles begin to increasingly fuse as the temperatures increase the amount of surface states decrease and the amount of bulk traps increase with more grain boundries. Bulk traps have fast trapping and slow de-trapping kinetics and therefore the more that are present the greater likelihood that the transport resistance will increase [10]. It has been shown however that at higher temperatures ZnO increases its crystallinity and at 450°C this is the dominant factor present [11]. As the crystallinity increases the amount of bulk traps decreases and the Rt will decrease as shown in Figure 6.4. This is reinforced by results shown in Figure 6.5 where the electron lifetimes decrease from 150°C to 350°C and then begin to increase at 450°C as the resistance of the films again begins to decrease.

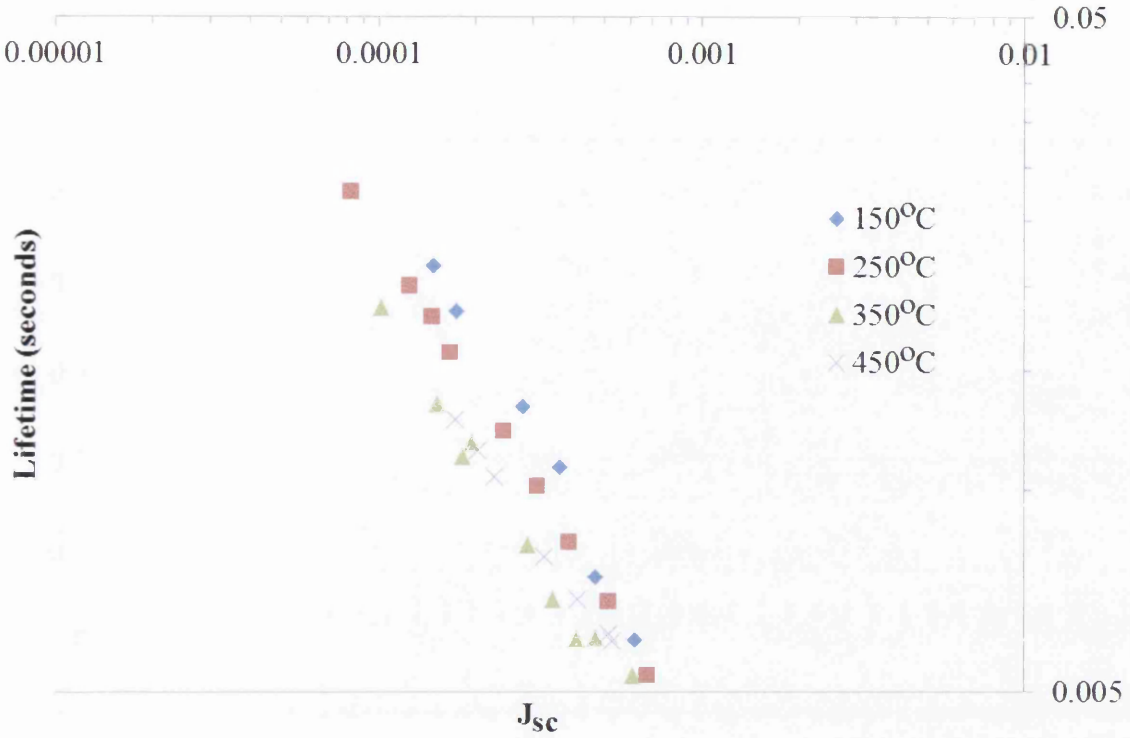

Figure 6.5. Change in electron lifetime as the J_{sc} obtained from the transient measurements changes for full DSC made with ZnO sintered at varying temperatures. Average of 5 cells per data point.

6.2.4. IV Performance Parameters

Complete devices were made with ZnO layers sintered at different temperatures and tested under 1sun and the performance parameters extracted. From the data shown in Figure 6.6 it can be seen that the V_{oc} of cells with ZnO films sintered at varying temperatures increases as the sintering temperature increases. This will be as a direct result of the increased Rct as shown previously. However the overall change on the V_{oc} is very slight, which is promising for the use of lower temperatures for production of ZnO DSC.

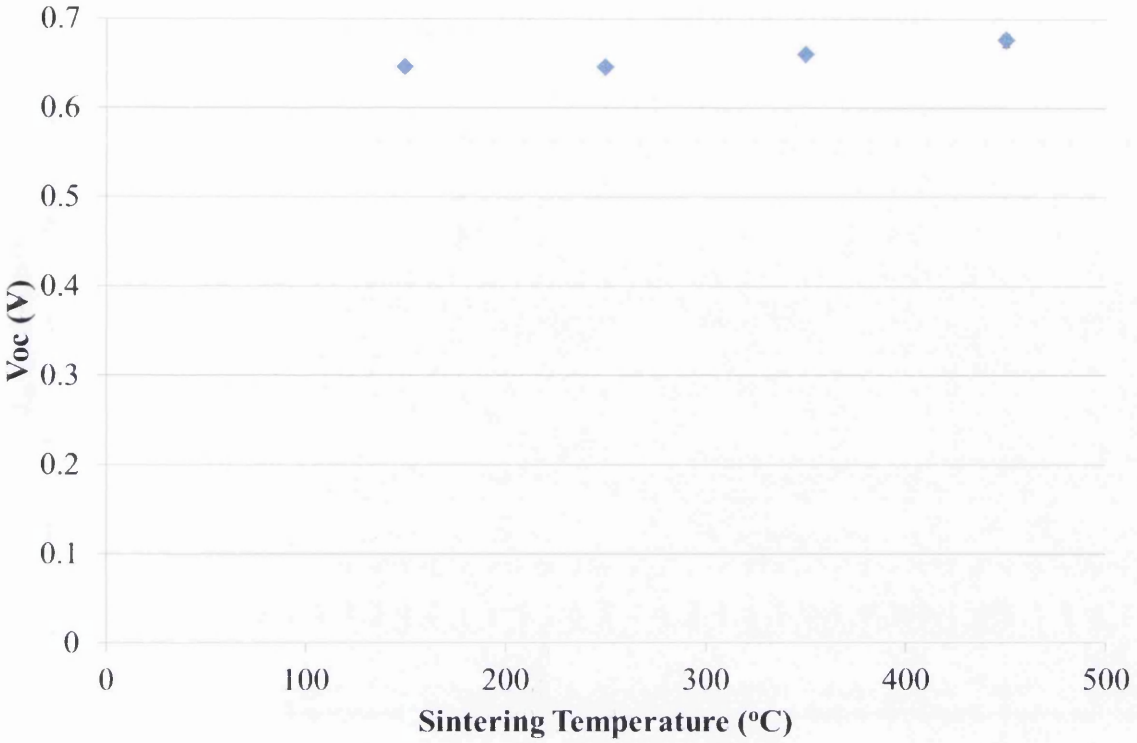

Figure 6.6: Charting the change in V_{oc} of full DSCs as the temperature used to sinter their relevant ZnO films changed (measured under 1 sun AM 1.5). Average of 5 cells per data point.

The J_{sc} data shown in Figure 6.7 shows an increase in J_{sc} as the sintering temperature of the ZnO films is increased. This trend is also replicated by IPCE data in Figure 6.8 which shows no sign of shifting the IPCE peak indicating that the films do not differ in the amount of scattering they achieve.

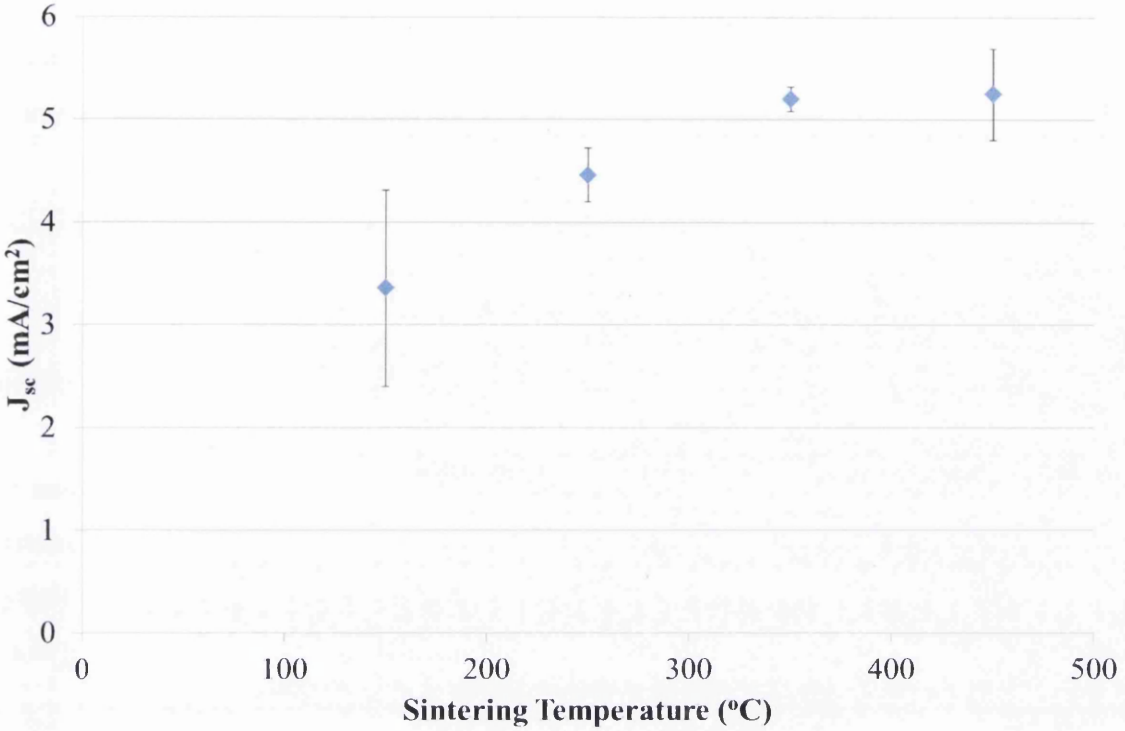

Figure 6.7. The change in J_{sc} of full DSC as the temperature used to sinter their relevant ZnO films changed measured under 1 sun, AM 1.5. Average of 5 cells per data point.

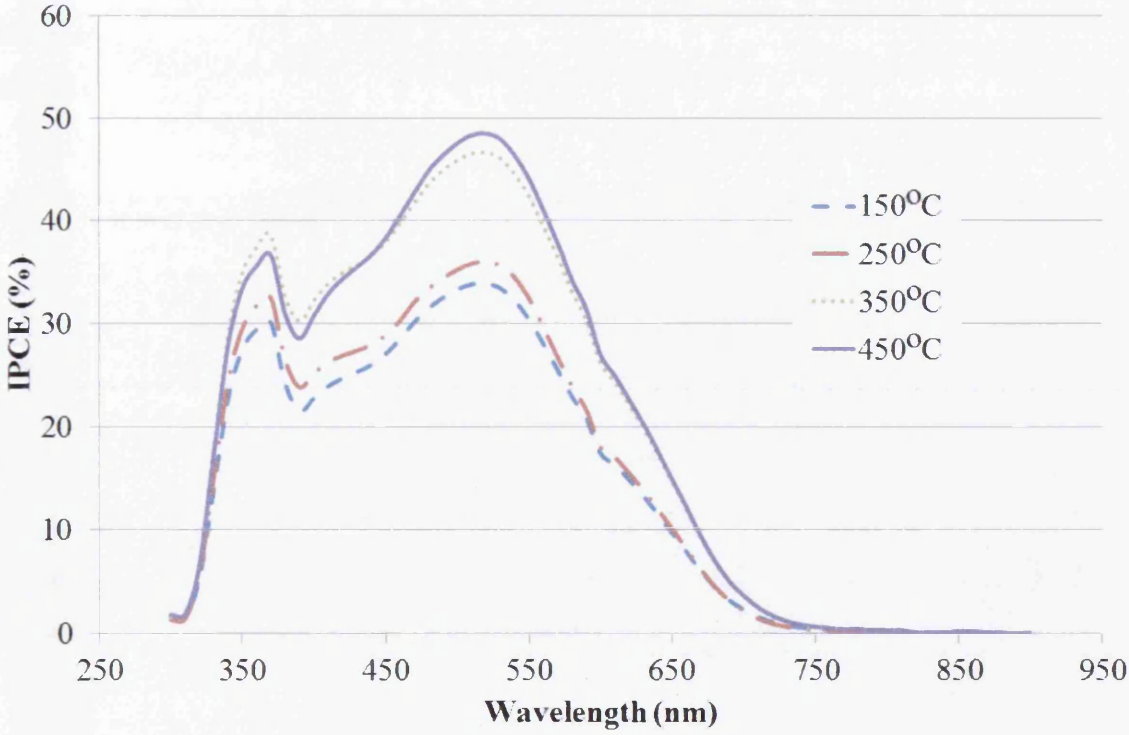

Figure 6.8. The IPCE of full DSCs made using different sintering temperatures for the ZnO working electrode film plotted against wavelength. Average of 5 cells per data point.

The trend in the J_{sc} appears to go against the results shown by the R_t and also the amount of dye absorbed on the films shown previously in this work. The IPCE can be summarised by Equation 6.2 [12].

$$IPCE(\lambda) = LHE(\lambda) \cdot \varphi_{inj} \cdot \eta_{coll} \qquad \text{(Eq 6.2)}$$

Whereby LHE(λ) is the light harvesting efficiency, φ_{inj} is the quantum yield of charge injection and η_{coll} the efficiency of collecting the injecting charge.

η_{coll} will decrease as the transport resistance increases and the LHE(λ) will decrease as the amount of adsorbed dye decreases, both decreasing the overall IPCE. However an increase in crystallinity has been shown to significantly increase the φ_{inj} [5,11]. The crystallinity in the ZnO films produced here is increasing as the temperature increases and this in turn leads to a large increase in φ_{inj}, IPCE and ultimately J_{sc}.

The final conversion efficiency of the cells is shown in Figure 6.9 and it can be seen that the cell efficiency as a result of all the parameters previously discussed increases from 1.03% to 1.3% as the sintering temperature is increased from 150°C to 450°C. While this result is significant in terms of a scientific observation, it is not a significant decrease in efficiency for cells sintered between 150-350°C which is a step towards low temperature sintered cells being considered for an industrial product.

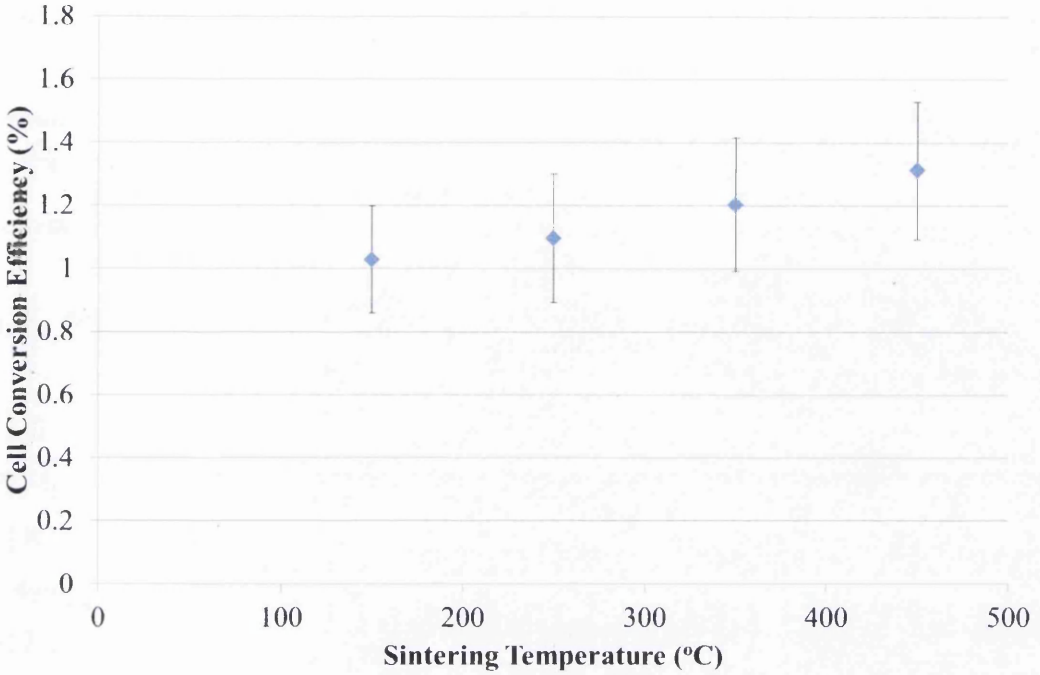

Figure 6.9. Change in Cell Conversion Efficiency of sets of 5 full DSC at the temperature used to sinter their relevant ZnO films changed measured under 1 sun, AM 1.5. Average of 5 cells per data point.

6.3. Conclusions

As the sintering temperature of ZnO films is increased from 150-450°C the level of sintering in the film is increased, as shown by the decreased dye adsorption by reduced active area. The increased sintering was shown to lead to an increased Rct and also an increased recombination lifetime, as shown by EIS and transient measurements. The increase in sintering was also shown to decrease the R_t as the level of bulk traps increased, but then decreased as possibly the level of crystallinity within the film became significant and the R_t decreased, a trend which was reflected by the electron lifetime transient measurements.

The change in R_{ct}, R_t, total crystal size and increased crystallinity caused the V_{oc} and J_{sc} to both increase. However with the trend being only slight the impact on the overall conversion efficiency was an increase of less than 0.3% between the 150°C and 450°C. This result demonstrates that a reduction in sintering temperature can be achieved without a significant compromise in performance and that 250°C could be a viable sintering

temperature for ZnO based DSC. This work suggests a cost saving opportunity in scale up and fabrication of DSC through a reduction in oven temperatures and subsequent manufacturing costs however the overall performance of ZnO based DSC is still behind that of TiO_2 based cells and would need improving significantly before its true potential is realised.

6.4. References

[1] G. Redmond, *Chem. Mater.,* **6**(5), 686 (1994)

[2] M. Law, *J. Phys. Chem. B.,* **110**, 22652 (2006)

[2] R. Schölin, M. Quintana, E. Johansson, M. Hahlin, T. Marinado, A. Hagfeldt, and H. Rensmo, *J. Phys. Chem. C.,* **115** (39), 19274 (2011)

[4] J. Bisquert, and F. Fabregat-Santiago, *Impedance* K. Kalyanasundaram, Editor 2010, EPFL Press: Lausanne

[5] L. Lu, R. Li, K. Fan, T. Peng, *J. Solar Energy.,* **84,** 844 (2010)

[6] P. Teesetsopan, S. Kumar and J. Dutta, *Int. J. Electrochem. Sci.,* **7,** 4988 (2012)

[7] J. Bisquert, *J. Phys. Chem. C.*, **113**(40), 17278 (2009)

[8] J. Bisquert, Arie Zaban, M. Greenshtein and Iva´n Mora-Sero, *J. Am. Chem. Soc.*, **126,** 13550 (2004)

[9] F. Fabregat-Santiago, G. Garcia-Belmonte, J. Bisquert, A. Zaban and P. Salvador, *J. Phys. Chem. B.,* **106**, 334 (2002)

[10] L. Peter, *J. Electroanalytical Chem.,* **599**, 233–240 (2007)

[11] K.J. Chen, T.H. Fang, F.Y. Hung, L.W. Ji, S.J. Chang, S.J. Young, Y.J. Hsiao, *App. Surf. Sci.,* **254**, 5791 (2008)

[12] D. Zhao, T. Peng, L. Lu, P. Cai, P. Jiang, Z Bian, *J. Phys. Chem. C.,* **112**, 8486 (2008)

7. Room Temperature TCA-Laminate technology to enable the mass manufacture of flexible s-DSCs

7.1. Introduction

One of the major steps in the manufacture of hybrid organic photovoltaics (such as solid-state dye sensitised solar cells (s-DSC), organic inorganic lead-halide perovskite and organic photovoltaics (OPV)) is the production of a flexible top electrode that can easily be applied in a continuous manufacturing process.

At the laboratory research stage of solid state third generation PV technologies, the counter electrode is typically applied by sputtering or evaporating of an opaque metallic contact onto the cell [1]. This limits their potential for scale up as the metals used are inherently expensive gold or silver, and vacuum processing increases the capital and processing costs. Furthermore this standard architecture dictates that the working electrode of the cell must be transparent.

Both FTO and ITO coated glass working electrodes are used with the transparent conducting oxide the base for attaching the active layer (with or without an additional blocking layer). Whilst these are dimensionally stable and can withstand sintering, they have the disadvantage of not being flexible that is a requirement for building integrated photovoltaics (BIPV). For this reason, a cost-effective metal foil such as carbon steel is ideal as a fully flexible working electrode.

For such fully flexible PV cells to be produced using a R2R process on a metal substrate a new approach is required for the counter electrode. Since an opaque metallic substrate requires reverse illumination and the conventional metallic back contact would not allow light to enter the cell, see Figure 7.1.

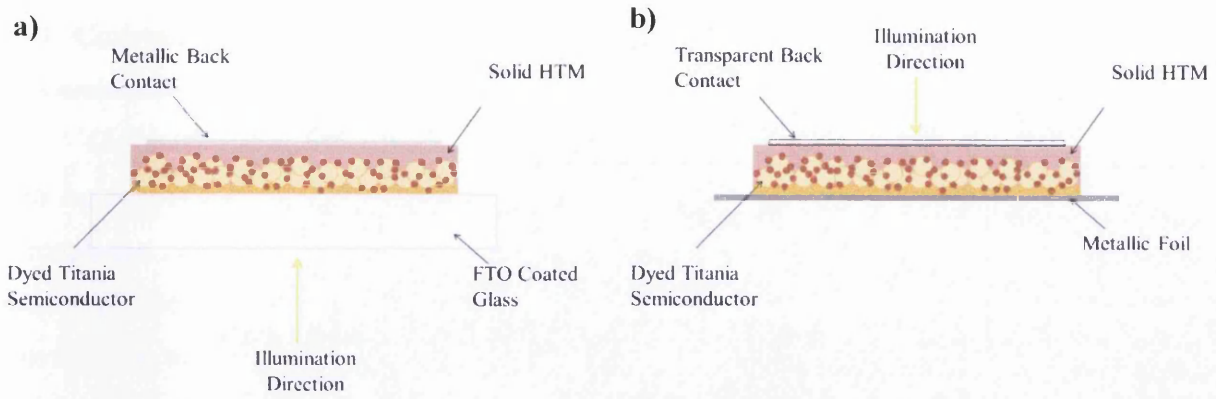

Figure 7.1. Schematic cross section of s-DSC made using a) conventional architecture of an FTO coated glass substrate and a metallic back contact and b) a metallic foil substrate, which would need a transparent back contact, with the illumination direction forwards (a) and reverse (b) needed for both.

Previously the only way to create a transparent back contact compatible with s-DSC was to use a thin layer of evaporated gold (which still has the inherent disadvantages of being expensive, vacuum deposited and allowed relatively little light through [2]). This chapter aims to use the work presented in Chapters 3 and 4 to utilise the transparent conductive adhesive (TCA) system and the information gathered with respect to PEDOT:PSS to create a new s-DSC architecture, free of vacuum processes, Ag and Au, that is roll-to-roll (R2R) processable and compatible with flexible substrates.

7.2. Experimental

The fabrication method for solid state DSC is outline in Section 2.5 including the various back contact methods. In order to cure the PEDOT:PSS layer by NIR cells had a 4:1:1 solution of PEDOT:PSS (EL-P3145, Agfa) :ethanol:IPA bar coated on to the surface as described in section 2.5.3, however instead of drying using hot air convection they were passed under an NIR lamp for times and power settings outlined in Section 7.3.4. The cells were then back contacted further using the method outlined in Section 2.5.3

7.3. Results and Discussion

7.3.1. Conventional s-DSC cells fabricated using evaporated metallic back contacts for benchmarking

Currently the best performing conventional s-DSCs are based on FTO coated glass with Ag evaporated back contacts while the best performing s-DSCs in reverse illumination (through the non-FTO glass side) have a thin semi-transparent Au layer as a back contact instead of the opaque Ag[2-4]. To act as a benchmark for any cells made in a non-conventional way in this chapter cells made on FTO glass with Au and Ag evaporated back contacts were fabricated. The Au was deposited in a sufficiently thin layer that it could be semi-transparent (25nm as opposed to the normal 50-75nm) and as a result tested in a forwards and reverse set illumination. In addition the impact of the Spiro-OMeTAD capping layer thickness was also investigated. s-DSCs were fabricated as described in Section 2.5 but using two different speeds of 500 and 1000RPM during the spin coating of the Spiro-OMeTAD layer, giving a capping layer height of 100-200nm and 200-450nm respectively. The results for these variables are shown in Table 7.1 and Figure 7.2.

Table 7.1. The device performance of s-DSCs made using Ag evaporated back contacts with Spiro-OMeTAD deposited at 1000 & 500RPM spin coating and s-DSCs fabricated using Au evaporated back contacts and a 1000RPM deposition. The values shown above are averaged values and standard deviations of 5 devices made under standard conditions.

	Capping Layer Thickness (nm)	V_{oc} (V)	J_{sc} (mA/cm^2)	Fill factor	Efficiency %	StDev(Eff)
Ag 1000 RPM	100-200	0.87	4.57	53.79	2.10	0.12
Ag 500 RPM	200-450	0.89	2.99	50.31	1.29	0.14
Au 1000RPM Forwards Illumination	100-200	0.90	1.68	65.96	1.01	0.24
Au 1000RPM Reverse Illumination	100-200	0.87	0.27	67.70	0.16	0.02

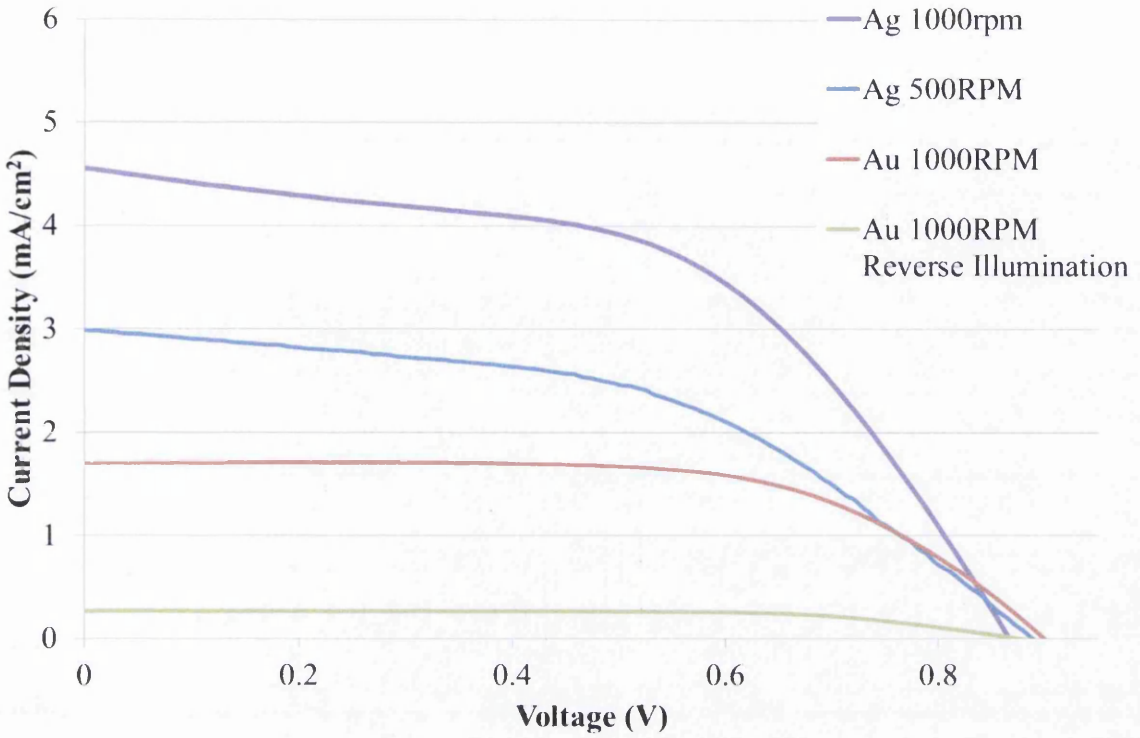

Figure 7.2. Current density–voltage (J–V) curves of typical solid-state dye-sensitized solar cells made using evaporated back contacts of Ag and Au at different Spiro-OMeTAD deposition speeds. All illuminated in forwards direction unless otherwise stated.

As has been suggested before the slower spin speed would increase the filling fraction of the TiO_2 pores, increasing FF. However it was also suggested due to Spiro-OMeTAD's poor conductivity, increasing the over layer (capping layer) on top of the cells increases the series resistance of the cells, negatively impacting on its performance [5]. As can be seen in Table 7.1 when the spin speed is decreased the J_{sc} drops from 4.57 to 2.99mA/cm^2. This can be attributed to a greater absorbance of light by the thicker Spiro-OMeTAD layer. It is known the reflection of the silver electrode will contribute to the J_{sc} [1], and if the light is passing through a thicker Spiro-OMeTAD layer before and after being reflected more of the light will be absorbed (the absorption of light by the Spiro-OMeTAD layer is shown in more detail in Section 7.3.2.1). While the FF does decrease from 53.79 to 50.31% the decrease is not significant considering the change in J_{sc}, however there is the positive impact of the potential increased pore filling fraction counteracting the decrease as also shown by an increase in V_{oc}. It can be seen that when Au is used in the forward configuration the efficiency drops by nearly half compared with Ag. The first reason for this is from the greater reflection the Ag

contact provides over the Au one in the visible region increasing light harvesting [1]. Secondly to make the Au contact transparent enough to allow light to pass through (for reverse illumination) the layer must be around 25nm thick, an Ag layer is commonly deposited at around 200nm and is opaque, reflecting a larger portion of the light again increasing light harvesting. The big change in performance comes when the Au cells are illuminated in the reverse configuration. The efficiency now drops from 1.01% to 0.15% corresponding most significantly to a large drop from the J_{sc}. Despite the Au being semi-transparent the 25nm gold layer still blocks ~80% of light at 530nm [3].

These cells act as reference to which any further cells can be related too. The best performing cells in reverse illumination are those with a thin layer of evaporated gold and these are still only around 0.15% efficient.

7.3.2. s-DSC Utilising a silver and gold free Transparent Conductive Adhesive-laminate stack.

As explained in Section 7.1 the aim of this chapter is to create an s-DSC on a metallic substrate, which requires an alternative to the conventional state of art metallic back contacts. In this section the transparent conductive adhesive (developed in Chapter 3) is applied to a transparent conducting sheet (henceforth known as a TCA-laminate) that is then laminated onto a s-DSC replacing the evaporated metallic contacts. Since the TCA is designed for industrial applications, it was decided from the beginning to use a newly developed Ni metallic microgrid from Epigem (Epimesh 300™) for its cost saving over ITO alternatives. The Epimesh 300™ had previously been in development as an alternative to ITO coated PET in liquid DSC. Hence the wealth of knowledge and experience that had been built up for its use in PV by Epigem further reaffirmed it as a first choice transparent conducting sheet. An SEM micrograph of the grid and the TCA coated onto its surface can be seen in Figure 7.3, with a schematic of an s-DSC containing a TCA-laminate stack with the Epimesh 300™ shown in Figure 7.4.

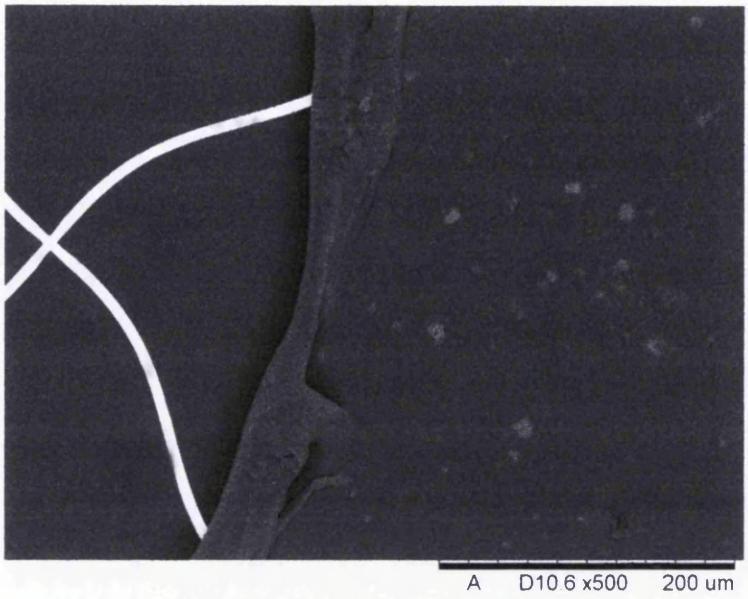

Figure 7.3. SEM micrograph of TCA-Laminate deposited onto a Epigem- Epimesh 300™ grid (visible on the left).

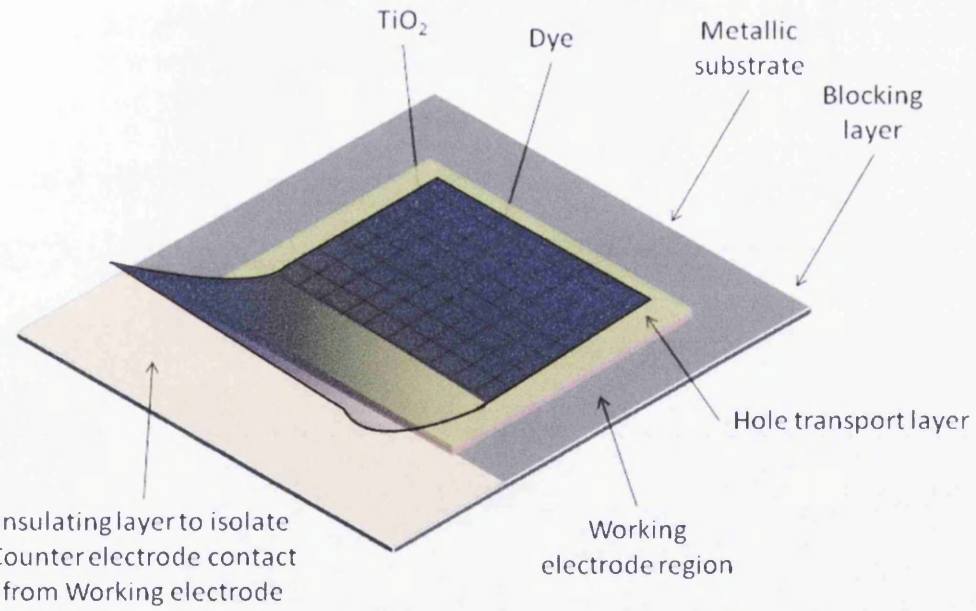

Figure 7.4. Schematic of s-DSC made using a metallic foil substrate and TCA-laminate.

In order to test the capability of the TCA-laminate in a conventional architecture (where forward measurements are also possible) s-DSCs with a TCA laminate were initially tested on FTO glass substrates. Ideally the TCA-laminate would be applied directly to the Spiro-OMeTAD over layer and this was the first method tried using a TCA containing 0.0175 PEDOT:PSS volume fraction. However cells fabricated in this way showed unusable, low currents as shown by Figure 7.5.

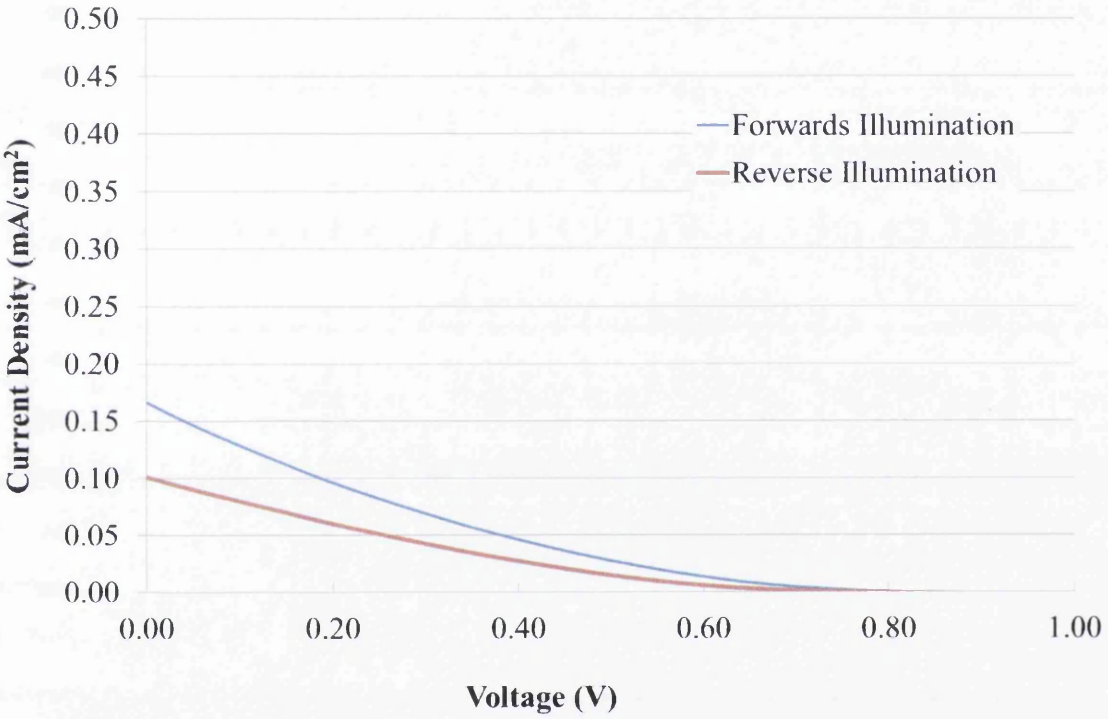

Figure 7.5. Photovoltaic performance of s-DSC cells made using a 0.0175 PEDOT:PSS ϕ TCA-laminate contacted directly onto the Spiro-OMeTAD capping layer in forwards and reverse illumination. Average of 5 cells.

The reason for this can be logically hypothesised as thus: owing to the poor conductivity of the Spiro-OMeTAD (2.0×10^{-5} S cm^{-1}) holes will be travelling only a short distance laterally and therefore the TCA will only collecting holes from directly under the PEDOT:PSS outcrops (outcrop shape and distribution shown in Figure 3.9) and a small region either side shown schematically in Figure 7.6. If a hole is produced at a location between two outcrops it is unlikely that it will be collected.

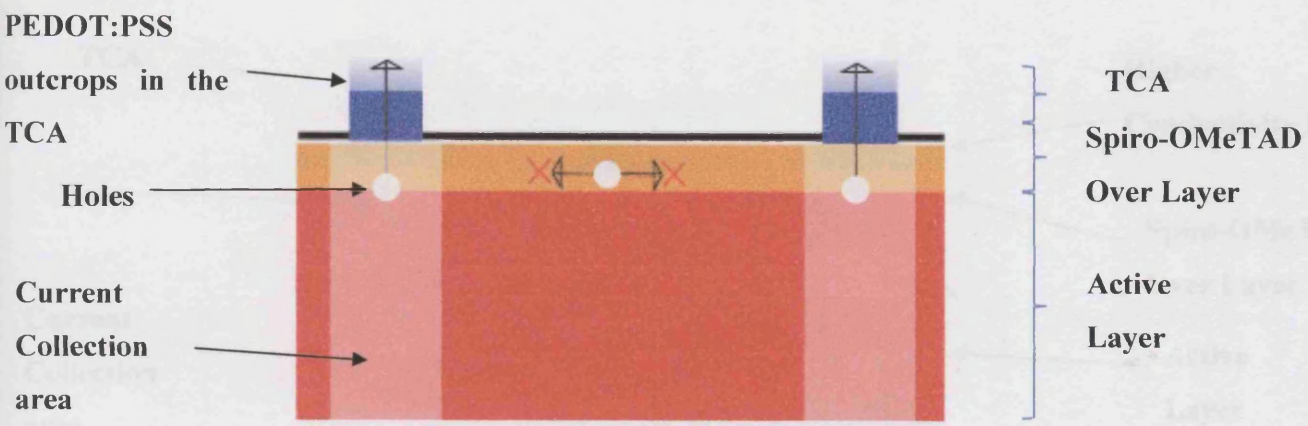

Figure 7.6. Schematic cross section through a s-DSC with a TCA contacted directly onto the Spiro-OMeTAD. Blue areas represent PEDOT:PSS outcrops in the TCA, faded areas are where current will be collected from.

Since in the TCA containing 0.0175 PEDOT:PSS volume fraction the total area of the outcrops would be ~1.75% (as shown in Section 3.2.3), disregarding other loss mechanisms, it can be assumed that the current will be 1.75% that of a s-DSC made with a Ag evaporated back contact (where it is assumed the coverage is 100%). Observing the J_{sc} in Figure 7.2 for the s-DSC contacted with an Ag evaporated contact and spin deposition at 1000RPM the current is 4.57mA/cm^2 and the J_{sc} of the cells in Figure 7.5 forwards illumination is 0.16mA/cm^2 which is 3.5% the J_{sc} of the Ag evaporated cell. The extra 1.75% can be accounted for by the fact that there will still be some, albeit small amount of, lateral movement of the holes in the Spiro-OMeTAD. There is also a second argument that the PEDOT:PSS in the TCA will not make intimate electrical contact with the Spiro-OMeTAD when just placed in contact such as would occur when the TCA in placed in contact with a Spiro-OMeTAD layer.

To increase the area for current collection, a material with a higher conductivity was placed between the TCA and the HTL such that a hole will be able to travel laterally within this layer over a larger distance than in the Spiro-OMeTAD. This makes it more likely to reach a PEDOT:PSS region in the TCA and be collected rather than recombining, shown schematically in Figure 7.7.

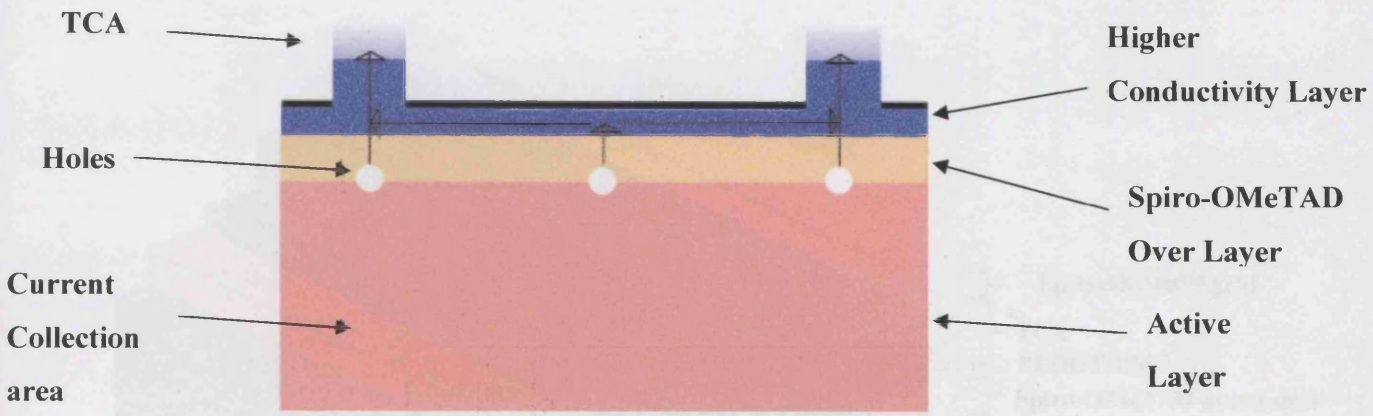

Figure 7.7. Schematic cross section through a s-DSC with a higher conducting layer between the Spiro-OMeTAD and the TCA. Blue areas represent PEDOT:PSS outcrops in the TCA, white area indicates current will be collected over the total width.

In addition, the laterally conducting layer requires transparency and so combined with its conductivity of 80 S cm^{-1} (4,000,000x that of Spiro-OMeTAD) PEDOT:PSS was the logical choice. PEDOT:PSS will also aid in increasing the electrical contact made, as PEDOT:PSS in the TCA should have a more compatible contact with a PEDOT:PSS layer as opposed to a Spiro-OMeTAD layer. Furthermore This PEDOT:PSS layer requires (a) a lower % water/propylene glycol content such that delamination of the Spiro-OMeTAD does not occur and (b) a curing regime lower than 120°C. Both these technical requirements were the motivation for the work presented in Chapter 4. Based on the findings of that work it was determined that a 4:1:1 mix of EL-P3145:Ethanol:IPA bar cast onto the surface of the Spiro-OMeTAD followed by drying with a high convection hot air dryer was the most appropriate approach. This would ensure the Spiro-OMeTAD in the cell stayed at as low a temperature as possible to stop any crystallizing of the Spiro-OMeTAD and dissociation of the dye from the titania [7]. The 4:1:1 PEDOT:PSS dilution still contained some water and this was found to delaminate the Spiro-OMeTAD, in order to mitigate this issue the Spiro-OMeTAD layer was deposited using 500rpm to give a thicker over-layer of Spiro-OMeTAD with the intention of stopping the wet solution coming into contact with the dye and/or titania. Indeed it was found when 1000rpm was used the cells simply did not function in this architecture even though it was demonstrated as optimum for metal evaporated contacts. The TCA was cast onto Epimesh 300™ (Epigem) and cured before lamination on top of the s-DSC using a finger pressure, the whole cell stack is therefore as shown in Figure 7.8.

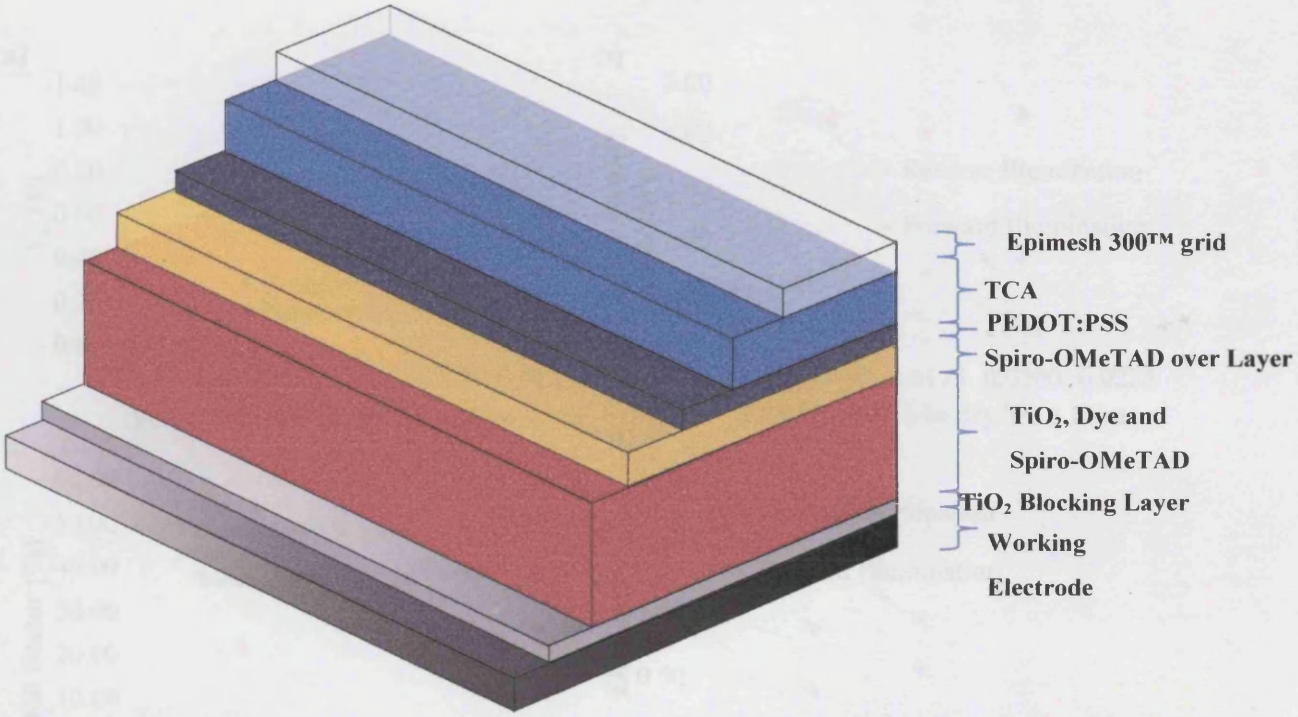

Figure 7.8. Schematic of an s-DSC made using a TCA-Laminate and PEDOT:PSS layer.

7.3.2.1 Impact on s-DSC performance of TCA made using differing ϕ of PEDOT:PSS in an acrylic emulsion matrix.

As shown in Chapter 3 the TCA can change its transparency, conductivity and tack depending on its PEDOT:PSS content and the dry film thickness. It is not immediately obvious which combination of PEDOT:PSS ϕ and dry film thickness would be most suited to s-DSC applications since the values are always a trade-off, higher conductivity – lower tack and transparency. To establish which TCA was most suitable for s-DSC first TCAs with varying ϕ were investigated, specifically those with 0.0100-0.0200 PEDOT:PSS ϕ in the dry TCA film. Cells utilising a TCA containing 0.0100-0.0125 adhesive did not show any notable performance, simply, the conductivity of the TCA was too poor to provide the external circuit with any significant current. Therefore Figure 7.9 shows the photovoltaic performance of cells made with 0.0150-0.0200 PEDOT:PSS ϕ in the dry TCA film for forwards and reverse illumination and for reference Table 7.2 shows the properties of the 0.0150, 0.0175 and 0.0200 TCAs.

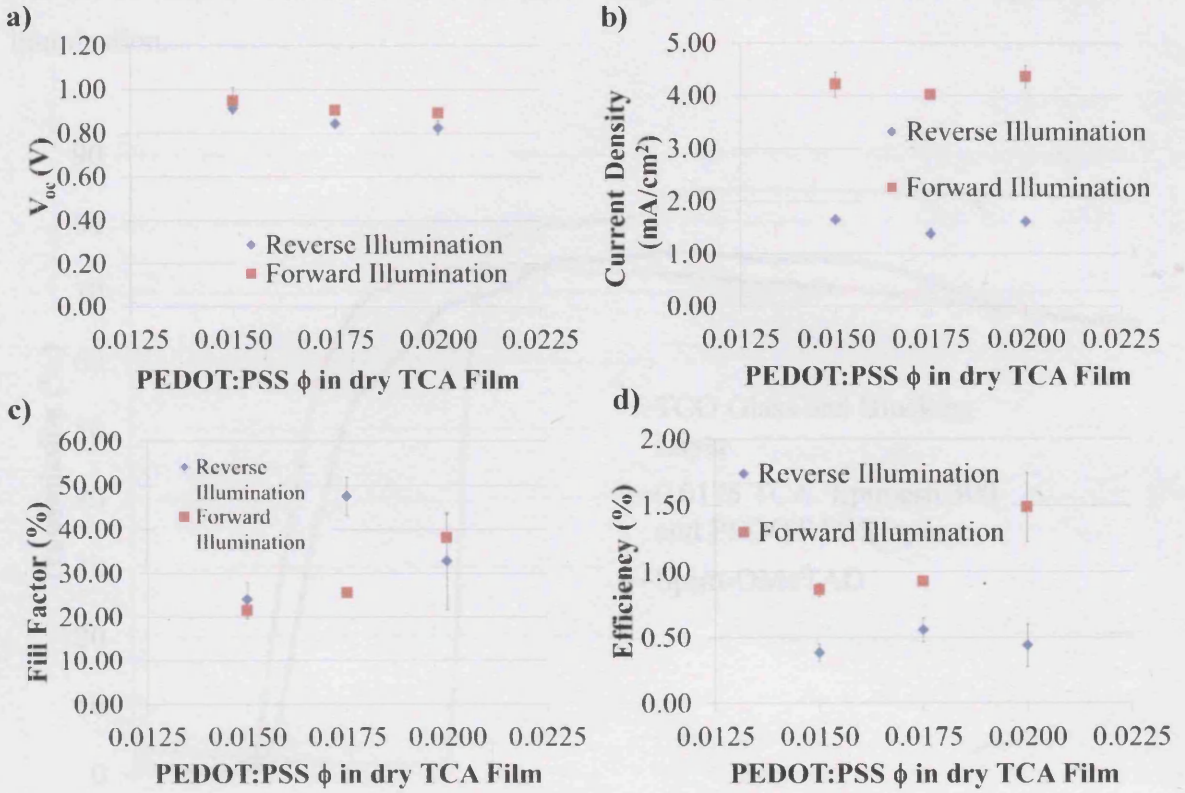

Figure 7.9. a)V_{oc}, b)J_{sc} c)FF and d)Efficiency of s-DSC cells made with a TCA-laminate of varying PEDOT:PSS ϕ in the dry film in forwards and reverse illumination. Average values for 5 cells per data point.

Table 7.2. Properties of TCAs made with 0.0150, 0.0175 and 0.0200 PEDOT:PSS ϕ cast at a wet film thickness of 90µm.

PEDOT:PSS ϕ	Dry Film Thickness (µm)	Conductivity (S cm^{-1})	Tack (cm)	Transparency (%)
0.0150	31.82	0.06	29.10	82.98
0.0175	29.11	0.13	35.20	81.58
0.0200	26.93	0.20	46.40	80.57

When looking at the values in Figure 7.9 it is immediately obvious that the efficiencies are lower in reverse illumination. The first thing to consider is the screening of light that would occur as the light travels through the two different electrodes. Figure 7.10

shows the transmission through (a) the TCO glass and blocking layer - forwards illumination and (b) the 32μm thick 0.0175 TCA, Epimesh 300™ and the PEDOT:PSS layer – reverse illumination.

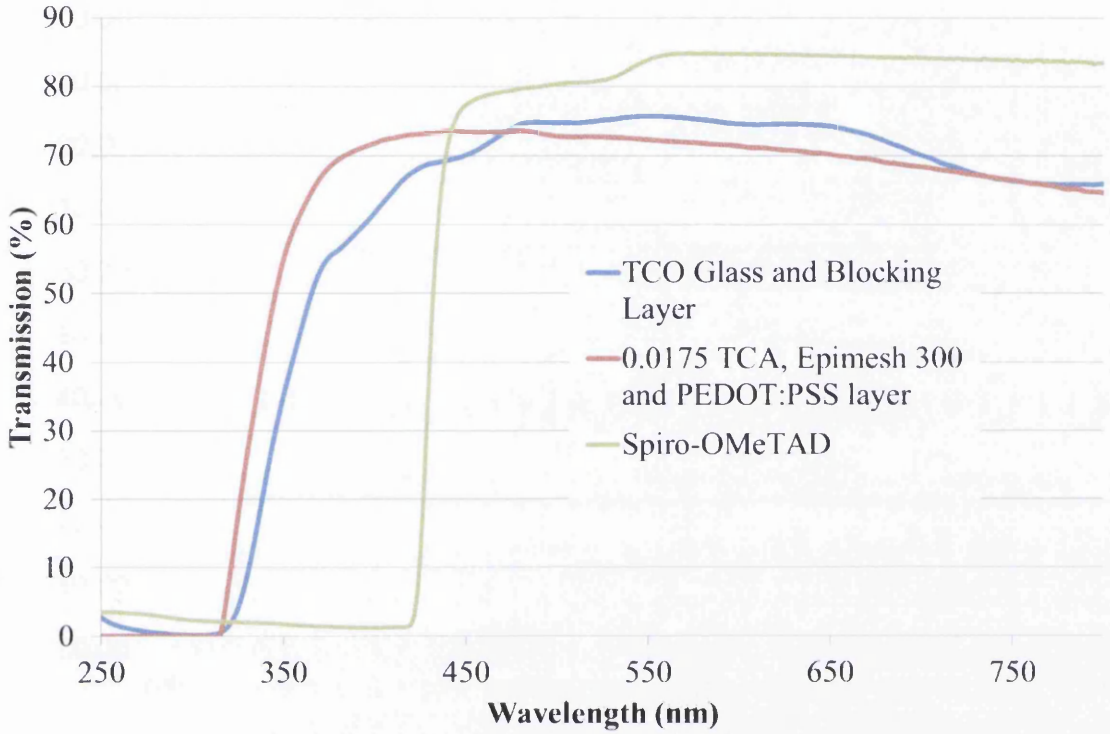

Figure 7.10. Transmittance of a TCO glass (TEC-7, Pilkington) and a blocking layer, a 37μm 0.0175 PEDOT:PSS ϕ TCA – Epimesh 300- PEDOT:PSS layer and a Spiro-OMeTAD layer.

It can be seen that there is no significant difference between the transmission of the TCO glass and blocking layer and that of the TCA-Epimesh 300™-PEDOT:PSS layer, with only a 3% difference at 530nm observed, therefore it would be hard to account for the drop in J_{sc} to the TCA, Epimesh 300™ or PEDOT:PSS layer. Also included in figure 7.10 is the transmission data for a film of just Spiro-OMeTAD and it can be seen that despite having a higher transmission above 440nm, it cuts off completely below. This suggests that a portion of the light that could have been utilised by the layer is screened by the Spiro-OMeTAD layer, lowering J_{sc}. Obviously light will have to travel through the TCA-laminate stack *and* the Spiro-OMeTAD layer making the overall transmission lower than for forwards illumination. The effect of this loss in transmission and filtering can be seen when observing the Incident Photon Conversion Efficiency (IPCE) in Figure 7.11. Not only is the IPCE curve

lower for cells in reverse but it shows no response before 410nm, due to the screening of the Spiro-OMeTAD + TCA-laminate (shown on the second axis) this is the same effect as has been shown previously when using UV filters [8]

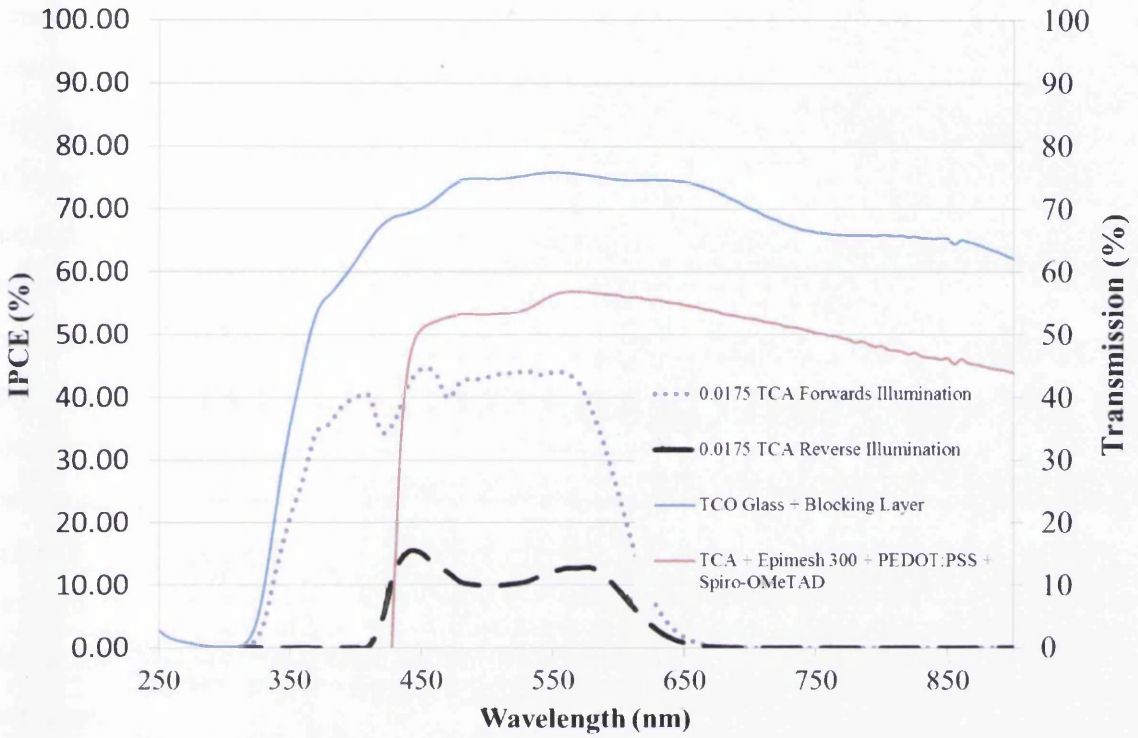

Figure 7.11. The IPCE of cells made with a 37μm 0.0175 TCA in forwards and reverse illumination set up with spro-OMeTAD included in the transmission.

It is interesting to note that there will be recombination losses associated with illumination in a reverse set up, similar to those found in liquid DSC, where the electron is generated at a point furthest away from the working electrode and as such has more chance to recombine. However since this is the first time these cells have been measured under reverse illumination (as previous studies involved a semi-transparent Au electrode) these loss mechanisms have not been previously investigated. It is therefore a next step in future work to look at the recombination dynamics and electron lifetimes of these cells in reverse, made possible by using this TCA-laminate.

When comparing the device properties of increasing PEDOT:PSS ϕ it can be seen that the transparency decreases as the PEDOT:PSS ϕ increases (as shown in Table 7.2) and this will contribute to the change in J_{sc} shown in reverse illumination. However at the same time the conductivity of the TCA is increasing which leads to no linear trend in the efficiency

being established. Table 7.2 also shows that the tack of the TCA will decreases as the PEDOT:PSS ϕ increases with the tack of the 0.0200 being lower than the 0.0175. This will affect how much and how well the PEDOT:PSS outcrops, in the TCA, will be in contact with under-layers. Firstly this will affect the performance of the cell and secondly it will affect the spread of data (accuracy and precision) as the same amount of contact area may not be consistent for each cell leading to the larger error bars seen in Figures 7.9a-d. For the reverse illuminated cells the conductivity increase associated with the increased PEDOT:PSS ϕ in the TCA will increase the fill factor, however, simultaneously the contact resistance will increase due a decrease in tack subsequently reducing fill factor. This again leads to no clear cut trend being established in the Fill Factor data for reverse illumination in Figure 7.9c. It can also be said that the effect of the increasing PEDOT:PSS content has in filtering out the UV and red end of the spectrum (shown in Section 3.2.6) could lead to the drop in V_{oc} by moving the quasi-fermi level, which is consistently lower for reverse than forwards illumination. It is hard to draw explicit trends from this data alone, and as outlined in Section 3.2.7 the changes in the TCA laminate are always a trade-off and therefore an optimal value for the cells will lie at an apex between maximum conductivity, transparency and tack. Errors in the data are largely caused by tack, or lack thereof, which decreases as the PEDOT:PSS ϕ in the TCA increases. A lack of tack means portions of the TCA (and ultimately the PEDOT:PSS sites) will not be in contact with the PEDOT:PSS layer and since this will be different between cells it manifests itself as a larger error.

The performance of the cells in forwards show a trend is more to be expected as the TCA conductivity is increased from 0.0150 to 0.0200, but the reasons for the trends are the same as those stated in reverse. The J_{sc} increases from 4.21 to 4.35 mA/cm^2, fill factor from 21.57 to 38.08% and the efficiency from 0.86 to 1.49% while the V_{oc} decreases from 0.95 to 0.89V. These are caused by an increase in the conductivity, decrease in contact resistance (as the conductivity of the TCA is the dominate factor in determining the contact resistance of the TCA as opposed to the tack, see Section 3.2.9), leading to less resistance in the cell, and more sites for current collection, this mainly leads to a marked increase in the FF which is the major factor in the efficiency change. Again there is larger errors in the data as the PEDOT:PSS ϕ in the TCA is increased due to the decrease in tack promoting uncertainty in individual cell output.

7.3.2.2. Impact of varying TCA thickness on s-DSC cells constructed with a TCA-Laminate

The previous section observed the impact on cell performance brought about by varying the PEDOT:PSS ϕ in the TCA. The other parameter of the TCA that can be changed is the dry film thickness. This mainly impacts on the light transmission through the TCA film (which wouldn't have an effect on s-DSCs in forwards illumination) and the tack of the film (as demonstrated in section 3.2.5). The tack will affect the number and contact of the PEDOT:PSS outcrops with the s-DSC. This will in turn affect the performance parameters of the cells and the error as outlined previously.

Firstly the performance of the cells in forwards illumination is considered. To measure this, the dry TCA film thickness was varied and its impact on the overall cell IV performance investigated with the results presented in Figure 7.12. Based on the results presented in Section 7.3.2.2 0.0175 and 0.0200 ϕ TCAs were chosen for this with the 0.0150 not used given its low FF and overall cell performance.

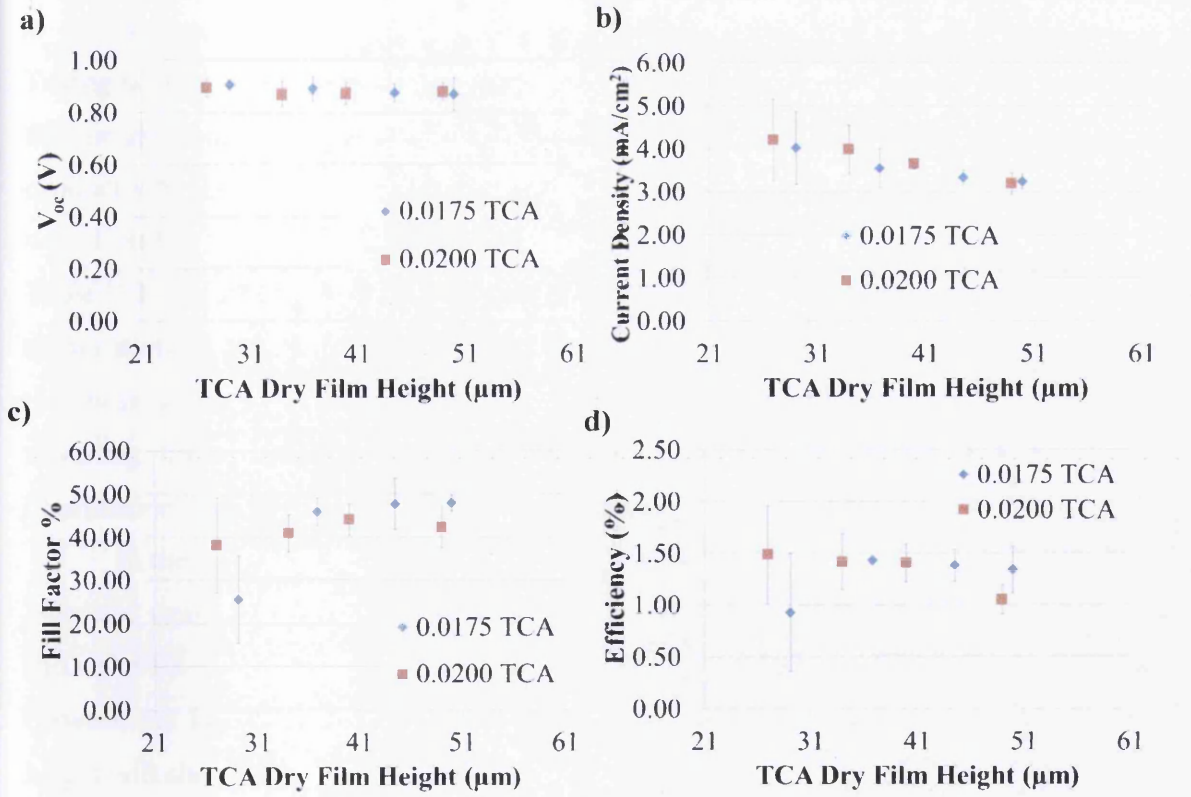

Figure 7.12. a)V_{oc}, b)J_{sc} c)FF and d)Efficiency of s-DSC cells made with a TCA-laminate of varying dry film thicknesses in forwards illumination. Average values for 5 cells per data point.

Table 7.3: Properties of TCAs made with 0.0175 and 0.0200 PEDOT:PSS ϕ with different dry film thicknesses.

0.0175	Dry Film Thickness (μm)	Conductivity (S cm^{-1})	Tack (cm)	Transmission at 530nm (%)
	29.11	0.13	35.20	81.52
	36.82	0.11	30.92	77.22
	45.00	0.09	27.55	73.88
	50.87	0.08	24.88	70.68
0.0200				
	26.93	0.31	46.40	80.57
	34.22	0.30	41.01	75.99
	40.00	0.28	30.88	75.47
	49.64	0.25	28.28	71.06

As can be seen in Figure 7.12 as dry film thickness is increased the J_{sc} decreases. Taking 0.0175 TCA as an example, J_{sc} drops from 4.27mA/cm^2 to 3.23mA/cm^2 as the dry film height is increased from 29 to 51μm. As the films have (within a range) the same bulk conductivity then the increasing distance of travel through the film (increasing resistance) would lead to this J_{sc} drop. As the dry film thickness increases so does the tack as shown in Table 7.3. As stated in previous sections this will decrease the resistance of the cell and shows itself as a higher FF which can be seen to increase in Figure 7.12.c as the dry film thickness increases. The V_{oc} remains largely constant between the two as the light is travelling through the same material in both the 0.0175 and 0.0200 cells in forwards illumination and similar filtering of the light would occur.

In the 0.0200 TCA the error in the fill factor and efficiency decrease as the film height increases again due to a more consistent and increased bonding between the TCA and the PEDOT:PSS layer. The J_{sc} and the efficiency all decrease despite the increased contact between the layers, again this is the same as for the 0.0175 TCA cells, as the increase in height will show an increased series resistance (see Section 3.2.4).

The impact of film thickness on IV performance of cells in reverse illumination (through the TCA-laminate) is an important consideration. IV data for TCA-laminate cells

made with 0.0175 and 0.0200 TCA of varying heights in reverse illumination and the results presented in Table 7.4.

Table 7.4 Cell performance properties of s-DSC cells with a TCA of 0.0175 and 0.0200 PEDOT:PSS volume fraction in the dry film in over a range of dry film heights in reverse illumination.

PEDOT:PSS ϕ in TCA	Dry TCA film height	V_{oc} /V	J_{sc} / mA/cm^2	Fill Factor /%	Efficiency /%
0.0175	29	0.84	1.39	47.54	0.56
	37	0.83	2.13	46.76	0.78
	45	0.82	2.77	37.31	0.86
	50	0.82	2.11	46.04	0.76
0.0200	27	0.83	1.61	32.81	0.44
	34	0.81	1.83	35.90	0.52
	40	0.81	1.66	39.60	0.52
	49	0.84	1.84	41.86	0.65

As can be seen in Table 7.4 there are increases and decreases similar to the results of the forward illumination, presented in Figure 7.12, following the trends of changing current, tack and light transmission. Interestingly when observing the 0.0175 data the J_{sc} initially increases from 1.39 to 2.77mA/cm^2 as the height of the TCA increases from 29 to 45μm and then decreases to 2.11mA/cm^2 as the height is again increased to 50μm. The initial increase is despite the fact that light transmission is decreasing and therefore can largely be due to an the exponential increase in the tack. Once the height is further increased to 50μm the tack will have begun to plateau and the dominating factor again would be loss of transmission and increased series resistance.

What this data ultimately shows is that the use of the TCA in s-DSC will always be a trade-off between its parameters and as such must be adapted accordingly. Also critically the V_{oc} in all the cells remains relatively high and therefore shows a good band matching between the PEDOT:PSS and the Spiro-OMeTAD. For these types of devices a TCA with 0.0175 PEDOT:PSS ϕ and a dry film thickness of 37μm offers the highest efficiency of 1.43% combined with the lowest error, 0.02% StDev in forwards illumination and 0.78%

with 0.02% StDev in reverse illumination and therefore has been selected for further investigation.

It is noteworthy to compare this data to the conventional metal evaporated cells presented in Section 7.3.1. The cells made with a 0.0175 TCA at 37μm dry film height showed an efficiency that was almost 70% of the highest performing Ag evaporated contact cell (2.08% using Spiro-OMeTAD deposited at 1000rpm) and more important it was almost 5x higher than the highest performing reverse illuminated device (0.16% using Au evaporated contact).The reason for this is quite simply due to the amount of light that reaches the active area. The Au cells have a ~20% transmission whereas the PEDOT:PSS laminate stack has a 72% transmission at 530nm. In addition the combination of an Epimesh 300™ grid with low sheet resistance and a thin (37μm) TCA leads to a comparatively higher conductivity collection electrode than a thin Au evaporated layer

7.3.2.3. Considerations for s-DSC stack and design using a TCA-Laminate

An argument could be used that since the PEDOT:PSS is capable of lateral conduction there is little need for a TCA- grid combination. Whilst this is true over small distances the current collection becomes poor over larger areas.

Figure 7.13 shows the different areas of current collection for cells made with: no laminate (the back contact is simply PEDOT:PSS contacted with silver paint on one edge), cells made with the 0.0175 TCA – masked so that on the area of the cell with laminate on it is exposed and those same cells measured but without masking i.e. collection will also occur from PEDOT:PSS around the edge of the TCA. The resulting cell performance is shown in Figure 7.14.

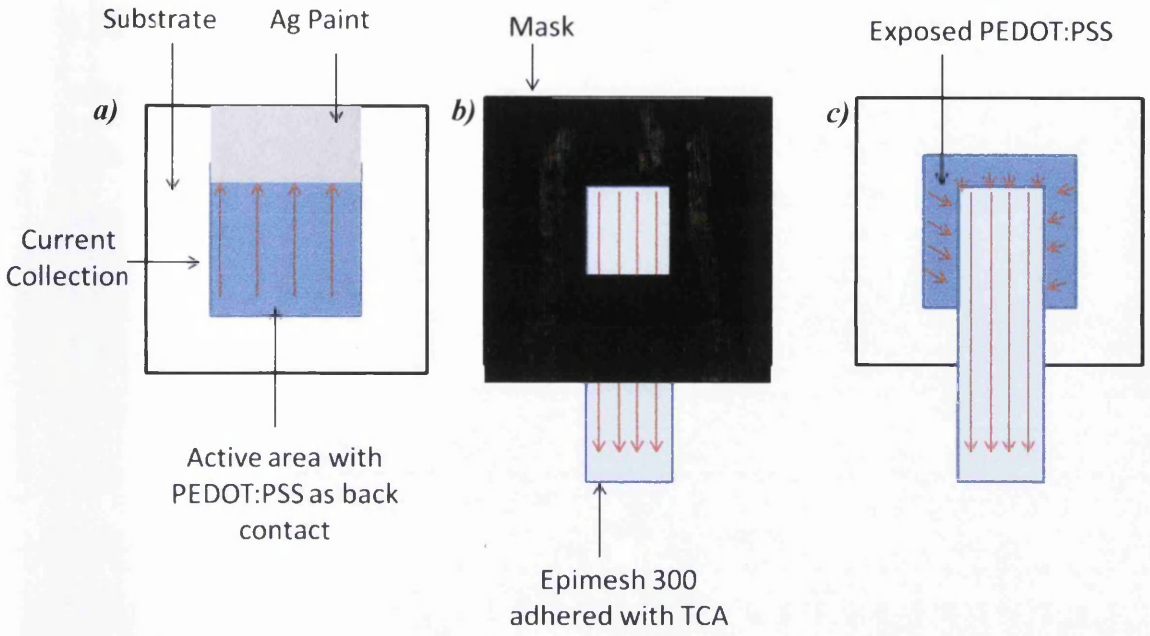

Figure 7.13. Schematic of cells made with a) PEDOT:PSS as the back contact (with Ag paint as a contact for measurement) b) with the addition of a grid and TCA as the back contact on to A and masked for testing and c) As B but without a mask. Red lines indicate areas and directions of current collection.

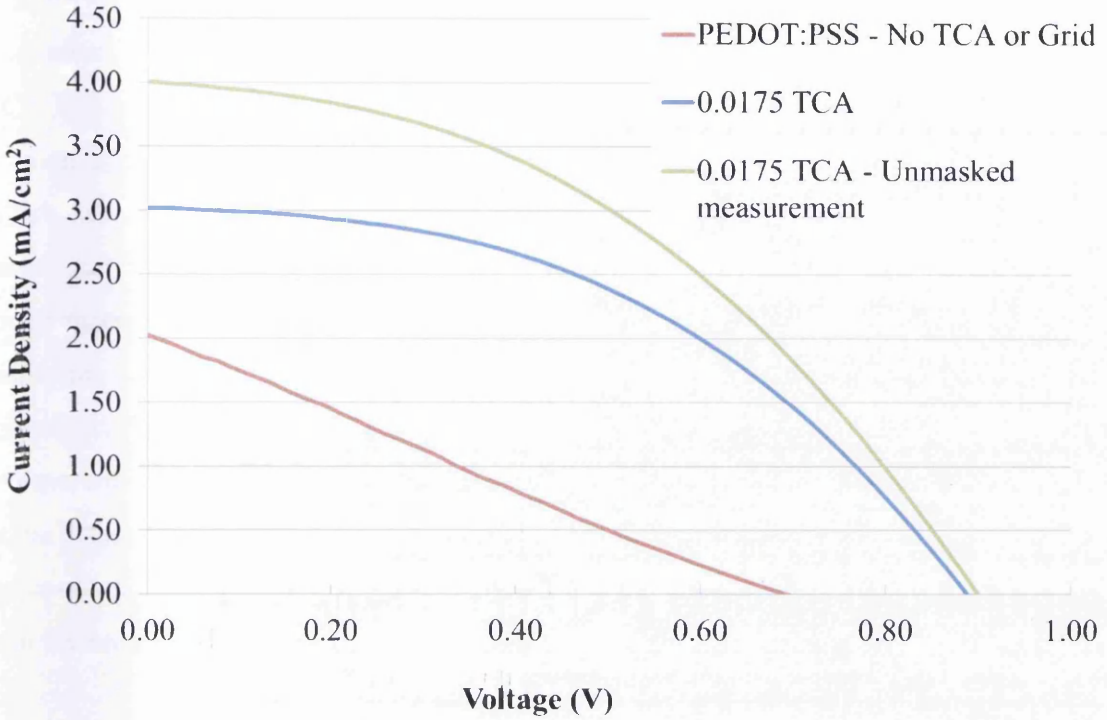

Figure 7.14. Current voltage characteristics of s-DSC cells made with (a) PEDOT:PSS (b) TCA-grid masked and (c) TCA-grid unmasked

It can be seen from the graph in Figure 7.14 that the cells made with just PEDOT:PSS (1.2cm^2 active area) and no TCA or grid show poor photovoltaic properties including poor fill factors (25%). This shows that while current is being generated and collected there is significant resistance through the PEDOT:PSS layer, exacerbated by the lateral distance. When the TCA and grid are added (and measured masked) the J_{sc} rises from 2.02 to 3.54mA/cm^2 with a large change in the fill factor increasing from 25 to 45%. This is to be expected since the lateral conductivity of the grid (Epimesh 300™) is quoted as 1.2ohm/sq [9] compared to the PEDOT:PSS (EL-P3145) at 240ohm/sq [10]. The bulk resistivity of the TCA is higher than that of the PEDOT:PSS but in this architecture the current is only passing through a 37μm layer. To put it another way, a hole generated at the furthest distance from the silver contact in the cells made without a grid will have to travel 1cm through a 240Ω/□ material whereas in the TCA and grid cells it has to travel (albeit a minimum) only 37μm through a material with a higher bulk resistivity and then 1cm through a material with 200x less sheet resistance. The discrepancy in the V_{oc} can be ascribed to the less than ideal contact made with the PEDOT:PSS by the silver paint and the lower conduction of the PEDOT:PSS increasing series resistance. While this does show that the TCA grid is needed it also shows

that the PEDOT:PSS *can* collect current on its own. As shown by the cells tested masked and unmasked in Figure 7.14 a larger current can be collected if an area not directly under the TCA is utilised. This is important from a scale up point of view since while the TCA does provide adhesion it is not a permanent bond. However one could envisage a TCA on a grid which was intersected periodically by a permanent adhesive (such as an epoxy). The permanent adhesive would ensure the TCA remained in contact with the PEDOT:PSS layer for an extended period of time and provided it had a degree of transparency, the PEDOT:PSS below the adhesive would still collect current enabling that area to be active. This is shown schematically in Figure 7.15 where provided that the permanent adhesive above it is transparent the area between the dashed lines can provide current to the cell. This is the same as the effect described in Section 7.3.2 where the PEDOT:PSS can laterally transfer current to the conducting outcrops of the TCA (however this is described on the centimetre scale rather than the nanometre).

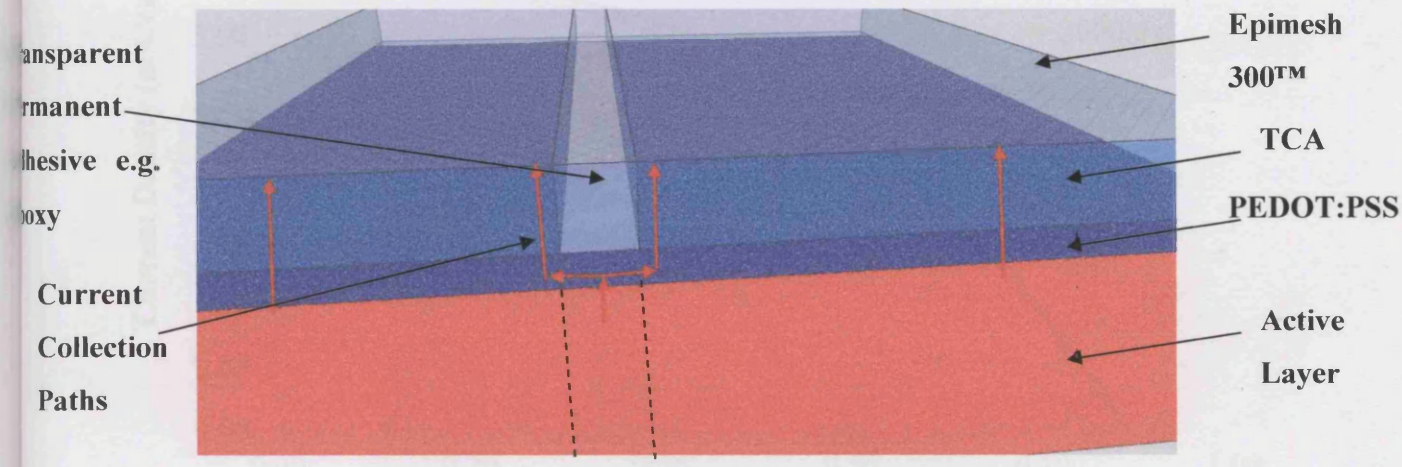

Figure 7.15. 3D representation of a TCA-laminate adhered onto an s-DSC and held securely by a strip of permanent adhesive. The dashed area represents an area that will still be active despite not being below an area of conductive adhesive.

7.3.2.4. Qualitative lifetime of s-DSCs constructed using a TCA-Laminate

While it has not been exclusively investigated within the scope of this study the lifetime of these cells is of the upmost importance. It is important to note that the cells here have not been exposed to rigorous standardised conditions but they act simply as an indication of what may happen to cells exposed over time. The results of s-DSC cells made with 0.0175 ϕ TCA at 37μm and VDC3 (a developmental laminate by Mitsubishi Plastics with water barrier and UV screening properties) film adhered to the top, measured initially and after 3000hrs in the dark in ambient lab conditions are shown in Figures 7.16-18.

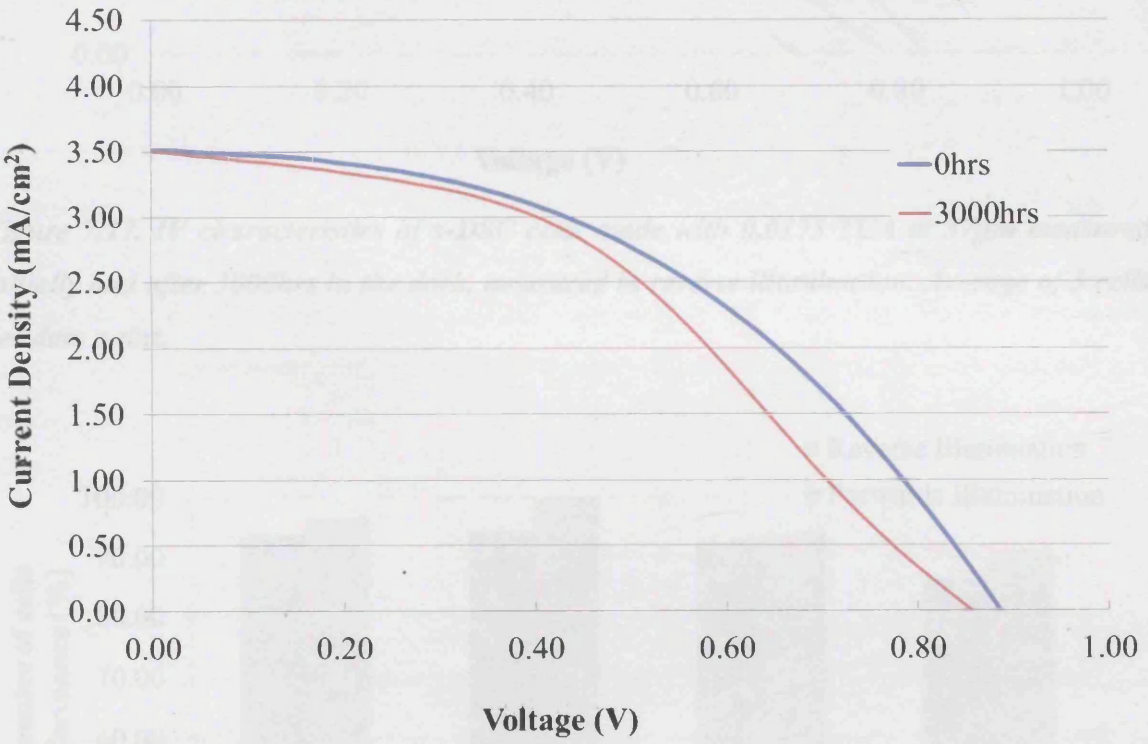

Figure 7.16. IV characteristics of s-DSC cells made with 0.0175 TCA at 37μm measured initially and after 3000hrs in the dark, measured in forwards illumination. Average of 5 cells per data point.

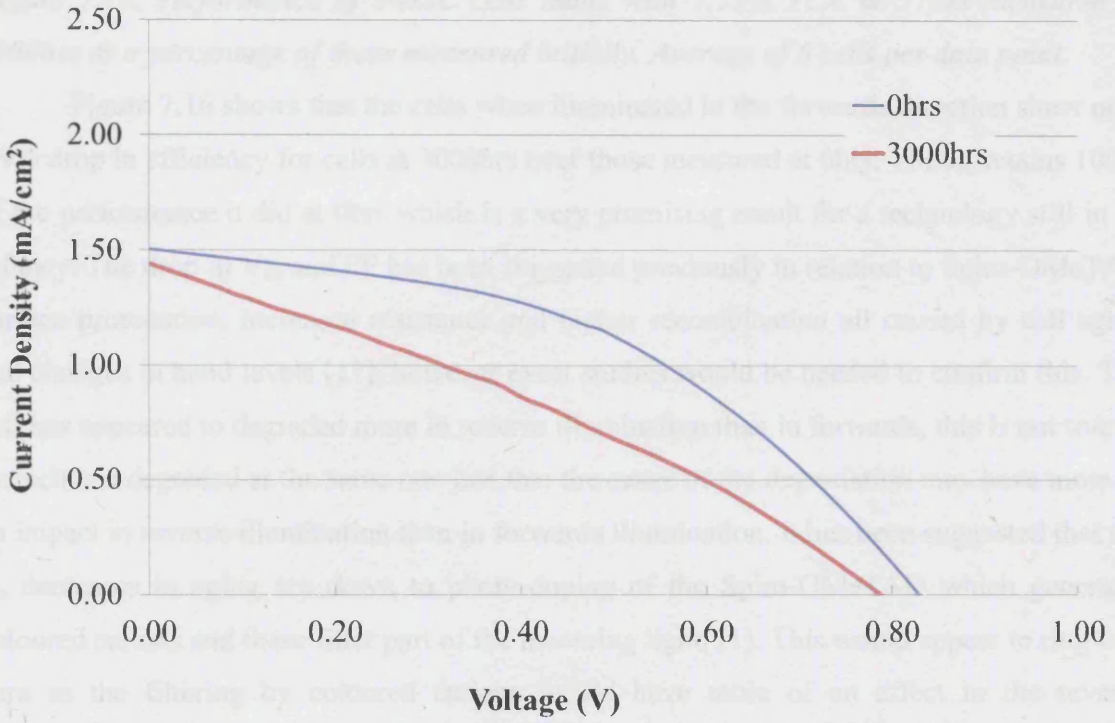

Figure 7.17. IV characteristics of s-DSC cells made with 0.0175 TCA at 37µm measured initially and after 3000hrs in the dark, measured in reverse illumination. Average of 5 cells per data point.

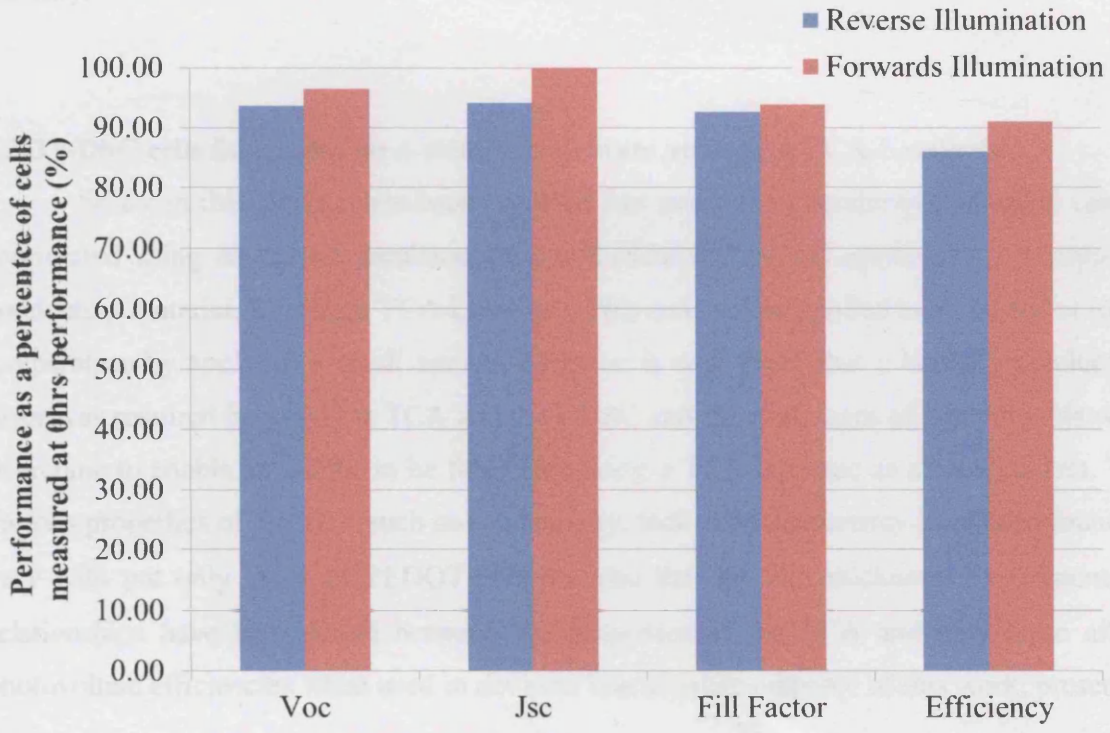

Figure 7.18. Performance of s-DSC cells made with 1.75% TCA at 37μm measured at 3000hrs as a percentage of those measured initially. Average of 5 cells per data point.

Figure 7.16 shows that the cells when illuminated in the forwards direction show only a 9% drop in efficiency for cells at 3000hrs over those measured at 0hrs. The J_{sc} retains 100% of the performance it did at 0hrs which is a very promising result for a technology still in its infancy. The drop in V_{oc} and FF has been suggested previously in relation to Spiro-OMeTAD surface protonation, increased resistance and higher recombination all caused by cell aging and changes in band levels [11], however exact studies would be needed to confirm this. The cell has appeared to degraded more in reverse illumination than in forwards, this is not true as the cell has degraded at the same rate just that the cause of the degradation may have more of an impact in reverse illumination than in forwards illumination. It has been suggested that the J_{sc} decreases in aging are down to photo-doping of the Spiro-OMeTAD which generates coloured cations and these filter part of the incoming light[11]. This would appear to ring true here as the filtering by coloured cations would have more of an effect in the reverse illumination, as the light has to travel through more of the Spiro-OMeTAD, which is what is shown by the data in Figures 7.17 and 7.18 however much more work would be needed to confirm this. It is important to note that the efficiency is still 86% after 3000 hours and this provides some encouragement for the developments required to achieve suitable lifetimes and stability.

7.3.3 s-DSC cells fabricated on a metallic substrate utilising a TCA-Laminate

So far in this thesis it has been reported that transparent conductive adhesive can be formulated using an acrylic emulsion PSA and PEDOT:PSS and applied to a transparent conducting material, forming a TCA-Laminate. This can then be applied to an s-DSC at room temperature by applying a small amount of force. It was found that a laterally conducting layer was required between the TCA and the s-DSC and the challenges of applying this were overcome to enable an s-DSC to be fabricated using a TCA-laminate as a back contact. The various properties of the TCA such as conductivity, tack and transparency have been found to vary with not only the ϕ of PEDOT:PSS but also the dry film thickness. Experimentally relationships have been found between the properties of the TCA and how these affect photovoltaic efficiencies when used in devices. The ultimate outcome of this work, presented

within this section, is to fabricate an s-DSC on a metallic substrate achieving the following technology developments,

1. Fully printed
2. Atmospherically produced
3. Silver and gold free
4. FTO/ITO free
5. Fabricated on steel substrates

A number of metallic substrates represented viable initial candidates (e.g. titanium) however one substrate appeared to be an obvious choice to test initially due to its provision from Tata steel and low cost commercial availability electrolytic chrome-coated steel (ECCS). This is due to its smooth surface finish (to prevent electrical shorting to the cathode) and its anti-oxidation layer to help prevent the formation of resistive oxides during sintering of the active layer. It was beyond the scope of this work to investigate how the metals various properties (surface roughness, composition *etc.*) affected photovoltaic performance and how other metallic substrates similarly had an impact on s-DSCs. However the understanding of the metals interaction and properties with photovoltaic performance is an area of significant interest and future work.

An FIB cross section of an s-DSC cell made on an ECCS substrate using a 0.0175 ϕ TCA-laminate can be seen in figure 7.19. In the previous section the TCA-laminate showed great potential and therefore have been compared to other s-DSCs made using conventional evaporation techniques and s-DSC made on FTO glass using a TCA-Laminate presented in previous sections of this chapter. For ease the data has been amalgamated in Table 7.5 for reference.

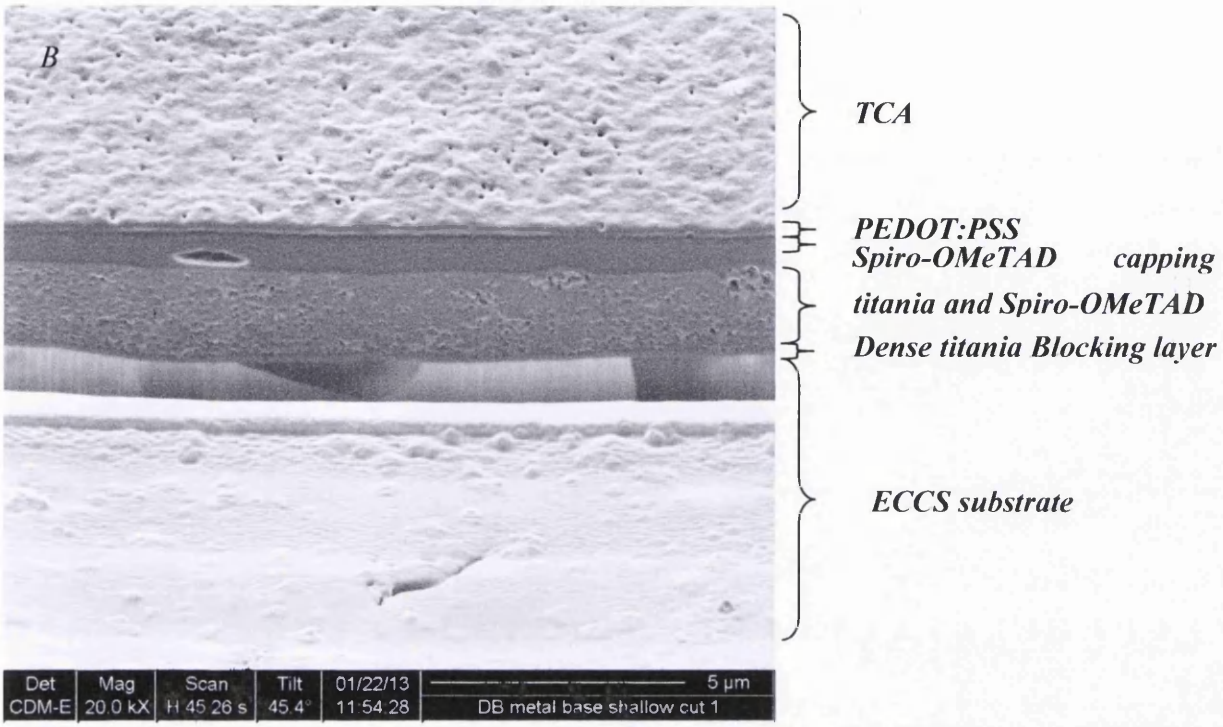

Figure 7.19. Focussed Ion Beam (FIB) micrograph of a cross-section through a complete TCA laminate s-DSC (layer thickness not accurate to scale due to tilt).

Table 7.5. Photovoltaic characteristics for s-DSC cells fabricated on a range of substrates. Average of 5 cells per data set

	Illumination Direction	V_{oc} (V)	J_{sc} (mA/cm^2)	Fill Factor	Efficiency (%)
Glass Substrate & Silver	Forward	0.89 (±0.01)	4.22 (±0.53)	55.58 (±4.60)	2.08 (±0.12)
Glass Substrate & Gold	Forward	0.90 (±0.03)	1.68 (±0.24)	65.96 (±6.94)	1.01 (±0.25)
Glass Substrate & TCA Laminate	Forward	0.89 (±0.04)	3.54 (±0.46)	45.85 (±3.14)	1.43 (±0.02)
ECCS & TCA Laminate	Reverse	0.85 (±0.04)	2.64 (±0.59)	65.31 (±10.19)	1.44 (±0.26)
Glass Substrate & Gold	Reverse	0.88 (±0.03)	0.27 (±0.05)	67.70 (±8.16)	0.16 (±0.03)
Glass Substrate & TCA Laminate	Reverse	0.83 (±0.04)	2.13 (±0.68)	46.76 (±13.90)	0.78 (±0.02)

It can be seen that much like the glass cells made with a TCA-Laminate the efficiency of the ECCS substrate cells is higher than the Au evaporated cells in reverse illumination.

Again this is due to the poor transparency of the Au compared with that of the TCA-Laminate. Another very promising aspect is that the cells made with a TCA laminate on ECCS have a higher efficiency than those made on glass in reverse illumination, mainly due to an increased J_{sc}. This is due to increased back reflection from ECCS substrate compared with an FTO glass substrate which can be seen in Figure 7.20. The increased reflection will in turn increase light harvesting within the cell, increasing the J_{sc}, which has been shown when evaporated silver contacts are used in conventional cells [1].

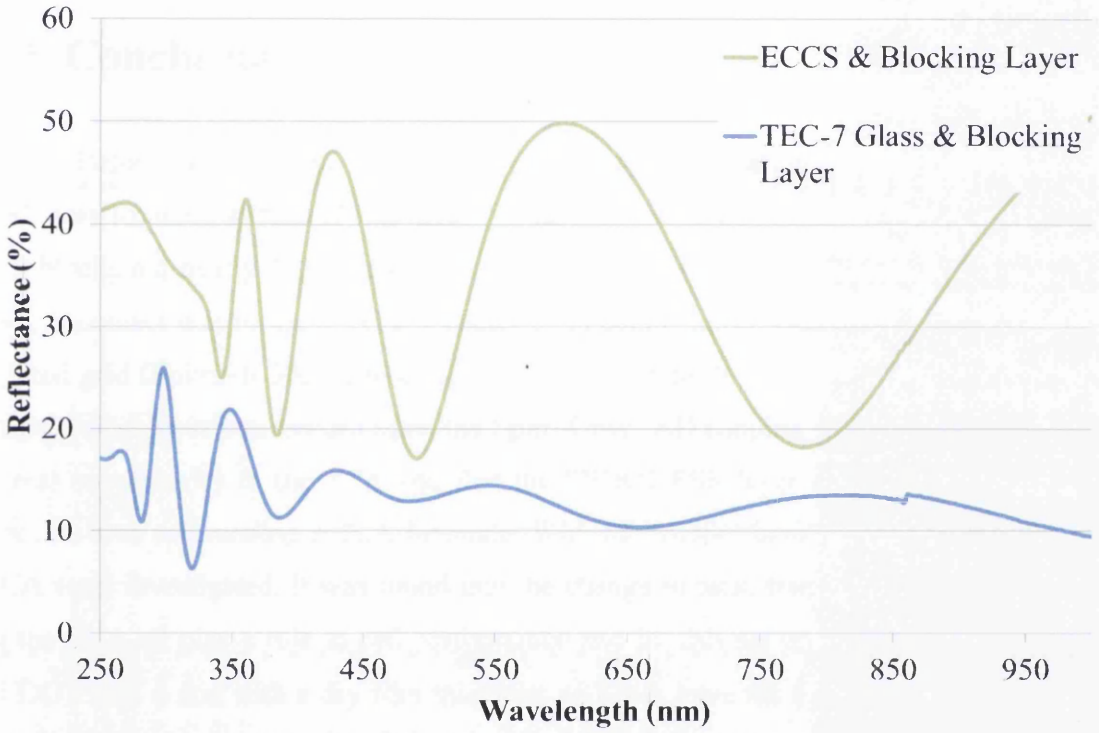

Figure 7.20. The reflectance spectra as a function of wavelength of FTO coated TEC-7 glass and ECCS with a titanium blocking layer on the surface showing the characteristics thin film interference patterns.

When compared with the TCA-Laminate cell made on glass in forwards illumination the ECCS based cell has a near identical efficiency. The J_{sc} and V_{oc} are both lower for metal based cells at 2.64mA/cm^2 and 0.85V respectively however the FF increases by 20%. As the substrate is metallic it has a much higher lateral conductivity that increases the current collecting properties of the substrate across the area of the cell. The ECCS based cells are still lower than the Ag evaporated contact s-DSCs for the same reasons as TCA-Laminate cells

made on glass in reverse; the screening of the incoming light by the Spiro-OMeTAD layer and its negative impact on the J_{sc} (as discussed in Section 7.3.1).

A newly developed TCA-Laminate material can be easily formulated and is applicable to photovoltaic applications. It has been shown that a solid state dye-sensitized solar cell device can be made on a metallic substrate, fabricated using a TCA-Laminate, that demonstrates comparable photovoltaic conversion efficiencies to conventional rigid devices made using FTO glass and an evaporated metal contact.

7.4. Conclusions

Before this work the most widely used method to obtain reverse illumination in s-DSC was to apply a thin (25nm) layer of Au. While this does provide semi-transparency it still blocks out nearly 80% of the incoming light and efficiencies are low. An alternative to the Au contact was to use a TCA (Chapter 3) in combination with a commercially available printed grid (Epimesh 300™) to create a TCA-Laminate. It was initially found that an extra PEDOT:PSS layer was needed upon the Spiro-OMeTAD capping layer to provide additional lateral conductivity to the TCA and that the PEDOT:PSS layer could even collect current from an area surrounding a TCA laminate. With this s-DSC laminate stack variations in the TCA were investigated. It was found that the change in tack, transparency and conductivity of the TCA all play a role in cell performance and for this set up a TCA containing 0.0175 PEDOT:PSS ϕ and with a dry film thickness of 37μm gave the best performing cells. From this cells were fabricated on ECCS substrate where it was found cells could be made with this substrate that performed better than TCA-Laminate cells made on glass in reverse illumination (due to better reflection off the substrate), as good as them in forwards illumination and only 0.64% behind glass based cells made with an Ag evaporated back contact. This has significant implications for this and other emerging photovoltaic technologies. This combined with some evidence that the TCA-Laminate s-DSCs do not significantly degrade up to 3000hrs represents a major breakthrough in this technology. Not only can s-DSCs cells be made on flexible, cheaper substrates but they now have the potential to be scaled up and produced continuously without the barriers previously inherent in their construction.

7.4. References

[1] H. Snaith, A. Moule, C. Klein, K. Meerholz, R. Friend, M. Grätzel, *Nano. Lett.* **7,** 3372, (2007).

[2] Konarka, WO 20120/107795 A1, 23 Sept (2010).

[3] I. Bruder, BASF Ludwigshafen, Unpublished Result, (2012)

[4] J. Burschka, A. Dualeh, F. Kessler, E. Baranoff, N-L. Cevey-Ha, C. Yi, M. Nazeeruddin, M. Grätzel, *Am. Chem. Soc.* **133,** 18042, (2011).

[5] I-K. Ding, Thesis, Stanford University, (2011).

[6] K. Kalyanasundaram, *Dye-Sensitized Solar Cells,* EPFL Press, (2010).

[7] B. Hardin, W. Gaynor, I-K. Ding, S. Rim, P. Peumans, M. McGehee, *Org. Electron.*, **12,** 875, (2011).

[8] M. Carnie, T. Watson, D. Worsley, *Int. J. Phot.*, 506132, (2012)

[9] http://epigem.co.uk/products/optical-film/epimesh-300s

[10] http://www.agfa.com/sp/global/en/binaries/Screen-Printing%20inks-2013v1.0_tcm611-86918.pdf

[11] S-J. Moon, Thesis no. 4977, EPFL, (2010).

[12] T. Watson, I. Mabbett, H. Wang, L. Peter, D. Worsley, *Prog. Photovol.,* **19,** 482, (2011).

8. Electroluminescent Devices Utilising a TCA

8.1. Introduction

Electroluminescent (EL) lighting is now considered a mature technology however one of the remaining issues still affecting the technology is that expensive ITO metal oxide coated substrate and/or vacuum deposit contacts are still used during their fabrication. While metal oxides still provide the highest transparency and conductivity their lack of easy processing and well has high cost has led to them becoming the barrier to success for many technologies [1]. Recently there has been great interest in the use of Poly-(3,4-ethylenedioxythiphene): Poly-(styrene-sulphonate) (PEDOT:PSS) as an alternative to metal oxide films [2]. Indeed it has been shown to be suitable replacement in OPV [3-4], PDLC [5] and also the aforementioned OLED [6]. Since the breakthrough in 1989, when doping of the PEDOT with the PSS counter-anion allowed a stable microdispersion to form in water, development of the technology has now lead to commercially available PEDOT:PSS formulations for a wide range of applications including light emitting devices.

It has been shown that PEDOT:PSS can be used in EL devices where the ITO coated substrate can be substituted for cheaper opaque substrates such as paper [5,7] as well as on other substrates such as polycarbonate [8]. Figure 8.1 illustrates the so called top emission set up whereby PEDOT:PSS is used as the transparent contact through which light is emitted. This not only means that an opaque substrate can be used but also that the device can now be fully printed. However using PEDOT:PSS directly only gives a performance of 50% when compared with a conventional cell and the reason for this is attributed to incomplete coverage of the phosphor particles by the thin PEDOT:PSS layer.

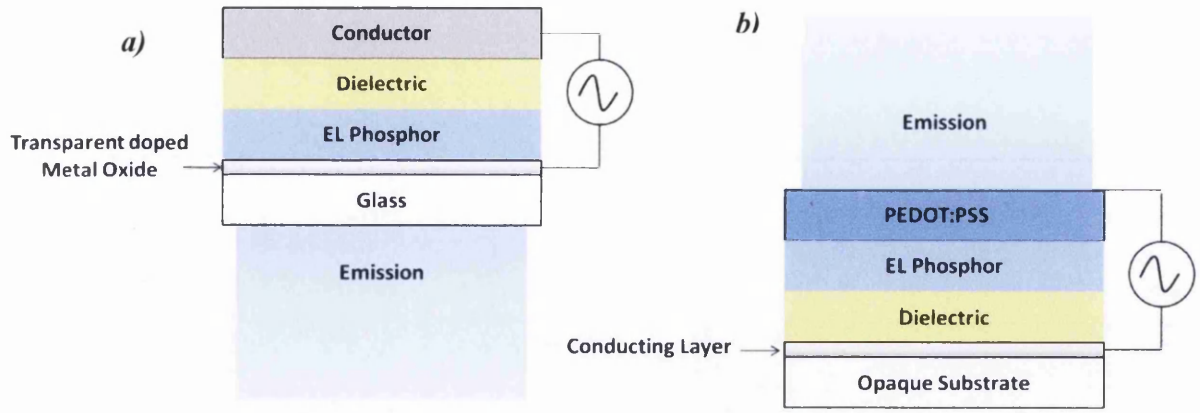

Figure 8.1. Cross section schematic of a) a conventional bottom emission EL device using a doped metal oxide coated glass and b) a top emission device using PEDOT:PSS and an opaque substrate.

In the previous chapters of this thesis it has been shown that when PEDOT:PSS is mixed with an acrylic based adhesive a Transparent Conductive Adhesive (TCA) can be made. As well as having the adhesive advantage over conventional PEDOT:PSS it can also be cured separately, applied at room temperature, contact moisture sensitive layers and the soft nature of the adhesive makes it conformal to a wide range of geometries. In this Chapter it is proposed to use this TCA, in conjunction with a printed grid, to form a transparent conducting contact to an EL device by lamination, eliminating the need for a printed silver contact and reducing cost.

In addition to this an EL device fabricated on aluminium using the TCA set up will also be tested. Aluminium has may advantages over previously used substrate materials in that it is low cost, widely available, has excellent barrier properties, can be made in a variety of different thicknesses depending on the application. In addition to this aluminium is already coated on a continuous roll-to-roll process and coating of an EL and lamination is applicable without significant additional cost. The aim of this investigation was to demonstrate that a TCA can be utilised within an opto-electronic device that emitted light (EL lamp) rather than received it (s-DSC) and operated using a high AC electric field (rather than electron injection). How the properties of the TCA influence lamp emission and its application to an aluminium substrate will be considered

This method of fabrication opens up the possibility of creating building integrated lighting for illuminating large areas, such as the inside of warehouses, without significantly changing the design of the building. Using aluminium sheet instead of ITO coated PET reduces the cost by a factor of 10 initially – ITO PET: €20 per m^2, Aluminium sheet: €2 per m^2. In addition to an obvious cost saving a device fabricated using a lamination configuration

would enable typical large scale coating processes leading to the potential for building integrated scale.

8.2. Experimental

EL lamps were fabricated as outlined in Section 2.6. Lamps are quoted as the % output of a conventional EL device that has a silver ink back contact made on a FTO substrate (Tec-7, Pilkington).

A TCA was fabricated as has been reported in Chapter 3 using PEDOT:PSS (EL-P3145, AGFA) within an acrylic based adhesive matrix (F46, Styccobond™) coated onto a micro grid on PET (Epimesh 300™, Epigem). The PEDOT:PSS in the TCA is quoted as the volume fraction (ϕ) of PEDOT:PSS within the dry film (Section 2.1) which varied between 0.0100 – 0.0175.

8.3. Results and Discussion

A summary of the TCA's properties at different PEDOT:PSS ϕ and wet film thicknesses is shown in Table 8.1, see Chapter 3 for more details, and results of how a 0.0100 TCA coated onto an Epimesh 300™ substrate performed in a complete EL device compared with conventional devices are shown in Figure 8.2.

Table 8.1. TCA properties for a change in PEDOT:PSS ϕ and dry film height

PEDOT:PSS ϕ	Dry Film Height (µm)	Tack (cm)	Conductivity (S/cm)	Transmission (%)
0.0100	60.00	9.95	0.003	78.11
0.0125	57.00	13.67	0.008	75.03
0.0150	49.00	23.20	0.068	75.22
0.0175	45.00	27.55	0.100	73.88
0.0125	15.00	29.79	0.027	91.28
0.0125	27.80	21.67	0.019	86.87
0.0125	57.00	13.67	0.008	75.03
0.0125	80.00	9.50	0.012	66.82
0.0125	105.00	6.03	0.007	59.17

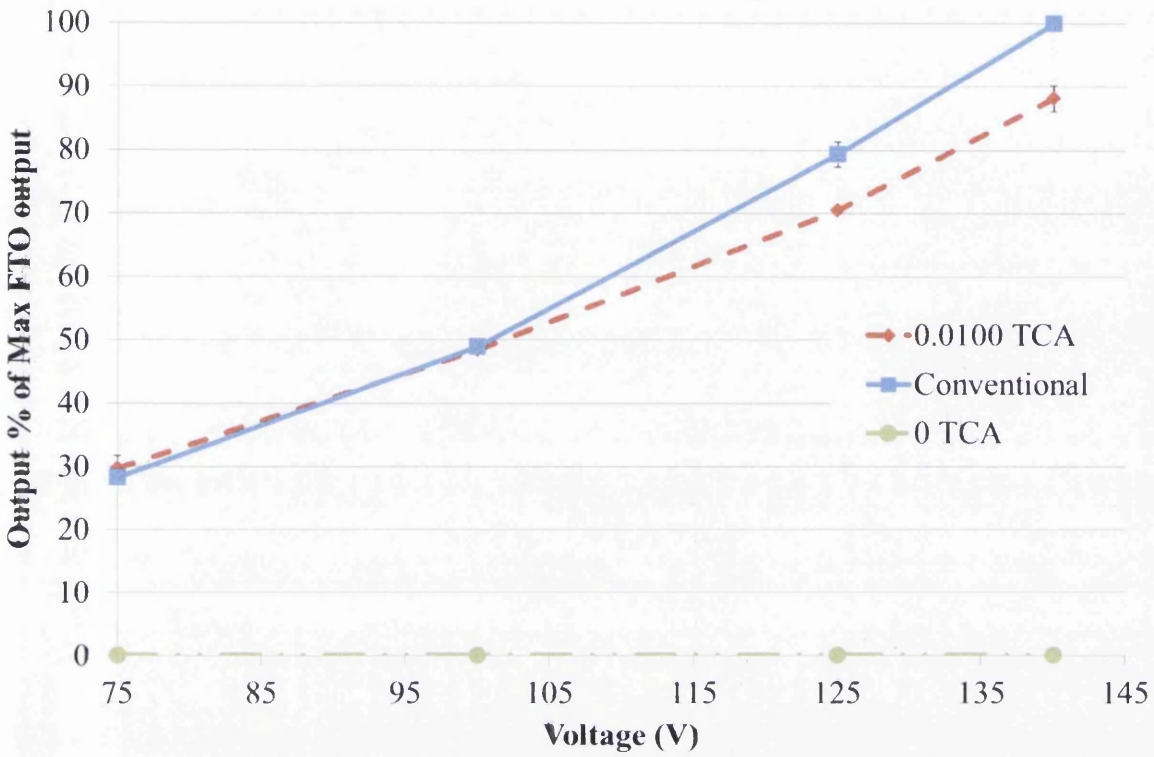

Figure 8.2. The performance of a top emission EL device made with a 0.0100 TCA coated onto an Epimesh 300™ grid as a back contact compared to a conventional EL device. Average of 3 lamps and 3 repeat measurements per data point.

In Figure 8.2 it can be seen that the top emission for an EL device made with a TCA with a 0.0100 PEDOT:PSS ϕ is around 88% that of a conventional built light with an FTO glass electrode at an applied A.C voltage of 140VAC. As the applied voltage is decreased the output of the lamp becomes more alike until at 100VAC they are the same. Figure 8.2 also shows an EL device made with a laminate that contained a 0 PEDOT:PSS ϕ showing no emission. The transmissions spectra of the layers of FTO glass and TCA can be seen in Figure 8.3. It is through these layers that the emitted light penetrates, figure 8.3 shows that at 490nm the TCA's transmission is lower than that of TEC-7 at 76.5 and 84.1% respectively. This data demonstrates the importance of PEDOT:PSS in the TCA as simply laminating a grid using a non-conducting adhesive provided no emission. It further shows that the 88% emission of the 0.0100 TCA EL devices correlates well with the difference in transmission

between the two films, 76.5 and 84.1% for TCA laminate and TEC-7 Glass respectively, shown in Figure 8.4, or the TCA has 90% the total transmission of TEC-7.

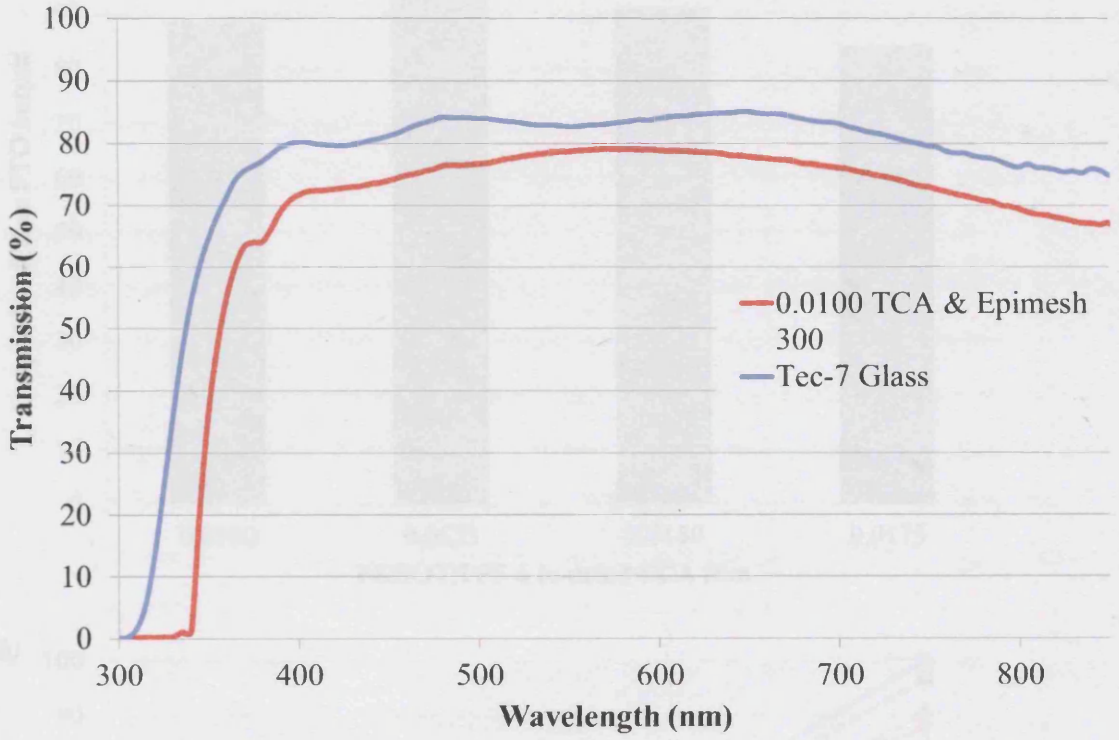

Figure 8.3. UV-Vis transmission spectra for a 0.0100 TCA- Laminate and TEC-7 glass from 300-850nm.

When the PEDOT:PSS volume fraction was increased from 0.0100-0.0175 the emission of the top illuminated device increased to 96% at a ϕ of 0.0125 then subsequently decreased to 91% and 84% as the ϕ increased to 0.0150 and 0.0175 respectively as shown in Figure 8.4a. This result is consistent across the applied voltage range apart from 0.0100 at 140VAC as shown in Figure 8.4b.

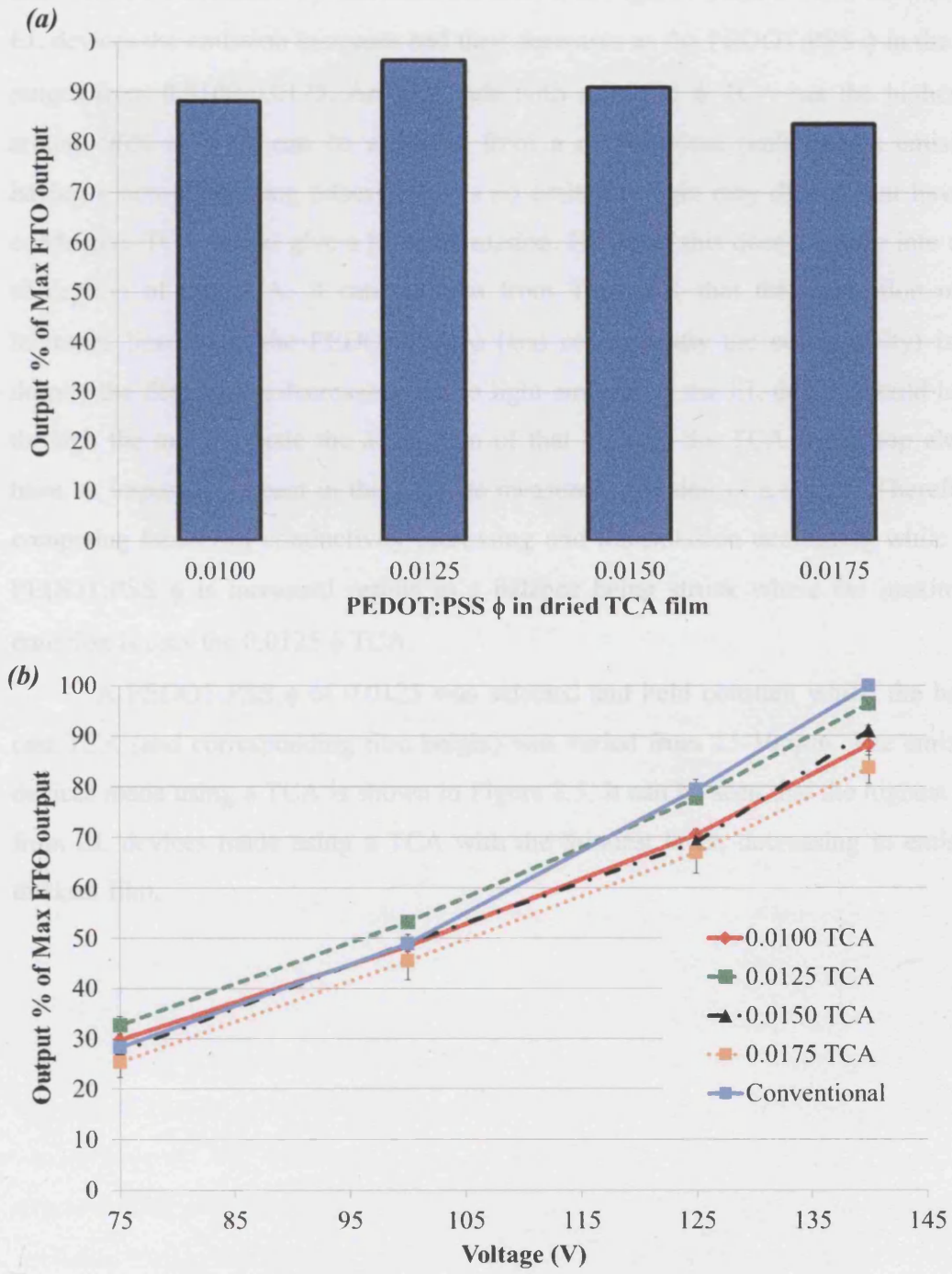

Figure 8.4. Performance of EL devices made with TCAs using varying volume fractions of PEDOT:PSS in the dried film at a) 140VAC and b) a range of VAC. Average of 3 lamps and 3 repeat measurements per data point.

Table 8.1 lists the properties of the TCA. It can be seen that as the PEDOT:PSS ϕ increases the film height decreases (for a given cast height) as does the absorption and the

tack whilst the conductivity increases. As shown in Figure 5a and b when the TCA is used in EL devices the emission increases and then decreases as the PEDOT:PSS ϕ in the dried TCA ranges from 0.0100-0.0175. An EL made with a 0.0125 ϕ TCA has the highest emission around 96% of what can be achieved from a conventional built lamp's emission. Since having a non-conducting adhesive gives no emission logic may dictate that having a more conductive TCA would give a higher emission. However this does not take into account the absorption of the TCA. It can be seen from Table 8.1 that the absorption of the TCA increases linearly as the PEDOT:PSS ϕ (and consequently the conductivity) is increased, despite the film height decreasing. Since light emitted by the EL device would be travelling through the top electrode the absorption of that light by the TCA in the top electrode will have an important impact in the ultimate measured emission of a device. Therefore the two competing factors of conductivity increasing and transmission decreasing while the TCA's PEDOT:PSS ϕ is increased results in a balance being struck where the maximum device emission is uses the 0.0125 ϕ TCA.

A PEDOT:PSS ϕ of 0.0125 was selected and held constant whilst the height of the cast TCA (and corresponding film height) was varied from 15-105μm. The emission of EL devices made using a TCA is shown in Figure 8.5. It can be seen that the highest emission is from EL devices made using a TCA with the thinnest layer, decreasing in emission to the thickest film.

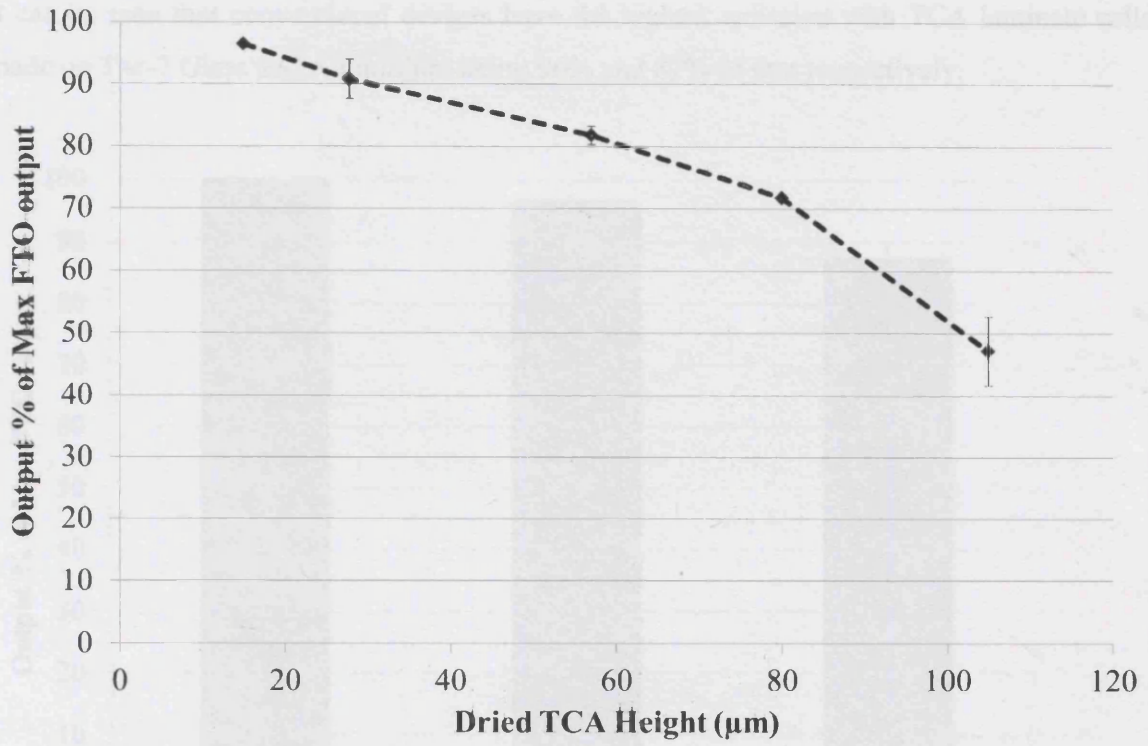

Figure 8.5. Comparative performance of EL devices using a 0.0125 TCA of different TCA dry film heights. Average of 3 lamps and 3 repeat measurements per data point.

The decrease in emission of the device can be explained when looking at the data presented in Table 8.1. This shows that an increase in film thickness will also increase absorption proving detrimental to the EL devices overall emission described above. Table 8.2 also shows the tack increasing as film thickness increases which suggests that either a higher tack results in a lower transmission or more likely the increase in tack has no effect or isn't significant compared with other factor that influence the device emission. Ultimately these results suggests that although all factors will have an influence on the emission to some degree out of tack, absorption and TCA conductivity it is indeed an increase in absorption, increased through either film thickness or an increase in PEDOT:PSS ϕ, once the ϕ is over 0.0125, that is most detrimental to the EL device emission. Therefore in this set up a TCA with 0.0125 PEDOT:PSS ϕ and cast height of 15µm has a value of conductivity and absorption that appears to be optimal and was selected for further study of EL devices fabricated on aluminium substrates.

A comparison of EL devices made on aluminium substrates with ones made on Tec-7 glass both with 0.0125 TCA top electrode and conventional devices are shown in Figure 8.6.

It can be seen that conventional devices have the highest emission with TCA laminate cells made on Tec-7 Glass and Aluminium being 96% and 87% of that respectively.

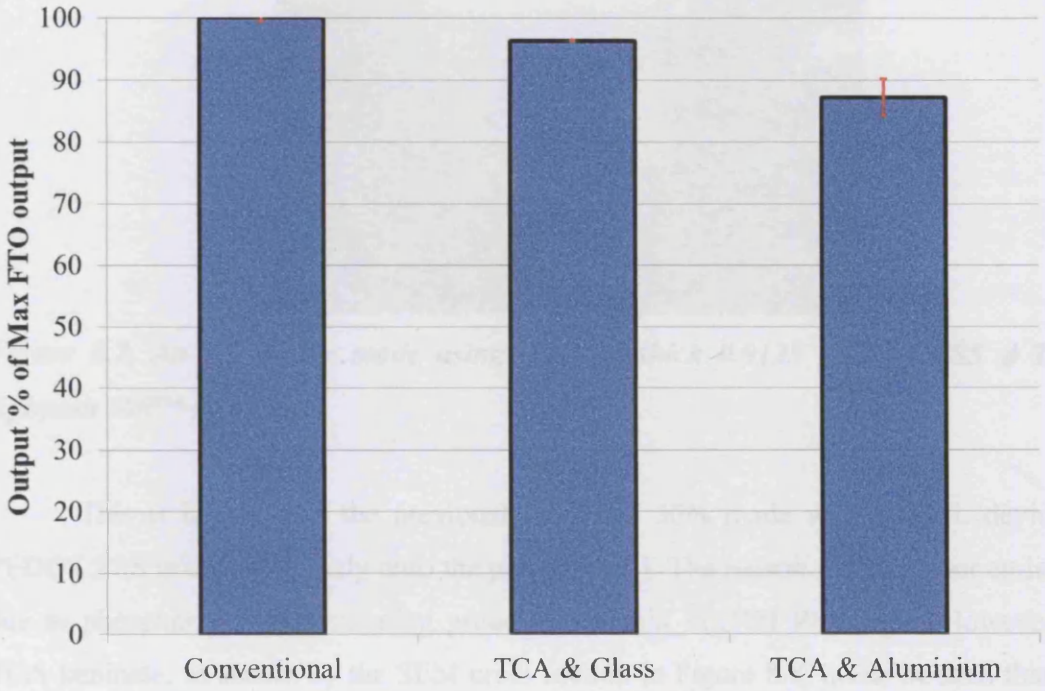

Figure 8.6. Comparative results for EL devices made conventionally on TEC-7 glass, and top emission devices using 0.0125 TCA on Tec-7 Glass and aluminium substrates. Average of 3 lamps and 3 repeat measurements per data point.

This shows that EL devices made on Aluminium substrate lagged only 13% behind the total emission of conventional FTO illuminated device. The drop between devices made on TEC-7 glass and Aluminium substrates can be attributed to the variation in flatness of the aluminium substrate and its subsequent effect on the casted layers. This is shown to manifest itself as larger error seen in Figure 8.6. This highlights the importance of not only high tolerance on the flatness of the substrate but also of the printing method.

The highest emission achieved for an EL device made with a TCA was 96% of that made with a conventional device which is shown in Figure 8.7.

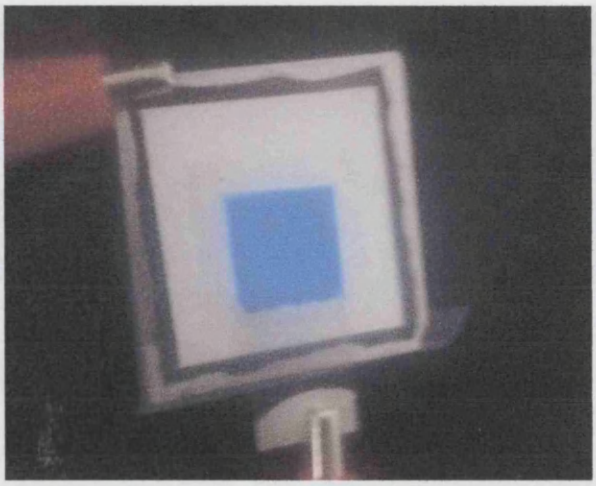

Figure 8.7. An EL device made using a 15μm thick 0.0125 PEDOT:PSS ϕ TCA and Epimesh 300™ grid

This is higher than the previously reported 50% made with and EL device where PEDOT:PSS is coated directly onto the phosphor [7]. The reason for the lower emission was due to phosphor particles standing proud of the thin PEDOT:PSS layer. However for the TCA laminate, as shown by the SEM cross section in Figure 8.8, it can be seen that the soft TCA conforms to the rough phosphor layer ensuring complete coverage of the particles at no loss in sheet resistance. In a paper by Jewell et al [7] the devices were dependant on the sheet resistance of the PEDOT:PSS alone – quoted at 240ohm.sq, in these experiments the laminate set up utilises the Epimesh 300™ grid for lateral conduction, quoted at 1.2ohms.sq.

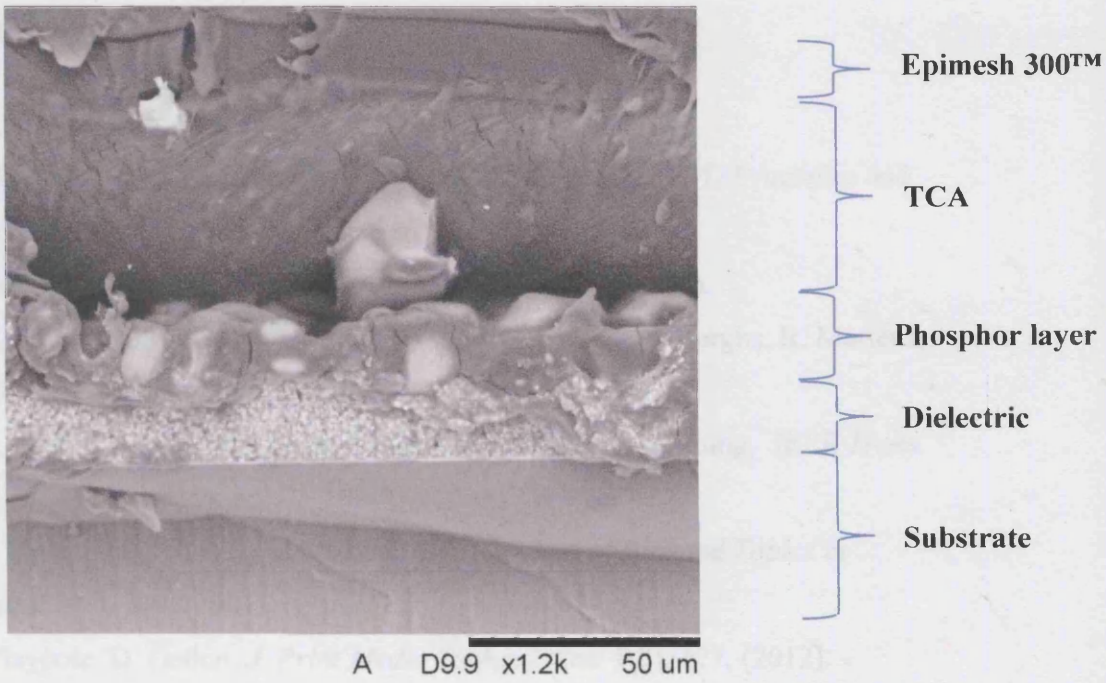

Figure 8.8. SEM micrograph of a cross section through an EL device made with a TCA showing the conformity of the TCA layer to a raised phosphor particle.

The significance of this result, where a TCA is applied to a glass and aluminium mounted EL, suggests that a flexible top emission device can be made that is FTO and ITO free with an emission close to that of a conventional bottom emission device made on FTO coated substrate. Potentially this TCA laminate could be applied to an EL device fabricated onto aluminised paper, reducing cost even further than what is presented here or to OLED devices opening up the opportunity for new technologies and architectures to emerge.

8.3. Conclusions

Top illuminated electroluminescent devices made with a TCA have shown to achieve 96% of the emission of a conventional FTO glass illuminated device. Varying the film height and the PEDOT:PSS ϕ showed the dominant factor influencing the emission of the devices to be the absorbance of the TCA film. The method was also shown to be viable using an aluminium substrate creating a vacuum, silver and indium free fully printed flexible top illuminated EL device.

8.4. References

[1] S. Kirchmeyer, K. Reuter, *J. Mat. Chem.* **15,** 2077, (2005)

[2] A. Elscher, S. Kirchmeyer, W. Lovenich, U. Merker, K. Reuter, PEDOT: Principles and Applications of an intrinsically conductive polymer. CRC. (2010).

[3] B. Winther-Jensen, F. Krebs, *Sol. Ener. Mat. Sol. Cell.,* **90,** 123, (2006).

[4] T. Aernouts, P. Vanlaeke, W. Geens, J. Poortmans, P. Heremans, S. Borghs, R. Mertens, R. Andriessen, L. Leenders, *Thin Sol. Films,* **451,** 22, (2004)

[5] J-Y. Kim, S-H. Park, T. Jeong, M. Bae, S. Songs, J. Lee, I-T. Han, D. Jung, *IEEE Trans. Electron. Devices*, **57,** 1470, (2010).

[6] G. Jabbour, R. Radspinner, N. Peyghambarian, *IEEE Journal of Selected Topics in Quantum Electronics*, 7(5), 769, (2001).

[7] E. Jewell, T. Claypole, D. Gethin, *J. Print Media Technol. Res.* 1(3), 177, (2012).

[8] K. Weigelt, E. Jewell, C. Phillips, T. Claypole, A. Huebler, *Accepted for Publication in Journal of Print and Media Technology Research.* (2012).

9. Conclusions and further work

It was seen in Chapter 3 that a Transparent Conducting Adhesive (TCA) could be made by blending an solutions of Acrylic emulsion adhesive and PEDOT:PSS and curing using a two-step heating process. AFM imaging of the surface of the TCA confirmed that there was outcrops of PEDOT:PSS phases within the adhesive matrix. The TCA's conductivity followed percolation theory whereby the film didn't show any conductivity below a certain volume fraction of PEDOT:PSS (critical percolation threshold) and then increased its conductivity according to a power law at subsequent increases in volume fraction. What was especially interesting about this TCA was that the critical percolation threshold was close to 0.00780, whereas for randomly distributed phases it would be closer to 0.18. It was suggested that this is due to the segregation of the PEDOT:PSS between the particles in the acrylic emulsion which lead to ordering of the particles, however further work involving AFM imaging of cryo-sliced cross sections of the TCA would be needed to confirm this and it not available to the writer at the time of writing. The low volume fraction of the non-adhesive PEDOT:PSS phase lead to the films still having a reasonable tack however further work would be needed to quantify the films adhesive shear resistance and peel strength as well as other adhesive properties. The absorbance of light in the visible region was mainly due to PEDOT:PSS phase and therefore increased linearly with film thickness or PEDOT:PSS concentration. The contact resistance was linked to the surface outcrops of PEDOT:PSS (and therefore the bulk conductivity) as well as the Tack of the film. However it would be of interest to try and quantify the contact resistance on differing surfaces (not just the metallic surfaces used in the experiment) to evaluate if the Work Function of the PEDOT:PSS and the tack of the adhesive on different surfaces played a role. While the TCA was shown to be stable over 5000hrs in ambient conditions, rigorous testing of the TCA needs to be conducted, especially to humidity and UV.

This adhesive could be applied to a gird and applied to an Opto-Electronic device such as a EL lamp shown in Chapter 8 where the emission of the lamp through the TCA was a combination of the films tack, transparency and conductivity. The softer nature of the TCA helped it conform to the rough phosphor film which increased the emission of the lamps over that of a PEDOT:PSS layer alone. While the TCA on a grid could be shown to work on an EL device without the need for another layer, the same was not true for s-DSCs as the current collection of the TCA was too low on the poorly conducting Spiro-OMeTAD layer, as shown

in Chapter 7. For this an additional layer needed to be added on top of the Spiro-OMeTAD that was both of a higher conductivity, transparent and compatible with Roll-to-Roll coating. PEDOT:PSS was selected however the aqueous nature of the PEDOT:PSS dispersion meant that it de-laminated the Spiro-OMeTAD and the 120°C curing temperature left the s-DSCs unusable. Chapter 4 deals with how these challenges were overcome by adding solvents orthogonal to the Spiro-OMeTAD such as IPA and Ethanol in varying amounts. While the addition of the solvents did not affect the conductivity of the cured PEDOT:PSS film excessively the final conductivity of the film it did still affect it a certain amount and the reason for this is not clear at this time. It was shown that curing of the PEDOT:PSS could be done using a forced evaporation cure to keep the temperature below 60°C and the cured point of the PEDOT:PSS could be determined using a non-contact thermal imaging method. Again the change in conductivity and the structure of the films dried using evaporation could not be categorised and would be the subject of further investigation. Evaporation curing did cure the samples at a lower temperature however the time to cure was still in the 560 second time scale which is a long time for commercial roll-to-roll applications, therefore an alternative method of curing using NIR was used in Chapter 5. This showed that since the PEDOT:PSS in the NIR spectrum of the light NIR curing would indeed selectively heat and cure the PEDOT:PSS layer without damaging layers below in a matter of seconds. The conductivity of the PEDOT:PSS cured in this was did again change and the reason for this change could be down to imperfect films being formed due to the accelerated cure of the films. However what would be of interest is to study the films using AFM to find if the PEDOT and PSS phases within the film were affected by the NIR. This is because the PEDOT:PSS solutions have higher boiling point solvents added to them to allow the PEDOT and PSS phases to be mobile longer, forming larger phases in the final dried film and making it more conductive. However if the cure is too quick, even with the high boiling point solvents, the film structure may become 'frozen' with the phases being smaller so through AFM imaging the phase size and ultimately the kinetics of the phase formations could be quantified. Since the TCA also contained PEDOT:PSS it was shown that it could also be cured using NIR. The longer the time spent under the NIR lamp (at the same power settings) meant a less conductive film, however the reason for this has not been specifically concluded and looking at the PEDOT:PSS phase distribution, integrity as well as void formation within the film would be the subject of further work to tell which one of (or combination of) them was the contributing factor in the change in conductivity.

To try and make the s-DSCs even more compatible with current roll-to-roll processing techniques (such as painting of steels) ZnO was used to try and get the sintering of the semiconductor layer (450°C for TiO_2) closet to that of used by conventional paint ovens (~200-300°C). The electrochemical analysis of using ZnO, and sintering it at lower temperatures, was done in Chapter 7 using liquid based DSCs. This found that 250°C could be used as a sintering temperature for the semiconductor layer in the liquid DSCs. Further work would be to look at other low temperature processing methods such as chemical growth of ZnO structures to see if the efficiency of the cells could be pushed further.

The work in Chapters 3, 4, and 5 was then applied to an s-DSC fabrication first on glass and this showed that a s-DSC could be made using a TCA, PEDOT:PSS and grid combination to produce a cell of comparable performance to conventionally made devices using a silver evaporated back contact. The performance of the s-DSCs using a TCA would be a combination of the TCA's film thickness and PEDOT:PSS concentration (and ultimately its tack transparency and conductivity).

Chapter 7 also delivered the main aim of this thesis: to make a s-DSC on a metallic substrate suitable for commercialisation. It was shown that by using the newly developed TCA a s-DSC of comparable efficiency could indeed be made on a metallic substrate, thereby creating the first silver, gold and ITO free, flexible, roll-to-roll compatible, atmospherically produced solid state dye solar cell. This is a major step in the commercialisation of third generation photovoltaic technologies and is both and exciting and significant scientific development which should act as just the beginning of Opto-Electronic devices using TCAs. It is hoped that the easy formulation of the TCA will allow other versions to be formulated with different starting components and additives as to tailor its properties to different applications. This will allow the use of a TCA to be not only widespread within the field of emerging Opto-electronics but also others such as medical and circuit based electronics. Indeed one such field that has undergone rapid expansion and development since the writing of this thesis and its ultimate submission the field of organic-inorganic perovskite photovoltaics. Subsequently the TCA-laminate similar to the set-up presented in this thesis has been applied as an alternative back contact to organic-inorganic lead halide perovskite based solar cells with efficiencies of ~15% already being achieved on lab based cells. As this field continues to grow and develop it is an aim for TCA-laminate to be developed in parallel to match the performance of cells made with an evaporated metal contact. It is hoped that as organic-inorganic perovskite materials reach commercialisation the TCA-laminate will aid in the ability to be able manufacture large area modules for all the benefits it offers over

evaporated gold contacts and alternatives such as silver nanowires. However for this to happen there needs to be new scientific and industrial research into new materials and the application of transparent conducting adhesives such as what has been presented in this thesis.